Magnetic and Electronic Structure of few Perovskites in the form of Bulk and 2D- Superlattices

A Thesis Submitted to

Indian Institute of Technology Guwahati

Doctor of Philosophy in Physics

By

Ravi Kiran Dokala

Roll No: 186121101

Department of Physics
Indian Institute of Technology Guwahati
Guwahati-781039, India

July 2023

Dedicated to my beloved parents, Amma and Nanna

INDIAN INSTITUTE OF TECHNOLOGY GUWAHATI

Department of Physics

Guwahati- 781039

Declaration

"Magnetic and Electronic Structure of few Perovskites in the form of Bulk and 2D-Superlattices" is the result of my own doctoral research work. This work was carried out under the supervisions of Dr. Subhash Thota and Dr. Pankaj Kumar Mishra at the Department of Physics, Indian Institute of Technology Guwahati. To the best of my knowledge, the work presented in this thesis has not been submitted to any other Institute/University for the award of any degree.

Ravi Kiran Dokala
Research Scholar
Roll No: 186121101
Department of Physics
Indian Institute of Technology Guwahati
Guwahati-781039
India.

INDIAN INSTITUTE OF TECHNOLOGY GUWAHATI

Department of Physics

Guwahati- 781039

Certificate

It is certified that the work described in this thesis, entitled "Magnetic and Electronic Structure of few Perovskites in the form of Bulk and 2D-Superlattices", done by Mr. Ravi Kiran Dokala, a Ph.D. student of Department of Physics, Indian Institute of Technology Guwahati, for the award of degree of Doctor of Philosophy has been carried out under my supervision. This work has not been submitted elsewhere for the award of any degree.

Dr. Subhash Thota
Professor
Department of Physics
Indian Institute of Technology Guwahati
Guwahati-781039, India

Dr. Pankaj Kumar Mishra
Associate Professor
Department of Physics
Indian Institute of Technology Guwahati
Guwahati-781039, India

Synopsis report

Complex oxide perovskites have become a classic compound for the research because of their vast potential applications in magneto-electronics. Among various classes of perovskite compounds the *d*- and *f*-block transition metals-based perovskite have gained widespread attention due to the strong correlation between the electron-electron and electron-lattice interaction. The general chemical formula used to describe the perovskite materials is ABX_3, where A and B are cations with A larger than that of B and X is the anion usually oxides or halogens. In general, the rare-earth perovskites have the form $RCrO_3$ and R = Ce structure where R symbolized as rare earth elements. Usually, each corner of the unit-cell is shared by BO_6 octahedral with 12 coordinated A cation, each A site cations are occupied at the corners of the cube, B cations sit at the body centered sites and Oxygen at the face centered positions. The unique physical properties of perovskite materials have gained a huge research attention in recent past because of their applications in many of the magneto-electronic, optoelectronic and photovoltaic devices. Properties such as charge-ordering, large magnetic entropy change, long-range ambipolar charge transport, bipolar exchange bias, multiferroic behaviour make them even more attractive for the applications as well as fundamental research point of view. Apart from all the above characteristics the recent research trends reveal that alkali-halide and organometal halide perovskites can be considered as key materials for photovoltaic applications. Moreover, negative magnetization (NM) and magnetic compensation phenomena has become central theme of research in the rare-earth perovskites. The utilization of the NM and magnetization reversal phenomena in perovskites have opened-up a constructive approach in designating next generation switching devices especially in the field of volatile magnetic memory storage, thermo-magnetic switches, femtosecond optical laser induced high speed read/write magnetic memories, thermally assisted magnetic random-access memory (TAMRAM), etc. Motivated by such novel features and their exquisite applications here in this thesis we report a detailed study of rare-earth perovskites both in the form of bulk and thin-films superlattices. In what follows we present a detailed structure of the PhD thesis which is mainly divided into seven Chapters.

Chapter 1 deals with the introductory concepts including the basic crystal structure of perovskites followed by their intriguing characteristics and their applications. This chapter also deals with different magnetic exchange and related phenomena linking the strongly correlated aspects of the rare-earth perovskites which is very useful in understanding the key results discussed in the subsequent chapters of the thesis. This chapter also provides a brief discussion of some of the novel physical phenomenon like magnetocaloric effect, exchange bias, magnetocrystalline anisotropy, negative magnetization, *etc.* Finally, this chapter provides the key motivation and the central idea of the research problem undertaken in this thesis which is followed by the outline of the subsequent chapters.

Chapter 2 provides a detailed discussion pertaining to the experimental procedure including the synthesis of the proposed systems and their characterization. This chapter also provides the standard thin films fabrication method such as pulsed laser ablation method. Further we discuss about the details of various

characterization techniques employed in the current work such as X-ray diffraction, X-ray photoelectron spectroscopy, Atomic force microscopy, Raman spectroscopy, *dc*-magnetization measurements using VSM based Physical property measurement system.

Chapter 3 demonstrates the elastic strain control of electronic structure, and magnetic properties of $[Pr_{1-x}Ca_xMnO_3/SrTiO_3]_{15}$ superlattices. In this chapter, we focus mainly on the $Pr_{1-x}Ca_xMnO_3$ system along with the insulating $SrTiO_3$ layer with special emphasis on their combined superlattice configuration for two different compositions x = 0.5 and 0.3 grown by PLD technique. We explore the changes occurring on the magnetic ordering and electrical properties of the superlattice $[Pr_{1-x}Ca_xMnO_3/\ SrTiO_3]_{15}$ on (001) oriented $LaAlO_3$ and $SrTiO_3$ single crystal substrates. The main advantage of choosing different substrates is that one can tune the homogeneous strain state of these superlattices and study the interface driven modulated crystal structure, electronic states, magnetic property, and transport property. A systematic study of the role of the epitaxial strain on the physical properties of the proposed superlattice configuration is completely new and has not been reported in the literature until now. Our results and analysis provide the evidence that the residual strain between the substrate and thin films plays a major role in deciding the global magnetic ordering of the highly anisotropic $[Pr_{1-x}Ca_xMnO_3/SrTiO_3]_{15}$ superlattices.

We demonstrate the growth, electronic structure, and in-plane magnetic properties of pulsed laser deposition grown 2D superlattice structures $[Pr_{0.7}Ca_{0.3}MnO_3/SrTiO_3]_{15}$ and $[Pr_{0.5}Ca_{0.5}MnO_3/SrTiO_3]_{15}$ on (001) oriented $SrTiO_3$ and $LaAlO_3$ single crystal substrates. The x-ray reflectivity measurements reveal well-defined interfaces between the manganite and titanate layers along with the existence of Kiessig fringes, providing the evidence for the smooth periodic superlattice structure. On the basis of reciprocal space mapping analysis, we concluded that these superlattices exhibit weak tetragonal distortion. The electronic structure determined from the x-ray photoelectron spectroscopy reveals divalent Sr and Ca, tetravalent Ti, and mixed valent Mn with a pronounce shift of binding energy peaks toward the higher energy side in the superlattices grown on (001) oriented $LaAlO_3$ as compared to those grown on $SrTiO_3$. These superlattices exhibit highly anisotropic ferromagnetic character. We used the law of approach to saturation to determine the anisotropy field (H_K) and cubic anisotropy constant (K_1) for all the investigated superlattices. This analysis yields the highest $H_K \sim 9$ kOe and $K_1 \sim 8 \times 10^5$ erg/cc for the $[Pr_{0.7}Ca_{0.3}MnO_3/SrTiO_3]_{15}$ superlattice system. Furthermore, significant enhancement of the overall magnetic moment and a decrease in T_C (< 100 K) was observed in the case of $LaAlO_3$ grown superlattice, which indicates a substantial role of residual elastic strain on the magnetic ordering. Our results indicate that the strain induced elongation of MnO_6 octahedra leads to finite possibility of non-orthogonal overlapping of orbitals in the presence of large crystal field splitting of e_g levels, which, in turn, causes suppression of the ferromagnetic double exchange interaction. In this study, we have also shown that one can alter the magnetic structure of the superlattices under tensile strain, which may find potential utility in the fields of magnetoelectronic devices.

Chapter 4 emphasizes on the Magnetization reversal, field-induced transitions and H–T phase diagram of $Y_{1-x}Ce_xCrO_3$. In this chapter, we implemented a comprehensive study on the structural, electronic

and magnetic properties of bulk polycrystalline $Y_{1-x}Ce_xCrO_3$ solid solutions in which Ce incorporation has remarkable effect on the overall magnetic properties of the pristine $YCrO_3$ system. Four different compositions (x) of bulk polycrystalline perovskite systems of $Y_{1-x}Ce_xCrO_3$ (x = 0, 0.05, 0.1, 0.2) were synthesized using oxalate-based sol-gel technique. The tolerance factor (t) of the perovskite system $Y_{1-x}Ce_xCrO_3$ with compositions x = 0 and x = 0.1 are 0.853 and 0.855, respectively which makes the crystal structure to distort into the orthorhombic phase. Octahedral distortion parameter (Δ) of the BO_6 octahedra of the perovskite structure decreases from 11.9 to 9.3 with the doping of Ce as the radius of Ce^{3+} cation ($r_{Ce^{3+}}$) is greater than the radius of Y^{3+} cation ($r_{Y^{3+}}$).

The analysis of the magnetic field and thermal variation of the heat-capacity and dc susceptibility data below the antiferromagnetic (AFM) Néel temperature T_N (140–148 K) results the following key features; giant NM, field-induced, first-order, spin-reorientation transitions (16–22 K) accompanied by the thermal hysteresis in $M_{FCC}(T)$ and $M_{FCW}(T)$, intermediate paramagnetic transition (T_{IP}) and negative exchange-bias effect. Magnetic investigations reveal locked AFM and weak-FM configurations in $\Gamma_4\ (G_Z, F_y, A_x)$ phase of $YCrO_3$ (S = 3/2 ground state) unlocks into the $\Gamma_2\ (F_Z, G_y, C_x; F_z^R, C_x^R)$ phase of the canted AFM and FM structures with the dilute substitution of Ce ($x \geqslant 0.05$). Moreover, the easy axis spins continue to rotate in the bc-plane and give rise to a new magnetic phase $\Gamma_2\ (F_Z, G_y, C_x; F_z^R, C_x^R)$ at the low temperatures with a mixed phase Γ_{24} (C–AFM + WFM) between 30 K and 70 K evident as a broad hump in maximum magnetization at $T^* \sim$ 45 K. A detailed analysis of the differential M–H isotherms provides an unambiguous determination of the field-induced transitions across 50 kOe (for x = 0.1 at 50 K) whose temperature dependence clearly shows anomalies across the ordering temperature and spin-reorientation transitions. The asymmetric and symmetric exchange interaction ($J_{AS} \sim$ 0.11 meV and $J_S \sim$ 0.85 meV) between the trivalent Ce and Cr enable the positive quartic-anisotropy field ($H_{K_4} \sim 2.85 \times 10^2$ Oe) along with the second order anisotropy field ($H_{K_2} \sim 5.93 \times 10^2$ Oe). Unlike the pristine $YCrO_3$ compound, the Ce incorporated system exhibits a giant fourth-order anisotropy constant ($K_4 \sim 1.35 \times 10^5$ erg/c.c.) due to the asymmetric exchange interaction between the trivalent Ce–Cr which further lifts the free energy of the system and causes lag in the onset of AFM ordering showing the significant thermal hysteresis ($\Delta T \sim$ 10 K) in the field-cooled (FC)-warming measurement protocol as compared to the FC-cooling mode. The H–T phase diagram, mapped from the isothermal magnetization data and differential magnetic susceptibility data with different measurement protocols clearly distinguishes three prominent regions below the T_N ($\sim$ 150 K), viz (i) long-range canted AFM + weak FM phase ($\Gamma_4\ (G_Z, F_y, A_x)$), ($ii$) Γ_{24} mixed phase and (iii) robust $\Gamma_2\ (F_Z, G_y, C_x; F_z^R, C_x^R)$ AFM + FM phases. Tunable spin–flopped transition ($\sim$ 30 kOe), significant negative exchange-bias field ($H_{EB} \sim$ 2.5 kOe), huge coercive field ($H_C \sim$ 22 kOe) and large NM ($\Delta M \sim$ 280 emu/mole) are the unique characteristic features of the current investigated system. Based on all these results we established a detailed H–T phase diagram of this interesting system. Our results also demonstrate that tunable MR and spin-flip transition in these compounds, which may find profound applications in the field of thermo-magnetic switches/sensors and other memory storage applications.

Chapter 5 emphasizes the irreversible metamagnetic transitions and orbital-ordering in $(Pr_{0.45-x}Yb_x)Sr_{0.55}MnO_3$. we present an extensive experimental analysis to investigate the effect of Yb^{3+}-ion substitution at the Pr^{3+}-sites on the magnetic properties that exhibit irreversible field-induced metamagnetic transitions from AFM to FM at higher temperatures than in the case of $Pr_{0.5}Sr_{0.5}MnO_3$. We provide the details of our sample preparation and characterization methods. Polycrystalline samples of $Pr_{0.45-x}Yb_xSr_{0.55}MnO_3$ (x = 0.02, 0.05, 0.08, and 0.10) were synthesized by conventional solid-state reaction method. Crystal structure analysis was performed using the powder XRD patterns of all the samples x = 0.02 (Pr43), x = 0.05 (Pr40), x = 0.08 (Pr37), and x = 0.10 (Pr35) at the room temperature. The powder XRD patterns exhibit a single-phase perovskite-type structure of space group $I4_1/mcm$ and No. 140 with pseudo-tetragonal symmetry. The obtained lattice parameters of the sample $Pr_{0.35}Yb_{0.10}Sr_{0.55}MnO_3$ are a = 5.4069(1), b = 5.3990(1) Å, c = 7.6909(1) Å and V = 224.51(3) Å^3. The substitution of Yb^{3+} ($r_{Yb^{3+}} = 1.125$ Å) at the Pr^{3+}($r_{Pr^{3+}} = 1.266$ Å) occupied A-sites decrease the lattice parameter c which in turn reduces the volume of the unit cell further. X-ray photoelectron spectrum of Mn-2p with the $2p_{\frac{3}{2}}$ and $2p_{\frac{1}{2}}$ orbitals consisting of Mn^{3+} and Mn^{4+} contributes at a ratio, 39 % : 61 % and a spin-orbit splitting value, Δ_{S-O} = 11.57 eV. ABO_3 perovskite structure, Pr^{3+}, Sr^{2+} occupied A^{3+} - sites make the Mn-ions at the B^{3+}-site oxidize into Mn^{3+} and Mn^{4+} states. Our detailed analysis reveals that the Jahn-Teller active Mn^{3+} ion with the 3d electronic and orbital configuration $t_{2g}^3e_g^1$ gives rise to unusual magnetic-crystalline anisotropic properties along with the $t_{2g}^3e_g^0$, Mn^{4+}-ions by distorting the MnO_6 octahedra which appears to be responsible for altering the Mn-O-Mn bond angles and consequently their ordering behavior. Extensive magnetization measurements reveal the existence of orbital-ordering in $Pr_{0.45-x}Yb_xSr_{0.55}MnO_3$ accompanied by antiferromagnetic (AFM) Néel temperature, T_N at as low as 158 K below the high-T_C (302 K) ferromagnetic (FM) phase. Irreversible metamagnetic transitions from the AFM-FM phase occurs for a specific composition Pr40 (x = 0.05) till T ≤ 220 K. The admixture of metastable states of AFM and FM is quite robust in the investigated system whereas AFM state is mediated by Yb^{3+} ions, while, the FM state arising by field driven thermo-magnetic kinetics. These results open a constructive approach of designing novel spin-valve devices.

Chapter 6 demonstrates the evidence for the field-induced spin-flip transitions in Ce substituted polycrystalline $GdCrO_3$. In this chapter, we deal with the structural and magnetization studies on a polycrystalline perovskite $Gd_{0.9}Ce_{0.1}CrO_3$ prepared from the standard solid-state reaction technique. PPMS based temperature and field (100 Oe ≤ H_{DC} ≤ 1 kOe) dependent magnetization measurements under Field Cooled Cooling (FCC) protocol reveals the temperature and field-controlled spin-flip transition and negative magnetization phenomena which are the key features of the present investigated system. Under H_{DC}, the Cr^{3+} sublattice creates a local field to which the R^{3+} sublattice aligns anti-parallel and compensates the magnetization of the Cr^{3+} sublattice which in turn gives to negative magnetization (M_N ~ -7.15 emu/g at T = 3 K). The overall magnetization M(T) undergoes a second transition at the low temperatures associated with spin-flip transition triggered by the critical field, H_C = 200 Oe at T_{SF} (10 K). Gradual increase in the overall magnetization and cross-over due to spin-flip transition can be understood by the Zeeman interaction term

$E_{zeeman} = -\mu_0 M_{\text{Net}} H_{\text{Ext}} \text{Cos}\ \theta$, where θ is the angle between the M_{Net} and H_{Ext}. In the present system the magnetic ordering prefers the Γ_4 structure in which the spins flip from $(00\bar{1})$ to (001) where, the *c*-axis is the easy axis. The system exhibits better magneto-entropy value $-\Delta S_M$ = 42 J/Kg-K which is higher than the previously reported $GdCrO_3$ values. The reduction in the Cr-O-Cr bond angle through the substitution of Ce^{3+} at the Gd^{3+} site deduce such betterment in the magnetic entropy value. Such multiple thermo-magnetic switching of the investigated system plays a significant role in the development of the field of MRAM devices and as well as magnetic refrigeration.

The final **Chapter 7** presents a brief summary of important findings of our experimental results. In this chapter we also identify some open issues which are potentially interesting for the future studies.

List of Publications:

[1] Elastic strain control of electronic structure, and magnetic properties of $[Pr_{1-x}Ca_xMnO_3/SrTiO_3]_{15}$ superlattices
R. K. Dokala, S. Das, D. C. Joshi, S. Ghosh, Z. Yan, Y. Qi, S. Das and S. Thota,
J. Appl. Phys. 127, 175303 (2020).

[2] Magnetization reversal, field-induced transitions and H–T phase diagram of $Y_{1-x}Ce_xCrO_3$
R. K. Dokala, S Das, B Weise, R Medwal, R S Rawat and S Thota,
J. Phys.: Condens. Matter 34, 065801 (2022).

[3] Magnetic ordering in Ce Substituted Zirconite Nanostructures: Focus on Tunable Energy Bandgap and Local-atomic Environment
R. K. Dokala, S. Das, P. K. Mishra, and S. Thota
Phys. Scr. 98, 095946 (2023).

[4] Irreversible Metamagnetic Transitions in Yb^{3+}-distorted tetragonal $Pr_{0.45}Sr_{0.55}MnO_3$
R. K. Dokala, S. Das, G. Jangam, P. K. Mishra, and S. Thota
J. Phys. D.: Appl. Phys. (2023). (*accepted*)

[5] Phonon scattering and magnetic manifold switching in $(Gd,Sm)CrO_3$
S. Das, **R. K. Dokala**, B. Weise, R. Medwal, R. S. Rawat, P. K. Mishra and S. Thota.
Phys. Rev. Materials 7, 084410 (2023).

[6] Effect of Ce substitution on the local magnetic ordering and phonon instabilities in antiferromagnetic $DyCrO_3$ perovskites
S. Das, **R. K. Dokala**, B. Weise, R. Medwal, R. S. Rawat, P. K. Mishra and S. Thota,
J. Phys.: Condens. Matter **34**, 345803 (2022).

[7] Substrate orientation dependent characteristics of half-metallic and metallic superlattices $[La_{0.7}Sr_{0.3}MnO_3/LaNiO_3]_{10}$
S. Das, R. G. Tanguturi, S. Ghosh, **R. K. Dokala**, R. Medwal, S. Gupta, Z. Yan, Y. Qi, R. S. Rawat, and S. Thota.
J. Appl. Phys. **131**, 125305 (2022).

[8] The role of epitaxial strain on the electronic and magnetic structure of $La_{0.7}Sr_{0.3}MnO_3/LaCoO_3$ bilayers
S. Das, S. Ghosh, R. G. Tanguturi, R. Medwal, S. Gupta, **R. K. Dokala**, R. S. Rawat, S. Das, S. Thota.
AIP Advances **11**, 125115 (2021).

[9] Giant Magneto-caloric effect and field induced spin-flip transitions in Ce substituted $GdCrO_3$
R. K. Dokala, S. Das, P. K. Mishra and S. Thota
(Drafted) 2023

[10] Spin-orbit dynamics in orbital ordered $Pr_{0.45-x}Yb_xSr_{0.55}MnO_3$"
R. K. Dokala, S. Das, P. K. Mishra and S. Thota
(Drafted) 2023

International and national conferences/workshops:

[1] Poster presentation on "Degenerate spin states widening the metamagnetic phase in twinned anti-ferromagnetic Charge-Ordered $Pr_{0.35}Yb_{0.10}Sr_{0.55}MnO_3$" at 9th Forum on New Materials, **CIMTEC** (June 2022) at Perugia, Italy.

[2] Poster presentation on "Evidence for the field-induced Spin-flip transitions in Ce substituted $GdCrO_3$" at Perovskite Society of India Meet, **PSIM** (March 2023) at IIT Roorkee.

[3] Poster presentation on "Negative magnetization and field-induced transitions in $Y_{1-x}Ce_xCrO_3$" at National Conference on Quantum Condensed Matter, **QMAT** (December 2021) at TIFR Mumbai.

[4] Poster presentation on "Pulsed Lase growth of $[Pr_{1-x}Ca_xMnO_3/SrTiO_3]_{15}$ superlattices" at National conference on progress in Material science research, **PMSR** (February 2020) at Dibrugarh University.

[5] Poster presentation on "Crystal structure and magnetic properties of Ge-doped $MnCo_2O_4$" at **INUP** Familiarization workshop organized by CeNSe, (May 2019) at IISc Bangalore.

Acknowledgements

I am grateful to Dr. Subhash Thota and Dr. Pankaj Kumar Mishra for granting me the opportunity to pursue my PhD under their esteemed supervision. I am really grateful for their guidance and supervision throughout the PhD journey. Their expertise in the field and insightful suggestions have been invaluable in shaping my research. I would like to thank Subhash Sir for his constant encouragement and scrutiny about the work amidst the tough seasons of COVID-19 pandemic. His meticulous attention to detail and his support in overcoming challenges during the course of my research. I would like to express my sincere thanks to Pankaj Sir for his patience and help during the final stages of my PhD journey. I am truly grateful for his follow-up and efforts to ensure that everyone involved was on the same page. Their guidance, encouragement, and support have been invaluable, and I am fortunate to have had the opportunity to work under such exceptional supervision.

I would like to take this opportunity to express my gratitude to Dr. Sujit Das, Dr. Yajun Qi, and Dr. Deep Chandra Joshi for their valuable assistance and important suggestions regarding the superlattice work. I would also like to extend my sincere gratitude to Dr. Bruno Weise, Dr. R. Medwal, and Dr. R. S. Rawat for their contributions to the experimental measurements and insightful discussions. Furthermore, I would like to express my heartfelt thanks to Mr. G. Jangam for his support with the high magnetic field measurements. I would like to extend my gratitude and acknowledge the support provided by the funding programs DST FIST-I (XRD), DST FIST-II (PPMS), and the Central Instruments Facility (CIF) in facilitating my research work. I would like to express my heartfelt gratitude to the Council of Scientific and Industrial Research (CSIR), Ministry of Science and Technology, Government of India, for their financial support through CSIR-JRF and SRF grants throughout these years. I also wish to acknowledge the Department of Physics at IIT Guwahati for providing me with this invaluable opportunity.

I would like to thank my lab seniors Prativa Di and Sayan Da for their help and support in the initial days of my doctoral studies. I extend my heartfelt gratitude to them for their help in clearing doubts during the work and more importantly their friendship. Especially, their motivations during our supervisors' scolding. I also thank my juniors Shashank, Ankit, Hota, Shourya, Shalini, Ayush, Mahesh, Joya, Soumya, for the friendly times and talks. I would like to thank my contemporaries Maruti for his friendship. I thank Suchit for his help in the initial days of PPMS measurements. I would like to thank my current post-doctoral senior Dr. Priyanka Di for her happy greetings every day. I also thank my present juniors for their presence. I would like to thank my friend Shaona Das for her friendship and for being there in all my successes and failures and

took my side whenever required. The person who listens to all my discussions and trusts my processes more than me and appreciates the corrections professionally and personally. I would like to extend my thanks to her help and support for co-authoring in all of my journals as well.

I thank my friend Sam for his invaluable friendship and company through the first semester course work and helping me whenever I am stuck with technical stuff throughout the PhD journey. I extend my gratefulness to my pool cool buddies Tarik, Nikhil, Sam, Partha for the John Wick and Equalizer movie times, playing pool, eating outside foods and most importantly to go for bike trip. I thank Rajnandan, and Debabrata Pal for their friendships and times especially during the cricket matches. I would really like to thank my department Badminton group Karuna bhaiya, Sourav bhaiya, Juhi Di, Himanshu, Rahul, Sirshendu, Anterdipan, Akanshu, and Devender bhaiya for sharing the court with me, helping me to improve in playing and trusting me at times of decisions during the badminton tournaments. I thank my other department mates who really helped me and motivated me and shred a smile directly and indirectly.

I would like to thank Jagan anna, Srinivas anna for their fun-filled times and encouragement during the initial stage of my research. I also thank the badminton boys Uday, the accumulator, powerful smasher and Royal Enfield donor, Rohith, the loop holes finder and my financial helper, Krishna Chaitanya, the tournaments creator, and our sportive Captain, Sreekanth, the Inter-IITian, my cricket coach and handsome hunk, Anil, the Inter-IITian and my co-MSDian, Satish, the punch dialogue writer and badminton champion, Aditya, the undertaker of gang, Chandra, the player of sheer will, Big B of our batch, Pilli anna, the Sachin Tendulkar of our cricket team. I also express my sincere thanks to All other Telugu Titans teammates for making the days easier and entertaining with the cricket you brought. I also thank Sunanda, Situshna, Sumanth, Arun, for making me a consistent morning person with their calls to attend the badminton court and encouraged indirectly in becoming a good badminton player. I also thank them for their support and treatment like a family person.

I take this time to thank my ever-happy juniors from BTech - Bhanu, Vamsi(ECE), Vamsi(Civil), Likith, Ragava, Chetan, Parthiv, Ajay, Anudeep for the cricket times and food parties. Thanks for keeping my consistency in playing badminton which helped to stay healthy. The main player and my stress buster and my companion for years Mr. Sasi Sakesh for his wonderful times spent and introducing me to the whole BTech greats listed above. Thanks for the financial help whenever required and more than that for sharing your valuable times.

I thank Rajsekhar anna for his unconditional hospitality he provides every day and being a great support. I thank Rakesh for being the best-fellow, brother and friend. They both really helped in taking up many challenges here at IIT. I thank Vara kumar anna and family, Daniel uncle and family for being a great help at the church. I thank the Anil, Praneet, Pranathi, Persis, and Daya for their lovely times. I also thank, Nitish, Tharun anna, Jeswanth anna, Bhagat anna, Santosh uncle, Sunil anna, Anil anna, Mahesh, Chetan, Venkat anna, and more importantly Pamu Sir, and Roy Sir families. Thank for being a great support in making my life meaningful and joyous.

I take this time to thank Sagar, whose phone calls always helped me to get mentored and mentor him as well. His presence and phone call talks helped me to feel remebered at many times. I thank my mentor Varma anna for suggesting me IIT Guwahati for the PhD. His mentoring and lifestyle influenced me many times and helped me grow spiritually. I also thank my mentor Manoj anna for sharing a great times in Hyderabad in the last five years and for the meaningful and fun-filled phone call talks that really motivate me and feel secured many times. I thank Jose anna, Prem Chand, Jayakar anna, Naveen anna, Yerranna anna, Raju anna, Sujai anna, Rajesh anna, and Calvin, for their meaningful times whenever we met or talk. I would like to thank Pintu, Siva, Lal for being the greatest friends since childhood.

Sharing a major part of my life, and challenges, amma, nanna, and chelli, they have carried the yokes every time they get to know the things about me. They encouraged and morally supported, been my cheer, and joy all through my life. I thank you amma, nanna, chelli, for being such a great blessing in my life. I also thank Prem Raj annaya for his great contributions by inspiration and encouragement since my childhood.

Most importantly, I take this time and share wholehearted thanks to my Lord and Savior Jesus Christ who filled my heart with overwhelming joy through his teachings. He made me walk through the valleys and depths of sorrows and made me taste the heights of success and happiness. Never forsake me but let me learn the teachings of life with his unconditional love and grace. Thanking God for standing as the greatest motivation to achieve greater things in research that is benefitting the humanity and bring glory to His name. I thank you Lord for all the things you have done in my life. I remain grateful and share gratefulness with the people I meet.

Signing off with an overloaded heart with all the love you shared in my journey.

Ravi Kiran

Contents

List of Figures

Chapter 2

Chapter 3

Chapter 6

List of Tables

Chapter 6

List of Abbreviations and Symbols

XRD	–	X-ray diffraction
XPS	–	X-ray Photoelectron spectroscopy
MCE	–	magnetocaloric effect
Eg	–	band gap energy
T_N	–	Néel temperature
T_G	–	Magnetic-Glass temperature
h	–	hours
ZFC	–	Zero-Field Cooled
FCC	–	Field Cooled Cooling
FCW	–	Field Cooled Warming
FM	–	Ferromagnetic
AFM	–	Anti-ferromagnetic
PM	–	Paramagnetic
B. E	–	Binding energy
Å	–	Angstrom
χ	–	Magnetic susceptibility
K	–	Kelvin
M	–	Magnetization
H	–	Magnetic field
T	–	Temperature
U	–	Coulombic parameter
μ_B	–	Bohr magnetron
DM	–	Dzyaloshinskii-Moriya

Chapter 1
Introduction

In 1839, Gustav Rose named the $CaTiO_3$ mineral as "Perovskite" after the name of a Russian nobleman and mineralogist Count Lev Alekseyevich von Perovski who discovered this mineral. Naturally, these perovskites are available as oxides. Perovskites are a class of materials that have gained considerable attention in recent years due to their modern-day electronic device applications with their novel functionalities, and unique magnetic and electrical properties such as tunable metal–insulator transition, high spin polarization, colossal magnetoresistance (CMR), robust ferroelectric, and multiferroic properties [1–3]. General formula of perovskite materials is ABX_3, based on the elements occupying the A, B and X positions, these perovskites are classified into four different categories namely, inorganic perovskites, halide perovskites, hydride perovskites, and perovskite hydroxide [4–7]. Two kinds of inorganic perovskites are intrinsic perovskites and doped perovskites which have realized the phenomenon of piezoelectricity, ferroelectricity, and superconductivity in an unconventional way [3]. The oxygen vacancies and structural deviations from its' cubic symmetry occurring due to the A and B-site cations makes the electron and orbital interactions among the atoms gave a breakthrough in the field of multiferroics [1]. Realization of multiferroic properties in these complex oxide perovskites both in their and two dimensional (2D) heterostructures giving a confidence with their new phenomenon for the magnetic storage and spin-valve device applications [1]. Halide perovskites accommodate alkali halide perovskites and organometal halide perovskites that bear the formula ABX_3 with X = Cl, Br, F etc. The halide perovskite materials have been giving promising results in the field of photovoltaic and light-emitting device applications. Hydride perovskites contain the formula H at the X-site which are very known for hydrogen storage applications. A few examples are $NaMgH_3$, $MgFeH_3$, $MgCoH_3$ etc. which gets formed by heating it to ~ 673 K which can be reversible. Perovskite hydroxides are simply the perovskite structures with OH group occupying the X-sites which tend to stay in a stabilized phase with double perovskite structure [4].

Strongly correlated electron systems are a class of materials in which the behaviour of electrons cannot be described by simple independent particle models such as the Fermi gas or the band theory of solids. In these materials, the interplay between electrons spin, lattice, orbitals, and charge can be so strong that they dominate the material properties, leading to the formation of new phases of matter, such as magnetism, superconductivity, and metal-insulator transitions as shown in Fig. 1.1 [8]. These materials often exhibit rich and complex behaviour that is not well understood using traditional solid-state physics models. Examples of strongly correlated electron systems include transition metal oxides, heavy fermion compounds, and organic superconductors. Understanding strongly correlated electron systems is a major challenge in condensed matter physics and has important implications for a wide range of technologies, including energy storage, superconductivity, and quantum computing. One of the most well-known examples of a strongly correlated electron perovskite system is the high-temperature superconductor $La_{2-x}Sr_xCuO_4$ (LSCO) [9].

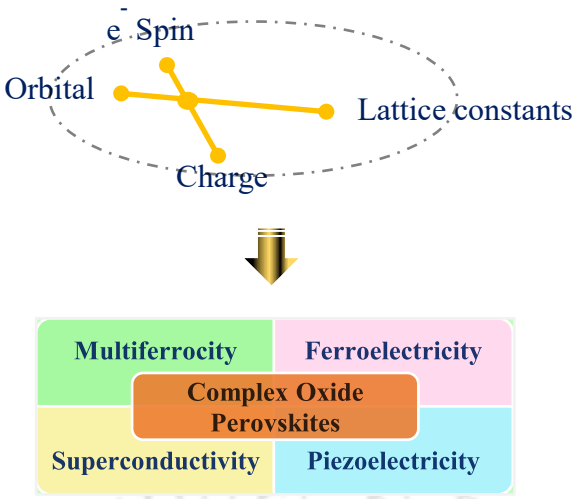

Fig. 1.1. Schematic of strongly correlations among different parameters in the complex oxide perovskite systems and their possible outcome phenomena.

This material exhibits superconductivity at temperatures up to 40 K, and its electronic properties are believed to be strongly influenced by the interactions between the *d*-electrons of the copper ions. Manganite perovskites such as $Pr_{1-x}Ca_xMnO_3$, $Pr_{1-x}Sr_xMnO_3$, $La_{1-x}Ca_xMnO_3$, $La_{1-x}Sr_xMnO_3$ exhibit rich electronic interaction that led to multiple magnetic phases and transport phases [10 –13]. This strong interplay among these electrons and their orbitals made these candidates potential for understanding the exchange interactions and their conducting or insulating phenomena.

Oxide perovskites such as $Pr_{1-x}Ca_xMnO_3$, $Pr_{1-x}Sr_xMnO_3$, $La_{1-x}Ca_xMnO_3$, $La_{1-x}Sr_xMnO_3$, *etc.* possess magnetically rich field-temperature (*H-T*) phase diagrams spanning over a wide range of *H* and *T* for different levels of substitution with their transitions towards the room temperature (*RT*) [14–17]. The concept of magnetization reversal (MR), negative magnetization (NM) and compensation phenomena (T_{Comp}) in the rare-earth (*R*) perovskites $GdCrO_3$, $CeCrO_3$, $YCrO_3$, $SmCrO_3$, $YbCrO_3$, etc. have swiftly reinvigorated the field of strongly correlated electronic oxides in the recent past [18–23]. The rare-earth family of perovskites have attracted immense attention because of their fascinating physical properties such as: multiferroic behaviour, switchable polarization driven by magnetostriction, mixed-phase behaviour. In this chapter, I discuss the crystal structure of the oxide perovskite, exchange interaction that govern the ordering of the charge, orbital and spin, the case for exchange bias (EB), magneto-caloric effect, and the phenomena of magnetization spin reversal.

In this chapter, I bring forth a brief introduction about the strongly correlated electron systems and their potentiality in finding application in the field of spintronics and magnetic device applications. It began with the complex oxide perovskite crystal structure of different space groups and symmetries followed by the discussion of tolerance factor (*t*) and Jahn-Teller (JT) effect. Following this, I have discussed the magnetic exchange interactions. Here, I present details of various magnetic interactions usually present in the perovskites (Direct exchange, Super-exchange, Double exchange, and Dzyaloshinskii–Moriya (DM)

interaction). Further, I discussed the intriguing magnetization features of the perovskite systems like exchange-bias, negative magnetization, magneto-caloric effect. Next, I have briefly explained the low dimensional thin films and superlattice structures and finally, I end the chapter with the motivation and brief description of the research problem presented in the subsequent chapters.

1.1. Crystal structure

Oxide perovskites are the compounds that have the crystal structure based on the perovskite structure of general formula ABO_3, with the cation A at the centre of the cubic unit cell, B cation at the corner of the cube surrounded by the six O anions forming six octahedra at the corners as shown in Fig. 1.2(a) and (b). Rare earth complex oxide perovskites consist of rare earth elements at the A-site, transition metal elements at the B-site and Oxygens at the corners of BO_6 octahedral arrangement. One of the unique properties of oxide perovskites is their ability to exhibit a wide range of electronic, magnetic, and catalytic properties depending on the choice of A and B cations, as well as their doping and crystal structure. The ideal perovskite structure is of cubic symmetry with space group $Pm\bar{3}m$ and space group No. 221. The naturally available oxide perovskite $CaTiO_3$ is not a perfectly cubic perovskite structure. Famously known perovskite structure with different symmetries depending on the different temperature ranges is $BaTiO_3$ comes up with Cubic, orthorhombic, tetragonal, and rhombohedral crystal symmetries as shown in the Fig. 1.3. [24]**.** Possible crystal structures, space groups and space group number with their Wyckoff positions are given in the Table 1.1 below.

Tolerance factor, *t* is a key parameter that governs the stability and crystal structure of perovskite materials. It is defined as the ratio of the radius of the A cation to the sum of the radii of the B cation and O anion. When perovskites are doped with a cation of a different size than the original A-site cation, the tolerance factor can change. In general, if the dopant cation is larger than the original A-site cation, the

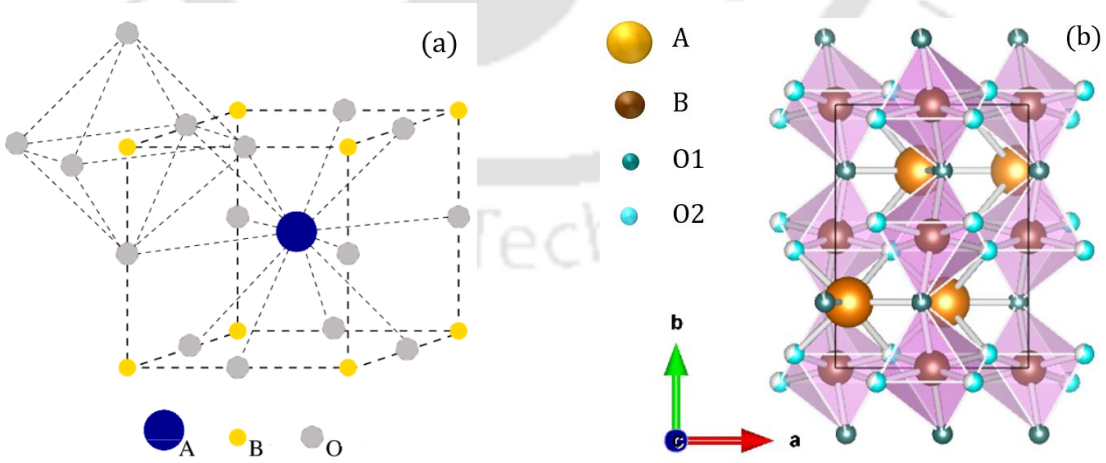

Fig. 1.2. (a) Schematic diagram of a cubic perovskite structure bearing the formula ABO_3 with BO_6 octahedra at the corner of the cube where, A-cation (*blue*), B-cation (*yellow*) and O-anion (*grey*). (b) Perovskite structure with orthorhombic symmetry where A = Y^{3+}/Ce^{3+} (*yellow*), and B = Cr^{3+}(*brown*).

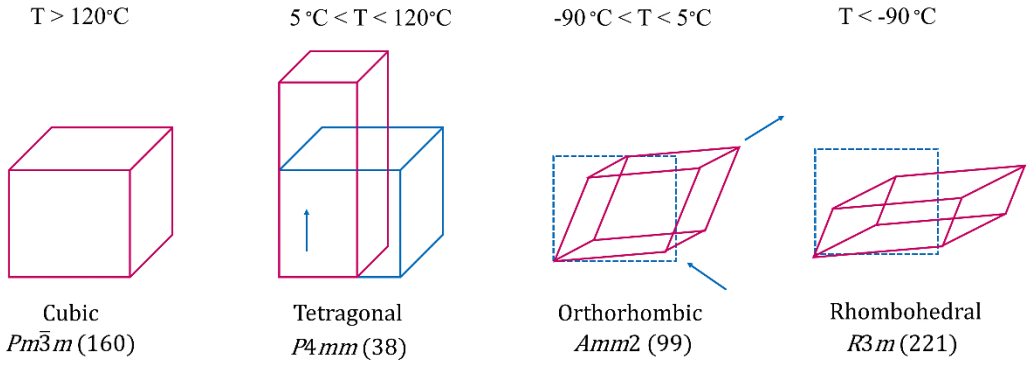

Fig. 1.3. Schematic of crystallographic phase changes in $BaTiO_3$ *w.r.t.* temperature [24].

Fig. 1.4. Schematic of different perovskite crystal structure symmetries exist in correspondence with Goldschmidt tolerance factor [25].

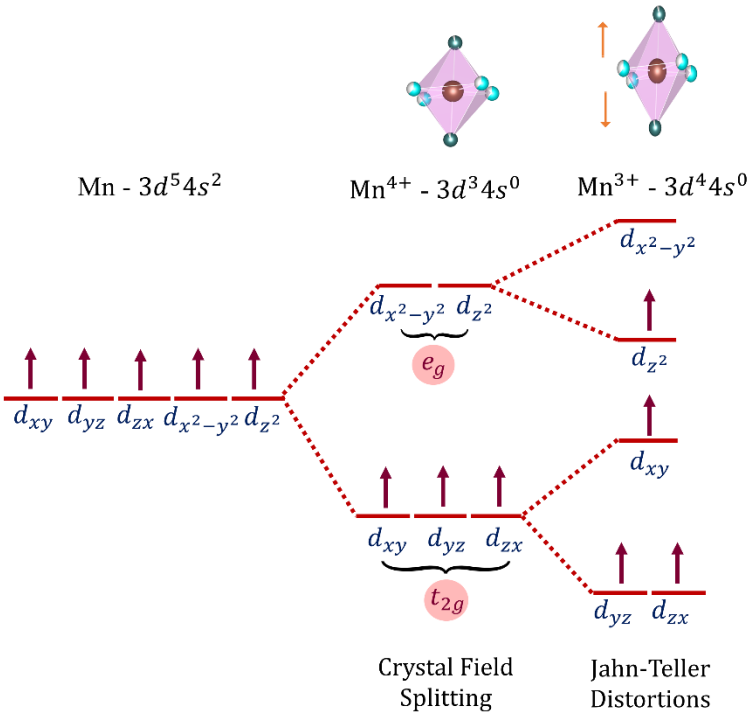

Fig. 1.5. Schematic showing the free Mn-ion degenerate orbitals, Mn^{4+}-non-degenerate orbitals splitted due to crystal field splitting and Mn^{3+} non-degenerate orbitals split further due to Jahn-Teller distortion. MnO_6 octahedra showing the elongation in the case of Mn^{3+} by means of arrows and actual octahedra in case of Mn^{4+}.

Table 1.1. Complex oxide perovskites crystal structures, lattice parameter conditions, space group and number, point group and corresponding Wyckoff positions [26–30].

Compounds	Crystal structure	Lattice parameters	Space group	Point group	Space group number	Wyckoff positions
$SrTiO_3$	Cubic	$a = b = c$ $\alpha = \beta = \gamma = 90$	$Pm\bar{3}m$	O_h	221	A (0,0,0) B $\left[\frac{1}{2},\frac{1}{2},\frac{1}{2}\right]$ O $\left[\frac{1}{2},\frac{1}{2},0\right]$, $\left[\frac{1}{2},0,\frac{1}{2}\right]$, $\left[0,\frac{1}{2},\frac{1}{2}\right]$
$Pr_{0.5}Sr_{0.5}MnO_3$	Tetragonal	$a = b \neq c$ $\alpha = \beta = \gamma = 90$	$I4/mcm$ $P4mm$	D_{4h}	140 99	A (0, 0, 0) B $[x, y, 0]$, $[-x, -y, 0]$, $\left[y, x, \frac{1}{2}\right]$, and $\left[-y, -x, \frac{1}{2}\right]$ O $\left[\frac{1}{2}, y, \frac{1}{2}\right]$, $\left[-\frac{1}{2}, -y, \frac{1}{2}\right]$, $\left[x, \frac{1}{2}, \frac{1}{2}\right]$, and $\left[-x, -\frac{1}{2}, \frac{1}{2}\right]$
$Pr_{0.3}Ca_{0.7}MnO_3$	Orthorhombic	$a \neq b \neq c$ $\alpha = \beta = \gamma = 90$	$Pnma$ $Amm2$	D_{2h}	62 68	A (0, 0, 0) B (x, y, z), (1-x, -y, z), (-x, 1-y, -z), (x, -y, -z), (-x, -y, z), (x, 1-y, -z), (-x, y, -z), and (1-x, 1-y, z) O $\left[\frac{1}{2}, y, \frac{1}{2}\right]$, $\left[-\frac{1}{2}, -y, \frac{1}{2}\right]$, $\left[x, \frac{1}{2}, z\right]$, $\left[-x, -\frac{1}{2}, z\right]$, $\left[x, -\frac{1}{2}, -z\right]$, $\left[-x, \frac{1}{2}, -z\right]$, $\left[\frac{1}{2}, y, -\frac{1}{2}\right]$, $\left[-\frac{1}{2}, -y, -\frac{1}{2}\right]$, $\left[x, \frac{1}{2}, -z\right]$, $\left[-x, -\frac{1}{2}, -z\right]$, $\left[x, -\frac{1}{2}, z\right]$, and $\left[-x, \frac{1}{2}, z\right]$
$BaTiO_3$	Rhombohedral	$a = b = c$ $\alpha \neq \beta \neq \gamma \neq 90$	$R3m$	$R\bar{3}c$	160	A $\left[0,0,\frac{1}{4}\right]$ B (0,0,0) O $\left[x,0,\frac{1}{4}\right]$
$SrSiO_3$	Hexagonal	$a = b = c$ $\alpha = \beta = \gamma = 120$	$P6_3cm$	D_{6h}		A 2a (0, 0, z) 4b $\left[\frac{1}{3},\frac{2}{2},z\right]$ B 6c $(x, 0, z)$ O 2a (0, 0, z) 4b $\left[\frac{1}{3},\frac{1}{2},z\right]$

tolerance factor increases, and the crystal structure becomes distorted, leading to a decrease in symmetry. Conversely, if the dopant cation is smaller than the original A-site cation, the tolerance factor decreases, and the crystal structure becomes more symmetrical. Goldschmidt tolerance factor [31], t can be estimated by the Eq. 1.1 given below:

$$t = \frac{r_A + r_O}{\sqrt{2}(r_B + r_O)} \tag{1.1}$$

where, 't' is the tolerance factor, r_A, r_B and r_O are the radii of the A-site cation, B-site cation, and O-anion, respectively. The occurrence of different perovskite crystal structure symmetries due to the tolerance factor have been evident from different compounds as shown in the Fig. 1.4 [25]. Following this, I understand the Jahn-Teller effect through the crystal-field splitting that modifies the internal electronic and orbital energy levels.

Any kind of non-linear molecular systems containing degenerate electronic states are unstable. They undergo distortions to lower the symmetry and lower the energy that removes the degeneracy. Such distortion of the transition metal complex octahedra occurs through compression or elongation by altering the two axial bonds of the BO_6 is called Jahn-Teller distortion [8, 9, 15, 32]. The phenomenon is well known as Jahn-Teller effect. For example, the high spin d^4 complexes containing the odd number of electrons in the e_g orbitals exhibit significant JT effect as shown in the Fig. 1.5. Especially, Mn^{3+} comprising the electronic configuration of $[Ar]4s^2 3d^4$ is a suitable candidate for this phenomenon while the Mn^{4+} with $[Ar]4s^2 3d^3$ doesn't exhibit Jahn-teller distortions [8].

1.2. Magnetic Exchange interactions

The origin of the "Weiss molecular field" theory keeps on incomprehensible until the beginning of quantum mechanics. Heisenberg showed that the exchange interaction has no classical analogy, and this field is the outcome of the quantum mechanical exchange interaction [33]. The main features of this theory based on the Heitler-London method together with some appropriate background materials are presented here. The normalized Hamiltonian of the two-electron wave function ($\hat{H}^{Spin}$) with spatial co-ordinates $\boldsymbol{r_1}$ and $\boldsymbol{r_2}$ and their corresponding states $\Psi_A(\boldsymbol{r_1})$ and $\Psi_B(\boldsymbol{r_2})$, respectively and spins $\boldsymbol{S_1}$and $\boldsymbol{S_2}$, is

$$\hat{H}^{Spin} = -2J\boldsymbol{S_1}.\boldsymbol{S_2} \tag{1.2}$$

where, the exchange integral can be equated like:

$$J = \int \Psi_A^*(\boldsymbol{r_1})\Psi_B^*(\boldsymbol{r_2})\hat{H}\Psi_A(\boldsymbol{r_2})\Psi_B(\boldsymbol{r_1})\, d\boldsymbol{r_1} d\boldsymbol{r_2} \tag{1.3}$$

where, from the above relation between the magnetic orientation and spatial position of the electron can be decided. When $J > 0$, the two electrons reside inside the same atom and $J < 0$ refers to the neighbouring atoms to kinetically favour the energy [33]. Fundamentally, exchange interactions are two types: (*i*) Direct exchange interaction, and (*ii*) Indirect exchange interaction, which are discussed briefly in the next sections.

1.2.1. Direct Exchange

Exchange interactions are very short ranged which are confined to the nearby orbitals within the same atom and interaction between nearest neighbour atoms. The exchange interaction that undergoes between the nearest neighbour atoms is known as Direct Exchange interaction [34]. The Hamiltonian ($\hat{H}_{dir}$) and effective exchange integral (J^{dir}) for the direct exchange interaction are given in the following equations:

$$\hat{H}_{dir} = J^{dir}\, \boldsymbol{S_a}.\boldsymbol{S_b} \tag{1.4}$$

where, $\boldsymbol{S_a}$, $\boldsymbol{S_b}$ are the respective spins of a^{th} and b^{th} atoms, follows

$$J^{dir} = \frac{1}{2S_aS_b}\sum_{\eta\zeta} J^{dir}_{\eta\zeta} \tag{1.5}$$

where, and, η, ζ are the summation integral variables. Direct exchange interaction plays a crucial role in determining the interaction among the largely spaced spin systems like radicals and in the case of 90° metal-ligand-metal geometry [34]. Further, I discuss the indirect exchange interaction consisting of super-exchange and inter exchange interactions.

1.2.2. Indirect exchange

Interactions that are mediated by another atom in between the two magnetic ions are usually comes under indirect interactions. Indirect interactions are super exchange interaction, double exchange interaction and Dzyaloshinskii-Moriya interaction.

1.2.2.1 Super exchange interaction

Many of the magnetic exchange interactions cannot be understood by the direct Heisenberg exchange interaction as any two magnetic ions are mediated by a non-magnetic ion through which the magnetic exchange of spins takes place. Superexchange interaction is one of such indirect exchange interaction mechanism which is well-known among the manganites. It plays a crucial role in governing the long-range magnetic order of the spin structure.

The Mn ions are interacting through an intermediate oxygen ion which consists of the energetically similar O-2p orbitals with the $Mn-3d$ orbitals. The orbitals of Mn and O^{2-} overlap and share the electrons forming a semi-covalent bond [35, 36]. Three possible interactions involving these Mn^{3+}/Mn^{4+} and O^{2-} ions were well described by the Goodenough-Kanamori-Anderson rules [37, 38]. As shown in the Fig. 1.6, the half-filled t_{2g} spins of two nearest Mn^{3+} ions align oppositely due to the Hund's rule and thus ferromagnetically align with their respective e_g spin. The two spins of the O-2p orbitals align oppositely with each other following the Pauli exclusion principle. The Mn^{3+} e_g spin and O-2p interact antiferromagnetically and thus making the Mn^{3+} ions to interact antiferromagnetically with each other giving

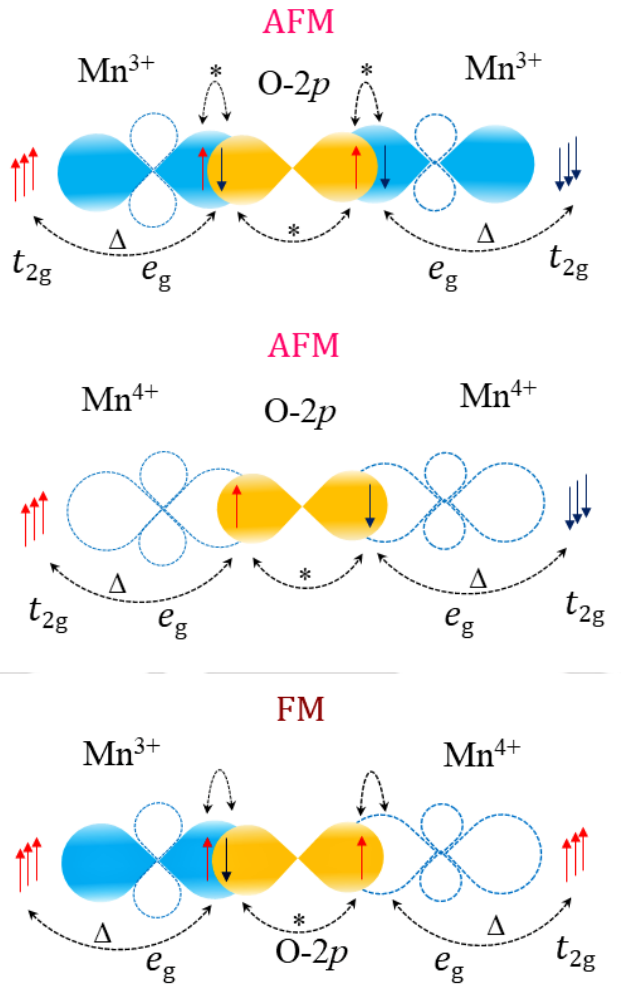

Fig. 1.6. Schematic of AFM superexchange interactions according to the Goodenough-Kanamori-Anderson rules between the (a) Mn^{3+} - Mn^{3+}, (b) Mn^{4+} - Mn^{4+} and weak FM superexchange interaction between the Mn^{3+} - Mn^{4+}. The symbols * and Δ refers to the Pauli exclusion principle and Hund's coupling, respectively.

rise to a strong anti-ferromagnetic (AFM) superexchange interaction between them. In the second case, the Mn^{4+} ions share the empty e_g orbitals with the O-2p spin, and thus making the two half-filled Mn^{4+} t_{2g} spins to align opposite to each other following the Hund's rule that gives rise to strong AFM superexchange interaction. And there is a weak ferromagnetic (FM) superexchange interaction is also possible which can occur between the Mn^{3+} and Mn^{4+} ions, as shown in the third case. Relative orientation and electron population strongly governs the sign and strength of the superexchange interactions. The tolerance factor and JT distortions strongly affects the $Mn - O - Mn$ bond lengths and bond angles as well that can alter the properties of superexchange interactions. As a complimentary exchange interaction that successfully explains the metallic behaviour between the Mn^{3+} and Mn^{4+} ions discussed in the following section.

1.2.2.2 Double exchange interaction

The superexchange interactions falling short of explaining the metallic transport properties among the Manganites. The Double exchange interaction has been understood to explain the metallic transport

properties successfully. The DE interactions deal with the itinerant electrons between the Mn^{3+} and Mn^{4+} ions while superexchange interactions deal with the localized electrons. In this DE interactions the Mn^{3+} and Mn^{3+} interact through the intermediate $O-2p$ orbital [39]. The electron transfers from the $O-2p$ orbital to the Mn^{4+} empty e_g orbital which is ferromagnetically coupled with the half-filled t_{2g} orbital. Simultaneously, the electron from Mn^{3+} e_g orbital hops into the $O-2p$ orbital as shown in the Fig. 1.7. The transfer process makes the electrons mobile between the Mn^{3+} and Mn^{4+} chains making the crystal spin structure conductive. The Mn-O-Mn bond angle closer to 180° favours the FM double exchange interaction the more. Nearest t_{2g} orbitals of the Mn^{3+} and Mn^{4+} align parallelly due to their higher bond angles and thus suggesting an easy transfer of electrons as there is no requirement for the electrons to flip when they hop from one to the other.

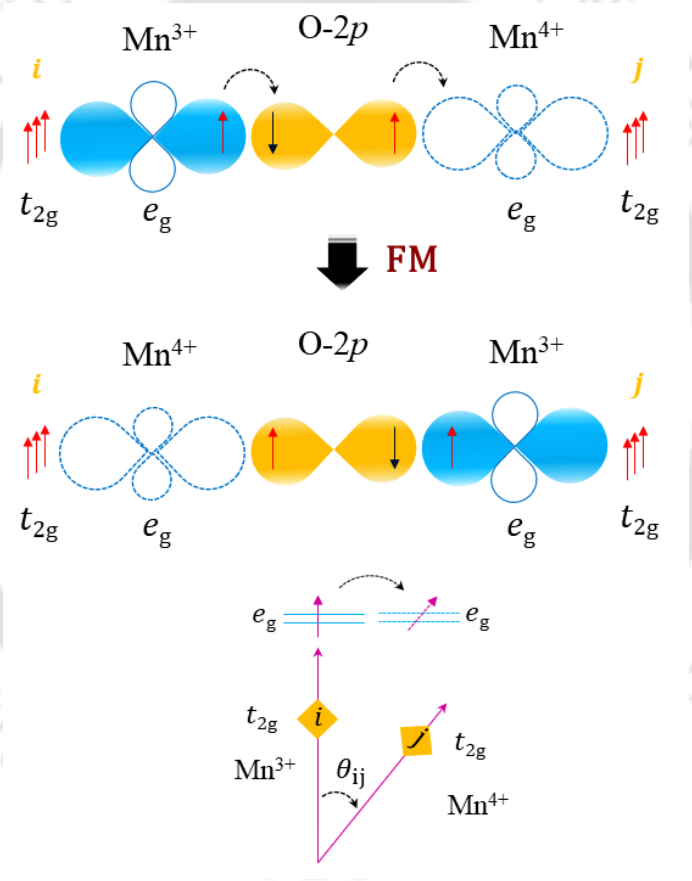

Fig. 1.7. Schematic of (a) Double exchange FM interaction taking place between the Mn^{3+} and Mn^{4+} ions by transfer of electrons through $O-2p$ orbital. (b) Electron transfer under the canting angle θ_{ij} between the Mn^{3+} and Mn^{4+} half-filled t_{2g} orbitals.

The electrons' effective hopping interaction between the Mn ions can be estimated by the following equation:

$$t_{ij} = t^0 \cos\left(\frac{\theta_{ij}}{2}\right) \quad (1.6)$$

where, t_{ij} is the electrons' effective hopping strength, t^0 is the normal transfer integral, θ_{ij} is the relative angle between the neighbouring *i* and *j* Mn ions' t_{2g} spins [40]. The conductivity band width decreases with the decrease in the Mn-$O_{(2)}$-Mn bond angle and thus weakens the FM interaction and conductivity.

1.2.2.3 Dzyaloshinskii- Moriya interaction

The weak ferromagnetism in Cr_2O_3 was explained by Igor Dzyaloshinskii in 1958 with the help of Landau's second order phase transition theory based on the interaction between the spin lattice and magnetic dipoles [41]. In 1960 the antisymmetric exchange interaction was described by means of second order quantization perturbation theory by Toru Moriya starting from the spin orbit coupling. Hence, this microscopic interaction depending on the magnetic moment of each two interacting ions in the system deficient of inversion symmetry has been named as Dzyaloshinskii- Moriya interaction in 1962 is able to interpret many unique phenomena namely magnetoelectric coupling, magnetic Skyrmions and magnetic frustration *etc*. [42]. As per the interest of the thesis, I will briefly elaborate the DM mechanism for rare earth *R*MO_3 perovskites. Considering the cubic symmetry, the angle between the transition oxide metals ions ($\angle M-O-M$) are all 180° with perfect rotational symmetry between the M-M axis as shown in Fig. 1.8(a). In the case of the ionic radii mismatch led reduction in structural symmetry to orthorhombic crystal structure, resulting in the collapsing of rotational symmetry in M-M axis as shown in Fig. 1.8(b). The Hamiltonian involving the DM interaction ($\hat{H}_{DM}$) can be written as in Eq. 1.7 considering $\boldsymbol{S_i}$ and $\boldsymbol{S_j}$ are the atomic spins:

$$\hat{H}_{DM} = \boldsymbol{D_{ij}}.(\boldsymbol{S_i} \times \boldsymbol{S_j}) \quad (1.7)$$

where $\boldsymbol{D_{ij}}$ is the asymmetric exchange interaction parameter which stands perpendicular to the $\angle M-O-M$ plane either pointing in or out the plane. Again, the oxygen ions get displaced from its equilibrium state ($\boldsymbol{d_0}$) due to the structural deformation as well as which is related to the $\boldsymbol{D_{ij}}$ as follows in Eq. 1.8 with γ symbolizing the coefficient and $\boldsymbol{e_{ij}}$ signifying the unit vector between $\boldsymbol{S_i}$ *and* $\boldsymbol{S_j}$:

$$\boldsymbol{D_{ij}} = \gamma\, \boldsymbol{e_{ij}} \times \boldsymbol{d_0} \quad (1.8)$$

For a cubic crystal symmetry, the $\boldsymbol{D_{ij}}$ is zero where for the distorted reduced symmetry like orthorhombic the value can be obtained by means of the deviation of the $\angle O-Mn-O$ from 180° based on the flexibility of the bonds [42]. This mechanism is responsible for the interlayer coupling between the ferromagnetic or(and) another ferromagnetic or(and) antiferromagnetic layer in the thin films. In order to elaborate and realize the competing interaction between the Heisenberg and DM exchange interaction, for a 1D system with spins $\boldsymbol{S_i}$ *and* $\boldsymbol{S_j}$ can be expressed as follows in Eq. 1.9 with J_{ij} represents the Heisenberg exchange interaction coefficient:

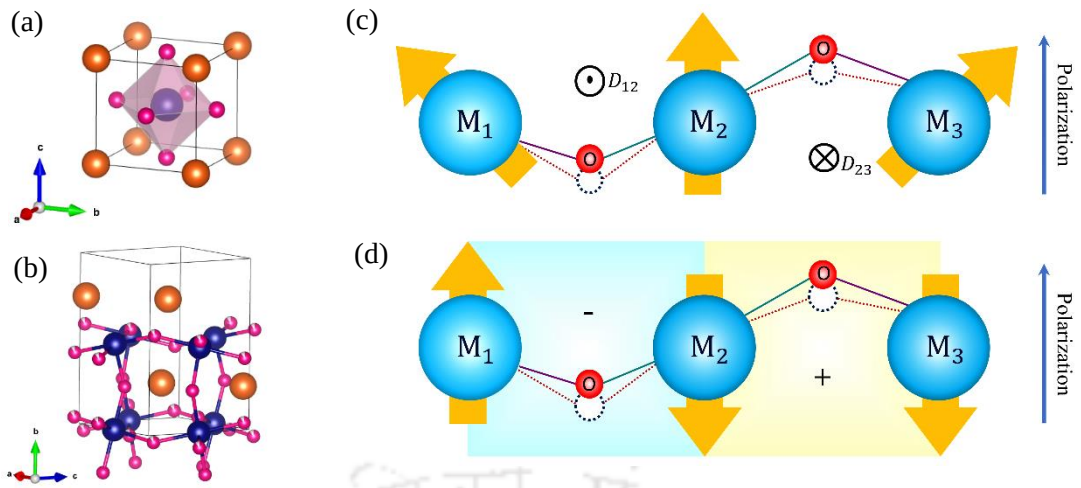

Fig. 1.8. (a) and (b) Crystal structure of an ABO_3 perovskite. (c) Schematic showing the DM interaction along with the respective symmetries and alignment of the vectors.

$$\hat{H} = \sum \{J_{ij}\, \boldsymbol{S_j} + \boldsymbol{D_{ij}} \cdot (\boldsymbol{S_i} \times \boldsymbol{S_j})\} \tag{1.9}$$

Here, the spiral spin order can be easily evaluated by $\tan^{-1}(|D|/J)$ with J is negative or 180° or (-) $\tan^{-1}(|D|/J)$ for J being positive with the condition of both of them are alike, hence a uniform magnitude, D can be generated in the spiral spin ordering system as a result of the DM interaction so that a uniform bias alteration of oxygen as well [42]. In the following sections I have given a brief account on the Spin, Orbital and Charge Ordering phenomena elucidated by the schematic pictorial demonstrations.

1.3. Spin, Orbital and Charge Ordering

Rare earth complex oxide perovskites, especially manganites with hole-doping at the *A*-site produce two different oxidation states of manganese Mn^{3+} and Mn^{4+}. Ordering of these two orbitals govern the whole magnetic behavior in these systems giving rise to spin, orbital and charge ordering phenomena. Charge ordering (CO) usually comes along with T_N or before T_N in the paramagnetic region giving rise to a CE-type AFM spin structure in which JT distorted $Mn^{3+}O_6$ octahedra with e_g orbitals $(3x^2 - r^2)$ and $(3y^2 - r^2)$ participating in the e^- sharing with O-2*p* orbital [14]. Further, arising the inter planar AFM coupling and orbitals ordered as shown in the checkerboard Fig. 1.9(a). This charge and orbital ordered lattice structure localize the charge to the Mn-sites increasing the resistivity to nearly five orders higher and making it an insulator below T_N / T_N^{CO} from metallic FM/PM at higher temperatures. On the other hand, orbital ordering favors A-type AFM spin structure that comes with the JT distorted $Mn^{3+}O_6$ octahedra with e_g orbitals $(x^2 - y^2)$ participating in the e^- sharing or transfer giving rise to a FM intralayer double exchange interactions and AFM inter layer coupling along the longer *c* – axis as shown in the Fig.1.9(b). A-type AFM conducts in the *ab*-plane due to the FM intralayer coupling along the zigzag chains of neighboring Mn^{3+} and

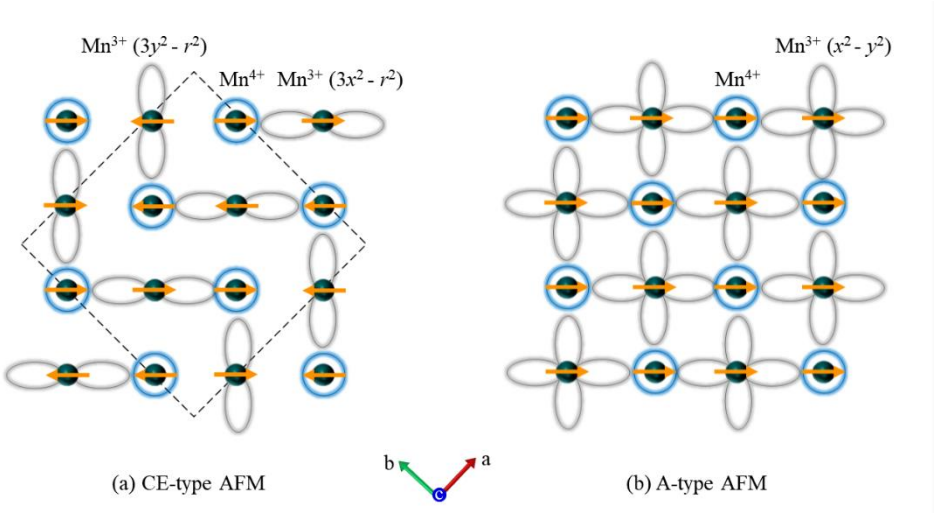

Fig. 1.9. Schematic of (a) CE-type AFM spin structure in the *ab*-plane suggesting the CO phenomena in $Ln_{1-x}A_xMnO_3$. (b) A-type AFM spin structure along the *ab*-plane.

Mn^{4+} e_g orbitals but insulating in the *c* - direction exhibiting interlayer AFM coupling. The phenomena of CO studied in the $La_{1-x}Ca_xMnO_3$, $Pr_{1-x}Ca_xMnO_3$, $Nd_{0.5}Sr_{0.5}MnO_3$, and OO in the $Nd_{0.45}Sr_{0.55}MnO_3$, $Pr_{0.5}Sr_{0.5}MnO_3$ etc. [10–13, 15, 16, 43, 44].

1.4. Metamagnetic Field Induced transitions

Spin Flip and Spin-flop are two examples of a metamagnetic transitions which depends on the magneto-crystalline anisotropy axis [45, 46]. For the antiferromagnetic systems, perpendicular component of magnetic susceptibility, $\chi^{\perp} > \chi^{\parallel}$, parallel magnetic susceptibility. The easy magnetization axis parallel to the applied magnetic field is less unstable while the state at which the magnetization easy axis is perpendicular to the applied field direction is more stable and favourable. Based on this fact, the spins of the magnetic sublattices rotate into the perpendicular direction to the applied magnetic fields. Two different anisotropic scenarios will favour with their weak and strong anisotropic conditions. In the case of spin-flop transition, the two sublattices' magnetization begins to rotate suddenly to a direction perpendicular to the easy magnetization axis (*z*-axis) parallel and to the applied field as shown in the Fig. 1.10(a). This sudden change in direction of the magnetization (*in pink*) driven by the rotation of the magnetic sublattice spins is known Spin-flop transition. In the other case (*in cyan blue*) magnetic moment continue to increase with increasing the magnetic field. In a spin-flip transition, the two sublattice magnetization moment which align antiparallelly along the direction of the easy magnetization axis will rotate suddenly at the external magnetic field, $H_{Ext} = H_{Cri}$, Critical field, in such a way that two magnetic sublattice moments are aligned in the direction of the applied magnetic field as shown in the Fig. 1.10(b). This is famously known as the "Spin-flip transition" which is also well dependent on Zeeman energy, E_{zeeman} that is directly proportional to the

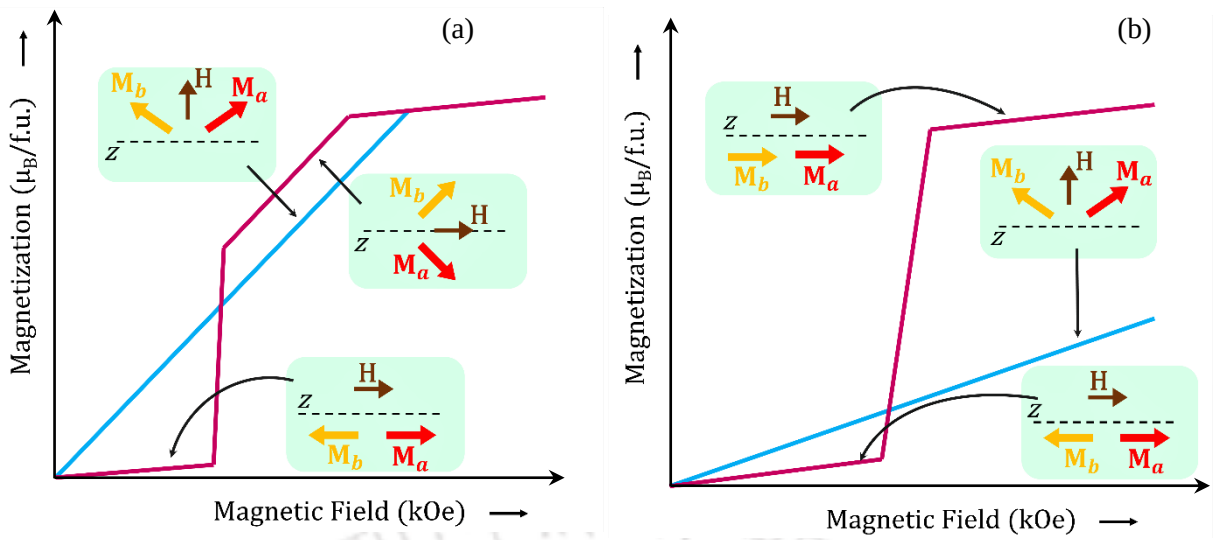

Fig. 1.10. Schematic of metamagnetic transitions evident through the simulated magnetization versus magnetic field graphs exhibiting (a) spin-flop transition (b) spin-flip transition.

applied magnetic field, H_{Ext} as given in the following equation:

$$E_{zeeman} = -\mu_0 M_{\mathrm{Net}} H_{\mathrm{Ext}} \mathrm{Cos}\,\theta \qquad (1.10)$$

where, θ is the angle between the net magnetization, M_{Net} and H_{Ext} and μ_0 is the permeability constant [47].

1.5. Exchange Bias

The unique unidirectional anisotropy resulting the lateral shift of hysteresis loop is nomenclatured as exchange anisotropy or exchange bias. It was first observed by Meiklejohn and Bean while working with ferromagnetic Co nanoparticles possessing T_C of 1390 K with a coating of antiferromagnetic CoO with T_N of 291 K in 1956 and this phenomenon was later explained by Néel [41]. Th ferromagnetic material holding smaller anisotropy and large exchange parameter is generally steady at higher temperature in nanometre range but antiferromagnetic materials possess higher anisotropy value and higher stability at even lower temperature. Hence, the exchange coupling between these two types of materials in heterostructures or bilayers lead to unidirectional anisotropy with major useful applications in magnetic recording as domain stabilizers, giant magnetoresistance (GMR) systems by decreasing the saturation field *etc*. From Fig. 1.11, I can explain the heterostructure containing FM and AFM spins, the application of external field rearranges the FM spins within the temperature region of $T_N < T < T_C$ with the AFM spins remaining scattered. Cooling below T_N, the AFM spins gets oriented antiferromagnetically with respect to the FM domain while the nearest layer of AFM spins order ferromagnetically (as shown in the case (*i*) of Fig. 1.11) and the magnetization reaches its maximum or saturation. With the reversal of the external field, the FM spins start to reorient themselves towards the modified field direction where the higher anisotropy of AFM spins hold them in the previous positions (as shown in the case (*ii*) of Fig. 1.11) along with wielding a interfacial

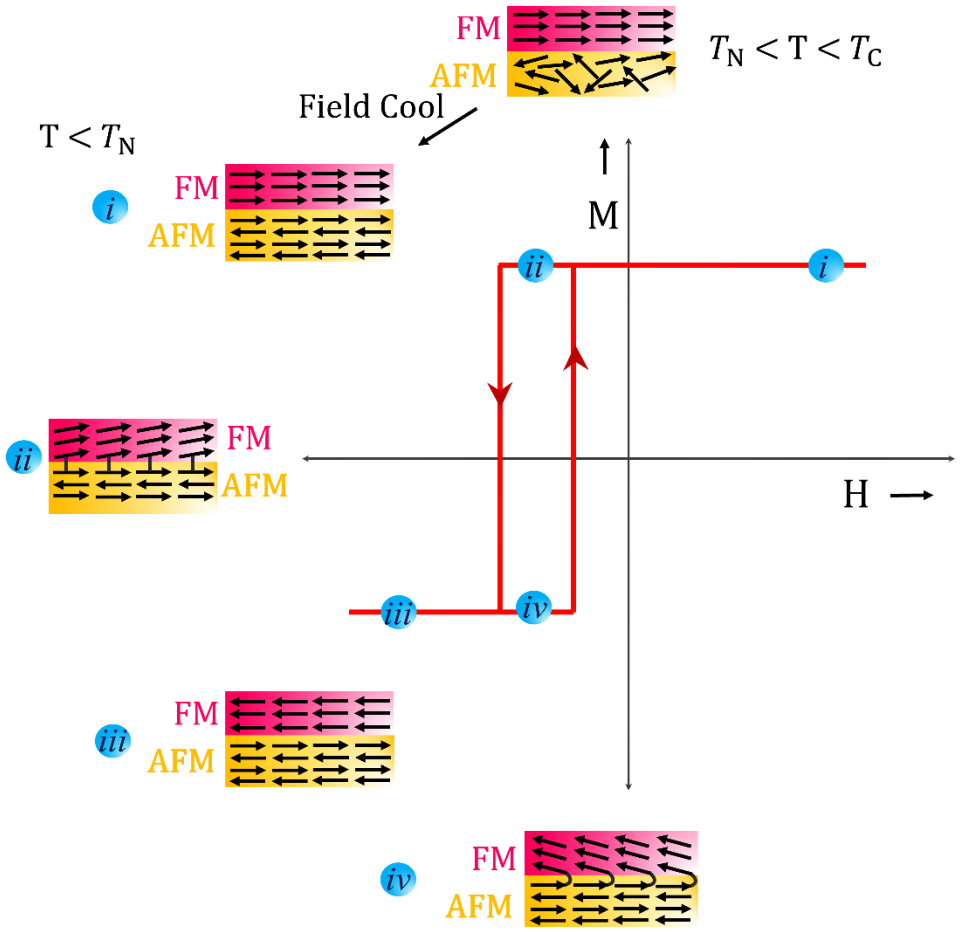

Fig. 1.11. Schematic of exchange bias observed through the simulated magnetization versus magnetic field loop at different cases occur due to the FM and AFM bilayer.

microscopic torque on the very next layer of the FM layer in order to stop them from rerating. Hence, the anisotropy of the FM domain becomes unidirectional, and the external field required to rotate the whole FM layer in presence of the coupled AFM layer is larger than that of the single FM layer in order to compensate the interfacial torque called as exchange bias. After attaining the saturation magnetization (as shown in the case (*iii*) of Fig. 1.11), next with the change of the field direction towards its original one, the FM spins try to regain its previous state by rotating towards the field with smaller magnitude itself as a result of the interactive torque exertion of the nearest AFM spin layer and hence reaches to the condition elaborated in the case (*iv*) of Fig. 1.11). In real case, various external parameters like roughness, anisotropy or spin dynamics make the system more complicated to explain the origin of exchange bias [32, 48].

The EB property has been detected in spin glass systems like amorphous $Fe_{1-x}Zr_x$ [49], ferrimagnetic materials like TbFe [50], GdCo [51], thin films of Fe-FeO [52], Ni-NiO [53], AFM materials like FeF_2 [54], metallic AFMs like $Fe_xNi_yMn_{1-x-y}$ [55], $Fe_{50}Mn_{50}$ [56] *etc.* This characteristic has also been well explored in rare earth chromate oxide perovskites like $La_{1-x}Sr_xMnO_3$, $Y_{1-x}Pr_xCrO_3$, $Y_{1-x}Ce_xCrO_3$ systems etc. [57–59].

1.6. Magneto-caloric Effect

Lord Kelvin first proposed the theoretical prediction of magnetocaloric effect in 1860 with the help of thermodynamical constraints for Ferrum in the presence and removal of external magnetic field while E. Warburg demonstrated the same experimentally in 1881. Temperature as low as 0.25 K was obtained using $Gd_2(SO_4)_3.8H_2O$ with liquid He as cooling agent and external filed of 800 Oe. First magnetic refrigerator using the magneto-caloric effect of temperature span 47 K was developed by Brown for Gadolinium metal [60,61]. The efficiency of such refrigerator can be increased up to 30% with comparison to the traditional vapor-compressor refrigerator. The microscopic origin of magneto-caloric effect is interaction between the magnetic sublattice and the external magnetic field leading to the alteration of the entropy of the system. The pictorial version for the understanding of magneto-caloric effect is given in Fig. 1.12. In comparison with an isothermal compression of gas, the isothermal magnetization of ferromagnet can be explained where increment in pressure with fixed temperature promotes the entropy reduction is analogous to decrease in magnetic entropy with the application of magnetic field. Now, entropy of ferromagnetic material consists of magnetic (S_{magnetic}), lattice (S_{lattice}) and electronic ($\Delta S_{\text{electronic}}$) entropies depending

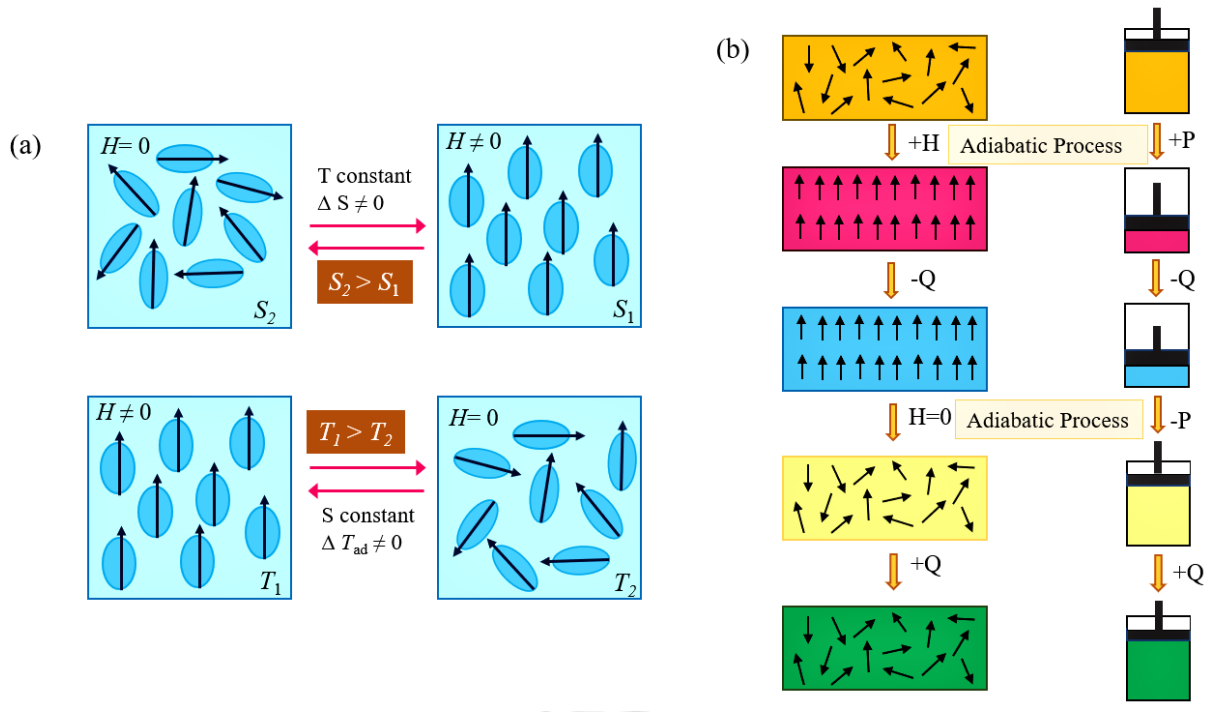

Fig. 1.12. (a) Schematic diagram portraying the two basic processes of the magnetocaloric effect when a magnetic field is applied or removed in a magnetic system considering the isothermal process, (leading to an entropy change) and the adiabatic process (resulting temperature variation). (b) Schematic diagram of the magnetic (left) and vapor-based (right) refrigeration cycles.

on both external field (H_{Ext}) and temperature (T) as given in the equation:

$$S_{\text{Total}} = S_{\text{magnetic}} + S_{\text{lattice}} + \Delta S_{\text{electronic}} \tag{1.11}$$

Now, in the presence of adiabatic H_{Ext} keeping the S_{Total} fixed i.e., S(T_{iniial}, H_{initial}) = S(T_{final}, H_{final}), the S_{magnetic} decreases hence the temperature rises with the adiabatic increase in temperature can be formulated as given in the equation:

$$\Delta T_{\text{adiabatic}} = T_{\text{final}} - T_{\text{initial}} \tag{1.12}$$

On the other way, with the application of isothermal H_{ext}, the S_{Total}, $H_{initial}$ and H_{final}, initial and final magnetic field, respectively being decreases with the decrement of S_{magnetic}:

$$\Delta S_{\text{magnetic}} = \text{S}(T_{\text{initial}}, H_{\text{initial}}) - \text{S}(T_{\text{initial}}, H_{\text{final}}). \tag{1.13}$$

Hence, the ferromagnetic material heats up with the increase in magnetic order with $\Delta T_{\text{adiabatic}}$ being positive and in the contrary, the lowering of magnetic field leads to negative $\Delta T_{\text{adiabatic}}$ and cooling of the material.

The magnitudes of $\Delta T_{\text{adiabatic}}$, $\Delta S_{\text{magnetic}}$ can be obtained using Maxwell's equation [33]:

$$\left(\frac{\delta S\ (T,H)}{\delta H}\right)_T = \left(\frac{\delta M\ (T,H)}{\delta T}\right)_H \tag{1.14}$$

Integrating I get,

$$\Delta S_{\text{magnetic}}(T,\Delta H) = \int_{H_1}^{H_2} \left(\frac{\delta M\ (T,H)}{\delta T}\right)_H dH \tag{1.15}$$

And,

$$(dT)_{adiabatic} = \left(\frac{\delta T}{\delta S}\right)_H \left(\frac{\delta\ S}{\delta H}\right)_H dH \tag{1.16}$$

I know, heat capacity (C_H),

$$C_H = (C\ (T,H))_H = T\ \left(\frac{\delta\ S}{\delta T}\right)_H \tag{1.17}$$

Now putting this value of $C\ (T,H)$ in using Eq. 1.16 and using Eq. 1.14, I get

$$(dT)_{\text{adiabatic}} = -\left(\frac{T}{C\ (T,H}\right)_H \left(\frac{\delta M\ (T,H)}{\delta T}\right)_H dH \tag{1.18}$$

Integrating I get,

$$\Delta T_{\text{adiabatic}}\ (T,\Delta H) = -\int_{H_1}^{H_2} \left(\frac{T}{C\ (T,H}\right)_H \left(\frac{\delta M\ (T,H)}{\delta T}\right)_H dH \tag{1.19}$$

The refrigeration cooling capacity (RCP) can be evaluated as follows:

$$RCP = \int_{T_1}^{T_2} \Delta S_{\text{magnetic}}(T,\Delta H)\, dT \tag{1.20}$$

1.7. Magneto-crystalline anisotropy

Magnetic anisotropy signifies the dependence of magnetic property of a material on the direction they are getting measured, and this has achieved a distinguished importance in commercial platform in order to engineer the magnetic material. The anisotropy can be of three main categories namely, magneto-crystalline anisotropy, shape anisotropy, and stress anisotropy and other types consisting of exchange anisotropy and anisotropy influenced by magnetic annealing, irradiation *etc.* Among all these, only magneto-crystalline anisotropy only refers to the intrinsic characteristic of the material.

Considering the 3*d* transition element ferromagnetic single crystals, their behaviour of exhibiting different saturation magnetization along different directions can be a good example of magneto-crystalline anisotropy i.e., for Fe [100] is the easy direction for getting magnetized where [111] is the hard direction in contrary to which Co finds [001] as the easy axis. The anisotropy energies (E_1) for different symmetries are as follows with α_i as the magnetization direction cosine values [32].

For a hexagonal system,

$$E_1 = K_1 sin^2\theta + K_2 sin^4\theta + K_3 sin^6\theta + K_3' sin^6\theta sin6\phi \quad (1.21)$$

and for cubic system,

$$E_1 = K_{1c}(\alpha_1^2\,\alpha_2^2 + \alpha_2^2\,\alpha_3^2 + \alpha_3^2\,\alpha_1^2) + K_{2c}\,(\alpha_1^2\,\alpha_2^2\,\alpha_3^2). \quad (1.22)$$

where, K_1, K_2, K_3 and K_3' symbolises the anisotropy constants, θ being the angle between the corresponding axis and the easy axis, ϕ is the angle taken from the two-fold axis in the basal plane and K_{1c} and K_{1c} are the anisotropy constants of cubic system. The probable two origin of this magneto-crystalline anisotropy are: single-ion involvement and two-ion involvement. The single-ion contribution is related to the magnetic electron consisting of orbitals influenced electrostatic interaction. The crystal field influences an orbit towards equilibrium while the spin-orbit interaction tries to orient the magnetic moment in a specific crystallographic direction. In case of a ferromagnetic material the resultant contribution of each single ion leads to the macroscopic energy value assuming all the local ion contribution are equivalent directional. For the case of two-ion anisotropy, it relays the dipole-dipole exchange interaction anisotropy. Two magnetic dipole each with moment m, one with parallel arrangement and another with back-to-back arrangement in a straight-line, the second one will be obtaining lesser energy value by magnitude of $3\mu_0 m^2/4\pi r^3$ with r being the distance from centre and μ_0 being permeability constant. For cubic crystal symmetry, the dipole interaction magnitude nullifies spreading throughout the lattice, but this clarifies the ferromagnetic anisotropy in case of lower symmetry crystals [62].

1.8. Negative magnetization

This section deals with the concept of negative magnetization and magnetization reversal because the majority of the manganites exhibits this unique phenomenon. When the magnetic sample is cooled under

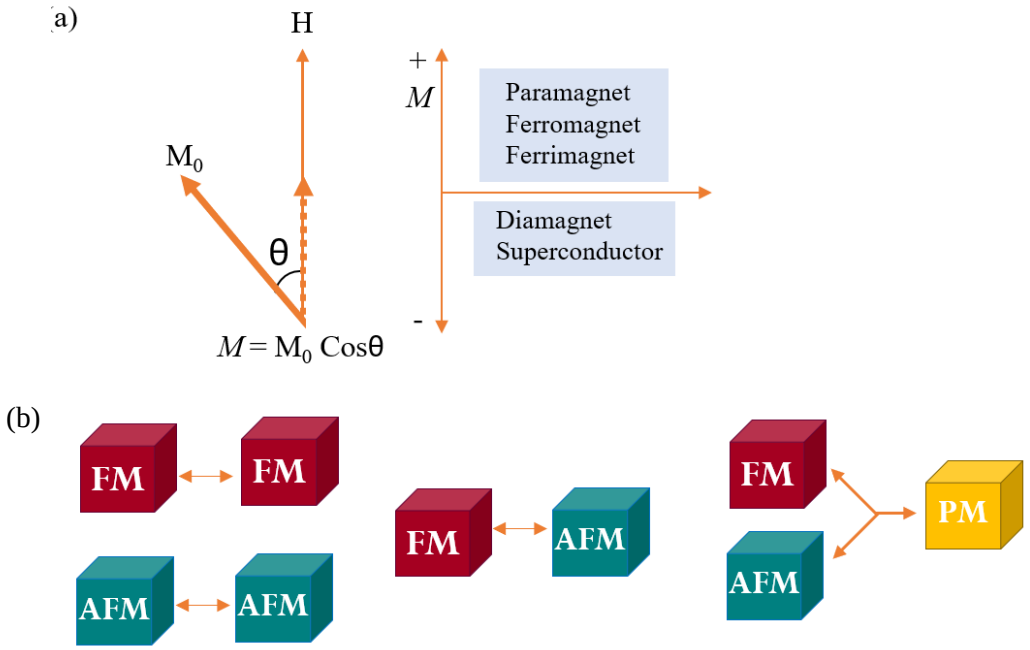

Fig. 1.13. Schematic of (a) the direction of DC magnetization component in the presence of the external magnetic field (H) direction (*shown on the left*). Sign of magnetization of various materials under the application of an external H (*shown on the right*). (b) Possibilities of negative exchange coupling that can occur between different magnetic sublattices.

the influence of the positive magnetic field, a crossover of the sign of magnetization from a positive value to a negative value is observed in the temperature dependence of magnetization which is popularly known as "Magnetization reversal" or "Negative Magnetization". The negative magnetization (with a positive differential susceptibility, $\frac{\partial(\chi T)}{\partial H}$ occurs in the PM, FM and ferrimagnetic materials is completely different from the diamagnetic state (with a negative differential susceptibility) which occurs in case of superconducting/diamagnetic materials (as shown in the Fig.1.13) [63]. Negative magnetization is observed in five different circumstances such as Negative exchange, NE coupling among FM sublattices, NE among canted AFM sublattices, NE among FM/CAFM and PM sublattices, Imbalance in the spin and orbital moments, and Interfacial exchange coupling between FM and AFM phases.

The phenomenon for the present work is focused on the CAFM sublattices and third categories *i.e.*, among FM/CAFM and PM sublattices, of the ABO_3 perovskite structures of orthochromites ($RCrO_3$) and orthomanganites ($RMnO_3$) where, R = rare earth element fall under these categories to show negative magnetization. Antiparallel coupling between the FM/CAFM and PM sublattices at different crystallographic sites give rise to negative magnetization in several *d* and *f*-block elements which have sufficient number of valence electrons in outer orbitals, respectively. This produces negative magnetization due to the interaction between them. Different temperature dependence of the two sublattices elements gives rise to the variations of their magnetic behavior which in-turn results in negative magnetization. Following Eq. 1.23 represents the Hamiltonian for the NE coupling between the canted-AFM sublattices [63]. In the

case of CAFM sublattices, the spin canting *w.r.t* the one and the other crystallographic site led to the exchange coupling to show negative magnetization in Eq. 1.23, where the consecutive terms are the Heisenberg isotropic exchange, DM exchange interaction, single ion anisotropy, and Zeeman energy, respectively. The parameters J_{ij} is the exchange coupling constant, $\boldsymbol{d_{ij}}$ is the DM vector, S_i and S_j are the spins of the i^{th} and j^{th} atoms and K is the magneto-crystalline anisotropy constant.

$$\mathrm{H} = -\sum_{ij} J_{ij}\boldsymbol{S_i}.\boldsymbol{S_j} + \sum_{ij} \boldsymbol{d_{ij}}\,(\boldsymbol{S_i} \times \boldsymbol{S_j}) - K\left[\sum_i S_i^2 + \sum_j S_j^2\right] - \mu H\left[\sum_i S_i + \sum_j S_j\right] \qquad (1.23)$$

Rare earth and transition metal oxides exhibit several technological applications useful in industries, renewable energy sectors and military technologies depending on their multifunctional aspects. In particular, the novel magnetic behavior of these systems is quite demanding in the field of information storage device applications such as thermally assisted magnetic random-access memory (TAMRAM). Furthermore, tunable magnetic entropy changes and large relative cooling powers of the perovskite systems have practical applications in the field of magnetic refrigeration technologies [64].

1.9. Quantum Well and Superlattice structures

The engineering techniques lead to the quantum confinement of the electrons flow and laid down a pathway to the production of *Quantum well* structures. Since the emission wavelength is in comparable range of the band gap energy of semi conducting materials, band-gap engineering became an important technique. Along with the assistance of epitaxial growth new electronic states have been designed by exploiting the quantum confinement properties. It paved a path for the scientists to explore the new intuitions into fundamental physics and also the engineers to use these unique properties in device applications. Quantum confined structures are the epitaxial grown crystal structures that allow the motion of electrons/holes in one or more directions by potential barriers [65]. Quantum size effect becomes more

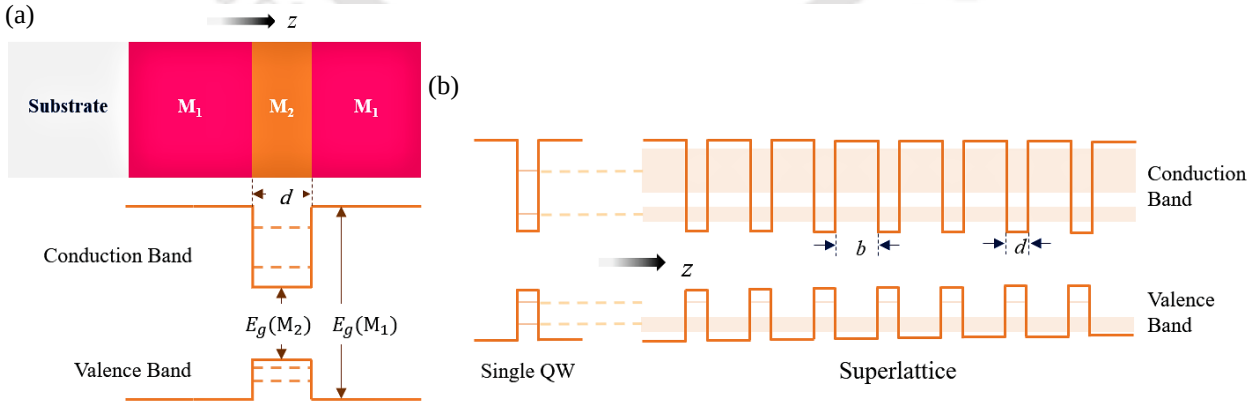

Fig. 1.14. Schematic diagram of (a) the grown layers of Material (M_1) and Material (M_2) and resulting band diagram for the quantum well of thickness *d*. (b) the superlattice structure of period $\Lambda = (b+d)$ where, *b* is the thickness of one material and *d* is the thickness of another material.

significant when the grown thickness of the layer is comparable to the de Broglie wavelength of electrons or holes. Quantum wells, quantum wires and quantum dots are the different engineering possibilities in band-gap engineering. The superlattice structures closely resemble the Quantum well picture and the only difference between them is the way both with thin barriers in between them as shown in the Fig.1.14(a). Superlattices designed like a periodic one-dimensional crystal in which periodicity is carried with the quantum well structures as shown in Fig.1.14(b). Structures with *mini bands* formed with the delocalization of electronic states to couple the wave functions together through the thin barriers that separate them. In contrast, Multiple Quantum wells (MQW) structure consists of thick barriers that prevent coupling of the wave functions together.

The sophisticated deposition techniques coupled with epitaxial growth ideas give rise to new properties of matter. The synthetic approaches include the following seven engineering techniques that modulate the properties by their unique way of growth. The seven engineering techniques are strain engineering, interface engineering, epitaxial nanocomposites, epitaxial stabilization, dimensional confinement, polarization doping and breaking symmetries [3].

1.10. Motivation

Reconstruction of crystal lattice structures contrasting from their bulk polycrystalline properties influences the magnetic and electronic properties in order to produce a wide variety of characteristics. Polarity discontinuities at the interfaces of heterostructures/superlattices lead to non-trivial local atomic and electronic structure due to dangling (unsatisfied valence on an immobile atom) bonds and incomplete atomic coordination ultimately leads to the observation of superconductivity, a 2D-electron gas [66–68]. *Ohtomo* et.al investigated the effects of the charge transfer and electronic states at the interface of two insulating oxide perovskites $LaAlO_3$ and $SrTiO_3$ with the large energy bandgaps 3.2 *eV* (of lattice constant, 3.789 *Å*) and 5.6 *eV* (lattice constant, 3.905 *Å*), respectively [2]. This investigation led to the extremely high magnitudes of Hall mobility exceeding 10,000 $cm^2V^{-1}s^{-1}$. The resultant Hall mobility, μ_H is extremely very high at the interface for the 60 Å thick layer of $LaAlO_3$. Thin films of $Pr_{0.5}Ca_{0.5}MnO_3$ grown on the [100] $SrTiO_3$ substrate exhibits an insulator-metal transition occurs below 240 K by applying a magnetic field of ~7 T. The thin film grown on $SrTiO_3$ undergoes tensile stress which melts the charge-ordering by the application of significantly lower magnetic field [69]. Strain effects make the systems physical properties more intriguing when they take the form of thin films. *S. K. Singh et.al* reports a magnetic field of ~ 4 T melts the charge ordering state and make the $Pr_{0.67}Ca_{0.33}MnO_3$ on $LaAlO_3$ substrate conducting like a metal and the insulator-metal transition is reversible for the magnetic field of ~ 8 T [70–72].

Turning to the polycrystalline bulk part of the thesis, the reports on $La_{0.5}Ca_{0.5}MnO_3$, $CeCrO_3$, $GdCrO_3$ and $Y_{0.9}Pr_{0.1}CrO_3$ motivated us to work towards the magnetization reversal, exchange bias, field induced metamagnetic transitions, magnetic glass, metal-insulator transitions, and magneto-caloric effect aiming to move the transitions towards the room temperature and also get the outstanding and enhanced

values of the parameters [47, 58, 73, 74]. $La_{1-x}Ca_xMnO_3$ shows an unusual glass like behavior by the kinetic arrest of FM moments in the AFM background which is evident through measurements under CHUF protocol, cooling (H_{CF}) and heating (H_{MF}) under different fields [73]. Cooling the sample at magnetic field 6 T and decreasing the field isothermally to 1 T at the low temperature below T_{MG}, magnetic glass transition temperature and measuring the FCW reveals the heterogenous nucleation and devitrification within a temperature range of ~ 5 K and falling into the AFM equilibrium state. Magnetic glass, fundamentally different from spin glass, is well investigated to probe the metallic nature in the insulating phase that gives rise to a metastable glassy ferromagnetic metallic (FMM) state.

Cao et. al reported multifunctional properties in materials like ferroelectricity and anti-ferromagnetism with magneto-electric coupling [47]. Polycrystalline samples of $CeCrO_3$ exhibit *Pbnm* space group exhibits AFM transition around T_N = 260 K, along with a low temperature magnetic compensation at 133 K. Spin-flip transition triggered by the Zeeman energy rotates the spin suddenly by 180° around 37 K and this is named as Spin-flip transition and its' dependency is well tuned by the external field. Here $GdCrO_3$ crystallize in orthorhombic structure (*Pbnm* space group) with AFM ordering temperature at 171 K with Γ_4 (G_x, A_y, Fz; F_R) spin configuration and go through spin-flip transition at 7 K with Γ_4' configuration attained by the Zeeman energy. $GdCrO_3$ attains a high isothermal entropy change of 36.9 J kg^{-1} K^{-1} with adiabatic temperature change ΔT of ~ 19 K (with relative cooling capacity of 542 J kg^{-1} (for ΔH ~ 7 T)) which is quite useful for the magnetic refrigeration [74]. $Y_{0.9}Pr_{0.1}CrO_3$ reports says that zero-field cooled exchange bias and positive conventional exchange bias are the characteristic features of this system [58]. The neutron diffraction patterns show the transition from Γ_4 at the high temperature to Γ_2 at the spin-reorientation at low temperatures. The Γ_4 configuration comes with the canted antiferromagnetic spins influenced by the Dzyaloshinskii-Moriya interactions at the T_N ~ 237 K. Anti-parallel coupling between the Pr^{3+} and Cr^{3+} sublattices venture into such unconventional behaviour in magnetic and electronic properties.

1.11. Gaps in the literature

A systematic study related to the $[Pr_{0.7}Ca_{0.3}MnO_3/SrTiO_3]_{15}$ superlattice structure deposited on (001) $SrTiO_3$ and (001) $LaAlO_3$ is not initiated in the literature till now. From here onwards this system is referred as (PCMO/STO) superlattices. A detailed study related to both orientation and thickness dependence of magnetization and electronic properties are still scarce in the literature. Therefore, I choose this system for the current PhD research plan. Nevertheless, a study on engineering these magnetic, and electronic studies still lacking in the literature. Elaborated studies are very important to understand the nature of magnetic interactions in this class of compounds.

Apart from this, among the CO/OO systems, $Pr_{1-x}Sr_xMnO_3$ shows unconventional magnetic and electronic properties results in metal-insulator transition applications. Especially, the compositions around the x = 0.5 preserves the FM and AFM long-range orderings *w.r.t.* temperature. Substitution of rare-earth elements with lesser/larger radius than the Pr^{3+} at the $Pr_{0.5}Sr_{0.5}MnO_3$ reveals interesting phenomena in

magnetic properties. I have chosen the $Pr_{0.45}Sr_{0.55}MnO_3$ and tuned the Pr^{3+} sites with Yb^{3+} in $Pr_{0.45-x}Yb_xSr_{0.55}MnO_3$ ($x \leq 0.10$) in order to pin the orbital ordering more efficiently and tune the ordering temperatures for the room temperature applications.

On the other hand, detailed research on Ce doped $YCrO_3$ ($Y_{1-x}Ce_xCrO_3$, $x \leq 0.2$) with variable dopant concentrations is a new idea and not implemented in the literature till now. This combination fills the gap in the literature. A detailed spectroscopic and morphological study linking with the magnetic and electronic properties are very much needed to understand the magnetic ground state of this system. Besides, I are interested in the Ce doped $GdCrO_3$ (composition $Gd_{1-x}Ce_xCrO_3$, $x \leq 0.1$) which is not studied in the literature till now. On the other hand, in collaboration I have studied the bulk poly crystals of $Dy_{1-x}Ce_xCrO_3$, $Gd_{1-x}Sm_xCrO_3$ and $Sm_{1-x}Ce_xMnO_3$ systems are also not studied in the literature which shows significant negative magnetization and composition effect.

Furthermore, there is a substantial demand for $YCrO_3$ and $GdCrO_3$, primarily driven by their potential applications in magnetic recording and magnetic refrigeration technology. As a result, I intend to conduct an in-depth investigation into these two bulk polycrystalline systems, alongside exploring the aforementioned superlattice structures and R^{3+} tuned bulk polycrystals for their magnetically enriched characteristics. Given that all the aforementioned parent compounds demonstrate noteworthy negative magnetization properties, which are pivotal in magneto-electronic device applications, embarking on this proposed study is of significant value. This planned examination of the bulk systems, incorporating the appropriate rare-earth and transition metal elements, will provide a comprehensive overview of the entire family.

1.12. Layout of the thesis

I have planned to grow the superlattice structures of $[Pr_{1-x}Ca_xMnO_3/SrTiO_3]_{15}$ layers on (001) oriented single crystal substrates $SrTiO_3$ and $LaAlO_3$ for the x = 0.3 and 0.5 compositions using the pulsed laser deposition. In this chapter 3, I have investigated the X-ray diffraction patterns and X-ray reflection patters to confirm the quality growth of the films and performed morphological scans using the atomic force microscopy to understand the uniform growth of the layers. Magnetic and electronic properties have been studied to understand the influence of the compressive and tensile strain on the magnetic properties. In chapter 4, I focused our studies on the synthesis of monophasic $Pr_{0.45-x}Yb_xSr_{0.55}MnO_3$ bulk polycrystals which reveals drastic changes in the bond-angles and bond-lengths through the Yb^{3+} substitution at the Pr^{3+}-site. The effect of these structural changes on the magnetic properties has been investigated to understand the reconstruction of the magnetic phases that gives promising ordering temperatures at the room temperature. Besides, in chapter 5, I attempted to replace the Y^{3+}-sites with Ce^{3+}-ions and succeeded in synthesising the monophasic sample which in turn changes the magnetic ordering of the whole system evident through the field-induced transitions, exchange-bias, and spin-reoriented configurations. Specific heat-studies and electronic investigations has been performed for a better understanding of the system. Finally, in chapter 6, I synthesized $Gd_{0.9}Ce_{0.1}CrO_3$ bulk polycrystalline solids trough which I structurally

engineered the bond-angle and bond-length that influence the exchange interactions to tune the spin-flip transitions more gradually. Giant magneto-caloric effect values have been recorded through the field dependent magnetic measurements that makes the system outstanding candidate among all the other rare-earth oxide chromates.

Chapter 2
Experimental Methodology

In order to advance our research and achieve state-of-the-art objectives, a range of experimental techniques and corresponding instruments were employed. This chapter provides a brief overview of these experimental methods, including the synthesis procedures and characterization techniques used. The synthesis section encompasses both the pulsed laser deposition (PLD) method for thin film superlattices and the solid-state and sol-gel methods for polycrystalline materials. In terms of material characterization, the focus is on several techniques, such as X-ray powder diffraction (XRD), X-ray refractivity (XRR), atomic force microscopy (AFM), Raman spectroscopy, physical property measurement system (PPMS), and superconducting-quantum-interference-device (SQUID). Each of these instruments and their working principles will be briefly explained.

2.1. Synthesis procedure

2.1.1. Pulsed laser deposition

Laser ablation, as a materials processing technique, emerged in the 1960s following the invention of the first commercial ruby laser [75]. However, it did not garner significant research interest as a thin film growth method until the late 1980s [76], when it was employed for the growth of high-temperature superconductor films. Since then, the development of pulsed laser deposition technique (depicted in Fig 2.1(a)) has progressed rapidly, accompanied by a significant increase in research dedicated to this area. The process of pulsed laser ablation is inherently complex. At a surface level, ablation can be perceived as the rapid boiling of material within a localized interaction volume near the target surface. However, a deeper investigation reveals the hidden complexities involved, as illustrated schematically in Fig 2.1(b). When a solid or liquid is irradiated by an intense laser beam, a small portion of the surface material is vaporized and expelled from the sample. This vapor comprises atoms, molecules, ions, and electrons, with their exact composition and kinetic energy dependent on laser parameters such as intensity, wavelength, and pulse width, as well as to some extent on the target sample properties. If this vapor encounters another surface, it may recondense and deposit onto that surface. The repetition of laser pulses and subsequent vapor plumes can lead to the build-up of material on the surface, ultimately forming a thin film.

The growth and quality of thin films are influenced by various fundamental parameters, including substrate selection, substrate temperature (T_S), and the kinetic energies and arrival rates of different constituents within the vapor plume. These factors can be affected by the excitation wavelength, laser pulse duration, energy, and intensity, the presence of background gas, and any secondary plasma activation in the gap between the target and substrate. The deposition process of thin films can be divided into three stages: laser-target interaction, plasma plume formation, and nucleation and growth of the thin films. The laser-

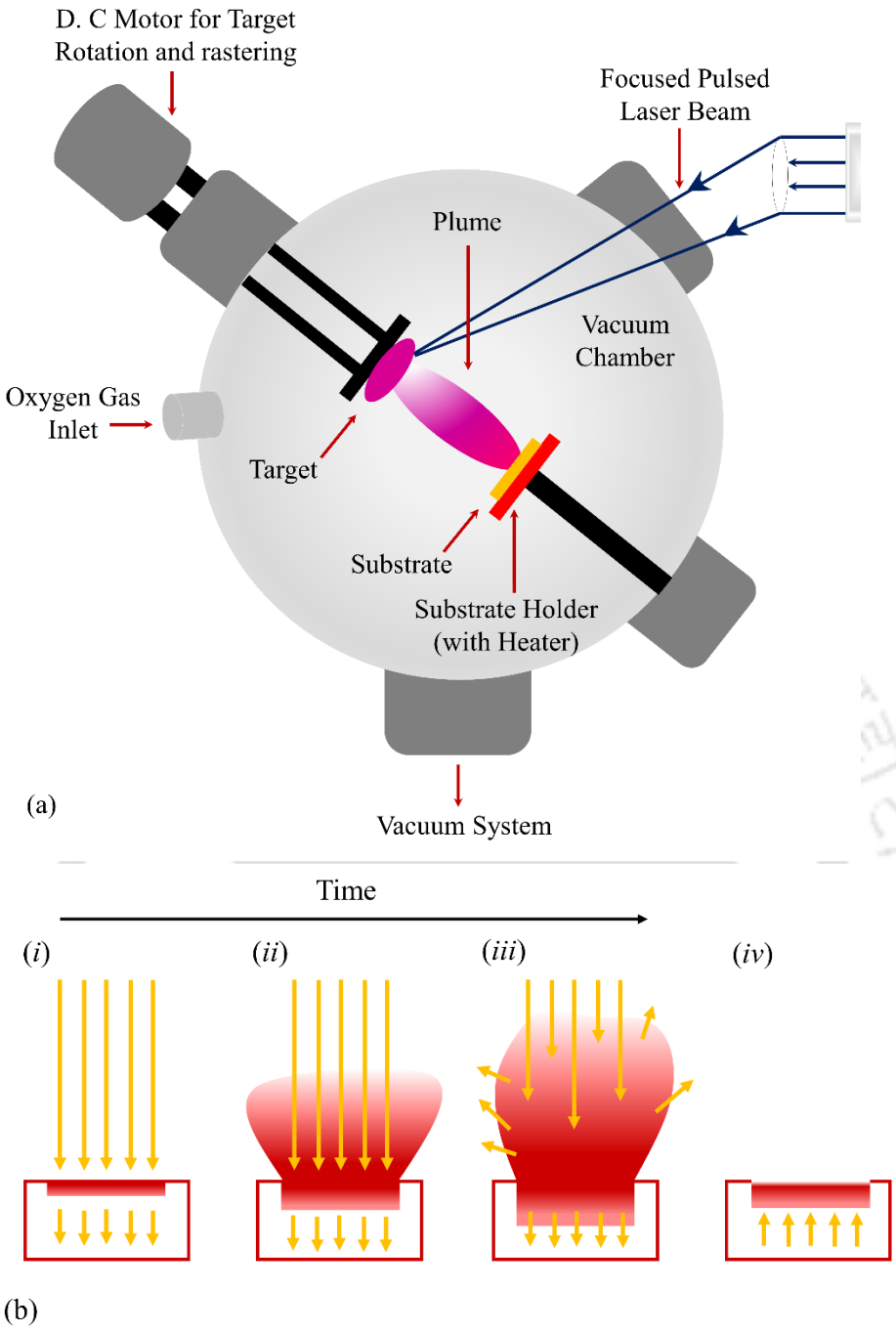

Fig. 2.1. (a) Schematic diagram of a pulsed laser deposition system. (b) Schematic illustrating key elements of the pulsed laser ablation event. (*i*) Initial absorption of laser radiation (indicated by long arrows), melting and vaporization begin (shaded area indicates melted material, short arrows indicate motion of solid-liquid interface). (*ii*) Melt front propagates into the solid, vaporization continues, and laser-plume interactions start to become important. (*iii*) Absorption of incident laser radiation by the plume, and plasma formation. (*iv*) Melt front recedes leading to eventual re-solidification.

target interaction serves as the driving mechanism in pulsed laser deposition (PLD). Over the years, theoretical models and experimental studies have been developed to elucidate the processes governing the PLD ablation process. These investigations have revealed that the ablation process is not governed by a

single mechanism, but rather by multiple mechanisms resulting from the interaction between the laser and target. When the laser pulse strikes the target, the absorbed energy leads to target ablation, which involves the sputtering and removal of target material.

Typically, laser flux densities higher than 10^5 W/cm^2 are required to generate a plasma plume for most materials [77]. Once the ablation threshold is reached, electrons, ions, and neutral particles are ejected, creating a shock wave followed by the formation of a plasma plume. These plasmas can reach temperatures in the tens of thousands of Kelvin range [78]. The material vapor plume becomes visible within the nanosecond time scale and propagates at a supersonic velocity of approximately 10^6 cm/s [79]. The quantity of target material present in the plume can be calculated as a vaporization flux, u_{vap} (atoms/cm^{2}s) using the Hertz-Knudsen equation represented by Eq. (2.1):

$$u_{vap} = \frac{1}{\rho}\,\beta p_0(T_S)\left[\frac{M}{2\pi k T_S}\right]^{\frac{1}{2}} \tag{2.1}$$

where, (Ts) is the target surface temperature in kelvin, (β) the evaporation coefficient, (ρ) is the target density, (M) target mass in kilograms, (k) is Boltzmann's constant, and ($p_0(T_S)$) is the equilibrium vapor pressure at (Ts) in pascals [80]. The Volmer-Weber, Frank-van der Merwe, and Stranski-Krastinov models explain the nucleation and growth of thin films near thermodynamic equilibrium. Each growth mode is determined by the balance of free energies between the film surface (γ_F), substrate surface (γ_S), and film-substrate interface (γ_I) [81]. In the Volmer-Weber mode, the film and substrate lack bonding because the total surface energy is greater than the substrate energy, $\gamma_F + \gamma_I > \gamma_S$, resulting in three-dimensional island growth. The Frank-van der MerI growth mode occurs when $\gamma_F + \gamma_I < \gamma_S$, leading to monolayer growth with strong bonding between the film and substrate. In this mode, the film grows as complete monolayers through nucleation and island clustering before additional clusters form the next monolayer [82]. The Frank-van der MerI growth mode is characteristic of homoepitaxial thin film growth. On the other hand, the Stranski-Krastinov mode can occur during heteroepitaxial growth due to lattice mismatch between the substrate and deposited thin film. Initially, the growth is monolayer, but it transitions to three-dimensional island growth due to biaxial strain induced by the lattice mismatch [82].

2.1.2. Polycrystalline method

Polycrystalline samples consist of small crystals, also known as grains, which exhibit random orientations of their crystallographic axes. The synthesis of polycrystalline materials is straightforward and cost-effective, making them popular in numerous engineering applications such as concrete, ceramics, and batteries. Additionally, polycrystalline samples are often considered precursors for single-crystal growth, making the production of high-quality polycrystalline samples crucial for both condensed matter science and modern industry. Among the various methods available for polycrystalline synthesis (as shown in Fig 2.2), the high-temperature solid-state reaction method is a commonly used approach. In this section, I present

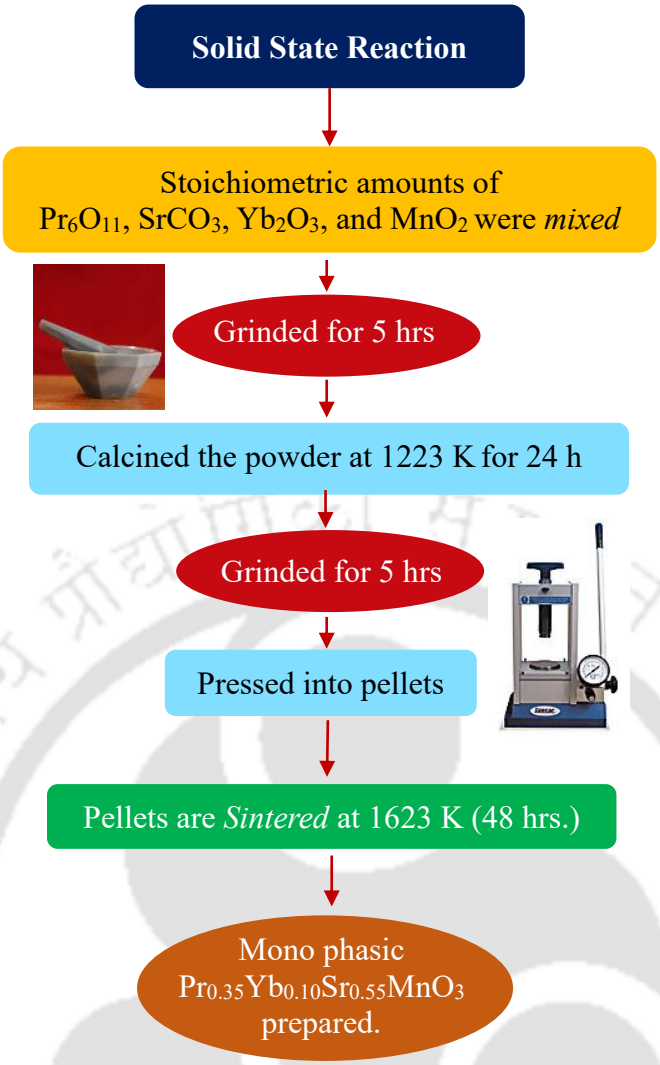

Fig. 2.2. The flow chart of the synthesis of polycrystalline sample with solid state reaction method and the freshly sintered pellets of $Pr_{0.35}Yb_{0.10}Sr_{0.55}MnO_3$ are shown.

the details of the solid-state reaction method using the preparation of polycrystalline samples of $Pr_{0.45-x}Yb_xSr_{0.55}MnO_3$ (x = 0.02, 0.05, 0.08, and 0.10) as an example. X-ray diffraction results are also included to confirm the phase purity of the synthesized polycrystalline samples. The polycrystalline $Pr_{0.45-x}Yb_xSr_{0.55}MnO_3$ (x = 0.02, 0.05, 0.08, and 0.10) series compounds were synthesized using raw materials with 99.9% purity, including Pr_6O_{11}, $SrCO_3$, YbO_2, and MnO_2 obtained from Alfa-Aesar GmbH. The detailed procedure is illustrated in Fig 2.2. After weighing, the raw materials were manually ground and mixed for 5 hours using an agate mortar to ensure homogeneity. During the mixing process, the mixed sample was intermittently placed in an oven at 373 K to maintain phase purity and prevent the materials from becoming deliquescent. Once mixed, the raw material mixture was transferred to an alumina crucible. Calcination was carried out using a muffle furnace. Initially, the raw material mixture underwent preliminary calcination by heating up to 1173 K and maintaining that temperature for 24 hours. The resulting product was then ground following the same procedure as described above. The final powdered material was pressed into cylindrical

pellets using a hydraulic press subsequently sintered at 1623 K for 24 hours in air. This process yielded black, dense polycrystalline bulk samples of $Pr_{0.45-x}Yb_xSr_{0.55}MnO_3$.

2.1.3. Sol-gel synthesis

Bulk polycrystalline perovskite systems of $Y_{1-x}Ce_xCrO_3$ (x = 0, 0.05, 0.1, 0.2) were synthesized using the oxalate-based sol-gel technique. This method involved using the nitrate salts of $Y(Y(NO_3)_3.6H_2O)$, $Ce(Ce(NO_3)_3.6H_2O)$ and $Cr(Cr(NO_3)_3.6H_2O)$ as precursors, with ethanol serving as the solvent. The process commenced with drying the gel in an oven, followed by complete digestion of the xerogel at temperatures ranging from 353 K to 373 K. Subsequently, calcination was conducted above 1473 K, resulting in the formation of fine-sized powders with a partly formed perovskite structure (after removing all volatile substances). However, to obtain the desired perovskite phase, the calcined powders were ground for 3 hours using an agate mortar and pestle. The resulting powders were then pressed into cylindrical pellets using a hydraulic press and sintered at 1573 K for 48 hours in air. This process yielded dense cylindrical pellets with large grain sizes. To ensure uniformity and perfect homogeneity of the compounds, the sintered pellets were crushed, reground for 2 hours, and re-pelletized. The re-pelletized samples were once again sintered at 1573 K for 48 hours in air. This entire procedure was repeated three times to achieve fully densified pellets with the desired compositions ($Y_{1-x}Ce_xCrO_3$, *Pnma*) exhibiting a single-phase perovskite structure, characterized by large grain sizes.

2.2. Characterization details

In this section, I will provide a brief overview of the characterization techniques employed in this comprehensive research study. Our discussion will begin with structural characterization, followed by morphological, electronic, Raman, and magnetization measurements.

2.2.1. Structural characterization

X-ray diffraction is a phenomenon in which the atomic planes of a crystal cause an incident beam of X-rays to interfere with each other upon exiting the crystal. This technique, discovered by Max von Laue in 1912, serves as a rapid analytical method primarily employed for phase identification of crystalline materials and provides valuable information about unit cell dimensions [83]. Over time, X-ray diffraction has become a common technique for studying crystal structures and atomic spacing. The underlying principle of X-ray diffraction involves the constructive interference of monochromatic X-rays with a crystalline sample. When the conditions satisfy Bragg's Law, the interaction of the incident rays with the sample results in constructive interference and the generation of diffracted rays. Bragg's Law establishes a relationship between the angles at which diffraction occurs and the distance between imaginary planes of atoms within the crystal. By considering the diffraction from a crystal as reflections from these planes, an equation can be formulated to predict the locations of diffraction maxima in a diffraction pattern.

Let's consider a pair of parallel X-rays striking a pair of horizontal parallel planes, as illustrated in

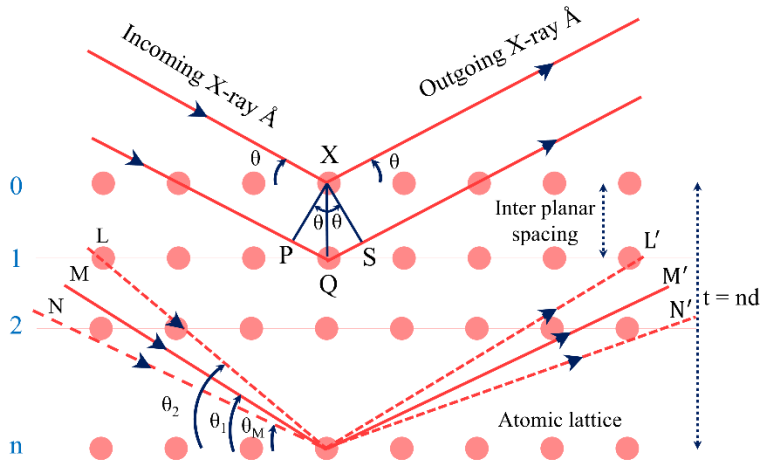

Fig. 2.3. Bragg's diffraction on the crystal.

Fig 2.3. The parallel rays reach the planes in phase, but due to the longer distance travelled by the lower ray compared to the upper ray, there is a path difference between them when they are both reflected. By applying simple trigonometry, it can be shown that $n\lambda = 2d_{hkl}\sin\theta$, where d_{hkl} represents the vector drawn from the origin of the unit cell to intersect the crystallographic plane (*hkl*) at an angle ($\theta = 90°$). This relationship, known as Bragg's Law, demonstrates that constructive interference of the waves occurs only when the path difference is a multiple of the wavelength, λ. The position of the diffraction peaks in the X-ray diffraction pattern is determined by the distance between the parallel planes of atoms within the crystal. The intensity of the diffraction peaks, denoted as I_{hkl}, is influenced by the arrangement of atoms throughout the entire crystal. This relationship is described by the following equations, Eq. 2.2 and Eq. 2.3:

$$I_{hkl} \propto |F_{\mathrm{hkl}}|^2 \tag{2.2}$$

$$F_{\mathrm{hkl}} = \sum_{j=1}^{m} N_j f_j exp\left[2\pi i\left(hx_j + ky_j + lz_j\right)\right] \tag{2.3}$$

The structure factor F_{hkl} represents the sum of the scattering contributions from all atoms within the unit cell, resulting in a diffraction peak from the (*hkl*) planes of atoms. The amplitude of the scattered light is determined by two factors: (a) the positions of the atoms on the atomic planes, expressed by fractional coordinates x_j, y_j, z_j and (b) the type of atoms present on the atomic planes. The efficiency of X-ray scattering at any angle is quantified by the scattering factor f_j, which corresponds to the group of electrons surrounding each atom. The scattering factor is equal to the number of electrons surrounding the atom at $\theta = 0°$ and decreases as θ increases. Additionally, N_j represents the fraction of every equivalent position occupied by atom j [84].

The diffraction angle for a set of planes in a crystal system is determined based on the atoms present within the unit cell. The expression to calculate the diffraction angle for any crystal system is provided below: Eq. (2.4):

$$d^2 = \frac{a^2}{(h^2 + k^2 + l^2)} \tag{2.4}$$

Here, (h, k, l) are the miller indices and it signifies planes in the lattice which means it does not represent one particular plane instead it denotes set of parallel planes which corresponds to the crystal plane direction, *d* is the inter-planar separation and *a* is the lattice constant. Substituting Eq. 2.4. in Bragg's law (shown in the Eq. 2.5) I get,

$$sin^2\theta = \frac{\lambda^2}{4a^2}(h^2 + k^2 + l^2) \tag{2.5}$$

Similarly, for orthorhombic system given in the following Eq. (2.6),

$$sin^2\theta = \frac{\lambda^2(h^2 + k^2 + l^2)}{4(a^2 + b^2 + c^2)} \tag{2.6}$$

In the case of X-ray reflectivity, precise determination of film thickness is essential for most technological applications of thin films. This is because the properties of thin films are often dependent on their thickness. XRR is a non-destructive and non-contact technique used for thickness determination in the range of 2-200 nm, with a precision of about 1-3 Å. Additionally, XRR can provide information about the density and roughness of films and multilayers with high precision. The XRR method involves measuring

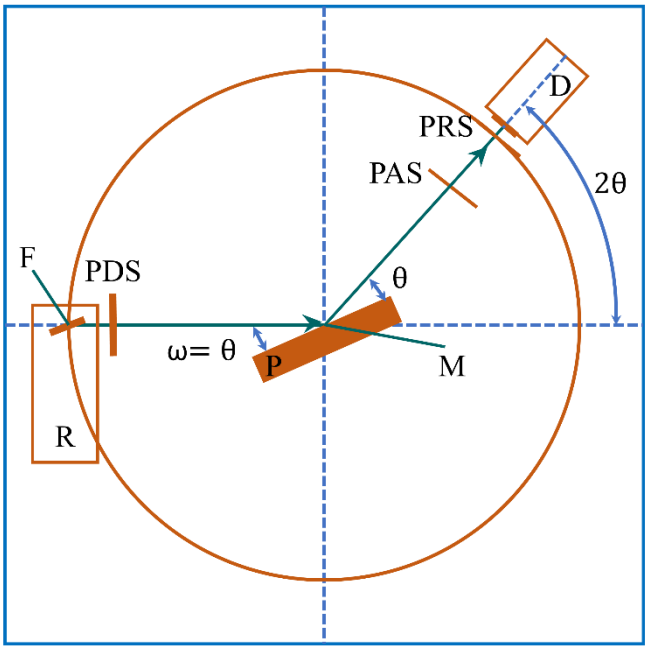

Fig. 2.4. θ/2θ-Scan: The condition of incident angle ω = (2θ)/2 = θ = outgoing angle is satisfied. The detector D rotates at twice the speed of the sample P. This arrangement is sensitive only to the planes parallel to the surface of the sample. The beam makes an incident angle ω with the surface of the sample P. The reflected intensity at angle of 2θ is measured. Both the rotation of the sample ω and the detector (2θ) are about the same axis MP (perpendicular to the drawing). The sample is adjusted so that the rotation axis lies on the sample surface. The Detector circle is fixed through the (programmable) detector slit (PRS, programmable receiving slit). The anode focus, F of the tube lies on the detector circle.

the intensity of a monochromatic X-ray beam reflected by a sample at grazing angles. A sample is irradiated with a diffraction monochromatic X-ray beam of wavelength λ at a grazing angle ω, and the reflected intensity at an angle 2θ is recorded by a detector (refer to Figure 2.4). This setup demonstrates specular reflection, where the condition ω = 2θ/2 is satisfied. The preferred mode of operation is the θ/2θ mode, ensuring that the incident angle is always half of the scattering angle. At incident angles θ below a critical angle θ_c (usually less than 0.3° for most materials), total external reflection occurs. The critical angle provides information about the density of the material. Above θ_c, reflections from different interfaces interfere, resulting in interference fringes. The period and intensity variation of these fringes are related to the thickness and roughness of the layer (or layers in the case of multilayers). The reflection can be analysed using the classical theory, such as the Fresnel equations. Typically, measurements are conducted in the range of 0° to 5° in θ. For incident angles greater than θ_c ($\theta > \theta_c$), the X-ray beam penetrates the film. Reflection occurs at the top and bottom surfaces of the film, and interference between the rays reflected from these surfaces results in angle-dependent interference fringes. Unlike optical spectroscopy, these fringes are not frequency-dependent but rather angle-dependent. Due to the low amplitude reflection coefficient ($\rho_{v,h} \sim 1/\sin^2\theta \Rightarrow R_{v,h} = |r_{v,h}| \sim 1/\sin^4\theta \approx 1/\theta^4$) of the interface between adjacent layers, the contributions of multiply reflected beams can be neglected. The m^{th} interference maximum for a path difference $\Delta = m\lambda$ and angle θ_m is determined by equations (2.7) to (2.10):

$$m\lambda = \Delta = 2dN_{X,1}(\theta_m) \tag{2.7}$$

$$\approx 2d\sqrt{\theta_m^2 - 2\delta} \qquad m \in \mathbb{N} \tag{2.8}$$

$$\leftrightarrow \quad \theta_m^2 \approx m^2 \frac{\lambda^2}{4d^2} + 2\delta \tag{2.9}$$

$$= m^2 \frac{\lambda^2}{4d^2} + \theta_C^2 \tag{2.10}$$

When the substrate is optically denser than the film, a phase difference of π occurs at the interface between the film and substrate. In this case, the value of m is replaced with m + 1/2. By utilizing Eq. (7) and calculating the difference between adjacent maxima and minima in the interference pattern, the film thickness can be determined. The thickness is given by Eq. (2.11) and (2.12):

$$d \approx \frac{\lambda}{2} \frac{1}{\sqrt{\theta_{m+1}^2 - \theta_C^2} - \sqrt{\theta_m^2 - \theta_C^2}} \tag{2.11}$$

$$\approx \frac{\lambda}{2} \frac{1}{\theta_{m+1} - \theta_m} \tag{2.12}$$

The thickness is often determined with a precision better than 1 Å for measurements exhibiting interference fringes in a bigger angular range.

2.2.2. Morphological Characterization

Atomic force microscopy (AFM) originated as an extension of the scanning tunnelling microscopy (STM) technique, specifically for investigating electrically non-conductive materials such as proteins. In 1986, Binnig and Quate introduced the concept of AFM, which utilized an ultra-small probe tip attached to a cantilever [85]. The following year, Wickramsinghe et al. developed an AFM setup employing a vibrating cantilever technique and the light-lever mechanism [86], AFM enables the acquisition of a three-dimensional profile of a surface at the nanoscale by measuring the forces between a sharp probe (typically less than 10 nm in size) and the surface at very close distances (0.2-10 nm probe-sample separation). The probe is mounted on a flexible cantilever. By gently bringing the AFM tip into contact with the surface, the instrument records the minute forces between the probe and the surface. The probe is located at the end of the cantilever, which can be considered as a spring-like structure. The magnitude of the force exerted between the probe and the sample depends on the spring constant (reflecting the stiffness of the cantilever) as well as the distance between the probe and the sample surface. Hooke's Law, given by Eq. (2.13), describes this force relationship:

$$F = -k.x \tag{2.13}$$

Where, F represents force, k represents the spring constant, and x denotes the deflection of the cantilever. Similar to STM, the motion of the probe across the surface in AFM is controlled using a feedback loop and piezoelectric scanners. However, the key difference lies in how the forces between the probe and sample surface are monitored. The deflection of the probe is commonly measured using a method known as "beam

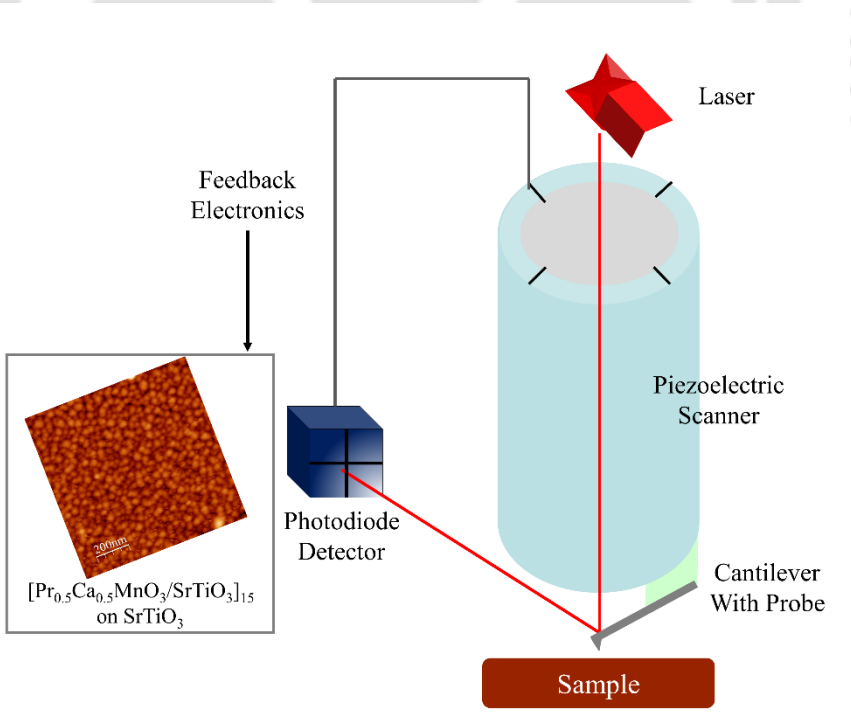

Fig. 2.5. Schematic of AFM instrument showing “beam bounce” method of detection using a laser and position sensitive photodiode detector.

bounce." In this technique, a semiconductor diode laser is directed onto the back of the cantilever and then reflected onto a position-sensitive photodiode detector (as illustrated in Fig 2.5). The photodiode detector records the bending of the cantilever as the tip scans over the sample. By measuring the deflection, a map of the surface topography can be generated. AFM offers three primary imaging modes: Contact AFM: In this mode, the probe-to-surface separation is less than 0.5 nm. Intermittent contact (tapping mode AFM): Here, the probe-to-surface separation ranges from 0.5 to 2 nm. Non-contact AFM: This mode involves a probe-to-surface separation between 0.1 and 10 nm.

In contact mode AFM (repulsive van der Waals), the cantilever bends when the spring constant is less than that of the surface. The force between the tip and the sample is repulsive. By maintaining a constant cantilever deflection through feedback loops, the force remains constant and an image of the surface is obtained. This mode offers advantages such as fast scanning and suitability for rough samples, making it useful for friction analysis. However, one drawback is the potential for damaging or deforming soft samples, although this issue can often be resolved when imaging in liquids. In intermittent mode (Tapping), the imaging process is similar to contact mode. However, in this mode, the cantilever is oscillated at its resonant frequency (as shown in Fig 2.5). The probe lightly "taps" the sample surface during scanning, making contact at the bottom of its swing. By maintaining a constant oscillation amplitude, a consistent tip-sample interaction is achieved, resulting in a surface image. This mode offers advantages such as high resolution for delicate or loosely held samples, making it suitable for biological samples. However, it can be more challenging to image in liquids, and slower scan speeds are often required. In non-contact mode (attractive van der Waals), the probe does not make direct contact with the sample surface but instead oscillates above the adsorbed fluid layer on the surface during scanning. By using a feedback loop to monitor changes in amplitude due to attractive van der Waals forces, the surface topography can be measured. The advantages of this mode include applying very low force on the sample (10^{-12} N) and extending the probe's lifetime. However, it generally offers lower resolution, and the presence of a contaminant layer on the surface can interfere with oscillation. Ultrahigh vacuum (UHV) conditions are often necessary for optimal imaging in this mode.

2.2.3. Raman Spectroscopy

Raman spectroscopy is a valuable technique used to investigate matter through the inelastic scattering of monochromatic light. It has found widespread applications in fields such as spectroscopy, biophysics, microscopy, geochemistry, and analytical chemistry. Unlike absorption or emission spectroscopy, Raman spectroscopy involves transitions among quantum levels induced by the absorption or emission of photons (IR, visible, UV). While Raman spectroscopy is less sensitive than other spectroscopic methods due to the inherent weakness of the scattering process, it offers several unique advantages. One significant advantage of Raman spectroscopy is the freedom to choose an incident wavelength that is not absorbed by the surrounding media. This is particularly beneficial for samples with strong IR absorption

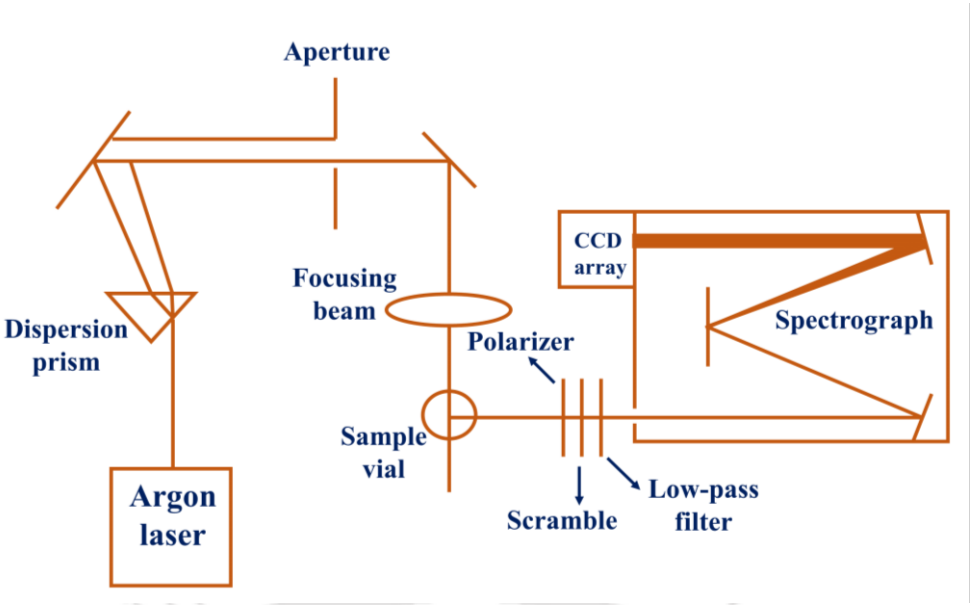

Fig. 2.6. Layout of typical Raman spectrometer.

bands, as well as for samples in aqueous or mineral environments. Additionally, Raman spectroscopy allows for the analysis of small volumes, as the light can be focused to micron-sized spots. Another advantage is the utilization of symmetry-based selection rules, enabling the detection of transitions that are "optically forbidden" in absorption spectroscopy. In a Raman experiment, a polarized monochromatic light source, typically a laser, is focused into the sample. The scattered light, which contains photons at the incident frequency ν_0 (elastic or Rayleigh scattering) as well as other frequencies $\nu_0 - \nu_i$, where ν_i corresponding to molecular transitions (such as rotational or vibrational transitions), is collected and dispersed by a high-resolution monochromator. The incident laser wavelength is fixed, and the dispersed and detected scattered light is used to obtain the frequency spectrum. Due to the weak intensity of the scattered light (typically less than 10^{-7} of the incident power), Raman spectrometers require monochromators with excellent stray light rejection and sensitive detectors. A standard Raman spectrometer setup involves a polarized monochromatic light source (usually a laser), a sample, and a high-resolution monochromator for collecting and dispersing the scattered light. Fig 2.6 shows a schematic of a typical Raman spectrometer setup.

A Raman spectrum is characterized by a series of peaks that are shifted to higher or lower frequencies compared to the incident frequency (known as the Rayleigh peak). Unlike absorption spectroscopy, where the incident photon resonates with a specific transition, in Raman spectroscopy the peaks represent inelastic scattering processes. The peaks appearing at lower frequencies are referred to as Stokes lines, while those at higher frequencies are called anti-Stokes lines, although they are typically weaker than the Stokes lines. Since both sets of lines exhibit the same frequencies, it is common practice to record only the Stokes spectrum. The Raman spectrum encompasses lines arising from both "Raman-active" vibrational transitions and rotational transitions. For the latter, the frequency displacements from the incident

light are very small (10-100 cm^{-1}), necessitating the use of high-resolution monochromators for accurate measurement.

Raman spectroscopy primarily focuses on the study of vibrational transitions, making it a branch of vibrational spectroscopy. It is considered complementary to IR absorption spectroscopy since certain transitions observed in the Raman spectrum are not observed in the IR spectrum, and vice versa. The appearance of lines in the Raman spectrum is governed by selection rules that differ from those for absorption. In a nonlinear polyatomic molecule consisting of N atoms, there are (3N-6) modes of vibration, known as "normal modes," each associated with a specific fundamental frequency of vibration and symmetry. By analysing both the IR and Raman spectra, all these modes can be observed, and their fundamental frequencies can be measured. In many cases, the Raman spectrum alone is sufficient for analysis. The degree of polarization of the scattered light provides information about the symmetry of the normal modes, which can aid in determining the molecular structure. Additionally, the shape of Raman lines in liquid samples can provide insights into dynamic processes occurring in the liquid state, such as rotational and vibrational relaxation. An important parameter of observation is the depolarization of the scattered light. When the incident light is polarized, the scattered light may retain the same polarization, or it may become depolarized, with some of the light possessing a polarization perpendicular to the incident light. The degree of depolarization is expressed by $\rho = I_{\perp}/ I_{\parallel}$, where $I_{\parallel}$ and $I_{\perp}$ represent the intensities of the scattered light polarized parallel and perpendicular to the exciting light, respectively [87]. The selection rules in Raman spectroscopy can be explained by the interaction of the electromagnetic field with the molecule's bonds. The induced dipole moment, P, in a molecule due to an external electric field, E, is proportional to the field: $P = \alpha E$, where the proportionality constant α represents the polarizability of the molecule.

In the classical theory, I can refer to the Raman effect as the effect of polarization of the dipole moment. The electric field (E) experienced by a molecule upon radiation of frequency υ is and E_0 being the intrinsic intensity and μ being the permeability is given in the following Eq. (2.14) and (2.15):

$$E = E_0 \sin 2\pi \upsilon t \tag{2.14}$$

$$\mu = \alpha E_0 \sin 2\pi \upsilon t \tag{2.15}$$

whereas, if the molecule undergoes rotation or vibration also (Raman Scattering), then the polarizability of it changes, hence the emitted frequencies also to υ_{vib} (shown in the Eq. (2.16)):

$$\alpha = \alpha_0 + \beta \sin 2\pi \upsilon_{\text{vib}} t \tag{2.16}$$

with α_0 being the equilibrium polarizability, β being the rate of change of polarizability with vibration. Hence, the induced dipole moment can be written as given in the Eq. (2.17):

$$\mu = \alpha_0 E_0 \sin 2\pi \upsilon t + \frac{1}{2} \beta E_0 [cos2\pi (\upsilon - \upsilon_{\text{vib}})t - cos2\pi (\upsilon + \upsilon_{\text{vib}})t] \tag{2.17}$$

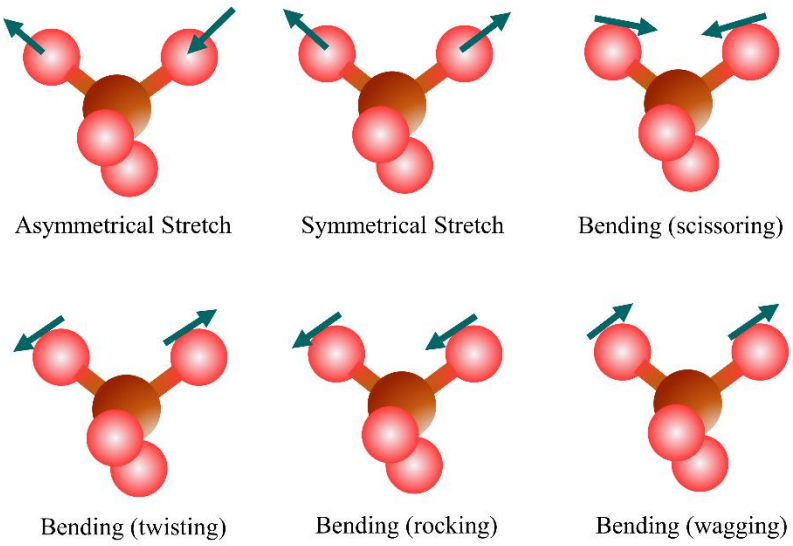

Fig. 2.7. Schematic of AFM instrument showing "beam bounce" method of detection using a laser and position sensitive photodiode detector.

where, the second term refers to the anti-stokes Raman line and the third term indicates the stokes Raman line. The polarizability of a molecule reflects the ease with which its electron cloud can be distorted. When an external electric field interacts with the molecule, the induced dipole emits or scatters light at the same frequency as the incident light wave. Raman scattering arises from changes in the polarizability within the molecular bond. The intensity of the scattered light is proportional to the square of the induced dipole moment. If a vibration does not significantly alter the polarizability, the derivative of polarizability will be close to zero, resulting in a low intensity Raman band. Vibrations involving highly polar moieties, such as the O-H bond, tend to exhibit weak Raman signals. This is because an external electric field cannot induce a substantial change in the dipole moment, and stretching or bending the bond does not significantly alter the situation. On the other hand, molecules with distributed electron clouds, like carbon-carbon double bonds, are often strong Raman scatterers. The pi-electron cloud of a double bond is easily distorted by an external electric field. Bending or stretching the bond leads to a significant change in the distribution of electron density, resulting in a large induced dipole moment. In polarizable molecules, the incident photon energy can excite vibrational modes, causing the scattered photons to possess less energy due to the vibrational transition. This energy reduction gives rise to the peaks observed in a Raman spectrum. The number of peaks in the spectrum corresponds to the number of degrees of freedom present in the molecule (Fig. 2.7).

Raman spectroscopy detects molecules with a change in polarizability, indicating the relative ease of distorting their electron cloud. The resulting Raman spectrum plots the intensity of the shifted light against frequency, with the Rayleigh band at 0 cm^{-1}. The band positions correspond to energy levels of functional group vibrations, allowing interpretation similar to infrared absorption spectra.

2.2.4. Magnetic characterization

The primary objective of the thesis was to investigate the magnetic properties of the systems, with a particular emphasis on magnetic phase transitions. To achieve this, I conducted dc-magnetization measurements on all the systems. For this purpose, I utilized two main instruments: the superconducting-quantum-interference-device (SQUID) based magnetometer from Quantum-Design, and the physical property measurement system (PPMS) equipped with a vibrating-sample-magnetometer (VSM), also from Quantum-Design. These instruments played a crucial role in conducting extensive magnetic measurements throughout the doctoral research.

The SQUID is based on Josephson's theory of tunnelling between superconductors, which he formulated in 1962 and for which he was awarded the Nobel Prize in 1972. According to Josephson's theory, a supercurrent can tunnel between two superconductors separated by a small insulating junction. This principle allows for the measurement of the phase difference between two superconducting materials. Since the phase of a quantum state is influenced by magnetic flux, SQUIDs can be used for precise magnetic flux measurements. Since their first construction in 1964, SQUIDs have played a vital role in condensed matter physics. They are commonly employed as highly accurate magnetometers but can also be adapted and applied to various other research areas and combined with innovative techniques. The fundamental building block of a SQUID is a Josephson junction, as depicted in Fig 2.8. A Josephson junction consists of two superconductors separated by an insulating material. The phenomenon of Cooper pair tunnelling across the insulating barrier gives rise to intriguing physics. Although this process has a quantum mechanical nature, I can understand it without delving into the BCS theory. Instead, I can adopt a phenomenological and macroscopic approach by using the superconductors' wave function, as described in Eq. (2.18).

$$\Psi(\vec{r}) = \sqrt{n_s}\,.\,e^{i\phi(\vec{r})} \tag{2.18}$$

Here $n_s = |\Psi|^2$ is the cooper pair density and $\varphi(\vec{r})$ is the phase. This wave function in and of itself is very interesting and gives a clear example of how superconductivity leads to quantum behaviour on a macroscopic scale. Here the wave function describes a large number of cooper pairs which are phase coherent, so I can see a quantum mechanical behaviour on a classical length scale. Therefore, I can

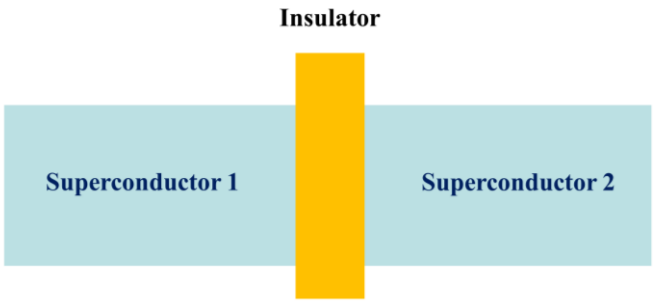

Fig. 2.8. A Josephson junction: It is made of two superconductors connected through a small insulating layer.

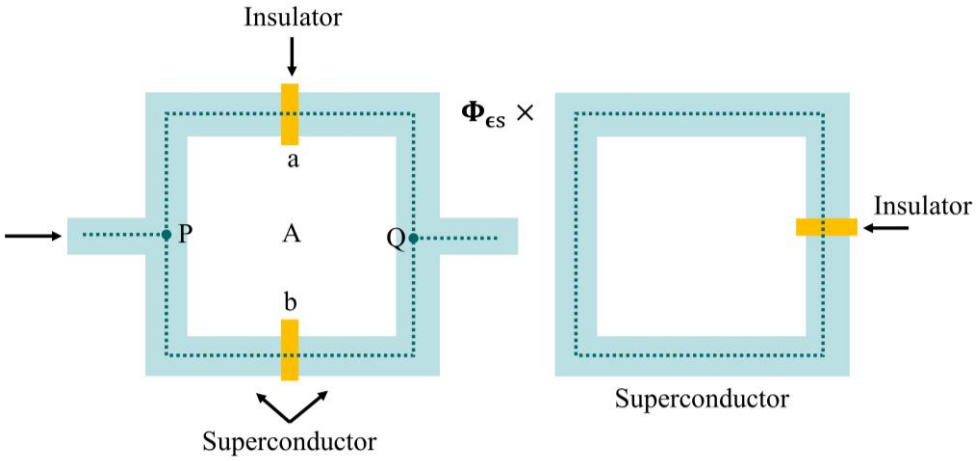

Fig. 2.9. (a) A **DC SUID** is made up of two Josephson junctions a and b connected in parallel. (b) A one junction superconducting loop in an external magnetic field.

assume that the two superconductors in Fig. 2.8 have wave functions $\Psi(\bar{r}) = \sqrt{n_1}.e^{i\varphi_1(\bar{r})}$ and $\Psi(\bar{r}) = \sqrt{n_2}.e^{i\varphi_2(\bar{r})}$. Given that the typical width of the insulator is around 100nm, I can also assume that the two superconductors are weakly coupled with a coupling constant K, i.e., cooper pairs can tunnel between the two superconductors, but they still separate enough that they are described by different wavefunctions. The Schrodinger equation for the two superconductors (i, j ∈ {1, 2} and i ≠ j) then reads as Eq. (2.19):

$$i\hbar \frac{\partial \Psi_i(\bar{r})}{\partial t} = E_i \Psi_i + K\Psi_j \tag{2.19}$$

Assuming that I have the same type of superconducting material on each side of the barrier (a reasonable assumption, since in practice I can design the Josephson Junction out of whatever material I choose), I know that $E_1 = E_2$. But I will also connect this Josephson Junction to a battery such that I have a potential difference $E_1 - E_2 = qV$. Choosing the reference point for energy in the middle between the energies, the Schrodinger Equation given in the Eq. (2.20) becomes [88–90]:

$$i\hbar \frac{\partial \Psi_i(\bar{r})}{\partial t} = (-1)^{i+1}\frac{qV}{2}\Psi_i + K\Psi_j \tag{2.20}$$

There are two types of SQUIDs commonly used in applications: a DC SQUID, which contains two parallel junctions, and an RF SQUID (as shown in Fig.2.9(a)), which contains just one junction. The DC SQUID (as shown in Fig.2.9(b)) consists of two Josephson Junctions connected in parallel on a Superconducting loop [91]. In some systems a resistive shunt is also connected across the Josephson junctions (in parallel) to eliminate hysteresis in it's I-V characteristics graph. James Zimmerman continued to work with Arnold Silver and succeeded in making a SQUID which had only a single Josephson Junction [92]. The RF SQUID which is shown in the Fig. 2.9(a) was cheaper and easier to produce compared to its predecessors. The rf SQUID consists of only a single Josephson Junction in a superconducting loop. For the same reason, it is cheaper and easier (not just to its predecessors even compared to the DC SQUID)

but also less sensitive than the DC SQUID [93]. Also, the rf SQUID could operate at much higher temperatures compared to the traditional 4 K cooled superconductors and SQUIDs because the cryogenic cooling in this case was done in liquid hydrogen which was much more easily available [91]. Based on the principles outlined above, it is clear that SQUIDs enable the precise measurement of magnetic flux and therefore, the magnetization of crystal samples. But many issues arise in application that require more complex experimental setups than those. In practice, however, one might be interested in measuring the magnetization at temperatures and magnetic fields far above the T_C or H_C of the SQUID. Therefore, designs are used that isolate the SQUID from the sample.

The Physical Property Measurement System (PPMS) is a versatile and automated workstation that offers precise thermal control for various experiments. It enables magnetic, electro-transport, and thermo-electric measurements, and can also be customized for specific laboratory experiments. The base system includes essential hardware components such as a dewar, Model 6000 PPMS Controller, probe, vacuum pump, top-plate assembly, pumping lines, probe-lifting assembly, connection cables, electronics cabinet, and power cords (refer to Fig. 2.10).

The probe, shown in Fig. 2.11(a) and (b), is immersed in a liquid-helium bath within the Dewar. This delicate device incorporates temperature-control hardware, a superconducting magnet, a helium-level meter, gas lines, sample puck connectors, and electrical connections. Care must be taken to follow the probe handling instructions to avoid damage. The probe consists of concentric stainless-steel tubes and other essential elements. The outer layer isolates the sample chamber from the liquid-helium bath. Two concentric tubes, separated by a sealed, evacuated region, prevent heat exchange between the sample chamber and the helium bath. Reflective superinsulation in the vacuum space minimizes radiative power loss into the helium bath. An aluminium heat shield directs heat to the neck of the Dewar, where there is no liquid helium. A metal bellows at the bottom of the probe compensates for thermal expansion differences, while a protective cap allows liquid helium to flow freely.

Fig. 2.10. PPMS instrument.

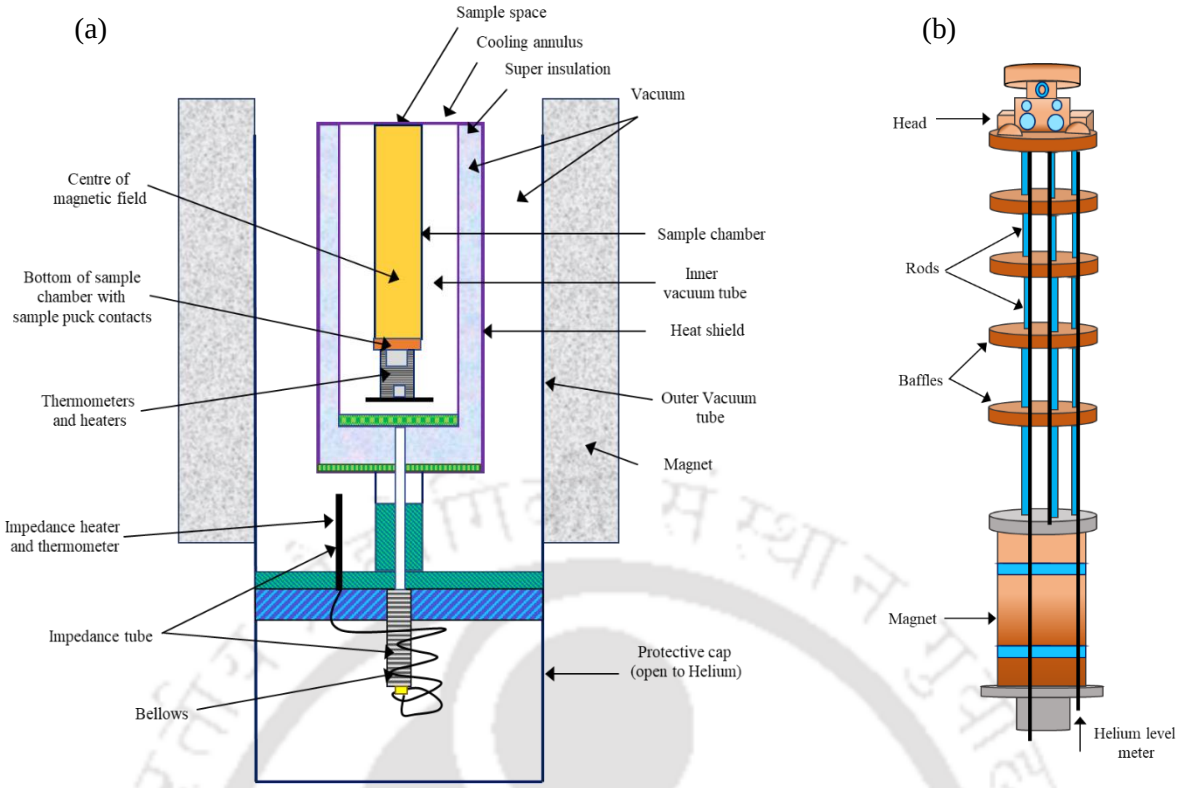

Fig. 2.11. (a) The schematic diagram of the interior of the probe inside PPMS. (b) The schematic diagram of the interior parts of PPMS.

The sample chamber, located between the vacuum tubes, features a copper construction in the lower portion to ensure uniform temperature distribution. A 12-pin connector at the base of the sample chamber contacts the sample puck. Thermometers and a heater beneath the sample puck connector maintain thermal contact during experiments. Electrical connections to the magnet and impedance assembly are housed within rods, one of which contains the helium-level meter. Baffles provide support for the rods, as they are delicate and cannot bear the full weight of the probe.

The outer layer of the probe, an evacuated region filled with reflective superinsulation, separates the liquid-helium bath and the cooling annulus. This arrangement minimizes thermal exchange and reduces helium consumption. The cooling annulus is the active region for temperature control, drawing helium vapours from the Dewar through the impedance tube. Helium flow rates in the annulus are regulated by a flow-control valve. The sample chamber is usually maintained at a few torr pressure with helium gas to ensure thermal contact with the sample. A top-plate baffle assembly isolates the sample space from room-temperature components, enabling lower temperatures. Temperature monitoring is achieved using a platinum resistance thermometer and a negative temperature coefficient thermometer located beneath the electrical connectors for the sample puck.

Chapter 3

Elastic strain control of electronic structure, and magnetic properties of $[Pr_{1-x}Ca_xMnO_3/SrTiO_3]_{15}$ superlattices

This chapter deals with the elastic strain control of electronic structure, and magnetic properties of $[Pr_{1-x}Ca_xMnO_3/SrTiO_3]_{15}$ superlattices. In this chapter, I focus mainly on the $Pr_{1-x}Ca_xMnO_3$ system along with the insulating $SrTiO_3$ layer with special emphasis on their combined superlattice configuration for two different compositions x = 0.5 and 0.3 grown by PLD technique. I explore the changes occurring on the magnetic ordering and electrical properties of the superlattice $[Pr_{1-x}Ca_xMnO_3/ SrTiO_3]_{15}$ on (001) oriented $LaAlO_3$ and $SrTiO_3$ single crystal substrates. The main advantage of choosing different substrates is that one can tune the homogeneous strain state of these superlattices and study the interface driven modulated crystal structure, electronic states, magnetic property, and transport property. A systematic study of the role of the epitaxial strain on the physical properties of the proposed superlattice configuration is completely new and has not been reported in the literature until now. Our results and analysis provide the evidence that the residual strain between the substrate and thin films plays a major role in deciding the global magnetic ordering of the highly anisotropic $[Pr_{1-x}Ca_xMnO_3/SrTiO_3]_{15}$ superlattices.

3.1. Introduction

The rare earth manganites $R_{1-x}M_xMnO_3$ (R = rare earth, M = Ca, Sr, Ba, Pr) have drawn immense scientific attention from fundamental and application perspectives, such as colossal magnetoresistance (CMR), superconductivity, and high electronic spin polarization [94, 95]. In particular, the unusual electronic properties and colossal electro-resistance (CER) of $La_{1-x}Ca_xMnO_3$ (LCMO) and $Pr_{1-x}Ca_xMnO_3$ (PCMO) make them a potential candidate for the non-volatile resistive random-access memories (ReRAMs) [96]. On the other hand, it is well known that superlattices and heterostructures have their exotic properties and novel functionalities that are different from their bulk counterparts [97–99]. Such features are attributed to lattice mismatch between the film and the substrate, and the substrate-induced strain influences the structural, electronic, magnetic, and transport properties [100–103]. Superlattices are also considered as model systems to study various physical phenomena in magnetic interlayers like interfacial coupling, spin-polarized tunnelling in heterointerfaces, and transport properties. Such properties are very important from the perspectives of technological applications in the field of magnetic sensors, magnetic recording, and memory devices and in emerging technologies like spintronic devices as well as in fundamental physics [104–106]. The exchange-bias effect and antiferromagnetic interlayer/interfacial coupling phenomena are the key observations in manganite superlattices reported in recent past [107–110]. The electric control of the ferroelectric polarization between the magnetic and ferroelectric interfaces allows the modulation of charge concentration, thus enhancing the magnetic moment and increasing the ferromagnetic to paramagnetic Curie temperature (T_C) [108]. Until date, many researchers reported on the suppression of magnitude of magnetization and T_C for $La_{1-x}Sr_xMnO_3/SrTiO_3$ or $La_{1-x}Ca_xMnO_3/SrTiO_3$

superlattices as the thickness of Mn-oxide layer decreases [109]. Millis et al. revealed that T_C is very sensitive to the biaxial strain present in the sample [111, 112]. It has been realized that elastic strain is a vital parameter that governs the electronic state of complex oxides and can change bond angles and bond lengths, consequently altering the magnetic exchange interactions significantly [69, 113, 114].

Moreover, the studies related to the tailoring of microscopic phase separation in the manganites family have attracted immense interest due to their unique physical properties. Usually, such phase separation leads to microscopic inhomogeneity due to the coexistence of insulating antiferromagnetic charge-ordered phase (originating from the Coulombic interaction of trivalent Mn and tetravalent Mn ions) and metallic ferromagnetic phase (arising due to Mn^{3+}-O-Mn^{4+} double exchange interaction) [115–118]. Among the family of manganites, the following systems are vital compounds that sets the charge ordering with sharp phase boundaries: $Nd_{1-x}Sr_xMnO_3$, $Pr_{1-x}Ca_xMnO_3$, $Ca_{1-x}Sm_xMnO_3$, $Gd_{1-x}Ca_xMnO_3$, and $Eu_{1-x}Ca_xMnO_3$ [115]. Among these compounds, $Pr_{1-x}Ca_xMnO_3$ exhibits unique compositional and magnetic field dependence of electronic properties such as the irreversible nature of metal–insulator phase transition in the H-T plane and the robust charge-ordering state between the compositions $0.3 \leq x \leq 0.5$ [114]. It is well known fact that numerous external probes have a significant role on the metallic and charge order phases. In most of the cases, external magnetic fields can drive the metal-to-insulator transitions in which both the magnetic structure and electrical conductivity vary markedly [114]. Kiryukhin et al. reported that illumination of X-rays can switch the insulating antiferromagnetic state to the metallic ferromagnetic state below 40 K in $Pr_{0.7}Ca_{0.3}MnO_3$ [119]. On the other hand, the bulk compound $Pr_{0.7}Ca_{0.3}MnO_3$ (and $0 \leq x \leq 0.3$) shows orthorhombic symmetry with complex canted magnetic ordering. Usually, two magnetic transitions appear in the samples having a canted spin structure. The first transition is the canted antiferromagnetic state occurring at 110 K, and the second one is the insulating canted ferromagnetic state. Previous reports suggest that canting is proportional to the doping concentration; however, beyond a critical composition x_{crit}, the $Pr_{1-x}Ca_xMnO_3$system exhibits ferromagnetic behaviour, but for the compositions between x = 0.3 and 0.5, the antiferromagnetic insulating phase exists in the charge-ordered insulating state [120].

In the form of thin films, the insulating charge-ordered state in $Pr_{0.5}Ca_{0.5}MnO_3$ is highly susceptible to the substrate-induced strain and thickness of the film. Prellier *et al.* reported that the lattice strain influences the charge-ordering considerably in $Pr_{0.5}Ca_{0.5}MnO_3$ thin films grown on $LaAlO_3$ (compressive) and $SrTiO_3$ (tensile) using the pulsed laser deposition (PLD) method. These authors also reported that both charge-ordering insulating and metallic state coexist up to moderate magnetic fields (50 kOe) in 75 nm thick $Pr_{0.5}Ca_{0.5}MnO_3$ films grown on $SrTiO_3$ substrates. However, the critical melting field drastically reduces to 70 kOe for the film thickness of 110 nm [121]. On the other hand, the charge-ordering temperature decreases with the decrease in lattice strain in the case of La substituted $Pr_{1-x}Ca_xMnO_3$ films [122]. Motivated by the above studies, in the present work, I focus mainly on the $Pr_{1-x}Ca_xMnO_3$ system along with the insulating $SrTiO_3$ layer with special emphasis on their combined superlattice configuration for two different compositions x = 0.5 and 0.3 grown by PLD technique. I explore the changes occurring on the magnetic

ordering and electrical properties of the superlattice $[Pr_{1-x}Ca_xMnO_3/SrTiO_3]_{15}$ on (001) oriented $LaAlO_3$ and $SrTiO_3$ single crystal substrates. The main advantage of choosing different substrates is that one can tune the homogeneous strain state of these superlattices and study the interface driven modulated crystal structure, electronic states, magnetic property, and transport property. A systematic study of the role of the epitaxial strain on the physical properties of the proposed superlattice configuration is completely new and has not been reported in the literature until now. Our results and analysis provide the evidence that the residual strain between the substrate and thin films plays a major role in deciding the global magnetic ordering of the highly anisotropic $[Pr_{1-x}Ca_xMnO_3/SrTiO_3]_{15}$ superlattices.

3.2. Fabrication and Characterization Details

$[Pr_{1-x}Ca_xMnO_3/SrTiO_3]_{15}$ superlattices (of two compositions x = 0.3 and 0.5) were simultaneously grown on (001)-oriented $LaAlO_3$ and $SrTiO_3$ substrates by PLD technique from the stoichiometric ceramic targets of $Pr_{0.7}Ca_{0.3}MnO_3$, $Pr_{0.5}Ca_{0.5}MnO_3$, and $SrTiO_3$. I employed the excimer (KrF) laser of wavelength 248 nm and an energy density of 2 J/cm2 for the deposition of the thin films. Schematic diagram of the superlattice is shown in the inset of Fig. 3.1(a). The substrate temperature was fixed at 943 K, and oxygen partial pressure was maintained at 0.15 mbar. In total, 15 double layers of $Pr_{1-x}Ca_xMnO_3$ and $SrTiO_3$ have been deposited on both the substrates. The structural characterization of these superlattices have been carried out by using a Phillips X'Pert X-ray diffractometer with Cu-Kα radiation. All the magnetization measurements were performed using a superconducting quantum interference device (SQUID) based magnetometer (MPMS) from quantum design. To probe the electronic structure of the superlattices, I performed X-ray photoelectron spectroscopy (XPS) measurements using the instrument Thermo Fisher Scientific 250 Xi. The same instrument has been employed to study the chemical state of the elements and the surface chemical composition of all the synthesized superlattice structure. The surface topology of the superlattices were examined by means of an Atomic Force Microscope (AFM) from Oxford (Model-Cypher).

3.3. Results and Discussions

Figure 3.1(a) shows the X-ray reflectivity curves of the superlattice on (001)-oriented $SrTiO_3$ and $LaAlO_3$. The reflectivity spectrum exhibits clear superlattice peaks originating from the chemical odulation from layer to layer along with the Kiessig fringes from the total thickness of the sample. These fringes provide evidence for a smooth and sharp layer structure and well-defined interfaces between the $Pr_{1-x}Ca_xMnO_3$ and $SrTiO_3$ layers. The total thickness of the samples has been calculated from $d = \lambda/(2\Delta\theta)$, where "$\lambda$" is the wavelength of the X-rays and $\Delta\theta = \theta_i - \theta_{i-1}$, θi is the angle of the i^{th} order fringe. I have evaluated the individual layer thicknesses by calibrating the single $Pr_{1-x}Ca_xMnO_3$ and $SrTiO_3$ films before the start of superlattice growth.

The magnitude of total thickness (d) in the superlattice structure is 112 nm, whereas the individual layer thickness of $Pr_{1-x}Ca_xMnO_3$ (d_1) and $SrTiO_3$ (d_2) being 1.8 nm and 5.7 nm for the layers grown on (001)-

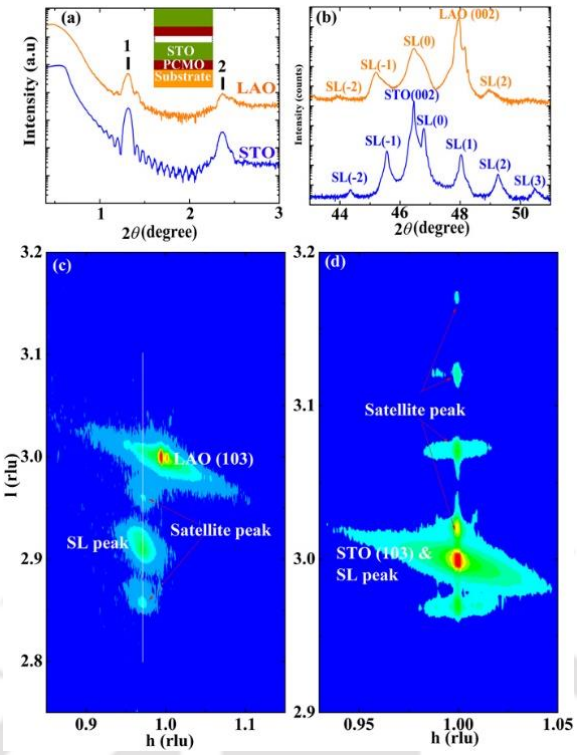

Fig. 3.1. The crystal structure of $[Pr_{1-x}Ca_xMnO_3/SrTiO_3]_{15}$ superlattices. (a) X-ray reflectivity measurements of $[Pr_{0.7}Ca_{0.3}MnO_3/SrTiO_3]_{15}$ superlattices grown on $LaAlO_3$ (orange curve) and $SrTiO_3$ (blue curve). The image shown in the inset provides schematic diagram of the superlattice structure. (b) θ–2θ x-ray diffraction (XRD) scans around the (002) reflection of superlattice grown on $LaAlO_3$ (orange curve) and $SrTiO_3$ (blue curve). The reciprocal space mapping (RSM) of the superlattice around the (103) reflection on $LaAlO_3$ (c) and $SrTiO_3$ (d).

oriented $SrTiO_3$ and $LaAlO_3$, respectively. Figure 3.1(b) represents the θ−2θ diffraction patterns near the (002) reflection of the $[Pr_{1-x}Ca_xMnO_3/SrTiO_3]_{15}$ superlattices (SLs). Several distinct satellite peaks [marked as SL(1), SL(2) … SL(−1), SL(−2), …] around the main peak (002) are clearly noticeable, which indicates a periodic structure of the superlattice architecture along with reasonably smooth interfaces. The position of the SL(0) peak is independent of super period (Λ) in both $LaAlO_3$ and $SrTiO_3$. The modulation period of the superlattices estimated using the expression $\Lambda=(n_i-n_{i-1})\lambda/[2(\sin\theta_i-\sin\theta_{i-1})]$, where n_i is the number corresponding to i^{th} order oscillation of the fringe and θi is the angle of that particular i^{th} order fringe. Accordingly, I estimated the magnitudes of Λ and these values are Λ = 7.5 nm and 7.6 nm for the SL on $SrTiO_3$ and $LaAlO_3$, respectively, which are in well agreement with those values obtained from the direct measurements of d_1 and d_2 ($\Lambda = d_1+d_2$). It should be noted that the SL(0) peak position is different for the different single crystal substrates, reflecting the fact that strain-induced change plays a significant role over the average out-of-plane lattice parameter (c). The calculated out-of-plane lattice parameters (c) from SL(0) peak position are 3.906 Å and 3.88 Å for the superlattices grown on (001) $LaAlO_3$ and $SrTiO_3$, respectively.

The in-plane (a) and out-of-plane (c) lattice parameters of the superlattices are also calculated from the reciprocal space map (RSM) around the (103) reflection as shown in Fig. 3.1(c) and Fig. 3.1(d). The

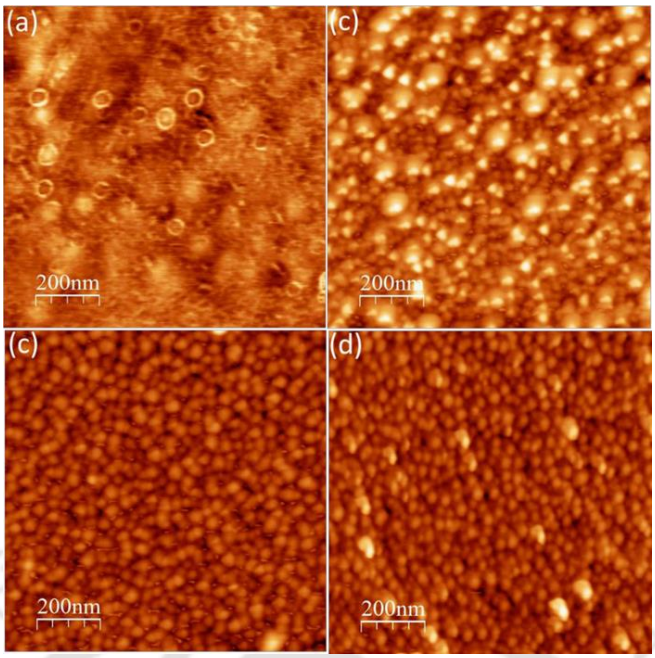

Fig. 3.2. The two-dimensional atomic force microscopic (AFM) surface morphology images of (a) $[Pr_{0.7}Ca_{0.3}MnO_3/SrTiO_3]_{15}$ superlattices grown on (001) oriented (a) $SrTiO_3$ and (b) $LaAlO_3$ substrates. AFM images (c) and (d) represent the $[Pr_{0.5}Ca_{0.5}MnO_3/SrTiO_3]_{15}$ superlattices grown on (001) oriented $SrTiO_3$ and $LaAlO_3$ substrates, respectively.

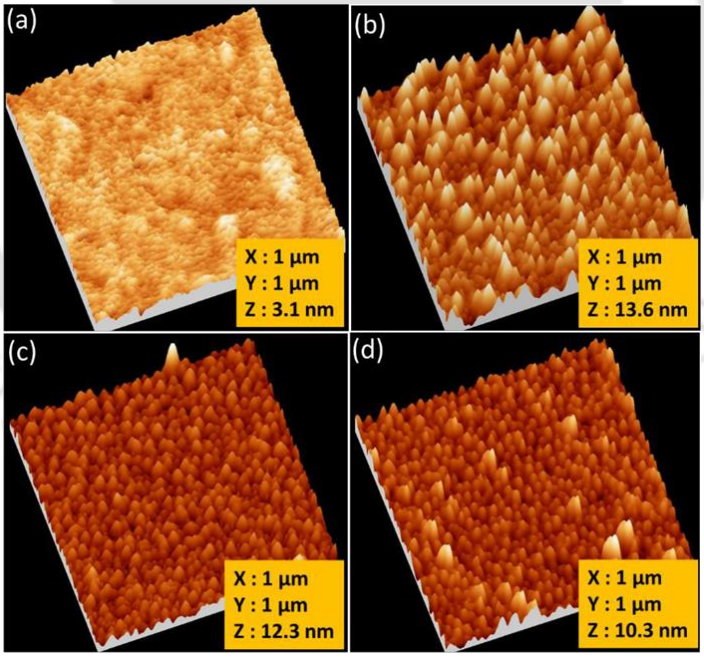

Fig. 3.3. The three-dimensional AFM surface morphology images of $[Pr_{0.7}Ca_{0.3}MnO_3/SrTiO_3]_{15}$ superlattices grown on (001) oriented (a) $SrTiO_3$ and (b) $LaAlO_3$ substrates. AFM images (c) and (d) represent the $[Pr_{0.5}Ca_{0.5}MnO_3/SrTiO_3]_{15}$ superlattices grown on (001) oriented $SrTiO_3$ and $LaAlO_3$ substrates, respectively.

average lattice parameters of the superlattices grown on $LaAlO_3/SrTiO_3$ are a = 3.88/3.905 Å and c = 3.906/3.88 Å, respectively. The c-axis lattice parameters measured using this procedure are in good agreement with the ones calculated from θ–2θ diffraction patterns. From these measurements, it is confirmed that the superlattices grown on $LaAlO_3$ assumes a compressive strain state, (i.e., $c/a > 1$), whereas the superlattices grown on $SrTiO_3$ exhibit a tensile strain state ($c/a < 1$). Considering the pseudo-cubic bulk lattice constants of $Pr_{1-x}Ca_xMnO_3$ (3.848 Å), I deduced the in-plane tensile strain that is equivalent to 0.8/1.5% for $Pr_{1-x}Ca_xMnO_3$ superlattices grown on $LaAlO_3/SrTiO_3$, respectively.

I have also studied the growth mechanism and surface morphology using the atomic force microscopic (AFM) measurements. Figures 3.2 and 3.3, respectively, represent the two-dimensional (2D) and three-dimensional (3D) AFM surface morphology images of $[Pr_{0.7}Ca_{0.3}MnO_3/SrTiO_3]_{15}$ superlattices grown on (001) oriented (a) $SrTiO_3$ and (b) $LaAlO_3$ substrates. The AFM images (c) and (d) represents the composition x = 0.5, $[Pr_{0.5}Ca_{0.5}MnO_3/SrTiO_3]_{15}$ superlattices grown on (001) oriented $SrTiO_3$ and $LaAlO_3$ substrates, respectively. All the samples exhibit uniform and homogeneous grain growth; however, from these 3D images, one can clearly notice different growth mechanism in the case of $[Pr_{0.7}Ca_{0.3}MnO_3/SrTiO_3]_{15}$ superlattices grown on (001) $SrTiO_3$ as compared to the 3D columnar grain growth structure of superlattices grown on (001) $LaAlO_3$ substrate. Furthermore, $[Pr_{0.5}Ca_{0.5}MnO_3/SrTiO_3]_{15}$ superlattices exhibit smaller grain size in both the cases ($SrTiO_3$ and $LaAlO_3$) as compared to the $[Pr_{0.7}Ca_{0.3}MnO_3/SrTiO_3]_{15}$ superlattices in which grains are connected by interconnecting channels, exhibiting an island growth mode. The root-mean-square surface roughness of all superlattices lie between 0.40 and 0.6 nm, indicating that a comparatively homogeneous and smooth surface of the bottom $Pr_{1-x}Ca_xMnO_3$ layer is favouring the high-quality growth of the top layer.

In order to understand the electronic structure and local environment, I performed XPS measurements. Figure 3.4 shows the x-ray photoelectron intensity vs binding energy of core-level spectra of Sr-3d [3.4(a), 3.4(f), and 3.4(k)], Ti-2p [3.4(b), 3.4(g), and 3.4(l)], Ca-2p [3.4(c), 3.4(h), and 3.4(m)], Mn-2p [3.4(d), 3.4(i), and 3.4(n)], and O-1s [3.4(e), 3.4(j), and 3.4(o)] for the superlattices $[Pr_{0.7}Ca_{0.3}MnO_3/SrTiO_3]_{15}$ grown on $LaAlO_3$ [3.4(a)– 3.4(e)] and $SrTiO_3$ [3.4(f)– 3.4(j)], whereas Figs. 3.4(k)– 3.4(o) represent XPS spectra of the $[Pr_{0.5}Ca_{0.5}MnO_3/SrTiO_3]_{15}$ superlattices grown on $LaAlO_3$. In all the superlattices, the core-level Sr-3d XPS spectra show three main peaks centred at 131.7(1), 133.4(2), and 137.3 eV. Here, the experimentally obtained raw data are shown as scattered symbols, whereas deconvoluted theoretical fits are shown as solid lines. The first two peaks (131.69 and 133.43 eV) are corresponding to the doublets of 3d electronic states of Sr with the binding energy separation of ~ 1.74 ± 0.02 eV. These results confirm the divalent oxidation state of Sr. The third peak, which is having very less intensity located at 137.49 eV, is corresponding to the satellite peak of Sr^{2+}. The intensity of these satellite peaks is higher in the case of $LaAlO_3$ grown films as compared to those of $SrTiO_3$ with slight shift in the peak positions.

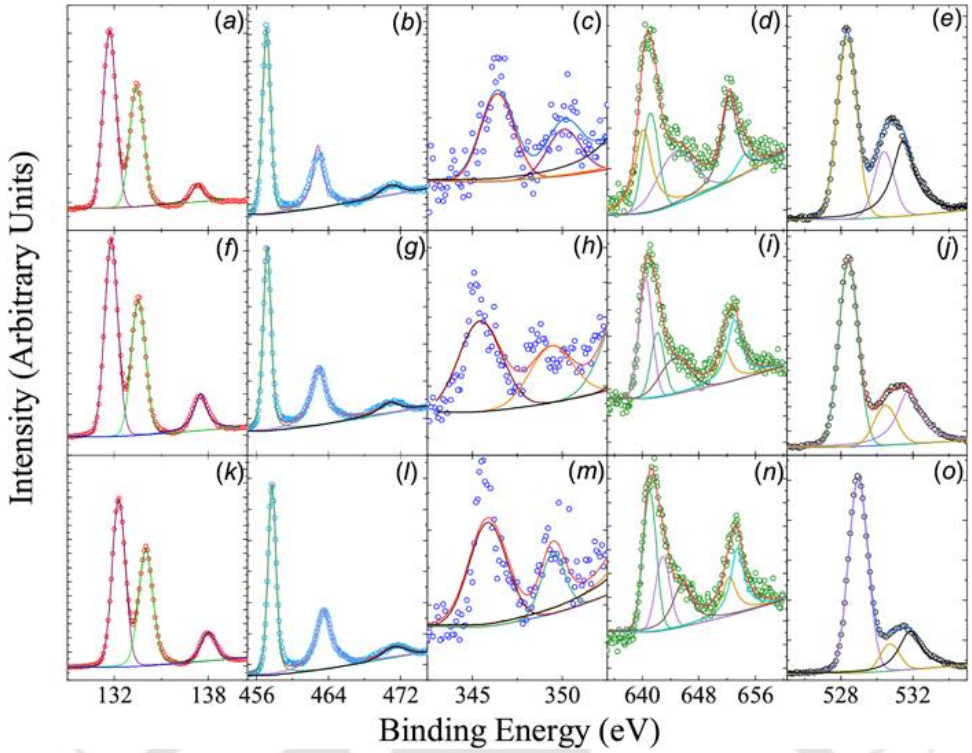

Fig. 3.4. The X-ray photoelectron spectra (XPS) of Sr-3*d* [(a), (f), and (k)], Ti-2*p* [(b), (g), and (l)], Ca-2*p* [(c), (h), and (m)], Mn-2*p* [(d), (i), and (n)], and O-1*s* [(e), (j), and (o)] of superlattices $[Pr_{0.7}Ca_{0.3}MnO_3/SrTiO_3]_{15}$ grown on $LaAlO_3$ [(a)–(e)] and $SrTiO_3$ [(f)–(j)]. (k)–(o) represent XPS spectra of the $[Pr_{0.5}Ca_{0.5}MnO_3/SrTiO_3]_{15}$ superlattices grown on $LaAlO_3$.

Nevertheless, all the core-level spectra of Sr-3*d* for $[Pr_{0.5}Ca_{0.5}MnO_3/SrTiO_3]_{15}$ superlattices grown on $LaAlO_3$ shifts significantly toward higher binding energy side. The core-level Ti-2*p* spectra exhibit two sharp peaks centred at 462.8 eV and 457.13 eV associated with the doublets Ti-$2p_{1/2}$ and Ti-$2p_{3/2}$, respectively. The spin–orbit splitting $\Delta(2p_{3/2}-2p_{1/2}) \sim 5.70 \pm 0.02$ eV suggests the tetravalent oxidation state of Ti. Moreover, a broad cusp observed across 471.5 eV is the satellite peak associated with Ti^{4+}. No significant change in the peak positions (or in intensity) was observed as the Pr compositions changes as well as with the change in the substrate. On the other hand, the photoelectron spectrum of "Mn" from 2*p* core level is resolved into five peaks, four main peaks located at 640.15 eV(P_1), 641.15 eV(P_2), 652.29 eV(P_3), and 654.46 eV(P_4) and one broad satellite peak at 644.7 eV(S_1). For the deconvolution, I have applied a mathematical fitting constraint on the full-width-at-half-maximum (FWHM) of the peak profile, i.e., the FWHM should range within 0.2 eV and this constraint is released at the final iteration. The main peaks are corresponding to the two doublets of Mn. The binding energy separation between the "Mn" doublets are $\Delta(P_1-P_3) \sim 11.25$ eV and $\Delta(P_2-P_4) \sim 10.66$ eV, providing the evidence for the mixed oxidation state of "Mn" (i.e., Mn^{3+} and Mn^{2+}). Generally, perovskites contain oxygen-deficient surface (10% oxygen vacancies) as compared to the bulk [123]. Since XPS is a surface sensitive technique the signature of Mn^{2+} can be noticed in the Mn-2*p* core-level spectrum. Another possible explanation would be the interfacial redox reaction between the electrodes (sputtered/deposited) and PCMO. The interfacial redox reaction leads

to the formation of an oxide layer on the metal electrode and an oxygen-deficient layer on the PCMO film [124–126]. The calculated Mn^{3+}/Mn^{2+} ratio by using the integrated intensities of Mn-2$p_{3/2}$ spectrum is ~ 1.84 a.u. Except the main peak P_1, no significant change in the peak positions (or in intensity) was noticed as the Pr compositions changes. The Ca-2*p* core-level photoelectron spectrum is deconvoluted into a doublet, Ca-2$p_{3/2}$ and Ca-2$p_{1/2}$, centred at 346.4 eV and 350.1 eV, respectively. The spin–orbit splitting between Ca-2$p_{3/2}$ and Ca-2$p_{1/2}$ is ~ 3.7 eV, confirming the divalent oxidation state of Ca in all the superlattice cases. Here, no significant alteration in these spectra were observed with the choice of substrate. Finally, the O-1*s* spectrum is deconvoluted into three Gaussian and Lorentzian peaks. All deconvoluted peaks have the FWHM of ~ 1.26 ± 0.20 eV. The first peak at lower binding energy (528.33 eV) is associated with the metal–oxygen (M–O) bonding, and the second peak (530.39 eV) is associated with the surface oxygen. Whereas the third peak (531.73 eV) signifies the presence of some excess oxygen at the surface of the samples. The intensity of M–O peak for $[Pr_{0.7}Ca_{0.3}MnO_3/SrTiO_3]_{15}$ grown on $SrTiO_3$ is relatively lower as compared to other samples, suggesting the domination of surface and excess oxygen in the sample.

Figure 3.5 shows the thermal variation of the magnetization M(T) of $Pr_{0.7}Ca_{0.3}MnO_3$ and $SrTiO_3$ superlattices and $Pr_{0.5}Ca_{0.5}MnO_3$ and $SrTiO_3$ superlattices grown on two different substrates (001) oriented $SrTiO_3$ and $LaAlO_3$ substrates. These measurements are performed under both zero-field-cooled (ZFC) and field-cooled (FC) conditions. I used two different external magnetic fields H_{DC} = 1 kOe and 10 kOe applied along the [100] direction (in-plane configuration). A clear bifurcation was noticed in both the M_{ZFC}(T) and

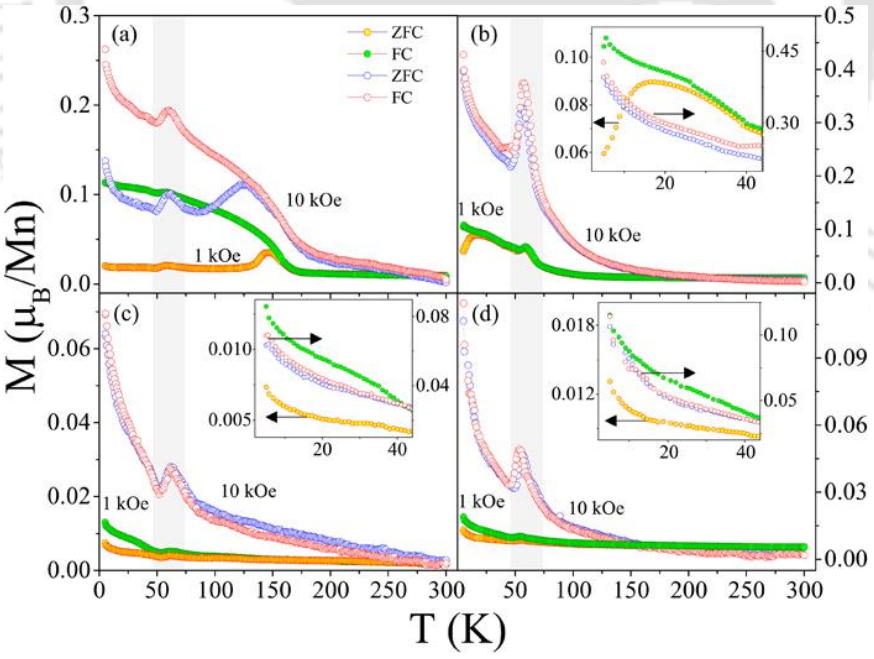

Fig. 3.5. Temperature dependence of magnetization M(T) measured under zero-field-cooled (ZFC) and field-cooled (FC) conditions of the superlattices $[Pr_{0.7}Ca_{0.3}MnO_3/SrTiO_3]_{15}$ grown on (001) oriented (a) $SrTiO_3$ and (b) $LaAlO_3$. Whereas (c) and (d) show the M(T) curves of $[Pr_{0.5}Ca_{0.5}MnO_3/SrTiO_3]_{15}$ superlattices grown on (001) oriented $SrTiO_3$ and $LaAlO_3$ single crystal substrates, respectively. All the M(T) measurements are performed at two different external magnetic fields H_{DC}=1 kOe and 10 kOe under warming condition. The insets represent zoomed view of the low temperature magnetization data.

M_{FC}(T) curves below 150 K for $[Pr_{0.7}Ca_{0.3}MnO_3/SrTiO_3]_{15}$ superlattices due to the either very high anisotropy or finite-size effects of the system. Also, the $[Pr_{0.7}Ca_{0.3}MnO_3/SrTiO_3]_{15}$ superlattice ferromagnetic behaviour with $T_C \sim 170$ K with a cusp at 148 K in M_{ZFC}(T) which shifts to 123 K with increasing the external field from 1 kOe to 10 kOe. However, the M(T) curves of $[Pr_{0.7}Ca_{0.3}MnO_3/SrTiO_3]_{15}$ superlattice grown on $LaAlO_3$ (001) substrate display no definite transition. Nevertheless, in all the samples, I noticed a low-temperature peak across 57 K due to the liquid oxygen that is paramagnetic in nature [127]. This observation is consistent with the XPS studies discussed above, where excess surface oxygen was detected in all the superlattices. The inset of Fig. 3.5(b) shows the magnified view of the magnetization curves below 45 K. These plots clearly show a low-temperature maximum in M_{ZFC}(T) at 17.36 K [14 K from the d(χT)/dT vs T plots (not shown)], which disappears in the presence of high magnetic fields. The origin of this peak is due to the loosely bound spins in the system. Moreover, no specific transition was observed in M(T) curves and no irreversibility in M_{FC}(T) and M_{ZFC}(T) curves in the case of low Pr content system $[Pr_{0.5}Ca_{0.5}MnO_3/SrTiO_3]_{15}$, instead these samples grown on either $LaAlO_3$ or $SrTiO_3$ substrates exhibit weak-ferromagnetic behaviour. In all these cases, I noticed that samples grown on $LaAlO_3$ (001) show enhanced magnetic moments and is much prominent at high magnetic fields but exhibit lower ordering temperatures [$T_C \sim 72.6$ K and 169.4 K, for $[Pr_{0.7}Ca_{0.3}MnO_3/SrTiO_3]_{15}$ grown on (001) $LaAlO_3$ and $[Pr_{0.7}Ca_{0.3}MnO_3/SrTiO_3]_{15}$ grown on (001) $SrTiO_3$, respectively]. The differential susceptibility [d(χT)/dT vs T] analysis yields to slightly lower ordering temperatures T_C = 158 K and the $Pr_{0.7}Ca_{0.3}MnO_3$ and $SrTiO_3$ superlattices grown on $SrTiO_3$ (001) in line with Fisher's relation (heat-capacity, $C_M \sim$ A.d(χT)/dT)

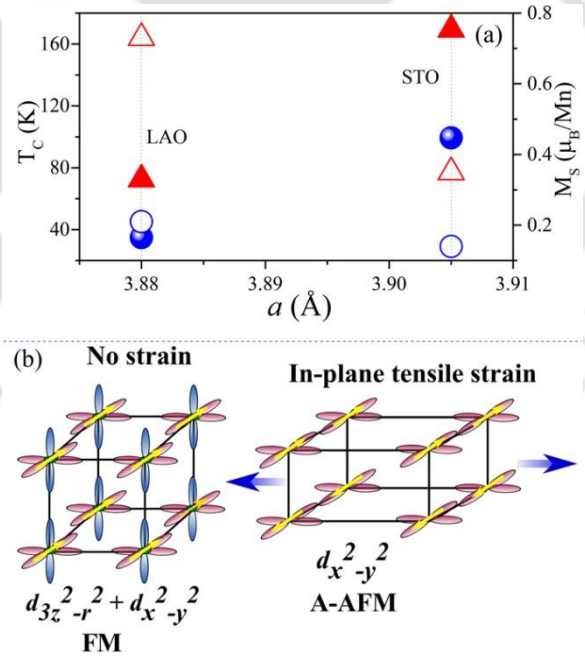

Fig. 3.6. (a) Variation of magnetic ordering temperatures (T_C, shown in solid symbols) and saturation magnetization (M_S, shown in hollow symbols) plotted as a function of lattice parameter (a) of the $[Pr_{0.7}Ca_{0.3}MnO_3/SrTiO_3]_{15}$ (red colour) and $[Pr_{0.5}Ca_{0.5}MnO_3/SrTiO_3]_{15}$ (blue colour) superlattices grown on (001) oriented $LaAlO_3$ and $SrTiO_3$ substrates, respectively. (b) Schematic diagram of d-orbitals corresponding to the FM configuration (without strain) and AFM arrangement (in-plane strain) of spins in the superlattices.

[128]. In ferromagnetic manganite heterostructures, double exchange interaction is the strongest for cubic symmetry (mediated by 180° Mn–O–Mn bond) unit cell [129], and the tensile strain reduces the T_C ferromagnetic manganite films [as shown in the Fig. 3.6(a)]. In Fig. 3.6(b), I have shown the schematic diagram of the *d*-orbitals to understand the spin configurations in the superlattices of AFM(FM) states, which occur due to the in-plane tensile strain (without strain). In our work, $Pr_{0.7}Ca_{0.3}MnO_3$ suffers less tensile strain on the $LaAlO_3$ substrate than $SrTiO_3$ substrates (as shown in the Fig. 3.6), which reflects difference in the magnetic properties of the superlattices grown on $LaAlO_3$ and SrTiO3. It is noted that the reduction of T_C from the bulk value for $Pr_{1-x}Ca_xMnO_3$ is also result of finite layer thickness of $Pr_{1-x}Ca_xMnO_3$ [130]. Previous neutron-diffraction studies on bulk $Pr_{0.7}Ca_{0.3}MnO_3$ provides evidence for the three different phase transitions in contrast to the present 2D superlattices case: (i) the change in the lattice symmetry across 200 K, (ii) collinear antiferromagnetic transition across 150 K, and (iii) the spin reorientation (from collinear and canted antiferromagnetic spin state) transition across 110 K [131]. The antiferromagnetic transition observed in the present case is in line with the above result except other two transitions.

Figure 3.7 shows the magnetization vs field hysteresis loops recorded at 5 K under the ZFC condition along the in-plane direction of all the superlattices after subtracting the diamagnetic contribution of the substrates using extrapolation method. All the samples exhibit finite coercivity (H_C) with small asymmetry in the loops (slight shift of M–H loop along the field direction and moves downward). Detailed analysis of these results leads to the following results. The superlattices $[Pr_{0.7}Ca_{0.3}MnO_3/SrTiO_3]_{15}$ grown on $SrTiO_3$ (001) exhibit larger H_C ~ 8.848 kOe and remanence magnetization M_R~0.12 μB/Mn with negligible

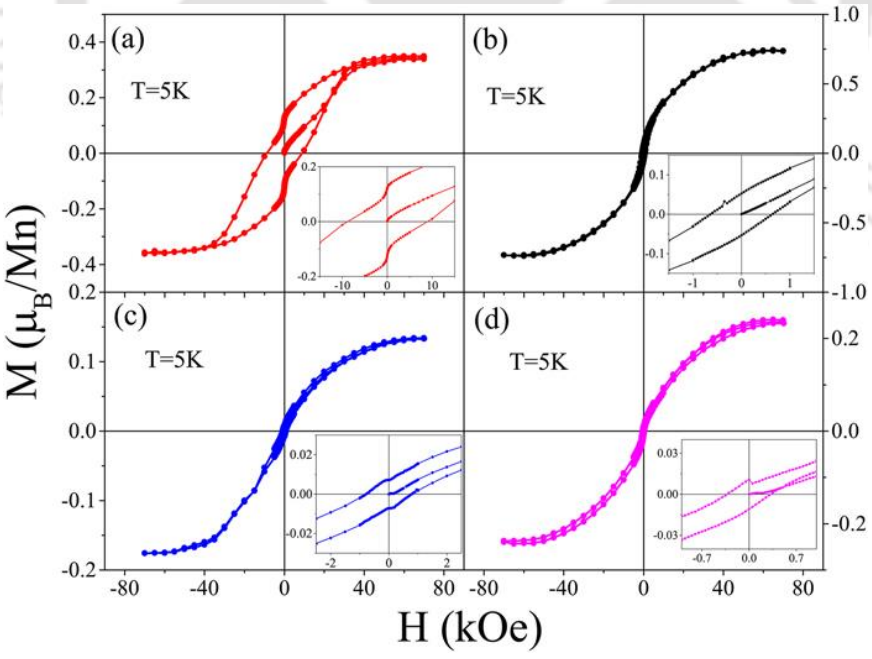

Fig. 3.7. Magnetic hysteresis (M-H) loops recorded at temperature (T=5 K) for the $[Pr_{0.7}Ca_{0.3}MnO_3/SrTiO_3]_{15}$ superlattices grown on (001) oriented (a) $SrTiO_3$ and (b) $LaAlO_3$. M-H loops shown in (c) and (d) correspond to the $[Pr_{0.5}Ca_{0.5}MnO_3/SrTiO_3]_{15}$ superlattices grown on (001) oriented $SrTiO_3$ and $LaAlO_3$, respectively. Insets clearly show the coercive field (H_C) and remanence magnetization (M_R) at low fields.

exchange-bias field of H_{EB} ~ 80 Oe. Whereas all the other superlattices exhibit very small H_C (~ 650 Oe) and M_R (0.05 μ_B/Mn) for $LaAlO_3$ (001) grown $[Pr_{0.7}Ca_{0.3}MnO_3/SrTiO_3]_{15}$ superlattices. For the system $[Pr_{0.5}Ca_{0.5}MnO_3/SrTiO_3]_{15}$ grown on $SrTiO_3$ (001), H_C ~ 800 Oe and M_R ~ 0.007 μ_B/Mn, whereas the same system grown on $LaAlO_3$ (001) exhibits further low H_C ~ 800 Oe but higher M_R ~ 0.01 μ_B/Mn. Nevertheless, all the superlattices grown on $LaAlO_3$ (001) substrates exhibit very higher saturation magnetization (M_S) values [M_S = 0.73 μ_B/Mn and 0.35 μ_B/Mn for $LaAlO_3$ (001) and $SrTiO_3$ (001) grown $[Pr_{0.7}Ca_{0.3}MnO_3/SrTiO_3]_{15}$ superlattices, respectively]. The bulk polycrystals of $Pr_{0.7}Ca_{0.3}MnO_3$ exhibit quite larger magnetic moment (M_{FC} ~ 4 μ_B/Mn) at low temperatures for H_{DC} ~ 30 kOe as compared to the present superlattice system (0.3 μ_B/Mn and 0.5 μ_B/Mn) for $[Pr_{0.7}Ca_{0.3}MnO_3/SrTiO_3]_{15}$ grown on $SrTiO_3$ (001) and $LaAlO_3$ (001) substrates, respectively [132]. Our results are consistent with the previous studies by Jiang et al. on the bulk $Pr_{1-x}Ca_xMnO_3$ system who reported significant decrease in magnetization values for x = 0.5 as compared to x = 0.3, which is related to the decrease of unit-cell volume and enhanced structural symmetry (with tolerance factor, t ~ 1) [133]. However, in the case of $Pr_{0.67}Ca_{0.33}MnO_3$ layers grown on the $LaAlO_3$ substrate with thickness ~ 1400 nm exhibit M_S ~ 300 emu/cc at 10 K, [70] which is close to $[Pr_{0.7}Ca_{0.3}MnO_3/SrTiO_3]_{15}$ superlattices grown on the $LaAlO_3$ (001) substrate.

In order to determine the magnetic anisotropy present in these superlattices, I used the Law of Approach to Saturation (LAS) model [134–136] and fitted the experimentally obtained virgin magnetization isotherm curve of the hysteresis loop for H > H_C with Eq. (3.1) given below. In general, near

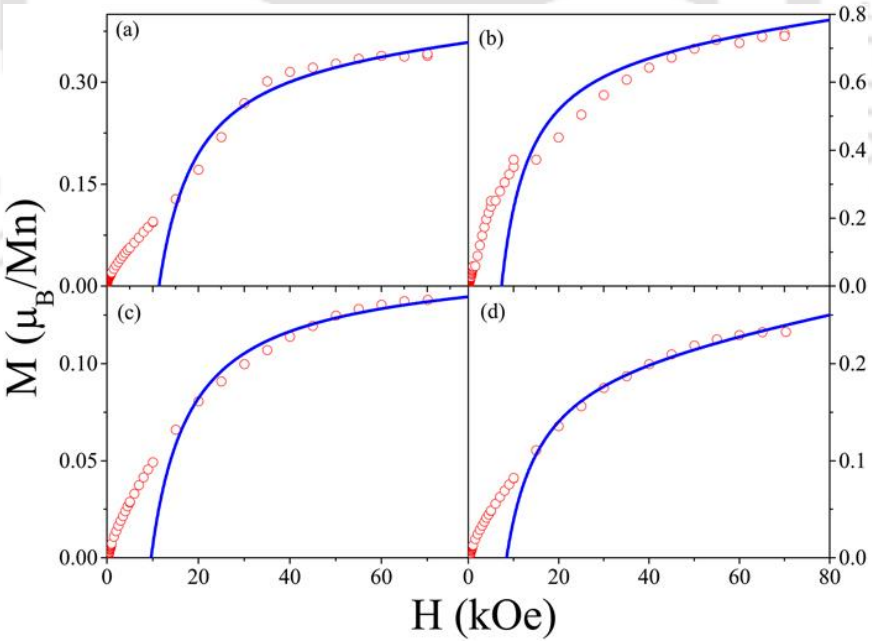

Fig. 3.8. The M-H isotherms (scattered symbols) and the corresponding theoretical fits (Eq. 3.1) based on the law of approach to saturation, LAS (solid line) recorded at 5 K for the superlattices $[Pr_{0.7}Ca_{0.3}MnO_3/SrTiO_3]_{15}$ grown on (001) oriented (a) $SrTiO_3$ and (b) $LaAlO_3$. (c) and (d) correspond to the $[Pr_{0.5}Ca_{0.5}MnO_3/SrTiO_3]_{15}$ superlattices grown on (001) oriented $SrTiO_3$ and $LaAlO_3$, respectively.

Table 3.1. List of various parameters obtained from the magnetization measurements. Saturation magnetization (M_S), magnetic anisotropy constant (K_1), and anisotropy field (H_K).

Superlattices/substrate	M_S (μ_B/Mn)	K_1 ($\times 10^4$ erg/cc)	H_K ($\times 10^3$ Oe)
$[Pr_{0.7}Ca_{0.3}MnO_3/SrTiO_3]_{15}/SrTiO_3$	0.35	80	9.0
$[Pr_{0.7}Ca_{0.3}MnO_3/SrTiO_3]_{15}/LaAlO_3$	0.74	5.77	0.31
$[Pr_{0.5}Ca_{0.5}MnO_3/SrTiO_3]_{15}/SrTiO_3$	0.14	1.42	0.38
$[Pr_{0.5}Ca_{0.5}MnO_3/SrTiO_3]_{15}/LaAlO_3$	0.21	1.77	0.33

the saturation magnetization (M_S), the magnetic moment of the samples can be expressed as follows:

$$M = M_S\left(1 - \frac{a}{H} - \frac{b}{H^2}\right) + \chi H \tag{3.1}$$

In the above equation, the term a/H is linked with the structural defects, whereas the magneto-crystalline anisotropy of the material is defined by the b/H^2 term, and the last term represents the paramagnetic behaviour of the system. Solid lines in Fig. 3.8 represents the best fit obtained using Eq. (3.1) to the experimental data points (scattered symbols). The corresponding fitting parameters evaluated using the above analysis is listed in Table 3.1. I observed higher values for $[Pr_{0.5}Ca_{0.5}MnO_3/SrTiO_3]_{15}$ superlattices grown on (001) oriented $SrTiO_3$ and $LaAlO_3$ substrates, which signifies the presence of large structural defects as compared to the $[Pr_{0.7}Ca_{0.3}MnO_3/SrTiO_3]_{15}$ superlattices grown on the similar substrates. The cubic magnetic anisotropy constant K_1 has been calculated using the following equation:

$$b = \frac{8}{105}\frac{K_1^2}{\mu_0^2 M_S^2} \tag{3.2}$$

where μ_0 is the free space permeability. For $[Pr_{0.7}Ca_{0.3}MnO_3/SrTiO_3]_{15}$ superlattices grown on $SrTiO_3$(001), the magnitude of K_1 is considerably larger ($\sim 8 \times 10^5$ erg/cc) than the other superlattices {1.42×10^4 erg/cc and 1.77×10^4 erg/cc for $[Pr_{0.5}Ca_{0.5}MnO_3/SrTiO_3]_{15}$ grown on (001)-oriented $SrTiO_3$ and $LaAlO_3$ substrates, respectively}. This may arise due to the ferromagnetic behaviour of the $[Pr_{0.7}Ca_{0.3}MnO_3/SrTiO_3]_{15}$ superlattices. On the other hand, the remaining superlattices exhibit weak-ferromagnetic behaviour in composition with the above samples. The superlattices $[Pr_{0.7}Ca_{0.3}MnO_3/SrTiO_3]_{15}$ grown on (001) oriented $LaAlO_3$ exhibit higher K_1 value than $[Pr_{0.5}Ca_{0.5}MnO_3/SrTiO_3]_{15}$. Furthermore, I evaluated the anisotropy field H_K using the relation: $H_K = \frac{2K_1}{\mu_0 M_S}$. Among all the systems, $[Pr_{0.7}Ca_{0.3}MnO_3/SrTiO_3]_{15}$ superlattices exhibit very high values of H_K ($\sim$ 8.84 kOe), whereas for the other systems, the magnitude of H_K is significantly low (between 301 Oe and 378 Oe). Such a drastic reduction in H_K generally occurs due to the decrease of the magnetic exchange interactions [136]. Previous studies on the angle dependent magneto-optical Kerr magnetometry studies on $La_{0.67}Sr_{0.33}MnO_3$ thin films grown on the (001) oriented $SrTiO_3$ substrate reveal large anisotropy features induced by the defects in the crystal structure rather than the

magnetoelastic effects [137]. The magnitude of K_1 obtained in the present case is comparable to that of $La_{0.7}Sr_{0.3}MnO_3$ thin films (~ 4.5 × 10^5 erg/cc) grown on (001) oriented $SrTiO_3$ and other 2D manganite/ruthanate systems (~ 4 × 10^6 erg/cc) reported using the ferromagnetic resonance studies [138, 139]. Conversely, in the present case, the magnitude of M_S increases in the case of $[Pr_{0.5}Ca_{0.5}MnO_3/SrTiO_3]_{15}$ superlattices grown on $LaAlO_3$ (001) as compared to the $SrTiO_3$ (001) grown $[Pr_{0.5}Ca_{0.5}MnO_3/SrTiO_3]_{15}$ systems. More elaborately, the strain might change the Mn–O–Mn bond distances and bond angles, which, in turn, causes alteration in the effective spin exchange energy [114, 140]. Also, the strain-induced elongation of MnO_6 octahedra leads to crystal field splitting of e_g levels as a consequence finite possibility of non-orthogonal overlapping between these orbitals may takes place, which can suppress the ferromagnetic double exchange coupling [141–143]. Nonetheless, the interface between the $Pr_{1-x}Ca_xMnO_3$ and $SrTiO_3$ layers plays a role beyond the strain effects. Furthermore, the interface will affect the magnetic order significantly at this low thickness of the manganite layers (~ 5 unit cells). Also, the degree of interdiffusion will affect magnetic ordering and a suppression of magnetic order with increasing interdiffusion is expected across the interfaces of the superlattices studied in the present case [114, 144, 145].

In what follows I provide a brief description of summary and conclusions of our work presented in this chapter.

3.4. Summary

In summary, I have successfully grown superlattices of $[Pr_{0.7}Ca_{0.3}MnO_3/SrTiO_3]_{15}$ and $[Pr_{0.5}Ca_{0.5}MnO_3/SrTiO_3]_{15}$ on (001) oriented $LaAlO_3$ and $SrTiO_3$ single crystal substrates by pulsed laser deposition technique. On the basis of reciprocal space mapping analysis, I concluded that these superlattices exhibit weak tetragonal distortion. The X-ray photoelectron spectroscopy results confirm the divalent electronic state of Sr and Ca, the tetravalent state of Ti, and mixed valency in Mn with a strong shift of binding energy separation toward the higher energy side in (001) $LaAlO_3$ grown superlattices as compared to those layers grown on (001) $SrTiO_3$. The temperature and magnetic field dependence of magnetization results demonstrate that $[Pr_{0.7}Ca_{0.3}MnO_3/SrTiO_3]_{15}/SrTiO_3$ superlattices exhibit a ferromagnetic character below 170 K with high degrees of anisotropy. Using the M-H isotherms and the law of approach to saturation for ferromagnets, I have estimated the cubic anisotropic constant (K_1) and anisotropy field (H_K) for all the investigated systems, where the superlattices $[Pr_{0.7}Ca_{0.3}MnO_3/SrTiO_3]_{15}/SrTiO_3$ exhibit the highest H_K ~ 9 kOe and K_1 ~ 8 × 10^5 erg/cc. However, upon changing the residual strain (which is induced by the substrate), a drastic decrease in the magnetic ordering temperatures and significant enhancement in the overall magnetic moments are noticed. In this study, I have also shown that one can alter the magnetic structure of the superlattices under tensile strain, which may find potential utility in the fields of magnetoelectronic devices.

Chapter 4
Magnetization reversal, field-induced transitions and H–T phase diagram of $Y_{1-x}Ce_xCrO_3$

This chapter emphasizes on the Magnetization reversal, field-induced transitions, and H–T phase diagram of $Y_{1-x}Ce_xCrO_3$. In this chapter, I implemented a comprehensive study on the structural, electronic, and magnetic properties of bulk polycrystalline $Y_{1-x}Ce_xCrO_3$ solid solutions in which Ce incorporation has remarkable effect on the overall magnetic properties of the pristine $YCrO_3$ system. Four different compositions (x) of bulk polycrystalline perovskite systems of $Y_{1-x}Ce_xCrO_3$ (x = 0, 0.05, 0.1, 0.2) were synthesized using oxalate-based sol-gel technique. The tolerance factor (t) of the perovskite system $Y_{1-x}Ce_xCrO_3$ with compositions x = 0 and x = 0.1 are 0.853 and 0.855, respectively which makes the crystal structure to distort into the orthorhombic phase. Octahedral distortion parameter (Δ) of the BO_6 octahedra of the perovskite structure decreases from 11.9 to 9.3 with the doping of Ce as the radius of Ce^{3+} cation ($r_{Ce^{3+}}$) is greater than the radius of Y^{3+} cation ($r_{Y^{3+}}$). The analysis of the magnetic field and thermal variation of the heat-capacity and dc susceptibility data below the AFM Néel temperature T_N (140–148 K) results the following key features such as giant NM, field-induced, first-order, spin-reorientation transitions (16 – 22 K) accompanied by the thermal hysteresis in $M_{FCC}(T)$ and $M_{FCW}(T)$, intermediate paramagnetic transition (T_{IP}) and negative exchange-bias effect.

4.1. Introduction

The concept of magnetization reversal (MR), negative magnetization (NM) and compensation phenomena (T_{Comp}) in the rare-earth (R) perovskites $R(Cr/Mn)O_3$ have swiftly reinvigorated the field of strongly correlated electronic oxides in the recent past [18–23]. Among the pool of distorted-orthorhombic (*Pbnm*) AFM perovskite family of compounds, yttrium manganite ($YMnO_3$) and yttrium chromite ($YCrO_3$) systems have attracted immense attention because of their fascinating physical properties such as: multiferroic behaviour, exchange-bias, switchable polarization driven by magnetostriction, mixed-phase behaviour (weak-ferromagnetism, WFM component along the c-axis below AFM ordering) *etc.* [146–148] These compounds attained prominence from the applications point of view since the above intriguing physical phenomena can be readily utilized for the development of many magneto-electronic devices including the read/write heads of hard-drives and spin-valves [47, 149–151]. Among the two yttrium-based perovskites, $YCrO_3$ system is a peculiar candidate (discovered by Looby and Katz way back in 1954) which exhibits canted G-type AFM spin structures below ~ 140 K (Néel temperature, T_N) due to the antisymmetric Cr^{3+}–O–Cr^{3+} superexchange interaction without any influence of the trivalent Y ion on the global magnetic ordering which is also very crucial for the low-temperature spin-reorientation transition (T_{SR}) [152–154]. Interestingly, this system also exhibits high temperature ferroelectric (FE) transition across 473 K supporting the earlier (1967) predictions by Rao *et al.* [155] who noticed breaks in the temperature dependence of

conductivity (log σ–T^{-1}) plots across 823 K which is similar to its sister compounds Yb/La/Dy/Ho/$LuCrO_3$ [146, 156]. Although the magnitude of WFM (popularly termed as Dzyaloshinskii–Moriya (DM), interaction) [42, 153, 154, 157, 158] is usually weak, yet it plays an important role (linking the spin and lattice degrees of freedom) on the other physical properties such as dielectric and ferroelastic features of $YCrO_3$ system [42, 159–161]. Jacobs *et al.* reported first experimental evidence for the existence of T_{SR} and WFM in both systems $YFeO_3$ and $YCrO_3$ which exhibits ground state spin configuration S = 5/2 and 3/2, respectively [162]. These observations are later supported by both dc-magnetization studies and frequency dependence of ac-susceptibility data reported by Yamaguchi *et al.*, and Morishita and Tsushima [152–154]. Moreover, very recently Mall and Pramanik reported anomalous spin fluctuations below T_N in polycrystalline pristine $YCrO_3$ compound using the temperature dependent 89Y nuclear magnetic resonance measurements, which links the WFM and spin-lattice relaxations following the power-law scaling behaviour ($T^{-\beta}$) [148]. Interestingly, the same authors reported a new phase transition (across 230 K) within the disordered intermediate paramagnetic region by means of the temperature dependence of electron spin resonance study [157,158,163].

Nevertheless, the degeneracy between the ground states of WFM and G–AFM can be lifted significantly (more prominent T_{SR} and WFM can be seen) if the non-magnetic trivalent Yttrium ions are replaced with other rare-earth ions (such as R^{3+} = Ce, Gd, Yb, La, Tb, Dy, Ho, Sm or Lu) possessing finite local magnetic moment which is the subject of this article. Such substitution causes transcendent interaction between the *d*-electrons of transition metal Cr^{3+} ($t_{2g}^3 e_g^0$, $\mu_B \sim 3.87$ and S = 3/2) and the electrons of f-block ions (Ce^{3+} in the present case, $\mu_B \sim 2.54$ and S = 3/2) in which the DM interaction significantly disrupts the inversion symmetry through incommensurate magnetization of trivalent Cr in the vicinity of T_N [157, 158]. Therefore, below T_N the magnetic behaviour of the solid solutions $R_{1-x}A_xCrO_3$ (A = Ce) becomes more complicated as the magnitude of the *f*-block element magnetization increases. Previous studies reported the emergence of few novel magnetic/dielectric phenomena (such as MR, NM, T_{CMP} and FE polarization) in various combinations of rare-earth ion substituted $YCrO_3$ as a consequence of incompletely occupied f-electrons coupling with the *d*-electron thereby causing tilting of CrO_6 octahedrons. Such unusual observations are the main motivation for carrying out detailed study on the Ce substituted $YCrO_3$ which is not explored till now in the literature.

Therefore, in this work I implemented a comprehensive study on the structural, electronic, and magnetic properties of bulk polycrystalline $Y_{1-x}Ce_xCrO_3$ solid solutions in which Ce incorporation has remarkable effect on the overall magnetic properties of the pristine $YCrO_3$ system. Our analysis provides clear signatures of enhanced antiferromagnetic ordering temperature with intermediate paramagnetic transition across 230 K, low-temperature spin-reorientation transition 15 K, negative exchange-bias and magnetic field induced transitions (50 kOe) all of which are very sensitive to the Ce–Cr exchange interaction in the octahedrally distorted perovskite lattice. Such details are interpreted in consonance with the H–T phase

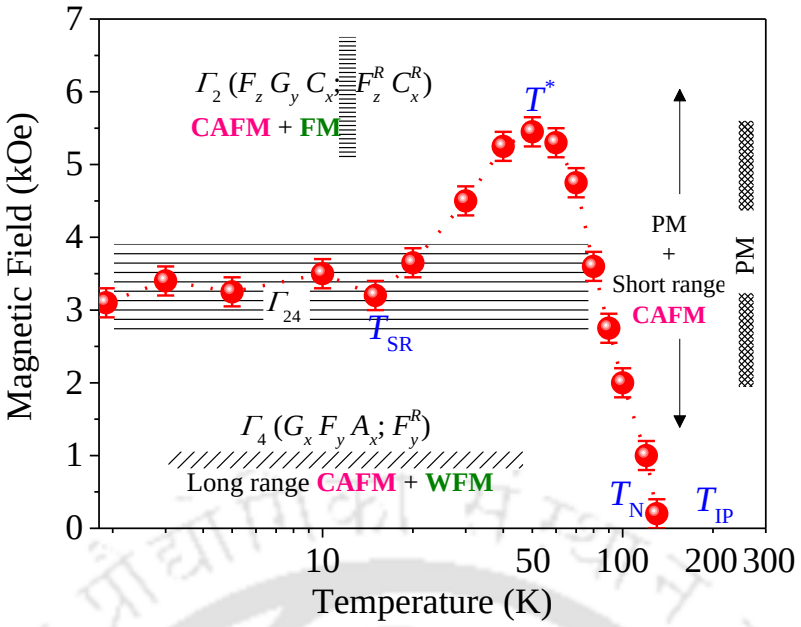

Fig. 4.1. Magnetic field-temperature (H–T) phase diagram of $Y_{0.9}Ce_{0.1}CrO_3$ polycrystals showing different regions of magnetic phases.

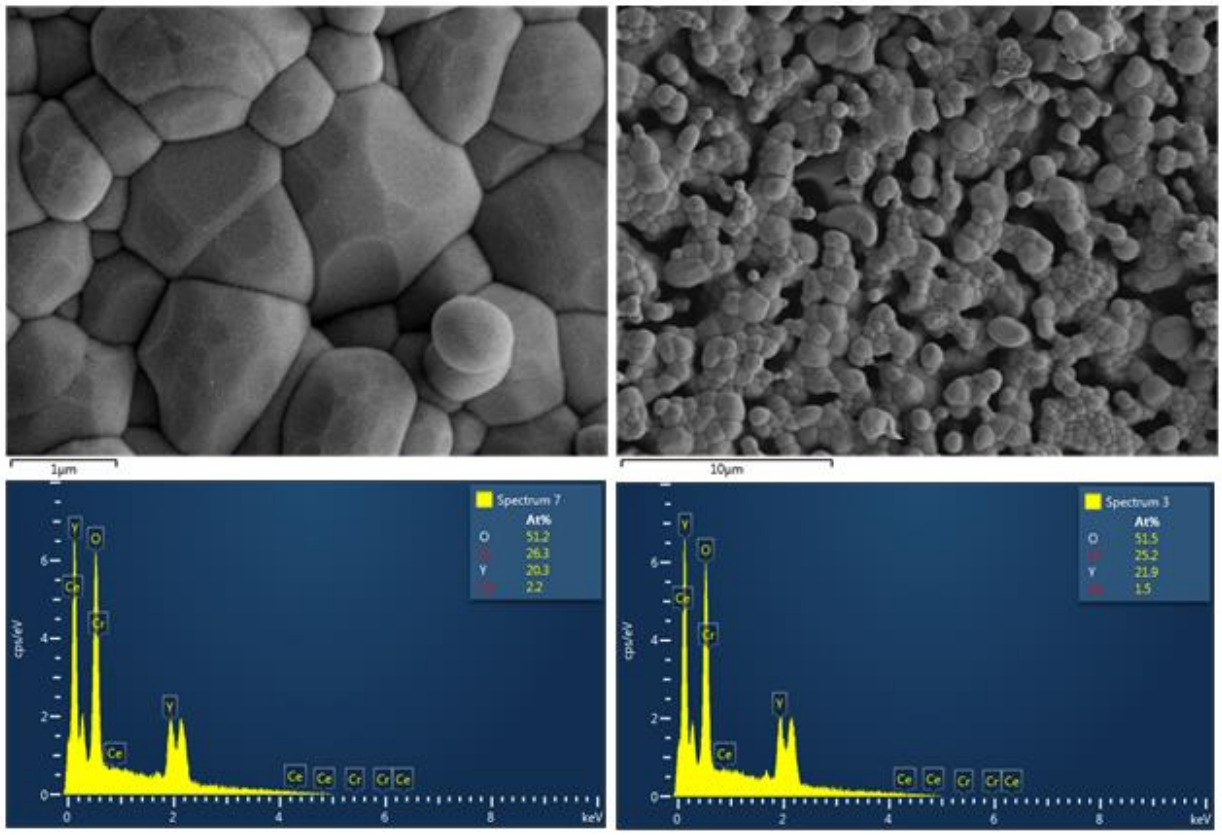

Fig. 4.2. Scanning electron micrographs (SEM) of $Y_{0.9}Ce_{0.1}CrO_3$ bulk polycrystals recorded under secondary electron (SE) mode displaying the formation of large grain samples of average size 2 μm.

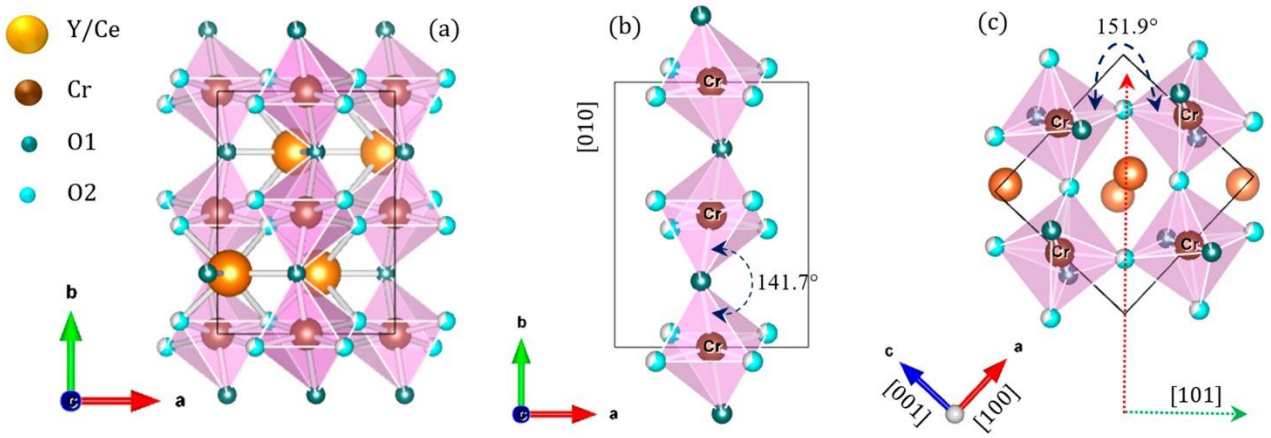

Fig. 4.3. The schematic representation of (a) distorted crystal structure of the perovskite $Y_{1-x}Ce_xCrO_3$ around *c*-axis, (b) representation of the crystal structure along *b*-axis and (c) along *a* and *c*-axes, which are generated from the VESTA, a 3D visualization programme for structural models.

diagram (Fig. 4.1) constructed from the temperature dependent field-induced transition which distinguishes the Γ_4 (G_z, F_y, A_x) phase (i.e., long-range canted AFM + weak FM) from Γ_{24} mixed phase and strong Γ_2 (F_z, G_y, C_x; F_z^R; C_x^R) AFM + FM region. Thorough explanation of these results along with the comparative analysis is provided in the following sections.

4.2. Experimental details with crystal and electronic structure characterizations

Four different compositions (*x*) of bulk polycrystalline perovskite systems of $Y_{1-x}Ce_xCrO_3$ (x = 0, 0.05, 0.1, 0.2) were synthesized using oxalate-based sol-gel technique. This process involves the nitrate salts of Y($Y(NO_3)_3.6H_2O$)), Ce($Ce(NO_3)_3.6H_2O$)) and Cr($Cr(NO_3)_3.6H_2O$)) as precursors and ethanol as solvent. Dying of the oven dried gel at 353 K – 373 K leads to complete digestion of the xerogel followed by calcination above 1473 K. Calcination of the oven dried precursor above 1473 K in air for 12 h leads to fine-size powders of partly formed perovskite structure (after the removal of all the volatile substances). However, in order to obtain the perfect perovskite phase, I grinded the calcined powders for 3 h in an agate mortar with pestle and pressed into cylindrical pellets using a hydraulic press followed by the high temperature sintering of the pellets at 1573 K for 48 h in air. This procedure resulted dense cylindrical pellets of large grain sizes. In order to ensure the uniformity and perfect homogeneity of the compounds I crushed these sintered pellets and regrinded for 2 h and re-pelletized followed by sintering at 1573 K for 48 h in air. This entire procedure is repeated thrice to yield fully densified large grain sizes pellets (Fig. 4.2) of desired compositions ($Y_{1-x}Ce_xCrO_3$ (*Pnma*)) of single-phase perovskite structure consistent with the literature JCPDS file no: 34-0365 (Fig. 4.3).

Table 4.1. Tabulated ttexture coefficients of the investigated system were calculated from the X-ray diffraction data using the Eq. (4.1).

TC	$x = 0$	$x = 0.05$	$x = 0.1$	$x = 0.2$
(111)	0.99	0.926	0.881	1.08
(200)	1.027	1.08	0.876	0.700
(121)	1.2	1.22	1.252	0.972
(002)	1.020	1.01	1.096	0.945
(202)	0.996	0.982	1.077	1.270
(123)	0.77	0.777	0.816	1.02

Texture coefficients of the investigated system were calculated from the X-ray diffraction data using the below equation [164, 165] are tabulated in Table 4.1:

$$TC\ (hkl) = \frac{\frac{I(hkl)}{I_0(hkl)}}{\frac{1}{N}\sum_N \frac{I(hkl)}{I_0(hkl)}} \tag{4.1}$$

where, TC (hkl) is texture coefficient for (hkl) plane, $I(hkl)$ is experimentally observed intensity, $I_0(hkl)$ is standard intensity and N is the number of peaks. The full widths at half maximum (FWHM) of the

$$\beta cos\theta = \frac{k\lambda}{t} + \eta sin\theta \tag{4.2}$$

diffraction pattern was determined by the Gaussian peak fitting and estimated the average crystallite size using the Williamson-Hall analysis according to the below equation [166, 167].

In the above expression t represent the average crystallite size, K is the dimensionless shape parameter (0.89 was used in this study in accordance with earlier reports of synthesis of similar materials [168, 169] λ is the wavelength of the X-ray source and β is the FWHM of the diffraction peaks at the Bragg angle (θ), and η is the micro-strain. The crystallite sizes determined by this method have large uncertainties arising from mean-squared error (MSE) between the data and the fitting to above expression. Accordingly, the magnitude of t for all the compositions is estimated (~ 80 - 500 nm for $x = 0.05$ - 0.1) which decreases with increasing the x up to a critical composition (x_C) beyond which a drastic change in the magnitude of 't' is noticed due to the formation of the secondary phase.

The crystal structure characterization was performed using the Rigaku X-ray diffractometer (model: Smart Lab, 9 kW) with Cu-K_α (1.543 Å) radiation as X-ray source. The orthorhombic monophasic perovskite structure is stable up to a critical dilute composition limit $x_c \leq 0.05$ and a marginal increase in the lattice parameters (0.5% increase in unit-cell volume) was noticed with the incorporation of Ce into the *Pnma* lattice (as shown in Fig. 4.4 and Table 4.2). Beyond a critical limit x_C, the cell volume shows anomalous changes due to formation of secondary phases. Beyond x_c, non-magnetic CeO_2 ($Fm3m$) emerges as secondary phase which increases progressively with increasing the composition irrespective of the heat-treatment conditions

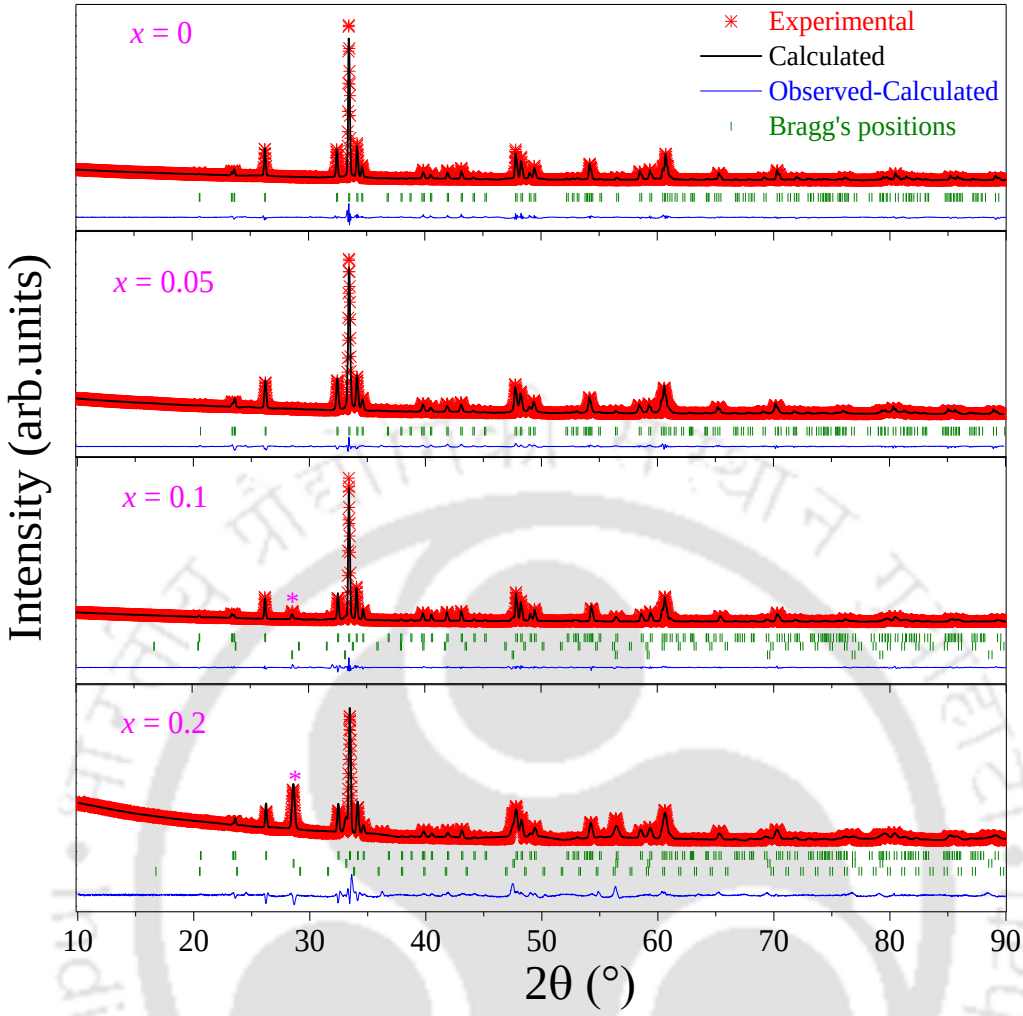

Fig. 4.4. X-ray diffraction patterns and the corresponding Rietveld refinement data for different compositions ($0.0 \leq x \leq 0.2$) of $Y_{1-x}Ce_xCrO_3$ bulk polycrystals. The Rietveld refinement was performed using the FullProf Suite.

and intermediate grindings. The tolerance factor (t) of the perovskite system $Y_{1-x}Ce_xCrO_3$ with compositions x = 0 and x = 0.1 are 0.853 and 0.855, respectively which makes the crystal structure to distort into the orthorhombic phase. Octahedral distortion parameter (Δ) of the BO_6 octahedra of the perovskite structure decreases from 11.9 to 9.3 with the doping of Ce as the radius of Ce^{3+} cation ($r_{Ce^{3+}} = 1.143$ Å) is greater than the radius of Y^{3+} cation ($r_{Y^{3+}} = 1.019$ Å) (Table 4.2). The electronic structure and chemical composition of the pelletized samples were probed using XPS. For this, I used Kratos analytical spectrometer (model: AXIS Supra+) configured with a dual monochromatic x-ray source Al K_α /Ag L_α (2984.2 eV) with spatial resolution less than 1 μm. The binding energy of carbon C–1*s* orbital (~ 284.8 eV) was used for the calibration of all the recorded core-level spectra. The core-level electronic spectra of all the elements Y, Cr, Ce and O are shown in the Fig. 4.5 which reveals the trivalent oxidation state of Y and Ce and partly mixed valence $(3^+_{75\%})/(4^+_{25\%})$ of Cr and standard divalence state of O consistent with the previous reports [163]. The

Table. 4.2. The list of crystal structure parameters including the atomic positions and the geometrical parameters characterizing the crystal structure of $Y_{1-x}Ce_xCrO_3$ system. The octahedral distortion parameter Δ of a polyhedron BO_6 with an average bond length B–O ⟨d⟩ is defined as $\Delta = \frac{1}{N}\sum_{n=1}^{N}\left[\frac{d_n - \langle d\rangle}{\langle d\rangle}\right]^2$. The tilt angles φ and θ for CrO_6 octahedra along the Miller indices of directions [010] and [101] of the pseudo-cubic lattice are obtained from the two angles θ_1 and θ_2. x', y' and z' are the coordinates x is the composition. The lattice parameters denoted by a, b, and c. V is the volume of the unit cell. Y, Ce, Cr, and O refers to the elements Yttrium, Cerium, Chromium and Oxygen. Cr-O1, Cr-O2, ⟨Cr-O2⟩ and ⟨Cr-O⟩ refers to the average bond length. Cr-O(1)-Cr and Cr-O(2)-Cr are the bond length along the oxygens O(1) and O(2).

Parameter		x = 0.0	x = 0.05	x = 0.10	x = 0.20
a (Å)		5.519	5.523	5.503	5.515
b (Å)		7.534	7.548	7.537	7.544
c (Å)		5.244	5.256	5.252	5.253
V (Å^3)		218.05	219.09	217.83	218.58
Y/Ce (x, 0.25, z)	x	0.0651	0.0638	0.0642	0.0634
	z	-0.0165	-0.0178	-0.0142	0.0136
Cr (0, 0, z)	z	0.5000	0.5000	0.5000	0.5000
O(1) (x, 0.25, z)	x	0.4454	0.4611	0.4645	0.4549
	z	0.1187	0.1178	0.0966	-0.0743
O(2)	x	0.2874	0.2855	0.2972	0.2842
	y	0.0532	0.0487	0.0560	0.0528
	z	-0.288	-0.293	-0.308	0.2880
Cr – O1:2		2.0064	1.9976	1.9612	1.9419
Cr – O2:2		1.9784	1.9509	1.9678	1.9633
Cr – O2:2		1.9536	1.9771	2.0089	1.9657
⟨Cr − O2⟩		1.966	1.9640	1.9884	1.9645
⟨Cr − O⟩		1.979	1.975	1.9793	1.9570
$\Delta\langle Cr - O\rangle \times 10^{-5}$		11.9	9.3	11.4	2.99
θ_1 : Cr – O(1) – Cr		140	142	148	153
θ_2 : Cr – O(2) – Cr		151	152	146	152
θ [010]		13.75	14.16	14.14	13.73
φ [101]		12.06	8.64	12.68	11.99

ratio of the composition of the four different elements present in the sample calculated using the below expression [170]:

$$\frac{\frac{A}{f_1}}{\left[\frac{A}{f_1}+\frac{B}{f_2}+\frac{C}{f_3}+\frac{D}{f_4}\right]} : \frac{\frac{B}{f_2}}{\left[\frac{A}{f_1}+\frac{B}{f_2}+\frac{C}{f_3}+\frac{D}{f_4}\right]} : \frac{\frac{C}{f_3}}{\left[\frac{A}{f_1}+\frac{B}{f_2}+\frac{C}{f_3}+\frac{D}{f_4}\right]} : \frac{\frac{D}{f_4}}{\left[\frac{A}{f_1}+\frac{B}{f_2}+\frac{C}{f_3}+\frac{D}{f_4}\right]}$$

where, A, B, C and D are the areas under the curves in the B.E vs Intensity plot of the X-ray photoelectron spectrum. f_1, f_2, f_3, and f_4 are the sensitivity factors. The obtained ratio for the sample $Y_{0.9}Ce_{0.1}CrO_3$ is 0.876 : 0.1 : 0.977 : 2.531. It suggests as $Y_{0.88}Ce_{0.1}Cr_{0.98}O_{2.5}$.

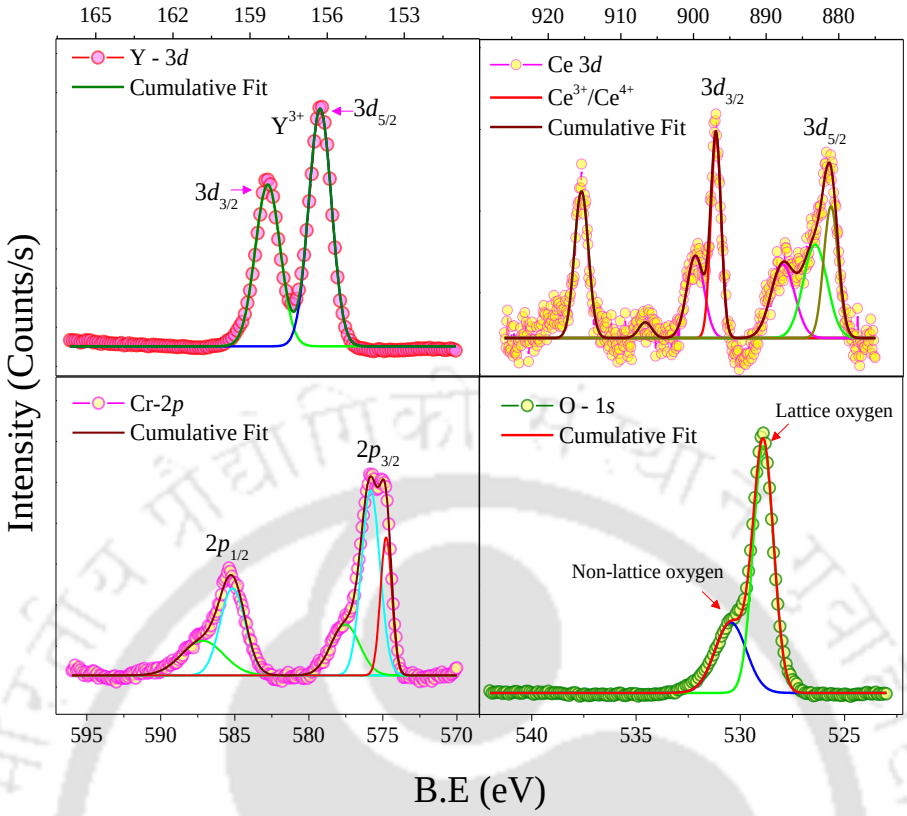

Fig. 4.5. X-ray photoelectron spectra (represented in terms of Intensity vs. Binding energy) of $Y_{0.9}Ce_{0.1}CrO_3$ polycrystalline perovskite system showing the core-level electronic spectra of (a) Y^{3+}-3*d* (b) Ce^{3+}-4*f* (c) Cr^{3+}-2*p* and (d) O^{2-}-1*s*.

All the magnetization measurements were performed using a physical property measurement system (PPMS) (from quantum design model: Dyna cool) with vibrating sample magnetometer accessory which is capable of reaching 1.9 K from 400 K with dc-magnetic field (H_{DC}) capacity ± 90 kOe. In addition, I performed the temperature dependence of specific heat, C_P(T) measurements were performed by PPMS (quantum design) with the standard heat-pulse calorimetry between 1.9 K to 240 K.

4.3. Temperature and Field dependant Magnetic characterizations, Specific Heat Analysis

Figure 4.6 shows temperature dependent magnetization M(T) measurements of four different compositions of $Y_{1-x}Ce_xCrO_3$ system measured under standard zero-field-cooled (ZFC) and field-cooled (FC) protocols under warming conditions in an externally applied H_{DC} ~ 100 Oe. All the samples exhibit standard G-type AFM ordering with substantial increase of the T_N from 142 K to 145 K for the compositions x = 0 to 0.2, respectively as estimated from the M–T data. The ordering temperature (141 K) for the pristine compound ($YCrO_3$) is consistent with the previous reports [146, 148]. The following eye-catching features are predominant in this system: (i) giant magnitude of the NM in M_{ZFC} branch (~ −127 emu/mol), (ii) large difference in the magnetization (ΔM ~ 280 emu/mol) between the M_{FC} and M_{ZFC} at low temperature T = 1.9 K and (iii) emergence of spin-reorientation transitions, T_{SR} at low-temperatures below which the strength of

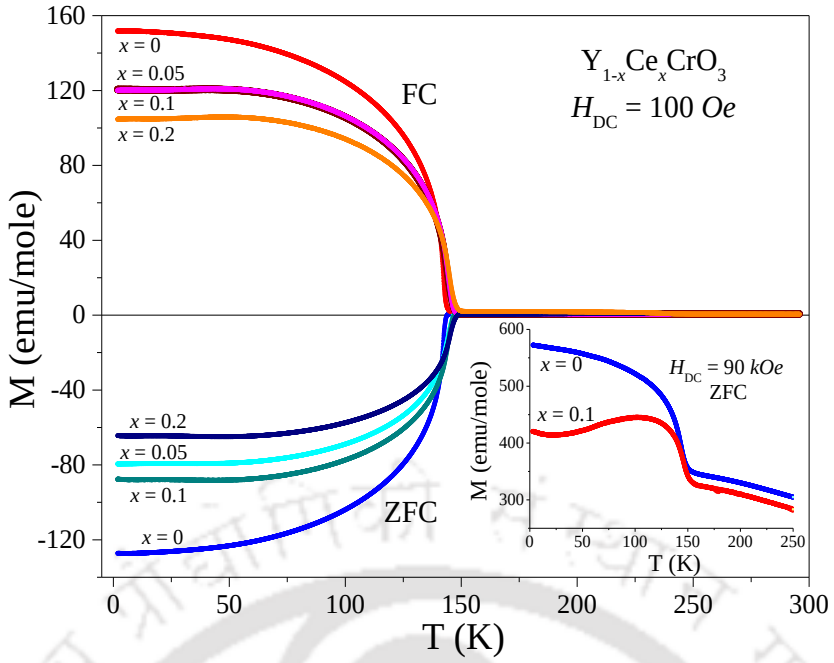

Fig. 4.6. Temperature dependence of magnetization M(T) plots of $Y_{1-x}Ce_xCrO_3$ (x = 0, 0.05, 0.1, 0.2) recorded under both ZFC and FC conditions measured with increasing the sample temperature in the presence of externally applied field H_{DC} = 100 Oe. Inset shows the high field (H_{DC} = 90 kOe) data of M–T measured under ZFC condition for x = 0 and 0.1 focussing the spin reorientation.

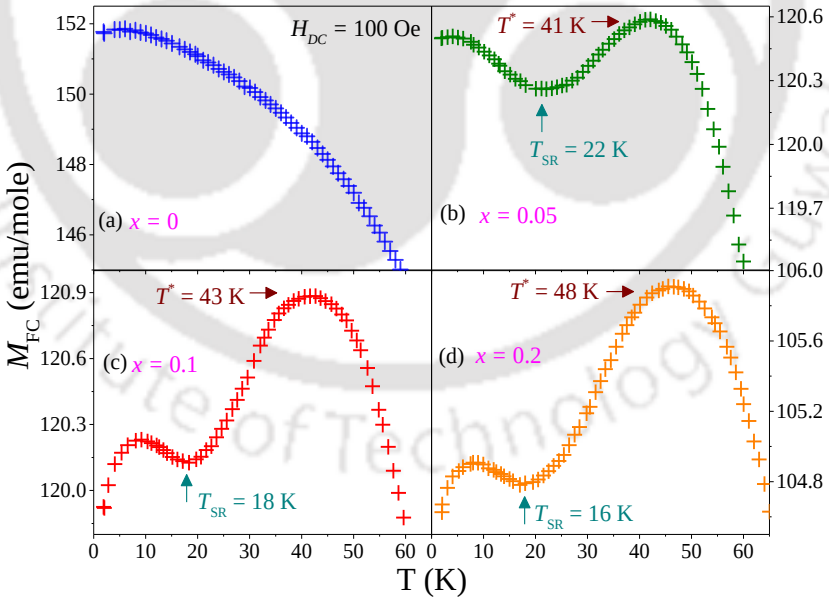

Fig. 4.7. Zoomed view of the low temperature $M(T)$ data measured under FC condition in the presence of the external magnetic field H_{DC} = 100 Oe for different compositions of $Y_{1-x}Ce_xCrO_3$ (a) x = 0, (b) x = 0.05, (c) x = 0.1, and (d) x = 0.2.

the ferromagnetic domains increase due to the incorporation of the Ce at the Y-sites of the sublattice.

The magnitudes of T_{SR} and T* being 22 and 41 K (for x = 0.05), ~18 K and 43 K (for x = 0.10) and ~16 K and 48 K (for x = 0.2) as shown by the arrows in the zoomed view of the M_{FC}–T plots in Fig. 4.7. Clearly the magnitude of T_{SR} shifts towards the low temperatures with increasing the composition (as well as field), T_{SR} ~ 17 K → 15 K for H_{DC} ~ 50 Oe → 1 kOe). The onset of decrease in the maximum magnetization ($M_{FC, max}$ ~ 121 (106) emu/mol for x = 0.1(0.2)) from T* ~ 41 K (for x = 0.1) confirms the combined effect of trivalent Ce and Cr moments in which both the moments align oppositely below T_N with Cr spins orient in opposite direction to the applied H_{DC} thereby creates a local field that influence the overall magnetic ordering. The magnitude of overall magnetization reduces significantly as the concentration of trivalent Ce increases and its contribution is more as compared to the moment of trivalent Cr. Moreover, the intermediate paramagnetic state T_{IP} across 230 K is evident in the semi-log plots of M vs T which is associated with the short-range ordering of trivalent Cr canted spins (Fig. 4.8) consistent with the previous reports [148, 163]. FC measurements recorded while cooling and warming cycles under the application of external H_{DC} = 500 Oe (given in the Fig. 4.9). In both the undoped and Ce substituted $YCrO_3$, FCC and FCW shows a hysteresis due to the first-order phase transition around the AFM ordering temperature T_N with contrasting behaviours of FCC lagging in x = 0 with ΔT = 4 K and leading in x = 0.05 with ΔT = 10 K.

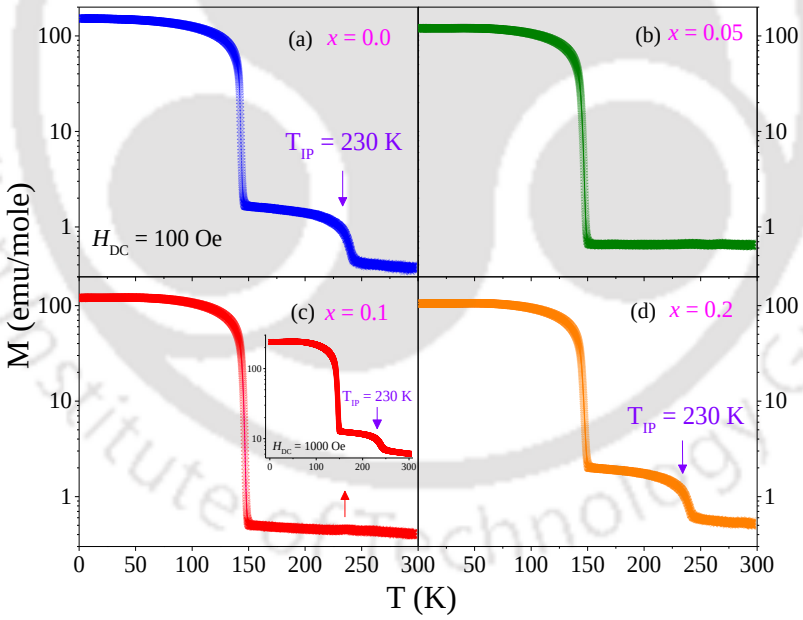

Fig. 4.8. Semi-log plots of M vs T recorded under FC condition of $Y_{1-x}Ce_xCrO_3$ measured in the presence of external magnetic field H_{DC} = 100 Oe for (a) x = 0, (b) x = 0.05, (c) x = 0.1, and (d) x = 0.2. Inset in figure (c) includes the semi-log plot of M vs T measured at H_{DC} = 1 kOe of x = 0.1 clearly depicting the intermediate paramagnetic transition.

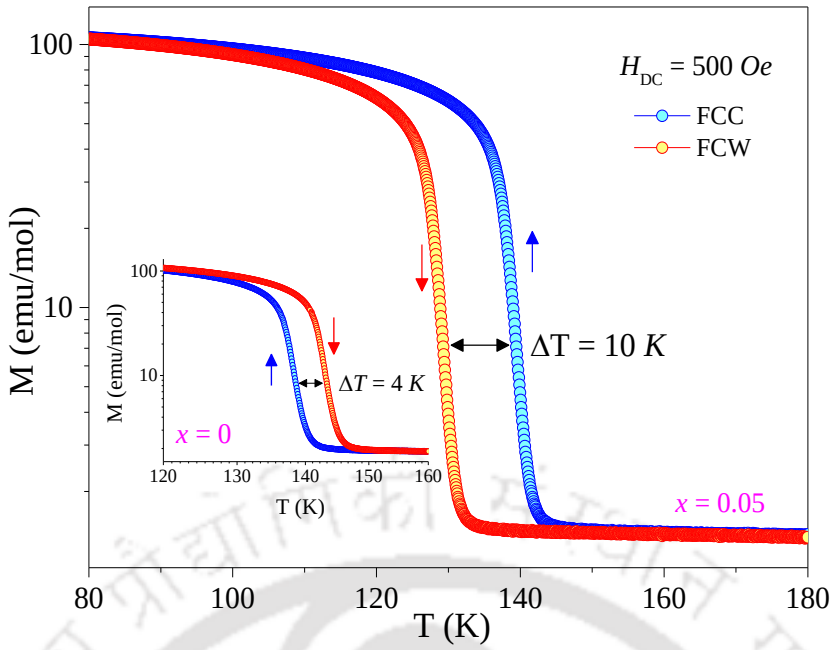

Fig. 4.9. Temperature dependence of magnetization of $Y_{1-x}Ce_xCrO_3$ (x = 0 (inset) and 0.05 under FCC (blue) and FCW (red) conditions measured at externally applied H_{DC} = 500 Oe.

For the precise determination of the AFM ordering temperature, I first evaluated the magnitude of magnetic susceptibility χ (= M/H) and it is multiplied with the temperature (χ T). The peak maximum singularity obtained from the derivative of this product χT with respect to T(d(χT)/dT) and its temperature dependence finally yields the exact magnitude of T_N (figures not given). Such variation of (d(χT)/dT vs T) closely resembles the temperature dependence of specific heat (C_P(T)) in the AFM systems and this procedure gives an accurate measure of the magnetic ordering temperature [128, 166, 171]. These values are few percentages smaller than the values obtained from the M–T plane which are listed in the Table 4.3 and all these values are consistent with the C_P(T) data discussed as following.

Table. 4.3. The list of parameters obtained from the magnetization data (both M(T) and M(H)): Maximum value of M_{FC} and M_{ZFC}, Néel Temperature (T_N), Intermediate Paramagnetic transition temperature (T_{IP}), Spin reorientation temperature (T_{SR}), Magnetization peak temperature (T^*) Compensation temperature (T_{Comp}), and effective magnetic moment (μ_{eff}) for different Ce substituted $YCrO_3$ samples.

x	$M_{FC, max}$ (emu/mole)	$M_{ZFC, max}$ (emu/mole)	T_N (K)	T_{SR} (K)	T_{Comp} (K)	T_{SR} (K)	T^* (K)
0	152	-127	142	--	144	--	--
0.05	120.6	-79	143.8	22	147	22	41
0.1	121	-88	144	18	147	18	43
0.2	106	-65	145	16	149	16	48

Figure 4.10 shows the $C_P(T)$ for x = 0.1 system measured both under zero-field H_{DC} = 0 and within the field H_{DC} = 90 kOe with anomaly across the AFM transition like a λ shaped peak usually noticed in standard $RCrO_3$ systems. With the application of high magnetic field, a significant broadening in the T_N is noticed and shifts by 2 K towards the high temperatures as expected in all AFM/FM systems (as shown in the inset of Fig. 4.10(a)). Furthermore, I have extracted the individual contributions of the lattice ($C_{P-Lattice}(T)$) and magnetic ($C_{P-Magnetic}(T)$) specific heats from the total specific heat $C_{P-Total}(T)$ using the below expression following the Debye model. It is well known that the contribution of $C_{P-Lattice}$ is a sum of both electronic $C_{P-Electron}$ and phonon $C_{P-Phonon}$ parts. Since the electronic contribution is significant only at very low temperatures, the contribution of phonon can be extracted from the following Eq.(4.3) and Eq. (4.4):

$$C_{P-Phonon} = Nf_D\left(\frac{\Theta_D}{T}\right) \tag{4.3}$$

$$C_{P-Phonon} = 9NR\left(\frac{T}{\Theta_D}\right)^3 \int_0^{\Theta_D/T} \frac{x^4 e^x}{(e^x-1)^2} dx \tag{4.4}$$

The left-hand-side scale of Fig. 4.10(b) shows the temperature dependence of the individual contributions of ($C_{P-Lattice}(T)$) and magnetic ($C_{P-Magnetic}(T)$) specific heats of bulk polycrystalline system $Y_{0.9}Ce_{0.1}CrO_3$. In the above expression, the quantity $f_D(\Theta_D/T)$ represents Debye function (= $9R(T/\Theta_D)^3 \int_0^{\Theta_D/T} x^4 e^x/(e^x-1)^2 dx$), where N is the number of atoms per formula unit, R is the universal gas constant (8.314 J mol^{-1} K^{-1}), x (= $h\upsilon_E/k_BT$, υ_E is Einstein frequency) and Θ_D is the Debye temperature.

To gauge the contribution of $C_{P-Phonon}$ and Θ_D, I have fitted the experimentally obtained $C_{P-Total}$ data with the above expression. Here the effect of magnetic contribution is expected to be negligible for the temperatures above T_N and T_{IP}. The above mathematical fitting analysis yields Θ_D = 470 K for $Y_{0.9}Ce_{0.1}CrO_3$ bulk sample which is significantly lower than the Θ_D of pristine $YCrO_3$ compound (Θ_D = 720 K) and Pr substituted (30 atomic%) bulk $YCrO_3$ system 645–655 K [42, 160, 172]. Nevertheless, it is interesting to note that $C_{P-Magnetic}(T)$ exhibits weak anomaly across 50 K consistent with the spin reorientation transitions (magnon excitations) noticed in the magnetization data which is in line with the previous reports on pure and Pr substituted $YCrO_3$ system where anomalous spin-correlations are noticed between 10 K and 60 K [160, 162, 172–174]. At the low temperatures ($T < T_N$), the orthogonal component of the spontaneous weak moment becomes prominent due to the smooth rotation of the canted AFM spins and significant interaction of Ce/Y and Cr as a result one can see the broad hump in the heat capacity (C_PT^{-3}) data under H_{DC} = 0 Oe condition (not shown). Previous studies reported such anomalous changes across 40 K in the temperature dependence of C_PT^{-3} data of pure $YCrO_3$ compound [172, 174–179].

In order to quantitatively probe the dominant exchange interactions, I fitted the high temperature susceptibility data with the DM interaction term and evaluated the relevant parameters [180]. The magnetic susceptibility data in majority of the rare-earth based canted antiferromagnetic perovskite systems above T_N follows the DM antisymmetric exchange interaction instead of the Curie–Weiss law ($\chi = C/T - \Theta$) [42]. It

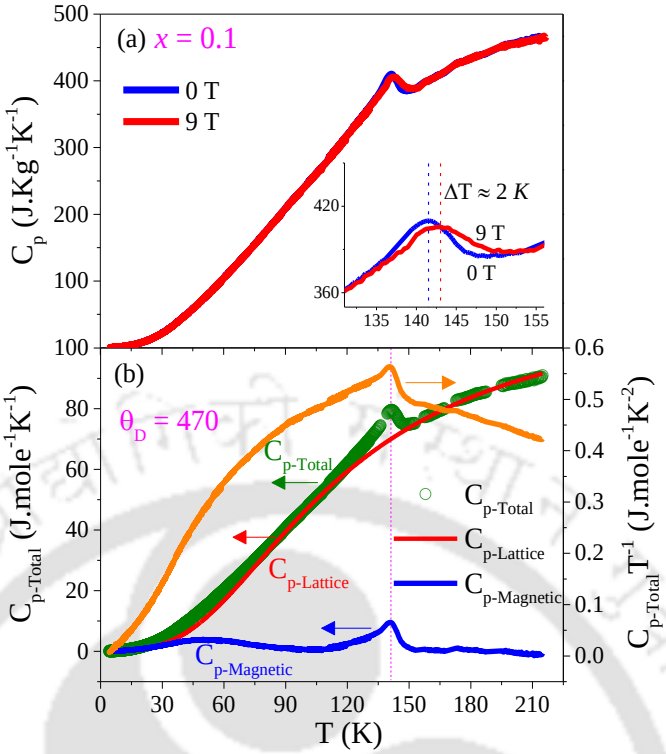

Fig. 4.10. (a) Temperature dependent specific heat of $Y_{0.9}Ce_{0.1}CrO_3$ sample measured under the external H_{DC} = 0 (blue) and 90 kOe (red). Inset shows the transitions and shift in transition temperature. (b) Left-scale—total specific heat data (green circles) of $Y_{0.9}Ce_{0.1}CrO_3$ polycrystalline sample measured at zero field. The red colour solid line represents the lattice contribution of specific heat calculated from numerical fits using equation $Cp_{\text{–Phonon}} = Nf_D\Theta_D/T = 9NR\left(\frac{T}{\Theta_D}\right)^3 \int_0^{\Theta_D/T} \frac{x^4 e^x}{(e^x-1)^2} dx$ as described in the text and blue solid line represents the magnetic contribution to the specific heat ($C_{\text{P–Magnetic}} = C_{\text{P–Total}} - C_{\text{P–Lattice}}$). Right-scale: temperature dependence of $C_{\text{P–Total}}/T$ showing the transition at ~141 K more explicitly.

is well known that the DM interaction accounts for the susceptibility perpendicular to the easy axis unlike the Curie–Weiss law, which applies to the susceptibility parallel to the easy axis of the crystal [181]. Hence, I employed the below Eq. (4.5) related to the DM interaction in understanding the temperature dependence of the paramagnetic susceptibility (χ(T)) although it is not possible to independently measure parallel and perpendicular susceptibilities in the present case as the investigated system is in polycrystalline form (merging the parallel and perpendicular components)

$$\chi = \frac{C}{(T-\Theta)} \frac{(T-T_0)}{(T-T_N)} \tag{4.5}$$

Here C is the Curie constant, Θ is the Weiss temperature, T_N is the Néel temperature of the system and T_0 is a fitted parameter. The inverse susceptibility χ^{-1}(T) plots of all the systems are fitted (solid lines) to the above expression (Fig. 4.11). The corresponding parameters evaluated from the best fits are listed in the supplementary Table 4.4. It should be noted that the magnitude of AFM ordering temperature obtained

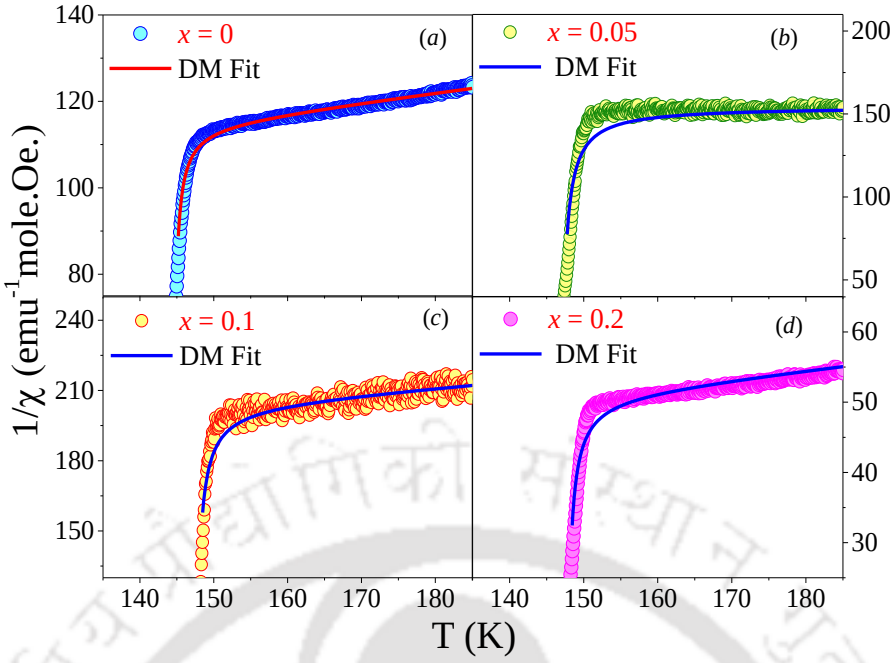

Fig. 4.11. Temperature dependence of inverse paramagnetic susceptibility data and the corresponding fits shown by solid lines (with Eq. (4.4)) for different compositions of $Y_{1-x}Ce_xCrO_3$ (a) x = 0, (b) x = 0.05, (c) x = 0.1, and (d) x = 0.2.

by the differential susceptibility data d(χT)/dT is in line with those estimated from the modified Curie–Weiss law which will be discussed later. It is clear that the role of the term in the above expression $(T - T_0)/(T - T_N)$ is significant in the vicinity of T_N which results a sharp falloff in the χ^{-1} since the variance between AFM ordering temperature and T_0 is < 3 K. Following the analysis proposed by Moriya [42] I estimated the dominant exchange interactions both symmetric JS and antisymmetric super-exchange interaction J_{AS} using the below relations which links the order parameter T_N, Boltzmann constant k_B, spin S, coordination number Z and fitting parameter T_0 (obtained from the $\chi^{-1}(T)$ and DM fits).

$$T_0 = \frac{2ZJ_S S(S+1)}{3k_B} \tag{4.6}$$

$$T_N = \frac{2ZJ_S S(S+1)}{3k_B} \tag{4.7}$$

Usually, from the modified Curie–Weiss law one can obtain the information about the J_S between Cr^{3+} ions while from the DM method the other exchange interactions J_{AS} (such as the Ce^{3+}–Ce^{3+} and Ce^{3+}–Cr^{3+} interactions) can be extracted. Consequently, using Eq. (4.6) considering the magnitudes of T_0 (144–147 K), Z (=6) and S (=3/2) the magnitude of J_S has been estimated which lies between 0.83–0.85 meV for x = 0 to 0.2). Whereas the magnitudes of antisymmetric interaction J_{AS} (0.085–0.12 meV) are estimated using the Eq. (4.7) and the corresponding T_N which are one order magnitude less than that of J_S as expected for trivalent Ce/Ce and Ce/Cr ions. From this analysis, I noticed significant enhancement of J_{AS} with increasing the Ce substitution at Y as compared to the exchange interaction for symmetric case. The effective

Table. 4.4. The list of parameters obtained from the fitting the dc-susceptibility data using the Eq. (4.5) for different composition of $Y_{1-x}Ce_xCrO_3$. The Néel temperature T_N (K), the fitting parameter T_0 (K), the symmetric exchange constant J_S (*meV*), the antisymmetric exchange constant J_{AS} (*meV*), the Weiss temperature Θ (K), Curie constant C (emu.K.Oe^{-1}mol^{-1}), and effective magnetic moments μ_{eff} (μ_B) for Ce substituted $YCrO_3$ samples.

	x = 0.0	x = 0.05	x = 0.10	x = 0.20
$\boldsymbol{T_N^{(a)}}$	142	143.7	144	144.8
T_N	144.5	144.9	147.5	147.8
$\boldsymbol{T_0}$	144.4	144.6	147.2	147.4
J_S	0.830	0.831	0.847	0.848
J_{AS}	0.084	0.099	0.108	0.120
Θ	- 386	- 450	- 664	- 279
C	1.7	1.8	1.9	2.2
$\boldsymbol{\mu_{eff}}$	3.67	3.83	3.92	4.19
$\boldsymbol{\mu_{eff}^{(b)}}$	3.87	3.91	3.95	4.03

magnetic moment obtained from the best fits increases progressively (μ_{eff} ~ 3.67(theoretical ~ 3.87), 3.8(3.91), 3.92(3.95), 4.19(4.03) μ_B /f.u.) with increasing the Ce content and consistent with the theoretical counterpart of trivalent Ce and Cr (having d^3, S = 3/2).

McDannald et al reports the J_S and J_{AS} values for the Y doped $DyCrO_3$ polycrystalline system to be 0.817 meV and 0.16 meV [181]. In addition, Er and Ho doped $DyCrO_3$ show the J_S values 0.806 meV and 0.823 meV, and J_{As} values to be 0.164 meV and 0.172 meV, respectively. These values are in good agreement with our present Ce doped $YCrO_3$ system in which R^{3+}–Cr^{3+} interactions evolved. While the Curie–Weiss temperatures, Θ lies between −386 K (x = 0) and −664 K (x = 0.2), in-line with the previous reports on pristine compound $YCrO_3$ as well as Pr substituted $YCrO_3$ wherein a wide range of Θ (−325 K to −461 K and −596 K) estimated from the standard magnetization data and by means of NMR Knight shift experiments [148, 172, 174, 179, 182–185.

In order to estimate the ground state spin configuration and probe the field induced transition if any arising in the investigated system I performed a detailed field (± 90 kOe) dependence of magnetization (M–H) measurements under two different protocols ZFC and FC (90 kOe) at different temperatures (1.9 K to 150 K) cooling from T_N. Figure 4.12 shows the M–H typical five cycle hysteresis loops recorded at 1.9 K measured under FC condition for different compositions which reveals giant values of the coercive field (H_C ~ 22 kOe, x = 0.1), remanent magnetization (M_R ~ 104 emu/mol, x = 0.1) and exchange bias field (H_{EB} ~ 2.5 kOe, x = 0.1). It is interesting to note that the temperature dependence of loop asymmetry and its magnitude (H_{EB}(T) and M_{EB}(T)) including the temperature dependent coercivity (H_C(T)) and remanance (M_R(T)) shows the clear anomalies across the T_{SR} and WFM regimes (Fig. 4.13) which is consistent with the C_P (T) and M(T) data discussed above. One can clearly notice the zero-crossover of these parameters and

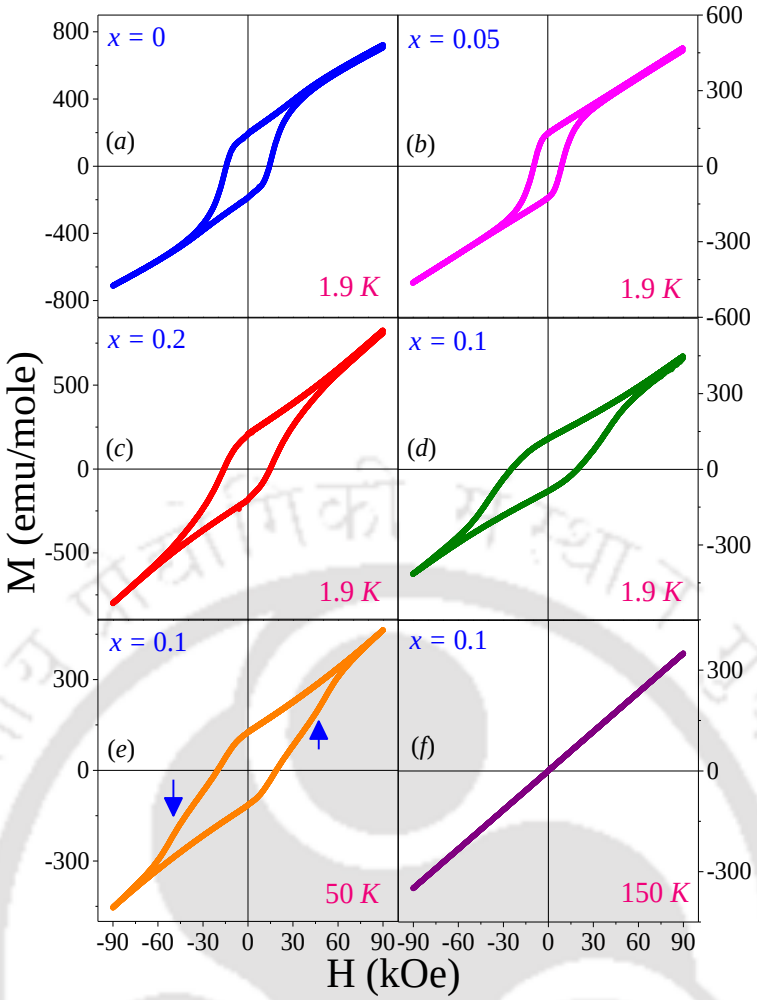

Fig. 4.12. The magnetic hysteresis (*M* vs *H*) measurements recorded under the FC condition (with H_{DC} = 90 kOe) for different compositions of $Y_{1-x}Ce_xCrO_3$ (a) x = 0, (b) x = 0.05, (c) x = 0.2, at 1.9 K and x = 0.1 at (d) 1.9 K (e) 50 K and (f) 150 K. Blue arrows in (e) indicates the field induced anomalies.

collapse as the temperature approaches to T_N. The important eye-catching feature is the emergence of field induced transition H_{FIT} = (10 (30) kOe at 1.9 K for x = 0 (0.1)) noticed in differential magnetization plots (dM/dH versus H) calculated from the virgin M–H isotherms for all the compositions (shown in the Fig. 4.14(a) and Fig. 4.14(b)). Figure 4.15 shows the temperature variation of the H_{FIT} obtained from the differential magnetization data shown in the vertical axis of the three-dimensional H–T phase diagram. One AFM ordering consistent with the previous results reported by Jacobs et al in the single crystals of $YCrO_3$ (H_{FIT-1} ~ 40 kOe, where the external field (H_{DC} applied along the *c*-axis in the *Pbnm* case) [162]. The temperature variation of the second field induced transition H_{FIT-2} reaches its maximum magnitude at 50 K and gradually falls-off as the temperature approaches to T_N, and finally disappears as shown in the left-hand-side-scale of Fig. 4.16. The high field (90 kOe) M_{ZFC}(T) plots recorded for both the compositions x = 0 and 0.1 further provides the evidence for the existence of H_{FIT} wherein a broad hump in the temperature range 20–120 K is quite clear (as shown in the inset of Fig. 4.6). As the trivalent spins of Cr ions reorient towards the *b*-axis from the anisotropy-*c*-axis one can notice significant change in the magnetic moment and is visible

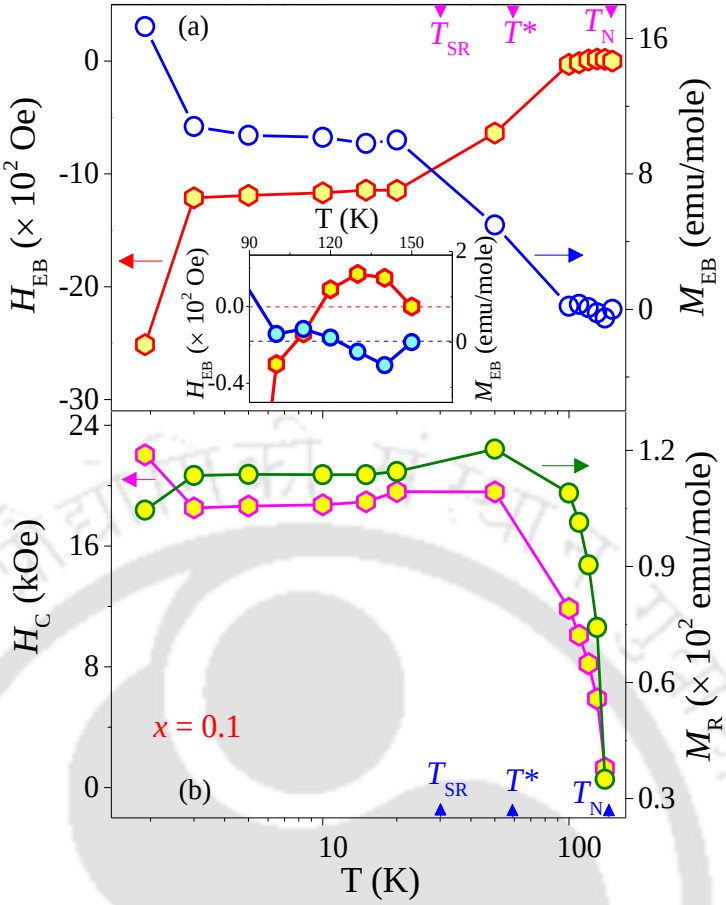

Fig. 4.13. (a) Semi-log plots of H_{EB} vs T (Left-scale) and M_{EB} vs T (Right-scale) (b) Semi-log plot of H_C vs T (Left-scale) and M_R vs T (Right-scale) for the x = 0.1 composition to represent the concordance of magnetic phase regimes in H_C, M_R, H_{EB} and M_{EB} w.r.t. temperature.

in the form of a broad shoulder across 50 K. It is well known from the previous studies that the antiferromagnetic easy axis lies along the *c*-axis in the pristine compound in the absence of the external magnetic field. However, application of a sufficiently large magnetic field at low temperatures causes the spins to rotate from *c*-axis towards the *b*-axis at a critical field H_{FIT} that can be understood using the free energy expression given below [162, 186].

$$F = \lambda M_1.M_2 - N.M_1 \times M_2 - \frac{K_2}{2M_0^2}(M_{1x}^2 + M_{2x}^2) + \frac{K_4}{2M_0^4}(M_{1x}^4 + M_{2x}^4) - H_{DC}(M_{1x} + M_{2x}) \quad (4.5)$$

In the above equation, M_1 and M_2 are the sublattice magnetization vectors (where $M_0 = |M_1| = |M_2|$ is the magnitude of the sublattice magnetization), α_1 and α_2 are the angles made by M_1 and M_2 with respect to the *c*-axis and the parameter ϕ denotes the canting angle (Fig. 4.17.). The relation between them is $\alpha_1 = \phi - \theta$ and $\alpha_2 = \phi + \theta$, in which θ is the rotation of the antiferromagnetic axis. The parameter λ represents the molecular field constant, N is the DM vector, K_2 and K_4 are the second and fourth order anisotropy in the c–*b* plane (while K_{eff} is the effective uniaxial magneto-crystalline anisotropy constant), and H_{DC} is the external

applied field along the *z*-direction. Here I define the super-exchange and antisymmetric exchange fields as $H_E = \lambda M_0$, $H_D = NM_0$. While the second and fourth-order anisotropy fields H_{K_2} and H_{K_4} corresponds to K_2/M_0 and K_4/M_0, respectively. Below a certain critical field ($H_z \leq H_{FIT}$) the magnetic susceptibility, exchange fields and canting angle (ϕ) are related as $\phi = (H_D + H_z \sin\theta)/(2H_E)$ and for $H_z \geq H_{Cr}$, $\phi = (H_D + H_z)/(2 H_E)$ with $\chi_x = (M_0 H_D^2)/[2H_E^2 (H_{K_2} - 2H_{K_4})]$. From these relations the critical/reorientation field can be obtained as $H_{FIT} = [-H_D + (H_D^2 + 8 H_E H_{K_2})^{1/2}]/2$.

Following the analysis by Cinader *et al.* and Jacobs et al the fourth-order anisotropy constant K_4 ($H_{K_4} = 0$) is negligible for the case of pristine compound $YCrO_3$ without any rare-earth ion substitution at Y sites [162, 186]. However, for Ce subsided systems I expect finite values of H_{K_2} and H_{K_4} because of significant interaction between the trivalent Ce and Cr. Usually, the positive quartic anisotropy term is not negligible if the interaction of Y^{3+}/Ce^{3+}–Cr^{3+} is moderately high as a consequence, the low temperature spin reorientation transition appears quite prominently (Fig. 4.12), in contrast to the case of Ce free $YCrO_3$ system which is having insignificant contribution of quartic anisotropy term to the free energy. The case of Ce free $YCrO_3$ sample H_{FIT} appears across 10 kOe significantly lower as compared to the single crystal $YCrO_3$ (40 kOe measured along easy axis (*x*-axis under *Pbnm*)). However, the Ce

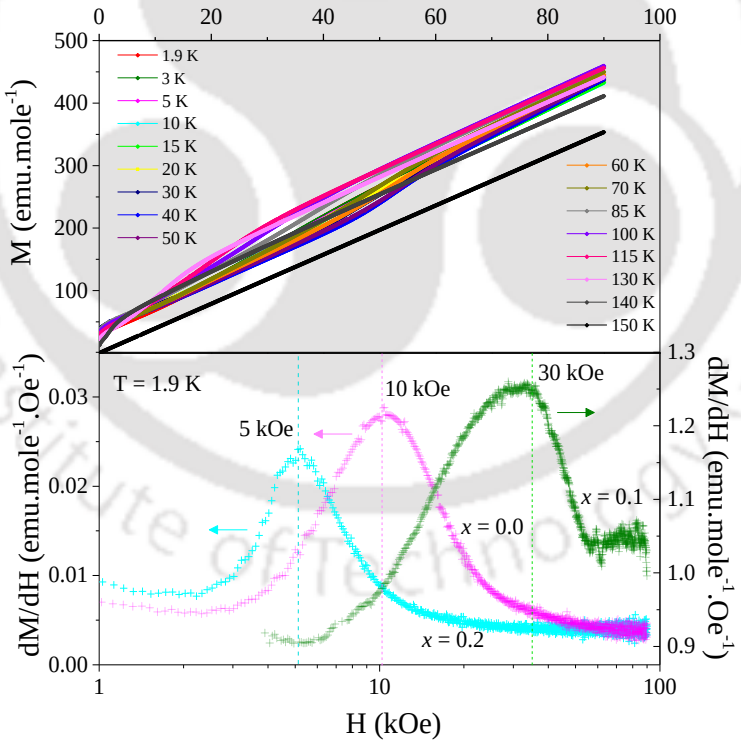

Fig. 4.14. (a) M-H isotherms measured at different temperatures between T = 1.9 K and 150 K under zero-field-cooled (ZFC) condition for the composition x = 0.1. (b) Differential magnetization (dM/dH) curves plotted as function of field for the compositions x = 0.0 and 0.2 (Left-hand scale), and x = 0.1 (Right-hand side scale).

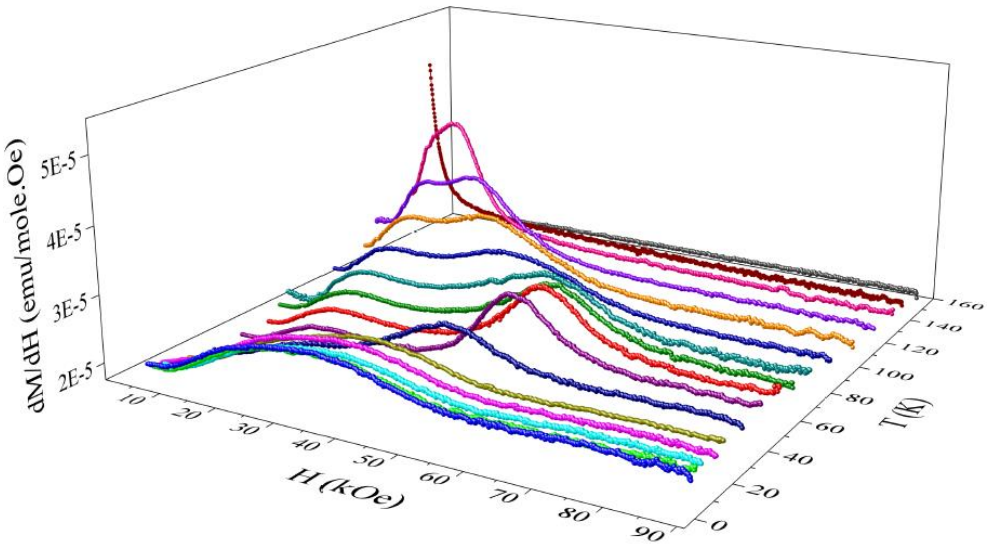

Fig. 4.15. Three-dimensional (T, H and dM/dH) representation of the differential magnetization plots dM/dH which obtained from the M–H isotherms recorded at different temperatures for x = 0.1.

incorporated $YCrO_3$ polycrystalline system exhibit quite higher H_{FIT} ~ 30 kOe. A systematic comparison of the double-ion anisotropy (H_{zy}) and anisotropy field with the critical field induced transitions provide a quantitative information about the weak ferromagnetic canting in terms of antisymmetric exchange field H_D ~ 61 kOe. On the other hand, in the present case I have evaluated the magnitudes of second and fourth-order anisotropy fields H_{K_2} ~ 154 Oe (593 Oe) and H_{K_4} ~ 52 Oe (~285 Oe) for x = 0 (0.1), respectively using the experimentally obtained values of H_{FIT}. Consequently, the strength of the anisotropy constants second order (K_2) and fourth order (K_4) in the AFM rotation plane (*bc*-plane) turns out to be ~7.5×10^4 erg/c.c. (2.8×10^5 erg/c.c.) and 2.5×10^4 erg/c.c. (1.35×10^5 erg/c.c.) for x = 0 (0.1), respectively. Larger values of H_{K_2} and H_{K_4} confirms the positive quartic anisotropy strength contribution to the spin reorientation which is quite evident in the present case at the lower temperatures due to the enhanced interactions of R^{3+}–Cr^{3+}. Moreover, the local double-ion anisotropy (H_{zy}) values lie in the range 207–800 Oe and the effective magneto-crystalline anisotropy constant K_{eff} ~ $1.0 \times 10^5 - 4.5 \times 10^5$ erg/c.c. which plays a key role on the global magnetic ordering of the system. As expected, the value of H_D increases progressively with increasing the substitution of trivalent magnetic rare-earth ion. Nevertheless, the effective anisotropy constant K_{eff} is estimated using the standard relation ($K_{eff} = H_C M_S/2$) and the order of magnitudes (~10^5 erg/c.c.) are consistent with the above discussion [187, 188].

Also, the temperature dependence of magnetic entropy change $-\Delta S_M$ (T) (shown in right-hand-side-scale of Fig. 4.16) calculated using Maxwell's expressions for a field change ΔH of 90 kOe using the isothermal magnetization plots (given in Fig. 4.14) shows zero-crossover signatures across the T_{SR}, T_N and the temperature at which polarity changes in H_{EB} befalls (left-hand-side scale of Fig. 4.13(a)). This

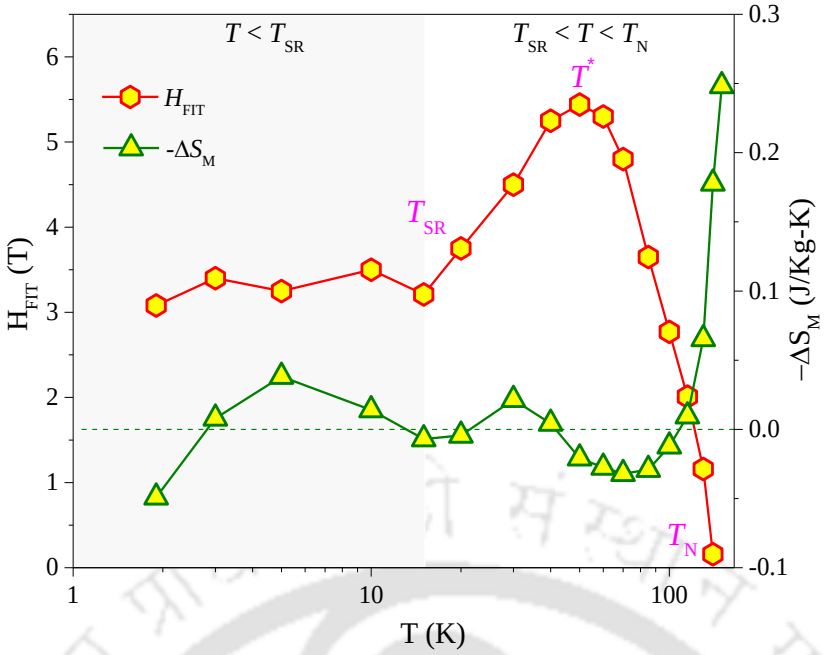

Fig. 4.16. Temperature dependence of H_{FIT} (Left-scale) and $-\Delta S_M$ (Right-scale) measured from the M vs H isotherms under FC condition for the x = 0.1 composition.

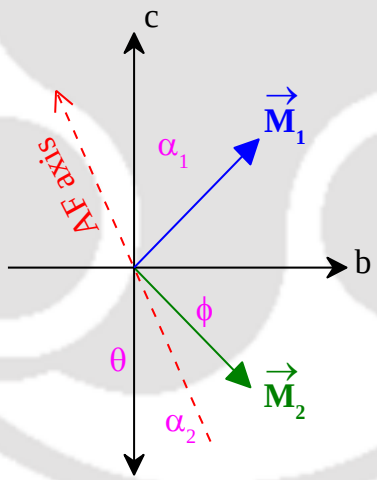

Fig. 4.17. Schematic representation of the sublattice magnetization vectors $\mathbf{M}_1$ and $\mathbf{M}_2$ in yz-plane making angles α_1 and α_2 with vertical axis. Here the AF axis is shown by dotted arrow making angle θ from z'-axis (ϕ from $\mathbf{M}_2$) [186].

scenario clearly suggests that the spin canting has significant impact on the magnetic entropy change and the parameters H_{FIT-2}(T) and $H_{C/EB}$(T). As an alternative method, I have estimated the nearest neighbour (NN) exchange interaction J_1 and next nearest neighbour (NNN) exchange interaction, J_2 (through the octahedral tilt from its 180° angle) based on molecular field theory, which enables electron hoping through the path Cr^{3+}–O^{2-}–O^{2-}–Cr^{3+}. By using the relations given below the strength of these interactions (J_1 and J_2) are calculated accordingly:

$$J_1 = \frac{k_B(\theta_{CW} - T_N)}{8S(S+1)}\ cm^{-1} \tag{4.6}$$

$$J_2 = \frac{k_B(\theta_{CW} + T_N)}{16S(S+1)}\ cm^{-1} \tag{4.7}$$

Quantitatively the J_1 (NN) is the mean value of the two exchange constants for the six neighbour Cr^{3+} ions along ($a \pm c$) and b axes. J_2 (NNN) is the mean value of the three exchange constants for the twelve Cr^{3+} ions. From the magnitude of θ_{CW} and T_N I have evaluated the magnitude of J_1 (∼−5.58 × 10^{-16} erg (−8.53 × 10^{-16} erg) for x = 0.0 (0.1)) and J_2 (∼−1.29 × 10^{-16} erg (−2.75 × 10^{-16} erg) for x = 0.0 (0.1)) for S = 3/2 of Cr^{3+} ions. These values are in line with the previous results on the polycrystals of pristine $YCrO_3$ (J_1 ∼ −4.28 × 10^{-16} erg and J_2 ∼ −1.09 × 10^{-16} erg) yet shows significant enhancement with the substitution of Ce in consonance with the increased magnitudes of T_N values. In addition, these values are consistent with the data available for the single crystals of $YCrO_3$ −2.76 × 10^{-16} erg and −3.6 × 10^{-17} erg [173, 182]. Such increment in the exchange constants justifies the fact that the magnetic trivalent Ce interacts with two trivalent Cr ions connected by two divalent O ions through the path Cr^{3+}–O^{2-}–Ce^{3+}–O^{2-}–Cr^{3+}.

4.4. Discussion

The trivalent Cr sublattice creates a local field by aligning anti-parallel to the applied H_{DC} ∼ 100 Oe. The onset of the alignment of Cr^{3+} sublattice moments begin from T_N ∼ 144 K (for x = 0.1) and increases the value of NM. This temperature dependent MR under the ZFC protocol referred as TMR effect. In the present study, the Y^{3+} non-magnetic sites replaced with Ce^{3+} magnetic ions which reduces the overall magneto-crystalline anisotropy of Cr^{3+} sublattice and resulted in the reduction of NM in Ce substituted systems in ZFC case. In case of pure $YCrO_3$, Y^{3+} ions are non-magnetic and the planes of Y^{3+} do not affect the magneto-crystalline anisotropy of Cr^{3+} ions. Here the Cr^{3+} sublattice aligns antiparallel with the externally applied H_{DC} as a consequence large NM as observed in Ce substituted $YCrO_3$. Similar trend was reported in the previous studies on $Sm_{1-x}Y_xCrO_3$ while Y^{3+} substitution at the Sm^{3+} sites enable the TMR affect in the isostructural system $SmCrO_3$ [189].

The trivalent Ce moments begin to align in opposite direction to the local field created by Cr^{3+} moments and competes with the Cr^{3+} sublattice magnetization. This scenario is much prominent at low temperatures. On the contrary, the magnetization measurements recorded under FCW protocol appear to be exactly in mirror symmetry with the x-axis bearing exactly the opposite behaviour with the ZFCW cycle. On the other hand, the drop in M_{FCW} below T* ∼ 43 K (for x = 0.1) clearly signifies the fact that the Ce^{3+} sublattice contribution is opposite in direction to the overall magnetic moment revealing the competition between the moments of Ce^{3+} and Cr^{3+} sublattices. In case of Ce free $YCrO_3$, below T* (∼ 60 K) the magnetic moments are locked to show mixed AFM + WFM phase behaviour Γ_4 (G_z, F_y, A_x) (following the Bertaut's notations as indicated in Fig. 4.18) [152, 190].

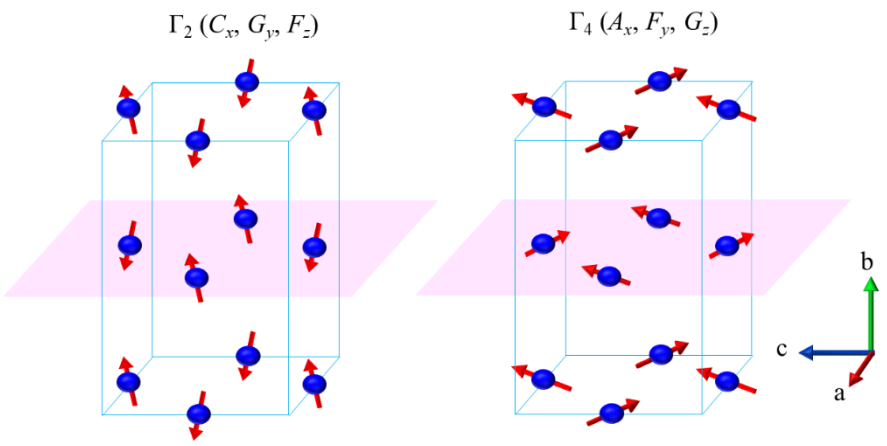

Fig. 4.18. Schematic representation of the spin structures following the Bertaut's notation for the magnetic phases Γ_2 and Γ_4. Here trivalent Cr sublattice spins reoriented (T_{SR}) from the lower temperature Γ_2 phase into the high temperature Γ_4 phase.

Such Γ_4 (G_z, F_y, A_x) phase usually shows the G-type AFM ordering along the *z*-axis yet FM ordering along the *y*-axis and A-type antiferromagnetic along the *x*-axis. Among the three, the easy axis must lie along the *z*-axis and rotation of the spins take place in the *bc*-plane in Ce–$YCrO_3$ system. While the Γ_2 (F_z, G_y, C_x) phase has the FM alignment along the *z*-axis, G-type AFM alignment along the *y*-axis and the C-type AFM alignment along the x-axis as shown in Fig. 4.18. Here the spins of trivalent Ce ions occupy the A-site in between the two Cr^{3+} octahedral planes ordered in the [010] direction which finally weakens the magneto-crystalline anisotropy of Cr^{3+} sublattice, thus, such rigid Γ_4(G_z, F_y, A_x) structure is disturbed by trivalent Ce ions and enables the spin reorientation such that the system finally attains a new Γ_2(F_z, G_y, C_x) phase towards the low temperatures. Although such temperature induced spin reorientation transition is not prominent in the present case as compared to the other well-known systems such as $SmCrO_3$ [189].

Gradual spin reorientation in the current study can be due to a mixed phase Γ_{24} that exists between Γ_4 (G_z, F_y, A_x) and Γ_2 (F_z, G_y, C_x) (shown in Fig. 4.19). On the basis of the M–H isotherms I examine the existence of such mixed phase behaviour and its role on the spin reorientation. As the system is cooled to 1.9 K in the presence of field, the appearance of broad hump corresponding to the H_{FIT-1} ~ 30 kOe implies that the spins are aligned into the Γ_2 (F_z, G_y, C_x, F_z^R, C_x^R) configuration which eventually shifts towards higher fields. From 20 K to 70 K, the derivatives of M–H isotherms clearly split into two cusps (H_{FIT-1} and H_{FIT-2}) which are associated with the Γ_4 (G_z, F_y, A_x; F_y^R) phase and the spin reorientation into the Γ_2 (F_z, G_y, C_x; F_z^R, C_x^R) phase, respectively. The two transitions H_{FIT-1} and H_{FIT-2} are separated by the mixed phase Γ_{24} where the Γ_2 boundary occurs at the higher field at ~50 K. As seen from the H–T phase diagram beyond 70 K, the Ce^{3+} interactions become inactive and the role of Cr^{3+} sublattice dominates the reorientation process as a result, the Γ_4(G_z, F_y, A_x) orientation is evident in the form of a single broad hump driven by Cr^{3+} sublattice which is conventional in pristine $YCrO_3$ system.

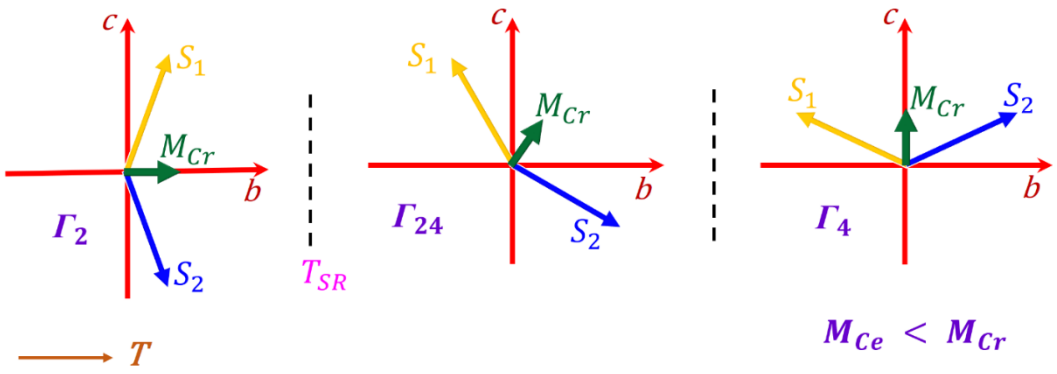

Fig. 4.19. Schematic illustration of the simplified vector diagram of spin-reorientation configuration with increasing temperature (see arrow) in $Y_{1-x}Ce_xCrO_3$ up to T_N. S_1 and S_2 are the two pairs of spins for trivalent Cr in the G-type AFM structure. M_{Cr} is corresponding to the net FM moment of trivalent Cr in $Y_{1-x}Ce_xCrO_3$ and M_{Ce} is the moment corresponding to trivalent Ce [186].

From the H–T phase diagram (Fig 4.1), I can observe that above the T_N transition to until T_{IP} the short range canted AFM ordering of Cr^{3+} spins with the PM is prevailed, and above the T_{IP} transition the system is completely PM. Below T_N, the system attains Γ_4 (G_z, F_y, A_x) phase due to the Cr^{3+} sublattice, but, while approaching 70 K, the Ce^{3+} sublattice spins start contributing and the ordering is in opposite to the local field created by the trivalent Cr sublattice. The Ce^{3+} spins start aligning with $\Gamma_4(F_y^R)$ spin structure and couples with the $\Gamma_4(G_z, F_y, A_x)$ of Cr^{3+} sublattice. The anti-parallel coupling of R^{3+} and Cr^{3+} sublattices initiates on approaching 70 K and spins start rotating in the bc-plane to give rise to a mixed phase Γ_{24} (F_{zy}, G_{yz}; F_{zy}^R). Furthermore, below 20 K, the Γ_2 region consists of AFM and FM spins of Ce^{3+}–Ce^{3+} and Ce^{3+}–Cr^{3+} couplings as shown in the phase diagram (Fig. 4.1). In contrast with the pure $YCrO_3$, the phase diagram provided by Mall et al for Ce–$YCrO_3$ shows a very significant H_{EB} and field induced spin reorientations below T_N [148, 163, 182]. Therefore, an intermediate mixed magnetic spin structure Γ_{24} (F_{zy}, G_{yz}; F_{zy}^R) emerges from Γ_2 and makes the spin reorientation process more gradual. The system arrives to a typical Γ_4 state with increasing the temperature from Γ_{24} phase of Cr^{3+} sublattice which is considered as the long-range CAFM phase. At higher fields the T* shifts to the higher temperatures (41 K → 48 K) and T_{SR} pushes to the lower temperatures (22 K → 16 K). Nevertheless, our results provide convincing evidence that the intermediate phase Γ_{24} (F_{zy}, G_{yz}; F_{zy}^R) is prone to Ce substitution and external magnetic fields.

Moreover, it is evident that the investigated system shows first-order phase transition below the T_N as noticed from the large hysteresis lag ($\Delta T \sim 10$ K) between M_{FCC}(T) and M_{FCW}(T) measurements as a consequence of the Γ_4 (G_z, F_y, A_x) → Γ_2 (F_z, G_y, C_x) transition. Also, the onset of transition in M_{FCC} is lower than M_{FCW} as compared to the pristine compound $YCrO_3$ which is quite opposite to the case of Ce substituted system. The intermediate phase Γ_{24} in FCW contributes to higher magnetization value at T* than in FCC case in which the magnetization falls more rapidly in the former case than the FCC case.

Usually, the Γ_4 phase is more robust in case of $YCrO_3$, with the mixed AFM and WFM configurations of Cr^{3+} spins and strong spin–orbit coupling clamps the H_{K_2} along *b*-axis direction which required little higher temperatures to break this coupling hence attains the paramagnetic state. Such situation is quite opposite to the case of Ce substituted system where single-ion anisotropy is disturbed by the intermediate plane of Ce in which H_{K_4} gradually come into account by weakening the H_{K_2}, thereby pushing the onset of disordering temperature well ahead in case of FCC than FCW protocol. This interpretation is also consistent with the negative slopes of Arrot plots (M^2 vs H/M) obtained from the M–H isotherms measured below the ordering temperature [191–193].

4.5. Summary

In this article, I have presented a systematic study on the magnetic properties of Ce substituted $YCrO_3$ polycrystals. The analysis of the magnetic field and thermal variation of the heat-capacity and dc susceptibility data below the antiferromagnetic (AFM) Néel temperature T_N (140–148 K) results the following key features; giant NM, field-induced, first-order, spin-reorientation transitions (16–22 K) accompanied by the thermal hysteresis in M_{FCC}(T) and M_{FCW}(T), intermediate paramagnetic transition (T_{IP}) and negative exchange-bias effect. These phenomena are primarily driven by the dilute dispersion of the Ce in the distorted Perovskite lattice of $YCrO_3$ leading to an antisymmetric and symmetric exchange interactions ($J_{AS} \sim 0.11$ meV and $J_S \sim 0.85$ meV) between Ce^{3+}–Cr^{3+} ions. As a result of these exchange interactions, positive quartic anisotropy term H_{K_4} ~2.85×10^2 Oe) with giant fourth-order anisotropy constant ($K_4 = 1.35 \times 10^5$ erg/c.c.) ascends together with the second order anisotropy term $H_{K_2} \sim 5.93 \times 10^2$ Oe). Moreover, the easy axis spins continue to rotate in the *bc*-plane and give rise to a new magnetic phase Γ_2 (F_z, G_y, C_x; F_z^R, C_x^R) at the low temperatures with a mixed phase Γ_{24} (C–AFM + WFM) between 30 K and 70 K evident as a broad hump in maximum magnetization at T* ~ 45 K. A detailed analysis of the differential M–H isotherms provides an unambiguous determination of the field-induced transitions across 50 kOe (for $x = 0.1$ at 50 K) whose temperature dependence clearly shows anomalies across the ordering temperature and spin-reorientation transitions. Based on all these results I established a detailed H–T phase diagram of this interesting system. Our results also demonstrate that tuneable MR and spin-flip transition in these compounds, which may find profound applications in the field of thermo-magnetic switches/sensors and other memory storage applications.

Chapter 5

Irreversible Metamagnetic Transitions in Distorted Tetragonal $(Pr_{0.45-x}Yb_x)Sr_{0.55}MnO_3$

This chapter emphasizes the irreversible metamagnetic transitions in distorted tetragonal $(Pr_{0.45-x}Yb_x)Sr_{0.55}MnO_3$. I present an extensive experimental analysis to investigate the effect of Yb^{3+}-ion substitution at the Pr^{3+}-sites on the magnetic properties that exhibit irreversible field-induced metamagnetic transitions from AFM to FM at higher temperatures than in the case of $Pr_{0.5}Sr_{0.5}MnO_3$. I provide the details of the sample preparation and characterization methods. Polycrystalline samples of $Pr_{0.45-x}Yb_xSr_{0.55}MnO_3$ (x = 0.02, 0.05, 0.08, and 0.10) were synthesized by conventional solid-state reaction method. Crystal structure analysis was performed using the powder XRD patterns of all the samples x = 0.02 (Yb2), x = 0.05 (Yb5), x = 0.08 (Yb8), and x = 0.10 (Yb10) at the room temperature. The admixture of metastable states of AFM and FM is quite robust in the investigated system whereas AFM state is mediated by Yb^{3+} ions, while the FM state arises by field driven thermo-magnetic kinetics. These results open a constructive approach of designing novel spin-valve devices.

5.1. Introduction

Robust spin dynamics of perovskite materials exhibiting magnetic history dependent properties have triggered lot of interest in the scientific community as they play pivotal role in the modern-day electronic devices [1, 3, 194]. Perovskites, $R_{1-x}X_xMnO_3$ (R = La, Pr, Nd, Gd, *etc.* and X = Ca, Sr) possess magnetically rich field and temperature (*H-T)* phase diagrams spanning over a wide range of H and T for different levels of substitution with their transitions towards the room temperature, RT ~ 300 K [14, 17, 120, 195]. $Pr_{1-x}Ca_xMnO_3$ and $Pr_{1-x}Sr_xMnO_3$ are widely recognized manganites known for their remarkable characteristics, with $Pr_{1-x}Ca_xMnO_3$ exhibiting a distinctive CE-type antiferromagnetic (AFM) behavior accompanied by charge-ordering (CO) and $Pr_{1-x}Sr_xMnO_3$ demonstrating an A-type AFM nature accompanied by orbital-ordering (OO) across a wide range of compositions [10, 120, 196]. The CO and OO are seemingly governed by mechanisms such as super exchange (SE) and double exchange (DE), which are influenced by the bond angles and bond lengths between the Mn^{3+}-$3d^4$ ($t_{2g}^3e_g^1$), Mn^{4+}-$3d^3$($t_{2g}^3e_g^0$), and O^{2-} states [14]. In many of the A-site substituted manganite perovskites, $AMnO_3$ {A = (Pr, Ca), (Pr, Sr), (La, Ca), etc.} specific compositions (x = 0.45 - 0.6) with a balanced ratio of Mn^{3+}/Mn^{4+} cations facilitate the efficient manifestation of CO and OO, leading to the emergence of intriguing long-range magnetic orderings alongside charge localization and charge liquid states, contributing to the exotic nature of these systems. The high-temperature FM state, characterized by high energy, and the low-temperature equilibrium AFM state, characterized by low energy, can be controlled by manipulating the ratios of Mn^{3+} and Mn^{4+} cations. [73, 197]. Furthermore, Furthermore, among the rare-earth manganite perovskites discussed above, an extraordinary glassy behavior is uniquely probed and observed in $La_{1-x}Ca_xMnO_3$ which exhibits the kinetic arrest of FM moments within an AFM background, giving rise to a metastable low-temperature FM state [73, 197, 198]. More specifically,

$Pr_{1-x}Sr_xMnO_3$ exhibits almost similar magnetic ground states as $La_{1-x}Ca_xMnO_3$ which exhibits a two folded magnetic behavior with FM and AFM. Similar magnetic phases and glassy behavior has been reported in other compounds such as $Y_{0.95}Ca_{0.05}BaCo_2O_{5.5}$, and $Fe_{0.955}Ni_{0.045}Rh$ [73, 197, 198].

Typically, decrement in the ionic radius of cations (*e.g.* $Sr^{2+} > Ca^{2+} > La^{3+} > Pr^{3+} > Sm^{3+} > Gd^{3+} > Yb^{3+}$) decreases the tolerance factor which further causes the lattice distortion with the substitution of smaller cations at Pr^{3+} - site. Different rare-earth cations such as Nd^{3+}, Sm^{3+}, and Gd^{3+} are substituted at the Pr^{3+}-site, where in $Pr_{0.5}Nd_{0.2}Sr_{0.5}MnO_3$, the magnetization does not exhibit a notable decline at low temperatures, indicating the absence of a significant CO/OO AFM transition [199-203]. In $Pr_{0.4}Gd_{0.1}Sr_{0.5}MnO_3$, a deep AFM ground state is absent but in $Pr_{0.25}Sm_{0.25}Sr_{0.5}MnO_3$, the magnetic phases are explicit with a deep AFM ground state yet in both of them, FM ordering reasonably distant from RT i.e. around 250 K [202, 203]. Single crystal $Pr_{0.5}Sr_{0.5}MnO_3$ exhibits a field-dependent magnetization switching from AFM to FM till ~ 150 K with T_C ~ 270 K which is still below RT [200]. $Pr_{0.46}Sr_{0.54}MnO_3$ shows metamagnetic transitions at higher temperatures, yet no explicit ferromagnetic transition observed in temperature-dependent magnetization response [201]. Previous studies on *A*-site substitutions in $Pr_{0.5}Sr_{0.5}MnO_3$ suggests that the changes in inter- and intra-MnO_6 octahedra' bond length and bond angle were found to be insufficient to maintain the equilibrium AFM phase at low temperatures and does not support two-folded long-range magnetic orderings and effective field-induced transitions at high temperatures [199–202]. So, a cation with more lesser ionic radius than Nd^{3+}, Sm^{3+}, and Gd^{3+} actually ventures a possibility of increasing the distortion and reduces the Mn-$O_{(2)}$-Mn bond angles which directly affects the long-range FM ordering temperatures.

In this chapter, I present an extensive experimental analysis on the structural and magnetic properties of Yb^{3+} substituted at *A*-site of $Pr_{0.45}Sr_{0.55}MnO_3$ which exhibit irreversible field-induced metamagnetic transitions from AFM to FM at higher temperatures and robust OO features near to the *RT* as compared to the pristine system $Pr_{0.5}Sr_{0.5}MnO_3$. Our detailed analysis reveals that the Jahn-Teller active Mn^{3+} ion with the 3*d* electronic and orbital configuration $t_{2g}^3e_g^1$ gives rise to unusual magneto-crystalline anisotropy along with the $t_{2g}^3e_g^0$, Mn^{4+}-ions by distorting the MnO_6 octahedra which appears to be responsible for altering the Mn-$O_{(2)}$-Mn bond angles and consequently their order parameters. I find that the substitution of more Yb^{3+} content leads to the formation of metastable AFM phases while the low Yb^{3+} with cooling and heating under unequal magnetic fields (CHUF) protocol confirms to the formation of metastable FM phase.

5.2. Experimental procedure

Polycrystalline samples of $Pr_{0.45-x}Yb_xSr_{0.55}MnO_3$ (x = 0.02, 0.05, 0.08, and 0.10) were synthesized by conventional solid-state reaction method. Stoichiometric amounts of Pr_6O_{11}, $SrCO_3$, YbO_2, MnO_2 were mixed and ground thoroughly. The powders were pressed into pellets and sintered at 1623 K for 24h. The crystal structure characterization was performed using the Rigaku X-ray diffractometer (Model: Smart Lab, 9 kW) with Cu-Kα (1.543 Å) radiation as X-ray source at 0.015 intervals in the range $2\theta = 10^o - 90^o$ and further analyzed using the Rietveld analysis program to ascertain the formation of single phase. The

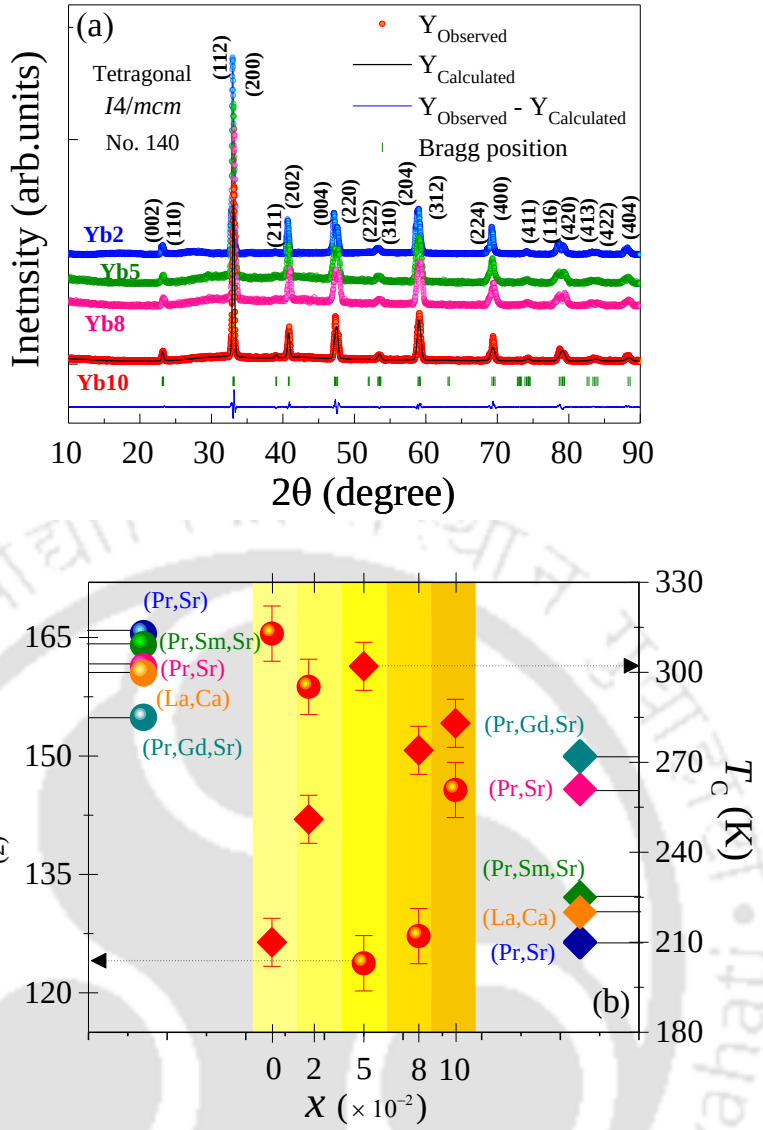

Fig. 5.1. (a) *X*-ray diffraction patterns of $Pr_{0.45-x}Yb_xSr_{0.55}MnO_3$ system for x = 0.02, 0.05, 0.08 and 0.10 at the room temperature. Rietveld refinement analysis of x = 0.10 shown in *black* line along Bragg positions and (*hkl*) indices. (b) X-ray photoelectron spectroscopy of $Pr_{0.40}Yb_{0.05}Sr_{0.55}MnO_3$ showing the electronic spectra of Mn-2*p*. (c) Mn-$O_{(2)}$ -Mn bond angle and curie temperature, T_C with respect to different Yb^{3+} substitution levels both show an anomaly at 5% substitution. $Pr_{0.45}Gd_{0.05}Sr_{0.5}MnO_3$ (*Dark Cyan*), $La_{1-x}Ca_xMnO_3$(*Orange*), $Pr_{0.5}Sr_{0.5}MnO_3$ (*pink*), $Pr_{0.25}Sm_{0.25}Sr_{0.5}MnO_3$, (*Olive*), $Pr_{0.46}Sr_{0.54}MnO_3$ (*Royal Blue*) – scaled only according to the *y*-scale Ref- [11, 200–203].

electronic structure of the powder samples was investigated through X-ray photoelectron spectroscopic (XPS) studies using the PHI 5000*Versa*Probe III Scanning XPS microprobe configured with X-ray source Al Kα (544 eV) with spatial resolution less than 1 μm. All the magnetization measurements were performed using a physical property measurement system (PPMS) from Quantum design (Model: Dyna cool) with vibrating sample magnetometer accessory which is capable of reaching 2 K from 380 K with dc-magnetic field (H_{DC}) capacity ±14 *T*.

5.3. Results and analysis

5.3.1. Crystal and electronic structure

Crystal structure analysis reveals that all the perovskites x = 0.02 (Yb2), x = 0.05 (Yb5), x = 0.08 (Yb8), and x = 0.10 (Yb10) stabilizes in the pseudo-tetragonal symmetry of space group $I4/mcm$ and No.

140 as shown in the Fig. 5.1(a). No secondary phase peaks are noticed in the XRD pattern signifying the phase purity of the synthesized compounds and the lattice parameters obtained after the Rietveld Refinement being a = 5.4069(1) Å, b = 5.3990(1) Å, c = 7.6909(1) Å for $Pr_{0.35}Yb_{0.10}Sr_{0.55}MnO_3$ with unit-cell volume V = 224.51(3) Å^3. The substitution of trivalent Yb ($r_{Yb^{3+}} = 1.042$ Å) at the A-sites of Pr^{3+}($r_{Pr^{3+}} = 1.179$ Å) causes the decrease in lattice parameter c which in turn reduces the volume of the unit cell further. As shown in the Fig. 5.2(*v*) the XPS spectra of Mn-2*p* is analysed by fitting the peaks through XPSPeak41 software for the analysis of peak position and its' parameters. I have used the "Tougaard" under the background type and fit the peaks within the binding energy range 634.48 eV to 674.48 eV which is usually the range of Mn^{3+} and Mn^{4+} *i.e.*, Mn-2p core level oxidation states. The peak number, peak position, area, full-width at half-maximum (FWHM) and percentage of Gaussian and Lorentzian of all the peaks in the Mn-2p spectra are given in the Table 5.1 given above. The peaks are best fitted with the mixture of Lorentzian and Gaussian components with a χ^2 ~ 1.4516. The peaks P_1 and P_3 identified to be Mn^{3+} oxidation states at the lower energies than the peaks P_2 and P_4 of Mn^{4+} state in their corresponding $2p_{\frac{3}{2}}$ *and* $2p_{\frac{1}{2}}$ orbitals, respectively. The areas under these peaks were calculated after creating a baseline as shown in the Fig. 5.2(*v*) and the areas under the peaks P_1, and P_3 are added to be the contribution from the Mn^{3+} oxidation state. Similarly, area under the peaks P_2, and P_4 are added to be the contribution from the Mn^{4+} oxidation state. Now, the ratio of these two contribution Mn^{3+}: Mn^{4+} coming out to be 39 %: 61 %. And the energy levels $2p_{\frac{3}{2}}$ *and* $2p_{\frac{1}{2}}$ and their corresponding highest intensity point shown from the *red* colour solid line are separated at a binding energy difference of ~ 11.57 eV which is identified to be the effect of the spin-orbit splitting, Δ_{S-O}. The Pr-3*d* spectra is deconvoluted in four peaks at 932.6 eV, 944.1 eV, 947.8 eV, and 953 eV and fitted with 80% Gaussian fittings corresponding to $3d_{3/2}$ and $3d_{5/2}$ core level with a satellite peak at 928.1 eV. The unfilled 4*f* sub-shell with 13 electrons of Yb^{3+} gives rise to three peaks at 184.9 eV, 190.4 eV and 198.8 eV where the sharpness increases for lower BE peaks. The Sr-3*d* core level fitted with Tougaard background correction is fitted with peaks at 131.8 eV, 133.2 eV and 135.1 eV corresponding to doublets $3d_{5/2}$ and $3d_{3/2}$. The O-1*s* core level consists of the peaks at 528.5 eV coming from the lattice oxygen. The one at 531.1 eV is related to oxygen vacancy created in the process of heat treatment and 531.1 eV. Another peak at 529.6 eV is related to the satellite peak commonly occur due to surface oxygen.

Trivalent manganese cation, Mn^{3+}, a Jahn-Teller active ion distorts the MnO_6 octahedra either by increasing or decreasing the Mn-$O_{(2)}$ bond lengths in the *ab*-plane as shown in the Fig. 5.3(a), (b), and (c). Consequently, a decreasing trend of the Mn-$O_{(2)}$-Mn bond angle was noticed till 5% Yb^{3+} substitution (*left*

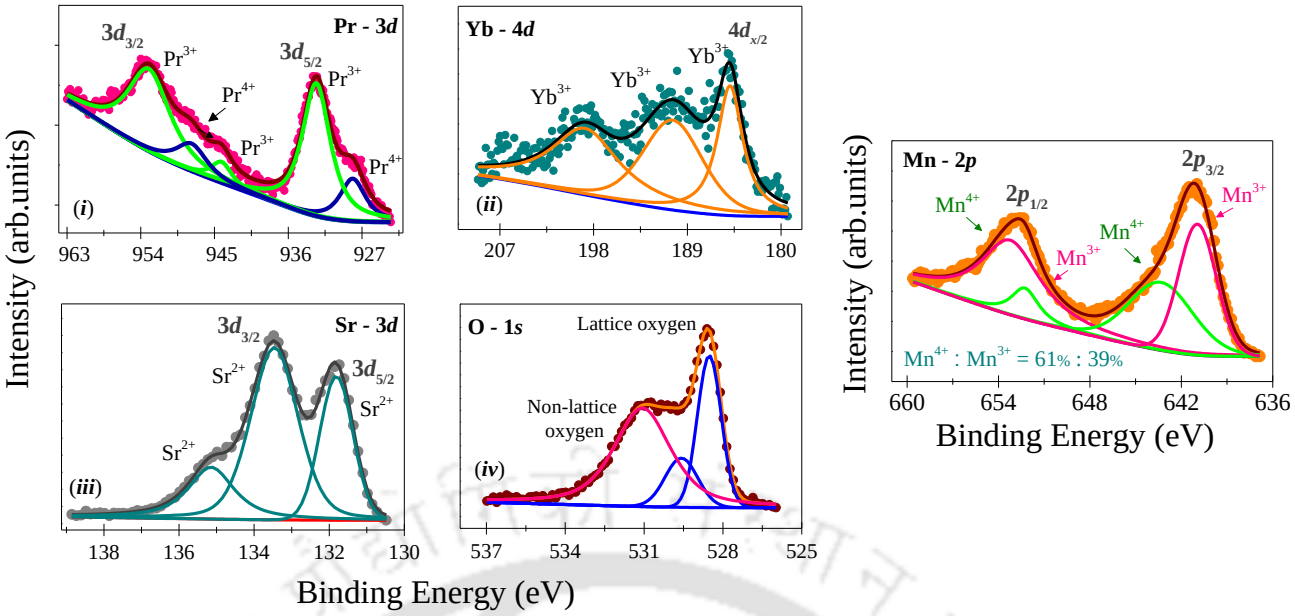

Fig. 5.2. X-ray photoelectron spectroscopy of $Pr_{0.40}Yb_{0.05}Sr_{0.55}MnO_3$ showing the electronic spectra of (*i*) Pr-3*d* (*ii*) Yb-4*d* (*iii*) Sr-3*d* (*iv*) O-1*s* and (*v*) Mn-2*p*.

Table 5.1. peak number, peak position, area, full-width at half-maximum (FWHM) and percentage of Gaussian and Lorentzian of all the peaks in the Mn-2*p* spectra.

Peak Number	**Peak Position** (eV)	**Area**	**FWHM**
1	653.223	17428.870	4.676
2	652.267	3253.404	2.127
3	643.324	12596.640	4.973
4	640.944	13490.280	2.908

hand scale of Fig. 5.1(b)) and shows an increasing trend upon further substitution of Yb^{3+}. While exactly contrasting behavior has been observed with the Curie temperature, T_C (*right hand scale* Fig. 5.1(b)). The Mn-$O_{(2)}$ bond lengths increase from lower compositions to till $x = 0.05$ and decrease on further substitution nevertheless, our structural analysis clearly indicates that the threshold percolation of the current system is around 5%.

At this point it is quite understandable that the structural properties are greatly affected by the A^{3+} and A^{2+} states which also causes change in the electronic structure of the magnetic ions Mn^{3+} and Mn^{4+} which essentially influence the nature of magnetic ordering. In what follows, I show the explicit dependence of the magnetic behavior on the structural distortion that is caused due to the Yb substitution. I will show that the distortion in the structure makes the system in the state of coexistence of both AFM and FM phases. This arrangement may lead to the appearance of a specific phase upon changing either the temperature or the magnetic field.

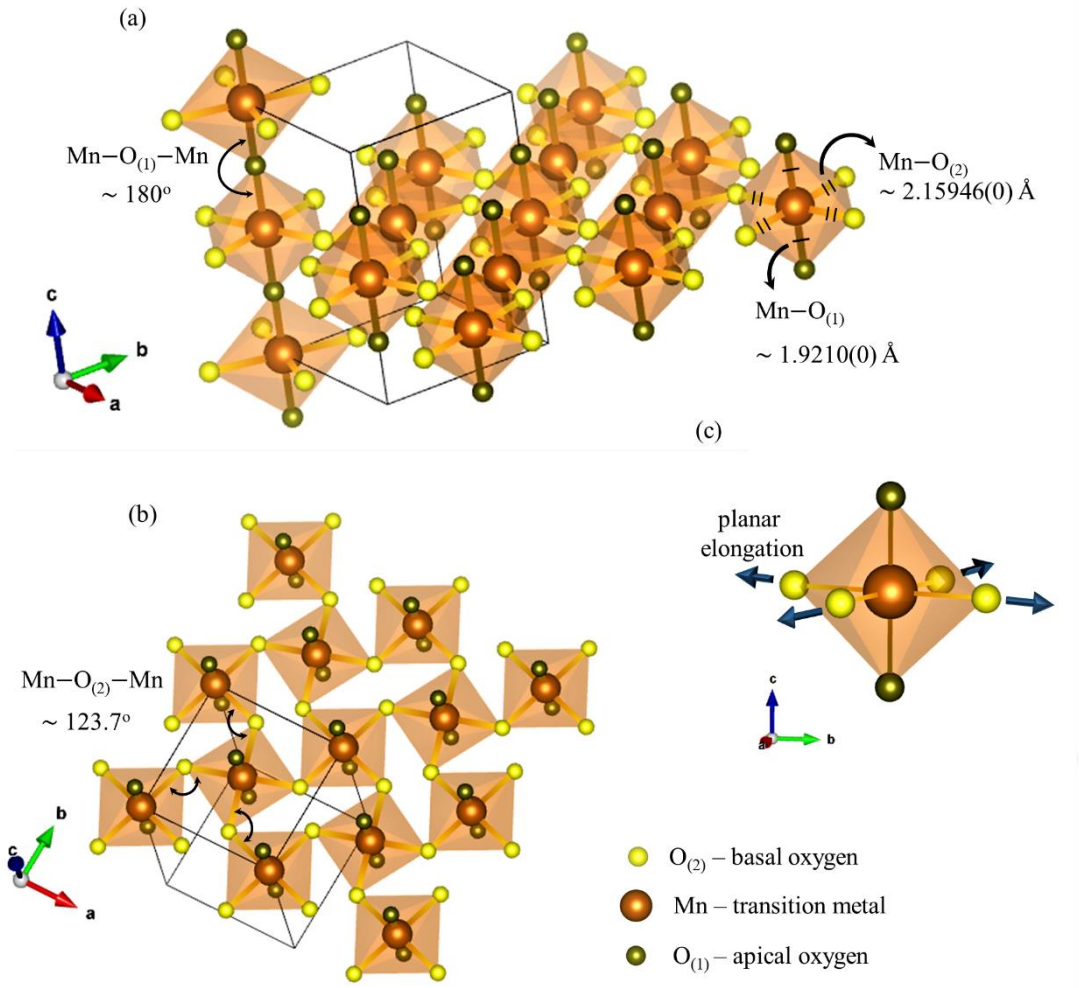

Fig. 5.3. Schematic diagram showing (a) the Mn-$O_{(1)}$-Mn bond angle along eh *c*-axis. (b) Mn-$O_{(2)}$-Mn bond angle in the *ab*-plane, and (c) elongation in the Mn-$O_{(2)}$ bond lengths such that the MnO_6 distortion can be evident.

5.3.2. Temperature dependent Magnetic characteristics

I have investigated the temperature dependence of magnetization under different measurement protocols like zero-field cooled warming (ZFCW), Field-cooled cooling (FCC) and Field-cooled warming (FCW). Magnetization response upon sweeping the temperature from 300 K to 3 K under an external magnetic field of 100 Oe of Yb2, Yb5, Yb8 and Yb10 shows clear magnetic phase transitions (as shown in Fig. 5.4). I have extracted the T_N and T_C values from the $\frac{d(\chi T)}{dT}$ versus T graph where, T_N and T_C are identified with the observation of peak in the positive and negative scale of $\frac{d(\chi T)}{dT}$ axis, respectively. Based on these peak values, I have referred the magnetic ordering regions of T_N, T_C and other ordering temperatures with the arrows. In Fig. 5.4(b), I find that Yb5 exhibits the magnetization change from the PM to FM ordering at

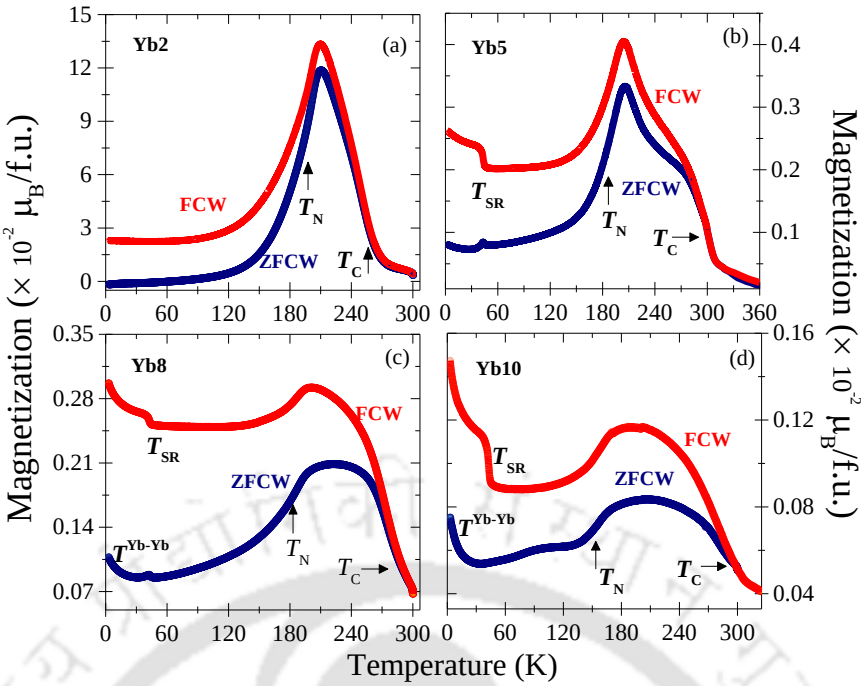

Fig. 5.4. Temperature dependent magnetization of the polycrystalline bulk $Pr_{0.45-x}Yb_xSr_{0.55}MnO_3$ (x = 0.02(a), 0.05(b), 0.08(c), and 0.10(d)) in both ZFCW and FCW protocols under the applied magnetic field H_{DC} = 100 Oe.

T_C = 302 K. Furthermore, a transformation into A-type AFM ordering at the Neel temperature, T_N = 196 K was observed where the parent system $Pr_{0.5}Sr_{0.5}MnO_3$ orders at T_C ~ 260 K with T_N ~ 150 K [204]. In Fig 5.4(d), Yb10 exhibits the AFM ordering at T_N (~ 158 K) bifurcating the AFM region at low temperatures from the FM phase. Here, the Yb^{3+} cations diffuse into Pr^{3+}- cationic sites, where $r_{Yb^{3+}} < r_{Pr^{3+}}$, increases the tilt in the Mn–$O_{(2)}$–Mn bond angle which coincidentally shifts T_C nearly 50 K towards the room temperature. Unlike the Yb2 composition which remained in the equilibrium magnetic ground state holding A-type AFM ordering below the T_N ~ 202 K, the Yb5 enables the influence of Yb^{3+} moments at the low temperatures below its T_N at 194 K. The T_{SR}^{Yb} will be the spin reorientations temperature which is due to the reorientation of the Mn-sublattice that is triggered basically due to the Yb^{3+} environment and the distortions it brought in the perovskite unit cell [205–207]. The signature of local $YbMnO_3$ AFM ordering temperature, T_N^{Yb} ~ 83 K is observed in the Fig. 5.4(d). The low temperature rare-earth short-range AFM transition, T^{Yb-Yb} is observed in the Fig. 5.4(b), (c), and (d) as well which is evident only in the compositions, $x \geq 0.05$ due to the increase in Yb^{3+} concentration of the system [205–207]. The magnetization gradually starts increasing at the low temperatures below 25 K in all the Yb^{3+} concentrated systems *i.e.*, for $x \geq 0.05$ and which actually shoots up to higher magnetization value in the x = 0.10 composition due to the richly available Yb^{3+} ions that is quite perceptible in rare earth complex oxide behaviour. The bifurcation between the ZFCW and FCW curves enhanced in the case of $x \geq 0.05$, as the Yb^{3+}-Yb^{3+} AFM interactions hold more unidirectional anisotropic energy resisting to devitrify into the lowest AFM equilibrium energy state during

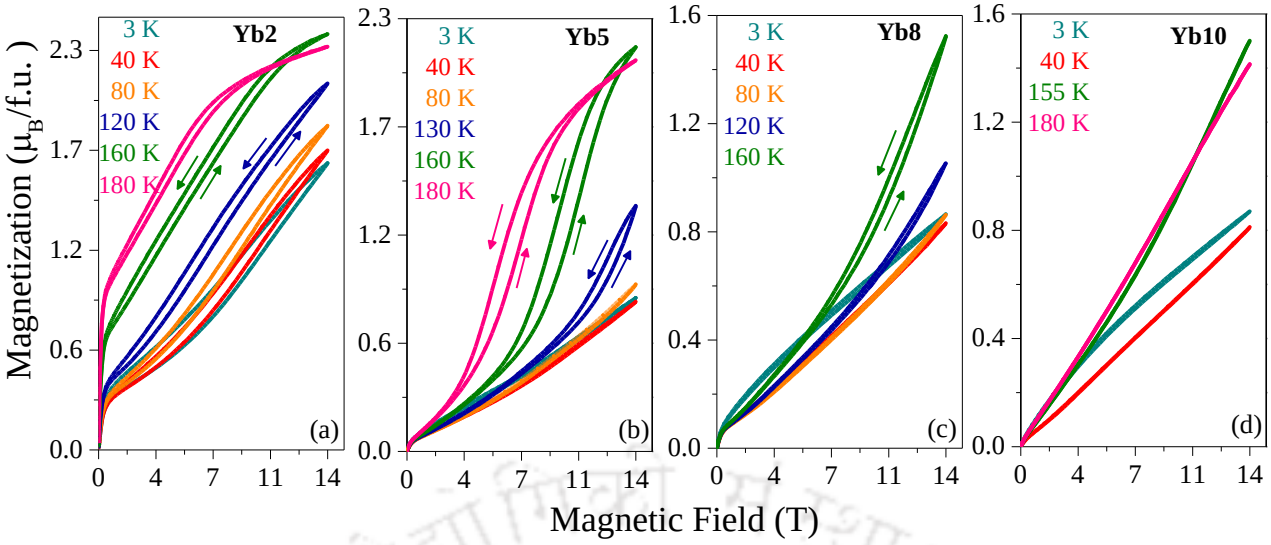

Fig. 5.5. Field dependent magnetization of the polycrystalline bulk $Pr_{0.45-x}Yb_xSr_{0.55}MnO_3$ where, (a) x = 0.02, (b) x = 0.05, (c) x = 0.08, and (d) x = 0.10) under ZFCW protocol at different temperatures. Up and down arrows indicate the direction of field sweep.

the FC conditions. The system retains the high magnetization values under the FC condition with dominated Yb^{3+}-interactions at the low temperatures.

5.3.3. Magnetic field dependent magnetization

To correlate the dominating magnetic ordering, exchange interactions, strength of AFM and FM spin structures, and its charge dynamics, the magnetic field dependent magnetization measurements were performed at different temperatures for all the systems as shown in Fig. 5.5. In the low temperature region where Yb^{3+}-Yb^{3+} interactions dominate, the AFM character is evident with a gradual slope change around 11 T, escalating the possibility of a metamagnetic transition from AFM to FM and may achieve greater saturation magnetization values at higher fields beyond 14 T. All the compositions, $x \geq 0.05$ show similar characteristics till 80 K. However, at higher temperatures Yb^{3+} ordering directly doesn't contribute to the magnetic transitions but indirectly alters the strength of AFM and FM ordering through the structural parameters. Unlike these, the Yb2 system exhibits a metamagnetic field-induced transition during the first curve at field, H_{C_1}~ 10.3 T during the first curve (at temperatures as low as 3 K) below 14 T. During the second curve, FM spin structure persists till lower magnetic field following a different path, retains AFM spin-structure, and demagnetizes completely at H = 0 T. Moreover, this kind of irreversible yet hysteretic nature is distinct from usual (Pr, Nd, ….)$_{1-x}Ca_xMnO_3$ charge/orbital-ordered systems and single crystals, revealing a strong equilibrium AFM ground state spin structure in the present polycrystalline system [14].

Next, I move to discuss the magnetic AFM and FM spin structure through cooling and heating under different fields which provide a quantitative idea of the amount of conversion of the FM phase into the AFM phase. Fig. 5.6 shows the magnetization measurements performed under the CHUF protocol, which displays the spin structure, and thus quantify the kinetic arrest of FM in the AFM background, which is often termed

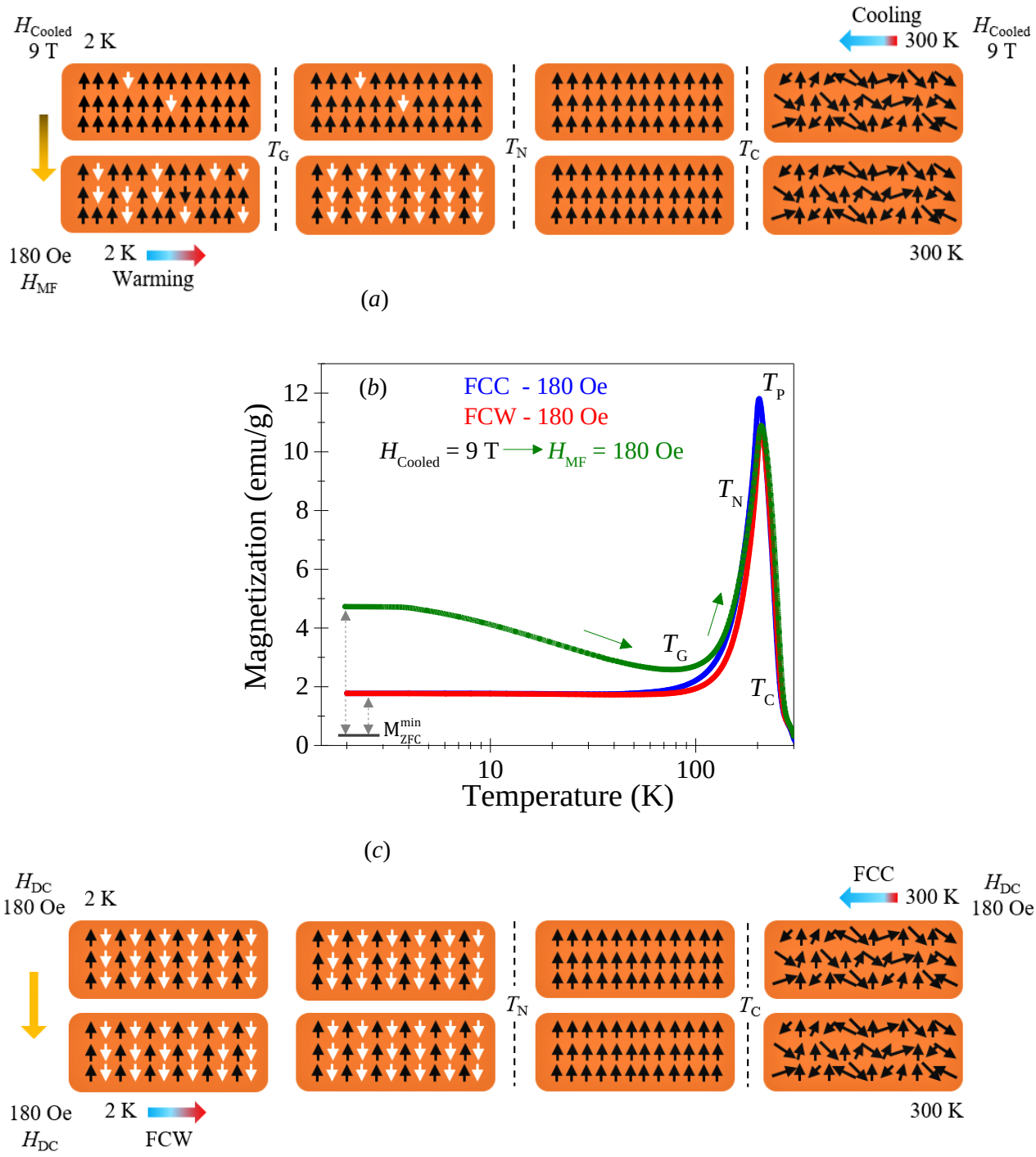

Fig. 5.6. (*a*) Schematic demonstrating the range of FM and AFM ordering *w.r.t.* temperature under the CHUF protocol, Cooling, at $H_{Cooling}$ = 9 T and Heating, at measuring field H_{MF} = 180 Oe. (*b*) Temperature dependent magnetization under conventional FCC, *blue curve* and FCW, *red curve* conditions at applied magnetic field, H = 180 Oe while *green curve*, magnetization under CHUF protocol. (*c*) Schematic demonstrating the range of FM and AFM ordering under the FCC and FCW protocols at H_{DC} = 180 Oe.

as "magnetic glass" [73, 197]. This particular feature is often noticed in the charge/orbital-ordered systems, especially in $La_{0.5}Ca_{0.5}MnO_3$ which shows similar magnetic trend as $Pr_{0.5}Sr_{0.5}MnO_3$, exhibiting metallic FM state with T_C at higher temperatures and an equilibrium AFM state with T_N at lower temperature unveiling the metal to insulator transition, and remains non-conducting till the lowest temperatures. In this chapter, I

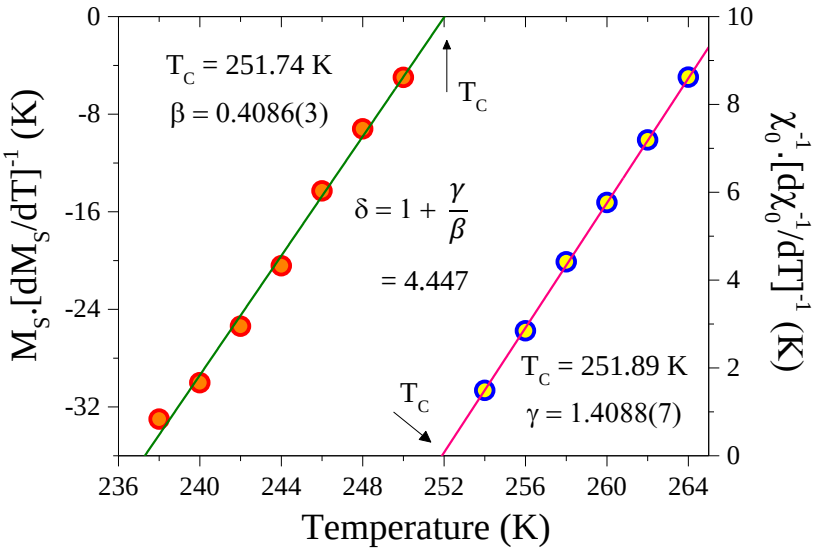

Fig. 5.7. Kouvel-Fisher plots for the spontaneous magnetization, M_S(T) and inverse susceptibility, χ_0^{-1}(T) data.

report the investigations on the Yb2 system, showing the magnetization under FCC and FCW at 180 Oe holding the global maxima of 11.8 emu/g (0.46 $\frac{\mu_B}{f.u}$) and 10.89 emu/g (0.42 $\frac{\mu_B}{f.u}$), respectively with the FM spin-structure accompanied by the unperturbed global minima of (0.068 $\frac{\mu_B}{f.u}$) in the AFM ground state.

Hysteresis in the magnetization demonstrates the first order phase transition with the FM spin-structure persevering the long-range ordering under the FCC. Furthermore, under CHUF protocol, cooling the sample at H_{CF} ~ 9 T from *RT* to 2 K and the field is changed to measuring field, H_{MF} ~ 180 Oe at 2 K as shown in the Fig. 5.6(a), (b) and (c). Subsequently the magnetization response has been recorded till 300 K. At T = 2 K, it shows a magnetic moment of ~ 4.73 emu/g and started to decrease with increase in the temperature till magnetic glass temperature, T_G ~ 85 K and starts to increase. The remnant magnetization value of 0.18 $\frac{\mu_B}{f.u}$ (4.73 emu/g) after removing the field of 9 T unable to align all the FM moments to AFM ground state. The mixture of FM moments in the AFM background establishes a magnetic glass state which exhibits the magnetization value ~ 44% of the maximum magnetization value possessing the FM spin-structure completely. The attained FM-AFM glassy state is metastable and devitrifies upon the increase in temperature towards the T_N which attains a minimum magnetization value at T_G, and increases further till the peak temperature, T_P. In order to examine the non-universal behavior in the magnetic ordering of Yb2, we have employed one of the mathematical approaches in which Kouvel-Fisher equations are fitted with the isotherms (as shown in the Fig. 5.7) across the T_C and deduced the critical exponents β = 0.4086, γ = 1.4088, and δ = 4.447 values falling in between the Mean Field and 3D-Heisenberg model slightly deviating from the pristine compound $Pr_{0.5}Sr_{0.5}MnO_3$, β = 0.448, γ = 1.334, and δ = 3.977. Kouvel-Fisher equations are given as following:

$$M_S\left[\frac{dM_S(T)}{dT}\right]^{-1} = \frac{T - T_C}{\beta} \qquad -------- \qquad (5.1)$$

$$\chi_0^{-1}\left[\frac{d\chi_0^{-1}(T)}{dT}\right]^{-1} = \frac{T - T_C}{\gamma} \qquad -------- \qquad (5.2)$$

where, M_S is the saturation magnetization, T_C is the Curie temperature, χ_0 is the magnetic susceptibility. The extracted β and γ values are used to calculate the δ using the Widom scaling relation given as follows:

$$\delta = 1 + \frac{\gamma}{\beta} \qquad -------- \qquad (5.3)$$

5.3.4. Phase diagrams

Figure 5.8(a) shows the *H-T* Magnetic Phase diagram of polycrystalline Yb5 and Yb2 along with the data reported in the single crystal $Pr_{0.5}Sr_{0.5}MnO_3$ [200]. The field-induced metamagnetic transition from AFM-FM phases is identified before and after the critical fields, H_{C_1} and H_{C_2}, through the first and second curves respectively where H_{C_1} *and* H_{C_2} are determined from the peak observed from the $\frac{dM}{dH}$ vs T graphical plot (not shown). Figure 5.8(b) shows the Yb per *R*-site vs *T* phase diagram showing the different ordering temperatures including the lower temperature magnetic ordering and higher magnetic ordering temperatures.

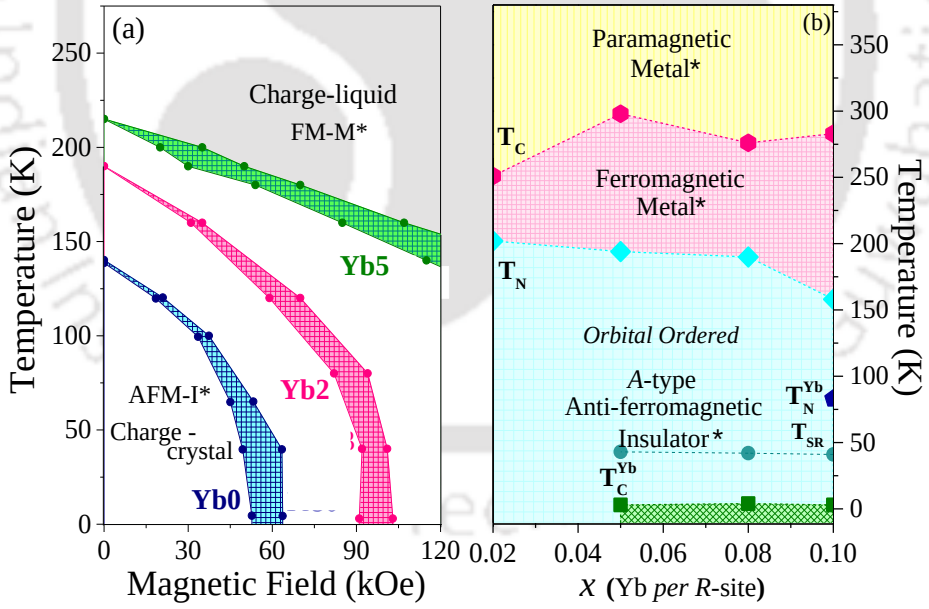

Fig. 5.8. (a) H-T phase diagram showing the field induced transitions (H_{C_1} and H_{C_2}) under 0 T – 14 T – 0 T sweep at different temperatures for the polycrystalline bulk $Pr_{0.45-x}Yb_xSr_{0.55}MnO_3$ ($Pr_{0.5}Sr_{0.5}MnO_3$, referred as Yb0, Ref- [200], 0.02, and 0.05) system. The textured region exhibits the expanse of irreversible metamagnetic transition. **(b)** Phase diagram showing the trend of magnetic ordering temperatures *w.r.t.* Yb^{3+} substitution. T_C – FM ordering temperature, T_N – Orbital-ordering temperature combined with AFM ordering temperature, T_N^{Yb} – Short range AFM ordering temperature of Yb^{3+} sublattice, T_{SR} – spin-reorientation of Yb^{3+} corresponding Mn-sublattice [Ref- [207], and T_C^{Yb} – short range FM ordering temperature of Yb^{3+} sublattice.

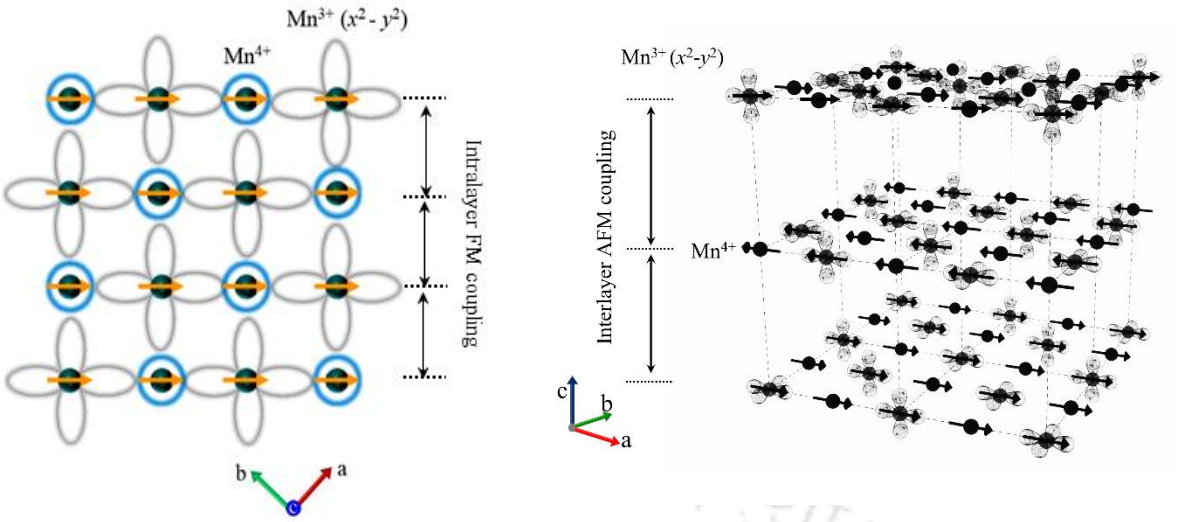

Fig. 5.9. Schematic diagram showing (a) the intralayer FM coupling in the *ab*-plane, (b) interlayer AFM coupling along the *c*-axis.

5.4. Discussions

Ordering of Mn^{3+} and Mn^{4+} orbitals control the magnetic behavior in these systems giving rise to charge, orbital, and spin ordering phenomena. The substitution of Yb^{3+} at the Pr^{+3} - site brought MnO_6 octahedral distortion due to its' smaller radius that bends the $Mn{-}O_{(2)}{-}Mn$ bond angle even more in the *ab* basal-plane as shown in Fig. 5.1(b) and Fig. 5.3(a), (b), and (c) which prefers the AFM superexchange interaction by sharing the e^- between the overlapped Mn^{3+}- $(x^2 - y^2)$ e_g orbital of the JT distorted $Mn^{3+}O_6$ octahedra and O-2*p* orbital. Thus, the orbital ordering under A-type AFM spin structure gives rise to a FM intralayer coupling along the *ab*-plane and AFM inter layer coupling along the *c* – axis as shown in the checkerboard Fig. 5.9(a) and (b). The second reason could probably be the Yb^{3+}- Yb^{3+} short range AFM ordering that is activated at the low temperatures creating a metastable state that is having higher energy than the AFM equilibrium ground state alienated by a thin magneto-crystalline energy barrier as shown in the Fig. 5.10(c). The Yb^{3+} ions strengthen A-type AFM spin structures at the low temperature region below the T_N and broadens the ΔT $[= T_C - T_N]$ with long range FM ordering near to the room temperature. This particular feature explains the persistence of AFM ordering in the $M - H$ curves and absence of metamagnetic transition till 14 T. The hysteresis observed at the T_N closely resembles a first-order phase transition from FM to AFM as the FM spin structure persists for a long range during the FCC curve which is a typical case in some perovskite systems such as $Pr_{1-x}Sr_xMnO_3$ and $La_{1-x}Ca_xMnO_3$ [11, 208]. Generally, the first-order phase transitions are observed from the first and second curves of $M - H$ curves providing evidence for the irreversible metamagnetic transition from AFM to FM and FM to AFM. Such phase transition can be understood well by the existence of heterogenous nucleation that led to another unusual phenomenon known as magnetic glass as shown in Fig. 5.6.

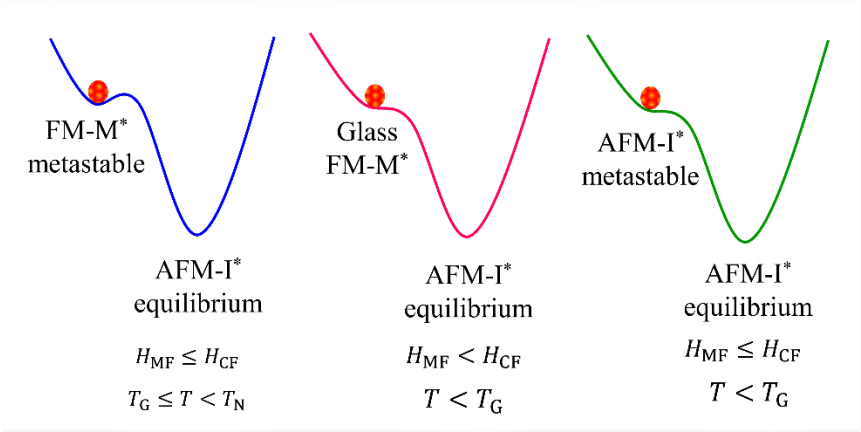

Fig. 5.10. Schematic of the Metastable states observed under different temperature and magnetic field conditions.

Fig. 5.10 explains the charge, spin and orbital dynamics that gives rise to a multiple magnetic phase. Especially from the magnetic measurements following CHUF protocol I can understand a new metastable FM phase that arises at the low temperatures below 90 K. That increases the possibility of FM double exchange interaction that actually invokes the electrons flow and make the system conduct. The metastable FM phase with chances of metallic behaviour is referred as FM-M*. Such FM-M* domains cannot be created homogenously below the T_G because during the process of CHUF protocol, H_{CF} is higher, ~ 9 T and doesn't allow the FM phase to turn into AFM phase till the lowest measuring temperature. So, FM magnetic moments existed completely with high application of magnetic field during the field-cooled cooling process, FCC. Now, during the measurement under field cooled warming, FCW, I reduced the external measuring in nature arresting the electrons flow in the crystal lattice. Noteworthy point in this whole process is, FM phase has been created inherently by using the external parameter, magnetic field. The phenomenon of FM moments becoming kinetically arrested in the AFM phase is commonly referred to as "magnetic glass".

The energy barrier for the kinetically arrested high energy metastable FM moments to flow into the AFM equilibrium phase is very less and that makes the magnetic glass metastable phase different from the conventional FM phase at high temperature, as shown in the Fig. 5.10(b) and (a), respectively. And whenever FM phase coming into existence it creates a possibility for the electron conduction and through double exchange interaction suggests a metallic nature. However, AFM phase with its' superexchange interaction makes the system localize the electrons and prohibit them from hopping and suggesting an insulating phase. magnetic field, H_{MF} ~ 180 Oe. This reduction of magnetic field could turn some percentage of the FM moments into AFM matrix. And, during this FCW measurement, from 3 K to T_G ~ 90 K, all the FM moments are gradually turned into AFM moments and reach an equilibrium AFM phase which is typically insulating.

However, these insulating and metallic natures can be well determined and confirmed only by the resistivity measurements. In the present work, I have confirmed the FM and AFM phases along with the

admixture of FM and AFM phase in the glass form due to kinetic arrest of spins. In the Fig. 8 I have used M*, I* as the metallic and insulating phases which are suggested for the further investigations. Yb^{3+}-Yb^{3+} moments produce a short-range AFM ordering that exists at the low temperature below the equilibrium AFM phase. This suggests that the new short-range AFM magnetic phase is metastable and suggests insulating nature as it is conventional to observe in all the rare-earth elements.

5.5. Conclusions

Finally, the results demonstrate that, by means of thermal and magnetic energies a switchable magnetic state can been realized between the AFM and FM state driven by the tunable superexchange and double exchange interactions, respectively. Such changes are closely associated with the changes occurring in the bond angle $Mn{-}O_{(2)}{-}Mn$ which may activate the electrons hopping process. In addition, I noticed an unconventional multi-phase magnetic structure over a wide temperature and field range. The current results related with the tuning of the magnetic and transport properties by allowing crystal-distortion up on substitution of magnetic element having different atomic radius may open a novel methodology to attain a robust charge/orbital-ordering behavior in the field of spintronics and magnetic memory devices.

Chapter 6
Tunable Spin-flip transitions, Negative magnetization and Giant-magnetocaloric effect in $Gd_{0.9}Ce_{0.1}CrO_3$

This chapter is dedicated to examining the synthesis of the polycrystalline perovskite chromate $Gd_{0.9}Ce_{0.1}CrO_3$, and delves into a comprehensive investigation of its structural, electronic, spectroscopic, and magnetic properties. Notably, $Gd_{0.9}Ce_{0.1}CrO_3$ showcases a unique field-induced magnetization spin reversal behavior. The compensation temperature corresponds to an additional phase transition induced by the spin-flip mechanism driven by Zeeman energy. This provides compelling evidence for the occurrence of field-induced spin-flip transitions in Ce-substituted polycrystalline $GdCrO_3$. Remarkably, this compound exhibits a substantial giant magneto-caloric effect at lower temperatures, surpassing the values observed in other rare-earth perovskite chromates.

6.1. Introduction

Heavy rare-earth perovskites especially the chromates ($RCrO_3$) with R = Pr, Ce, Gd, Sm etc. exhibit complex magnetic ordering which holds robust spin dynamics and strong exchange interactions between R^{3+}-Cr^{3+}, R^{3+}-R^{3+}, Cr^{3+}-Cr^{3+}. These systems exhibit some fascinating physical phenomena such as spin-flip transitions, negative magnetization, and compensation, multiferroic behaviour, giant magneto-caloric effect values and field-induced magnetic-phase transitions which play a vital role in designing spin-valve devices [1, 42, 194]. Rare earth orthochromites have been examined dynamically over the past few decades using various diverse characterization techniques such as heat capacity, neutron diffraction, Mossbauer analysis, magneto-dielectric and optical-absorption spectroscopy [47, 74, 209]. These investigations were widely utilised to probe the ferroelectricity driven by the co-existence of local non-central symmetry and multiple magnetic ordering (antiferromagnetic and ferromagnetic behaviour) in $RCrO_3$. Along with these properties phenomena such as exchange bias, spin reorientation transitions, negative magnetization and its reversal, spin glass state etc., have been the extensively studied in $RCrO_3$ related systems [19, 74, 209–211]. Magnetization reversal phenomenon noticed in these types of compounds is quite fascinating and gripping the huge scientific attention owing to different temperature dependence of magnetic moments between the cations of constituent sublattices. Here the net magnetization changes the polarity from positive to negative value after a specific temperature popularly termed as compensation temperature (T_{Comp}) which is the key feature of $RCrO_3$ related systems [212]. It is well known that the phenomena of magnetization reversal rely on the presence of two distinct states of the magnetization making the materials perfectly accessible for switchable devices such as volatile magnetic memory storage, thermo-magnetic switches, high speed read/write magnetic memories, thermally assisted magnetic random-access memory, etc. [213]. In general, most of the materials exhibit T_{Comp} far below the room temperatures limiting their potential applications in magneto-electronic devices. Therefore, it is pertinent from the research point of view to have a better understanding of tenability of T_{Comp} at high temperature for the above applications. The induced internal field

by the transition metal oxide sublattice (Cr^{3+}, Mn^{3+}, etc.) play a major role in magnetization reversal of $RCrO_3$ related systems, in which rare earth elements (Gd^{3+} and/or Ce^{3+}) couples antiferromagnetically with transition metal ions which polarizes them to get aligned in the opposite direction (with respect to applied field) causing reversal in the magnetization [59]. Most of the $RCrO_3$ materials (e.g. $PrCrO_3$, $YbCrO_3$, $HoCrO_3$) display the magnetization reversal under field cooled warming (FCW) protocol. However, the first end compound $GdCrO_3$ exhibits the negative magnetization only under field-cooled cooling (FCC) mode indicating the interesting measurement protocol/history dependent features [214].

Especially $GdCrO_3$ and $CeCrO_3$ are very well known anti-ferromagnetic systems exhibiting the magnetization spin reversal behaviour [47, 74]. $GdCrO_3$ is a *G*-type antiferromagnetic system showing the T_N ~ 169 K and T_{Comp} ~ 132 K. The spin-flip transition occurs at T_{SF} ~ 18 K at magnetic field as low as 100 Oe. Giant magnetocaloric effect has been reported at low temperatures with a $-\Delta S_M$ ~ 36.97 $J.Kg^{-1}K^{-1}$ at 70 kOe. $CeCrO_3$ on the other hand exhibits the *G*-type AFM behavior with the spin-flip transition gradually occurring at higher magnetic fields and compensating for the magnetization and ventures into the positive scale. Cao et. al. reports the T_N ~ 230 K and T_{Comp} ~ 100 K with spin flip transitions occurring at T_{SF} ~ 36 K at 1.2 kOe [47].

In this chapter, I report an investigation of the polycrystalline perovskite chromate system $G_{0.9}Ce_{0.1}CrO_3$ through their structural, electronic, magnetic properties. X-ray diffraction and Raman studies contribute to the understanding of the internal atomic atmosphere and their response to optical spectroscopic techniques. It exhibits the magnetization spin reversal along with the spin-flip transitions tunable with the externally applied magnetic field. Path independent spin-flip transitions are studied with unconventional magnetization protocol like CHUF. Giant-magnetocaloric effect exhibited by the system due to the internal distortions occurred through the substation of the Ce^{3+} at the smaller Gd^{3+} sites.

6.2. Experimental details

The polycrystalline $Gd_{0.9}Ce_{0.1}CrO_3$ (GCO) was synthesized by standard solid-state reaction method. The stoichiometric proportions of pure powder precursors of Gd_2O_3 (99.9%), CeO_2 (99.95%), and Cr_2O_3 (99.99%) were ground in an agate mortar and pestle in air for 5 hours, calcined at 1273 K for 24 hours under the ambient condition in order to prepare the highly homogeneous mixture. The sample was then ground again for 2 hours to break the agglomerates formed due to calcination and were pelletized and sintered afterwards at 1473 K for 24 hours in air in Nabertherm tube furnace (Germany) followed by natural cooling to room temperature. Phase purity of the final sintered samples were confirmed with the help of room temperature Rigaku; TTRAX III XRD equipped with 1.54056 Å wavelength laser source of Cu-$K_{\alpha 1}$ radiation with step size 0.02. In order to evaluate the charge states of the core level constituent elements, XPS experiment was performed using the high-resolution PHI 5000VVersaProbe III Scanning XPS with microprobe Al K_α (544 eV). DC magnetization measurements were performed using a Dyna-cool model physical property measurement system (PPMS) from Quantum designs. The magnetization values were

recorded at different external fields (50 Oe to 20 kOe) with respect to temperature and at variable temperatures (3 K to 300 K) with respect to field under different protocols zero-filed cooled warming (ZFCW), field cooled cooling (FCC), field cooled warming (FCW). Isothermal field dependent magnetization hysteresis loops were recorded in the range of +90 kOe to -90 kOe at particular selected temperatures. The time stamp experiments under all the ZFCW, FCC and FCW protocols were executed at certain field and temperatures. The room temperature Raman spectrum were recorded within the range of 100 cm^{-1} to 800 cm^{-1} and separately 100 cm^{-1} and 200 cm^{-1} with the help of HR Raman spectrometer from Horiba Jobin Yvon (model: Lab Ram HR) with the excitation of He-Ne laser of fixed power 20 mW. The THMS600 module was supplemented for the temperature variant readings up to 80 K for both the samples within the lower range of wavelength.

6.3. Results and Discussion

6.3.1. Structural analysis

Both $GdCrO_3$ and $CeCrO_3$ are stable in slightly distorted orthorhombic perovskite with space group *Pbnm* [215]. Doping larger size Ce adjusts itself at the at the A site for both the pristine compounds in place of Gd and Sm with 12-fold coordination and B site remains unaltered with Cr with 6-fold coordination. Figure 6.1 displays the X-ray crystallographic phase for the sample $Gd_{0.9}Ce_{0.1}CrO_3$ (GCO). The diffraction pattern confirms the phase purity of the samples without any signature of secondary impurity phase. The pattern is analysed with the help of FULLPROF software Rietveld refinement technique [216]. The Bragg peaks are indexed according to the *Pbnm* (no. 62) space group and no extra Bragg peak was observed. The goodness of the fitting is close to unity ($\chi^2 \approx 2.42$ and 2.63) indicates the reliability of the fitting. The occupation number of Gd, and Ce are refined during the fitting in order to justify the A site cation ratio and the refined value of Gd/Ce is nearly exact to the stoichiometric value of the samples. I can observe the trend of fluctuated increase in the lattice parameters *a*, *b* with the doping of higher ionic radii cations (Ce

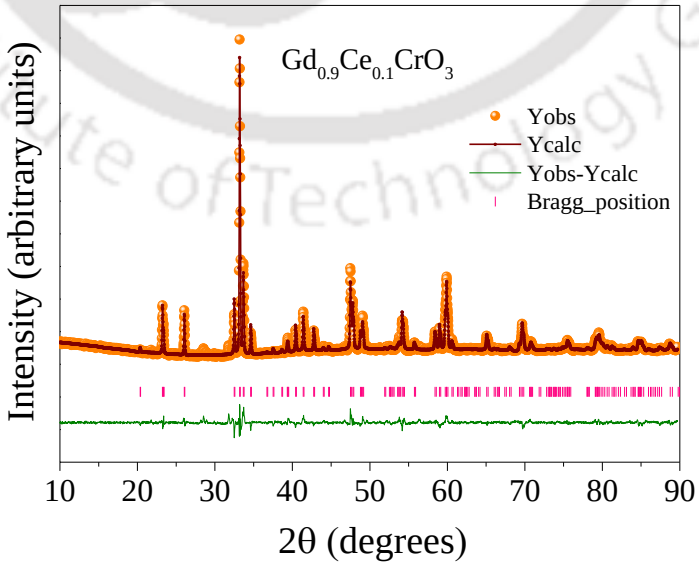

Fig. 6.1. Rietveld refined X-ray diffraction patterns of $Gd_{0.9}Ce_{0.1}CrO_3$ showing single phase *Pbnm* orthorhombic perovskite structure.

and Sm) at the Gd site. The volume increases 0.072% for Ce doped $GdCrO_3$ due to the effective iodic radius of Ce^{3+}(1.143 Å) being larger than Gd^{3+}(1.053 Å) with 8-coordinatio number while the in-plane *c* parameter increases [47, 74]. In order to understand the internal crystallographic behaviour, I tabulated all the structural parameters refined and calculated along with the comparative study of the pristine compounds from the previous reported literature in Table 6.1. The modification can be explained with the help of difference of average radius of A site cation: $r_{avg} = \sqrt{(0.9) \times R_{Gd^{3+}}^2 + 0.1 \times R_{Ce^{3+}}^2}$ for GCO sample which increases to 1.063 Å compared to 1.053 Å for undoped compound with $R_{Gd^{3+}}$ = 1.053 Å with VIII coordination number and that of $R_{Ce^{3+}}$ = 1.143 Å with same coordination number [217]. The substitution of larger cation impacts the crystal symmetry by introducing the distortion which can be termed as tolerance factor (t), given in the following Eq. (6.1):

$$t = \frac{((1-x) \times R_{Gd^{3+}} + x \times R_{Ce^{3+}}) + R_{O^{2-}})}{\sqrt{R_{Cr}^{3+} R_{O}^{2-}}} \quad 6.1$$

From the table I can observe that the octahedral distortion (Δ) expressed in Eq. (6.2):

$$\Delta = \left(\frac{1}{N}\right) \sum_{n=1,N} \{(d_n - \{d\}) \prec d \succ\}^2 \quad 6.2$$

Apical Cr-$O_{(1)}$-Cr bond angle (θ_1), basal Cr-$O_{(2)}$-Cr bond angle (θ_2) and the tilt angles θ and ϕ inside the CrO_6 octahedra along the pseudo-cubic axes [110] and [001] calculated from the bond angles exhibit visible deviations with the A-site cation substitution than that of the average bond lengths between the Cr and the O anions (changes ~ 0.54 %) directing towards the bond rigidity expected in octahedral symmetry surrounding for Cr^{3+} [218]. I have also calculated the tilt angles from the lattice parameters, $\theta = cos^{-1} \frac{\sqrt{2}a}{b}$, $\varphi = cos^{-1} \frac{a}{b}$ and the magnitudes well match with the previously reported values of similar systems [219, 220]. Along with the tilting of the CrO_6 octahedra generating due to the mismatch between the A -site Gd/Ce and B-site Cr cations, an impulsive reduction in the strain parameter *s* with increment of ~ 2.2 % in the average radius of the A-site cation encompasses the Wyckoff position eccentricities of Gd (4c) and the Cr (4b) sites.

6.3.2. Electronic Properties

Figure 6.2 demonstrates the room temperature XPS spectra of the investigated sample GCO in order to confirm the oxidation states and further validate the phase purity, where the scattered symbols are the experimental data, and the curves are the fitted lines with the combination of Lorentzian and Gaussian functions. The collected high resolution XPS spectra possess the binding energy resolution of 0.1 eV. I used the Tougaard algorithm for the background correction and a nonlinear least square fitting procedure for resolving all the constituent chemicals. The core level of the spectra is calibrated with the C-1*s* binding energy 285 eV. I examined all the surface level particle electronic configuration of the constituent elements of the sample.

Table 6.1. The refined crystallographic parameters obtained from XRD of $Gd_{0.9}Ce_{0.1}CrO_3$ and $Sm_{0.9}Ce_{0.1}CrO_3$. The parameters, *a, b, c, and V* are lattice constants and lattice volume respectively. θ_1 and θ_2 are the Cr-$O_{(1)}$-Cr and Cr-$O_{(2)}$-Cr bond angles. θ and ϕ are the in-phase and out-of-phase tilt angles *w.r.t.* 110] and [001] respectively. Δ, octahedral distortion, *t*, tolerance factor, r_{avg}, average radius of the R^{3+} cation.

Parameter		Atomic positions		Bond lengths		Bond angles		Other parameters	
a	5.3194(1)	Gd/Ce	0.9936(1)	Gd/Ce-$O_{(1)}$	2.3256(0)	θ_1	155.3	θ [110]	12.36
b	5.5072(1)	(4c)	0.0584(0)	(*two*)	2.3779(0)	θ_2	145.5	ϕ [001]	14.92
c	7.6054(1)		0.2500(0)	Gd/Ce-$O_{(2)}$	2.6429(0)			θ	8.45
V	222.80(1)		1.0	(*six*)	(*two*)			(*from lattice parameters*)	
		Cr	0.0000(0)		2.5845(0)			ϕ	15.01
		(4b)	0.5000(0)		(*two*)			(*from lattice parameters*)	
			0.0000(0)		2.2850(0)			r_{avg}	1.062
			1.0		(*two*)			*t*	0.8663
		O1	0.0762(0)	Cr-$O_{(1)}$				Δ (×10^{-4})	1.2800
		(4c)	0.4827(1)	(*two*)	1.9464(0)			s	0.034(1)
			0.2500(0)		(*two*)			ϕ	17.174(1)
			0.9						
		O2	0.6806(1)	Cr-$O_{(2)}$					
		(8b)	0.2934(0)	(*four*)	1.9239(0)				
			0.0535(1)		(*two*)				
			1.599(0)		2.0845(0)				
					(*two*)				

Figure 6.2(a), (b), (c) and (d) shows the XPS spectra of Gd-4*d*, Ce-3*d*, Cr-2*p* and O-1*s* core level of GCO. All the binding energies magnitudes are persistent with the standard values of National Institute of Standards and Technology (NIST) database [221].

The deconvolution of Gd-4*d* core-level spectra is consisted of 2 doublets at $4d_{5/2}$ and $4d_{3/2}$ core levels. The $\chi^2 \sim 2.7$ confirming the goodness of the fitting. I have indexed the peaks at 138.45 eV, 140.8 eV, 144.66 eV and 146.74 eV with the support of previously available experimental data available in the literature [221]. Gd with Xenon like configuration with filled *s* orbital and singly occupied *f* and *d* orbitals get oxidised to Gd^{3+} resulting in the signature of the trivalent states in the XPS spectrum. The $4d_{5/2}$ gives rise to the peaks at lower energy level *i.e.*, 138.45 eV, 140.8 eV and the other two higher binding energy level corresponds to the $4d_{3/2}$ core level. I did not observe any satellite peaks or formation of any other oxidised state [222–224].

The XPS spectra of Cr-2*p* exhibit two peaks of $2p_{1/2}$ and $2p_{3/2}$ which further splits and exhibit 4 peaks in total residing at 583.44 eV, 585.45 eV, 573.61 eV and lastly 575.19 eV as shown in Fig. 6.2(c). The peaks at higher energy of 583 eV and 585 eV are generated from the doublet of $2p_{1/2}$ electronic state and the other two corresponds to the $2p_{3/2}$ state. The mere difference with the NIST database standard peak positions can be due to the change in r_{avg} resulting in the modified bond length in the CrO_6 octahedra.

Finally, the asymmetrical curve of O-1*s* core-level spectra raised two peaks and another extra hump originated as a result of surface absorbed oxygen species. The spectrum is well fitted with 23% Lorentzian

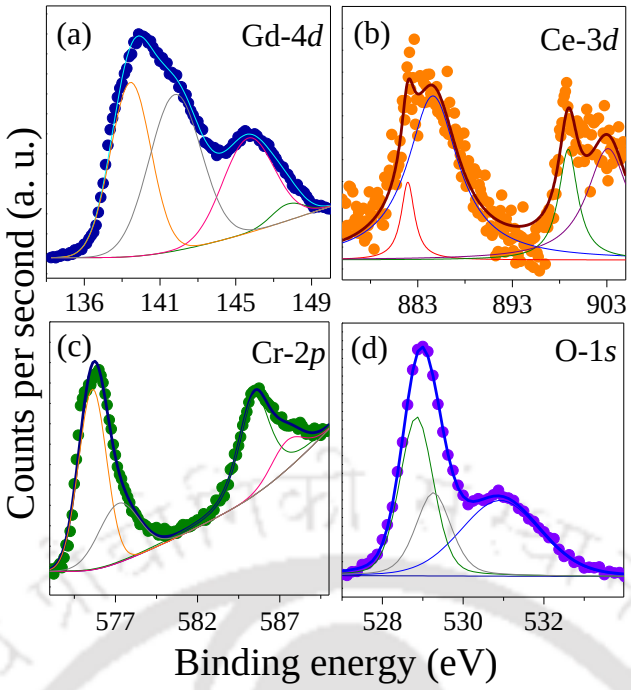

Fig. 6.2. X-ray photoelectron spectroscopy of (*a*) $Gd-4d$, (*b*) $Ce-4d$, (*c*) $Cr-2p$ and (*d*) $O-1s$.Scattered symbols represents the original data and solid lines are the fitted curves.

and 77 % Gaussian fitting with χ^2 value 2.01. The FWHM value was kept fixed at 1.03 for the best fitting purpose. The fitted peaks are indexed at 528.92 eV, 526.85 eV and 527.26 eV. The spectrum at 527.26 eV is the result of saturated O^{2-} ions along whereas the peak at 526.85 eV confirms the O-1*s* state [225]. The remaining one locating around 528.92 eV indicates towards the surface originated excess oxygen [226].

Figure 6.2(b) shows the XPS spectra of Ce-3*d* core-level with deconvoluted peaks at 879.05 eV, 884.57 eV, 902 eV and 903.52 eV. The core-level is consisted of two doublets of $3d_{5/2}$ and $3d_{3/2}$ electronic states, and I identified them based on the literature available [57]. Ce possess the Xenon like configuration with filled *s* orbital and singly occupied *f* and *d* orbitals easily prone to get oxidised to Ce^{4+} resulting in the signature of both of the states in the XPS spectrum [227]. But in the present experimental data, I did not find any signature of Ce^{4+} confirming the phase purity. The peaks positioned at 879.05 eV and 884.57 eV are the signature of spin-orbit coupling induced $3d_{3/2}$ state and the peaks at 902 eV and 903.52 eV specifies the 5/2 core level [227].

6.3.3. Raman spectroscopic analysis

Raman spectroscopy is an important method to probe and explain the local crystal symmetry changes as a result of modification at *A*-site cation. Figure 6.3 displays the temperature dependent Raman spectroscopy of $Gd_{0.9}Ce_{0.1}CrO_3$ sample along with the spectrum at room temperature ranging from 80 K to 293 K and wavenumber within 100 cm^{-1} to 800 cm^{-1}. I have followed the orthorhombic *Pbnm* structure following the Glazer's notation $a^-b^+a^-$ tilt showing the mirror reflection along [010] plane [217]. Considering the group

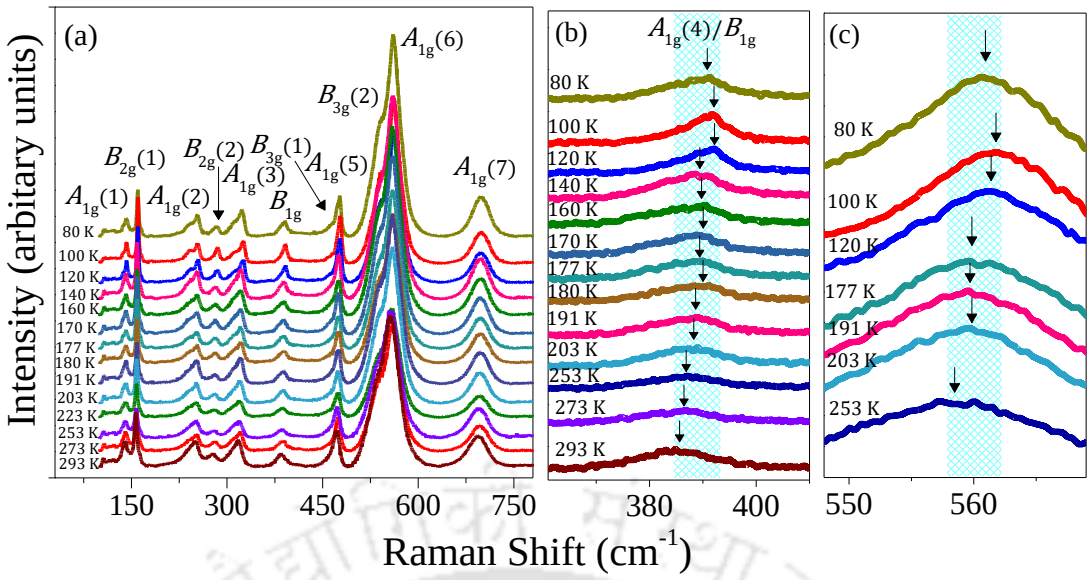

Fig. 6.3. Raman spectra of the $Gd_{0.9}Ce_{0.1}CrO_3$ taken from 80 K to 293 K indexed all the existing modes.

theory for *Pbnm* crystal structure containing four formula unit cell arising at the Brillouin zone centre, the active 24 Raman modes are: $7A_{1g} + 7B_{1g} + 5B_{2g} + 5B_{3g}$ These 24 modes are Raman active modes categorised in two symmetric ($A_g + B_{1g}$) and four antisymmetric octahedral stretching modes ($2B_{2g} + 2B_{3g}$), four bending modes ($A_g + 2B_{2g} + B_{3g}$), six rotation or tilt modes of the octahedral ($2A_g + B_{1g} + 2B_{2g} + B3g$) and eight modes associated with the A-site cation movement ($3A_g + 3B_{1g} + B_{2g} + B_{3g}$) among total 60 modes including other 25 infrared active, 8 silent and 3 acoustic modes. The active modes are the outcome of 3 different kind of variation in the crystal structure given by 1) distortion of the CrO_6 octahedra 2) Jahn-Teller (J-T) distortion 3) Displacement of the A-site cation [218, 219]. Here, for our investigated system, the second reason comes out to be irrelevant as the $RCrO_3$ with the transition metal Cr in its stable ionized state Cr^{3+} with $[Ar]3d^3$ configuration fail to show J-T phenomenon unlike Cr^{2+} with d^4 electrons exhibiting J-T effect in both high and low spin state. Hence, I can rule out the possibility of the J-T distortion leading to Cr-O bond rigidity [218]. Among all the 24 active modes, I noticed 11 modes within the investigated wavelength range exhibiting blue and red shift for the respective modes. I have fitted all the modes at 141, 159.9, 249.2, 281.6, 319.4, 389.2, 470.1, 474.7, 534.4, 561.5, 698.3 cm^{-1} (at 80 K) at every temperature with Lorentzian fitting as shown in Figure 6.4(a). The modes below 200 cm^{-1} corresponds to the rare earth A-site cation displacement in *x* and *z* direction relating to the mass (μ) of the A-site cation as: $\omega = \sqrt{(k/\mu)}$ with, k as the force constant. The two modes under this category are labelled as A_{1g} (1) and B_{2g} (2). The range higher than 200 cm^{-1} consists of modes arising due to vibration of Gd and O atoms, bending and stretching of Cr-O bonds. A_{1g} (2) along with its doublet B_{2g} (2) modes arises due to octahedral rotations around the crystallographic *y*-axis. The most prominent and intensified mode at ~ 561 cm^{-1} (at 80 K) is related to the octahedral bending inside the unit lattice cell whereas the second most strengthened mode at 698 cm^{-1} (at 80 K) corresponds to the antisymmetric stretching vibrations of CrO_6 octahedra. The A_{1g} (4)/B_{1g} and A_{1g} (6) modes tend to shift towards the lower wavenumber with increasing the temperature towards room temperature as shown in Fig. 6.4(b) and 6.4(c)

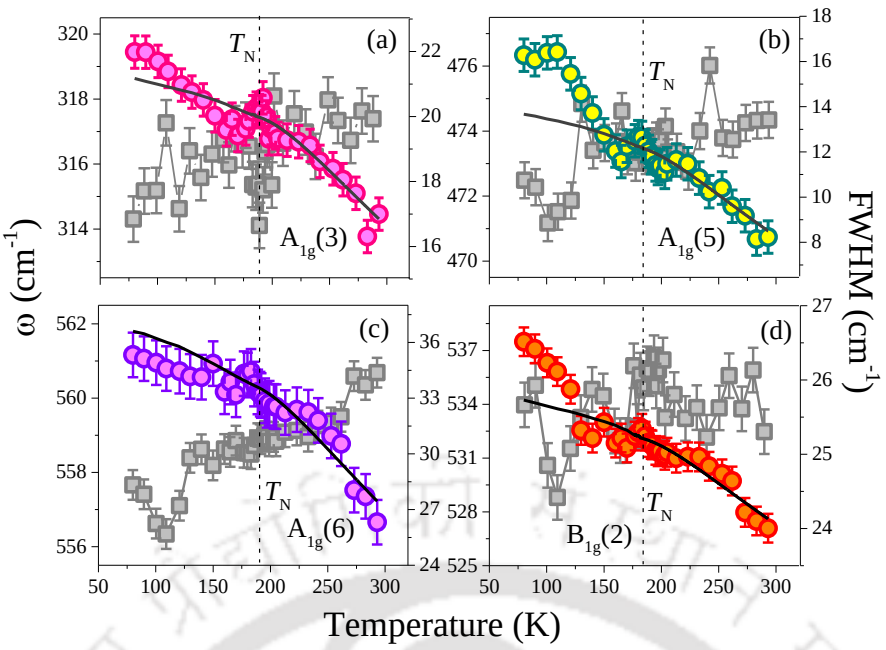

Fig. 6.4. Different modes with Raman shift (a) $A_{1g}(3)$, (b) $A_{1g}(5)$, (c) $A_{1g}(6)$, and (d) $B_{3g}(2)$ fitted with the Lorentzian function for the Raman spectra at room temperature (*left hand scale* with colour data points) and the corresponding FWHM of each mode (*right hand scale* with dark grey and grey).

indicates towards the Gd (Ce)/Cr-O bond lengths and increase in bond-angle O-Cr-O. I also observed the broadening of the modes while reaching room temperature signifying the reduction in structural degrees of order. Additionally, I have also demonstrated the temperature dependence of Raman shift and linewidth for some specific modes in order to correlate the origin of Raman active modes with the structural and magnetic transitions as shown in Fig. 6.4. The increase in the wavenumber with decreasing the temperature can be explained with the help of anharmonic effect signifying the change in the intrinsic anharmonic frequency at constant volume which can be expressed as given in the Eq. (6.3) [220]:

$$\omega_{anh}\,(T) = \omega_0 + A\left[1 + \frac{2}{e^{\frac{\hbar\omega_0}{2k_BT}} - 1}\right] + B\left[1 + \frac{3}{e^{\frac{\hbar\omega_0}{3k_BT}} - 1} + \frac{3}{(e^{\frac{\hbar\omega_0}{3k_BT}} - 1)^2}\right] \qquad 6.3$$

with A and B are the anharmonic coefficients obtained from the Raman data fitting above T_N and expression ω_0 is the frequency of the corresponding mode at absolute temperature. The Raman spectrum for specific modes $A_{1g}(3)$, $A_{1g}(5)$, $A_{1g}(6)$ and $B_{3g}(2)$ diverge from the Eq. (6.3) below T_N which can be result of either spin-phonon coupling or magnetostriction effect. The hardening of antisymmetric stretching mode $A_{1g}(6)$ can be understood as a result of exchange-striction effect or the presence of Cr^{3+}-Cr^{3+} AFM coupling. In order to understand this anomalous behaviour near the transition temperature, I have plotted the FWHM or linewidth of the chosen spectrum. The linewidth of the modes is related to the phonon-lifetime, but the lattice volume is unaltered that case opting out the possibility of magnetostriction effect which is consistent with the $GdCrO_3$ indicating a strong spin-phonon coupling of Gd^{3+}-Cr^{3+} interaction [221]. Further, this mode, related to octahedral bending shows a sharp deviation at T_N confirms the magnetic transition is closely related to the motion of Cr ions.

6.3.4. Magnetic Properties

6.3.4.1. Temperature dependant magnetization

Figure 6.5(a) exhibits the temperature dependent magnetization under ZFCW, FCC and FCW protocols. Under H_{DC} = 200 Oe, the three protocols exhibit the long-range magnetic ordering suggesting the canted anti-ferromagnetism with Néel temperature at T_N ~ 173.4 K. This is confirmed by the $\frac{d(\chi T)}{dT}$ vs T plot and Curie-Weiss linear fit at the high temperature paramagnetic region. The linear fit ventures into the negative temperature scale and meets the *X*-axis at Curie-Weiss temperature, θ_D ~ -28.6 K by extrapolation. Long-range magnetic ordering lead by the Cr^{3+} sublattice configured in the G-type CAFM structure with $\Gamma_4\ (G_z, F_y, A_x)$. The negative magnetization popped up during the FCC condition meets the compensation point at T_{Comp} ~ 121 K. Beyond the T_{Comp}, the Gd^{3+} and Ce^{3+} contribution increases which is evident through the increase in negative magnetization and attains a maximum till $34 \times 10^{-2} \frac{\mu_B}{f.u.}$ under H_{DC} = 200 Oe. From Fig. 6.5(b), under an applied magnetic field of 1 kOe, the magnetization in negative scale suddenly switches to the positive under FCC condition which can be understood as spin-flip transition which is known in the $GdCrO_3$ polycrystalline system [74]. Beyond the Spin-flip transition temperature, T_{SF} ~ 10 K the magnetic sublattice gains the Zeeman energy which is helpful for flipping the spins from $\Gamma_4\ (G_z, F_y, A_x)$ to $\Gamma_4'\ (G_z, F_y, A_x)$ from $(00\bar{1})$ to (001) where, the *c*-axis is the easy axis. The parameters and their influence on Zeeman energy of the system is given by the following Eq. (6.4):

$$E_{zeeman} = -\mu_0 M_{Net} H_{Ext} \text{Cos}\ \theta \qquad (6.4)$$

where θ is the angle between the M_{Net}, net magnetization and H_{Ext}, externally applied magnetic field. Net moments with $\theta = \pi$ contains large Zeeman energy and they are easy to be flipped, on the other hand the spins with $\theta < \pi$ will be flipped by applied more external magnetic field. The spins flipped increase the magnetization in the positive scale by crossing the magnetization compensation. During the FCW condition, the curve cannot reverse into the $\Gamma_4\ (G_z, F_y, A_x)$ configuration but continue in the $\Gamma_4'\ (G_z, F_y, A_x)$ condition and attains PM configuration after the T_N. Spin-flip phase transition occurred in this system is irreversible similar to the $GdCrO_3$ and $CeCrO_3$. From Fig. 6.5(c), the magnetization measurements performed under FCC at H_{DC} ~ -200 Oe and FCW at H_{DC} ~ +200 Oe in order to understand the reversible character of the magnetization on the applied field polarity. It is explicitly evident that the FCW curve doesn't even go through the compensation temperature. This suggest that even with the lower magnetic fields by changing their polarity the magnetization behaviour can be tuned for the desired applications.

In order to understand the field dependent magnetic sublattice behaviour at the low temperatures the FCC and FCW measurement has been performed at H_{DC} = 100 Oe, 200 Oe, 400 Oe, 500 Oe, 700 Oe, 1 kOe, 1.3 kOe, and 2 kOe as shown in the Fig. 6.6(a). The overall magnetization M(T) undergoing the second transition at the low temperatures associated with spin-flip transition triggered by the critical field, H_C = 200 Oe.

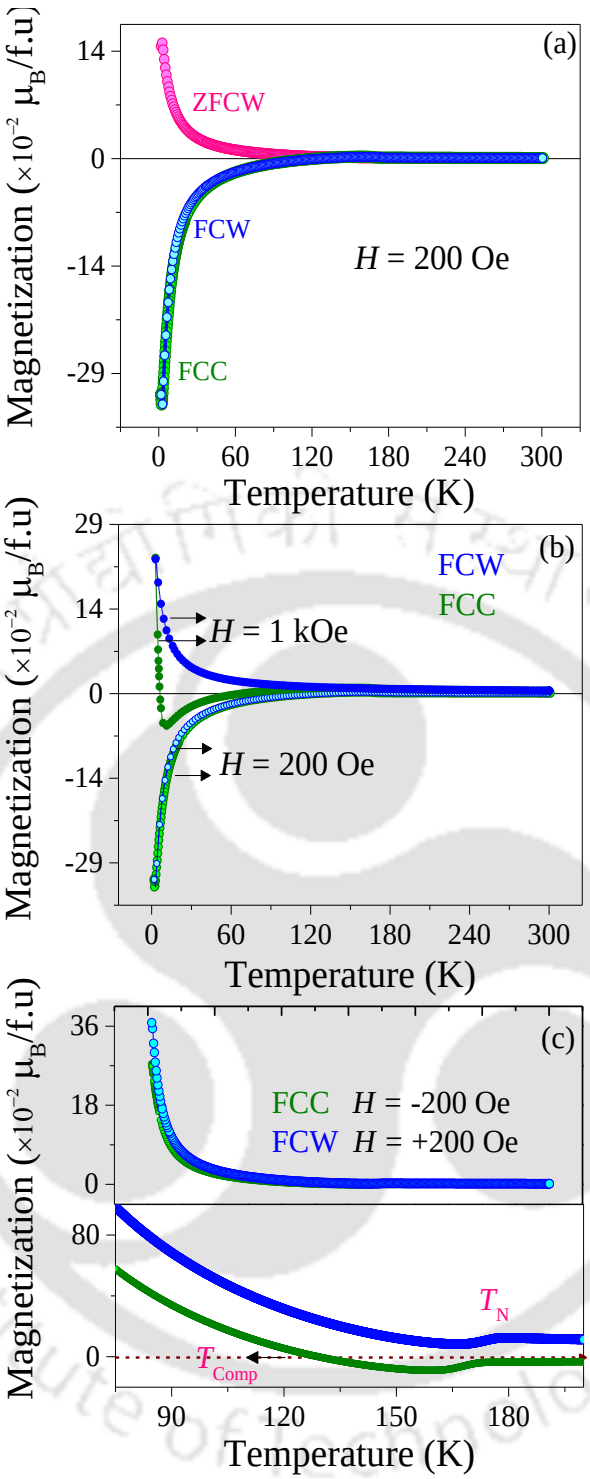

Fig. 6.5. (*a*) Temperature dependent magnetization of $Gd_{0.9}Ce_{0.1}CrO_3$ under (a) ZFCW, FCC, and FCW protocols. (*b*) FCC and FCW at field 1kOe and 200 Oe. Irreversible Spin-flip transition observed during the FCC at 1 kOe. (*c*) FCC under the applied field H = -200 Oe and FCW under the field H = +200 Oe. Zoomed view given below to show the T_{Comp} observed only under the FCW condition.

Beyond the T_{Comp}, the magnetic Zeeman energy gained by the magnetic sublattice flip the spins from Γ_4 to Γ_4'. The number of spins flipped depends on the amount of magnetic field applied which is clearly seen from Eq. 6.4. The gradual spin transitions observed in a tailored manner by the changing the externally

magnetic fields gradually and could witness a complete sublattice's spin-flip configuration from 1 kOe to above magnetic fields. The shift of T_{SF} from lower temperatures to higher temperatures has been noticed. The stability of the spins that gets flipped also investigated with the help of Time stamp measurements shown in the Fig. 6.6(b). The sample has been cooled under an applied filed of 100 Oe to 3 K where the negative magnetization persists as the Zeeman energy is not enough to flip the spins into Γ_4' configuration. Magnetization has been measured for 300 secs followed by measuring the magnetization at 200 Oe for 300 secs and increasing the field to 400 Oe, 700 Oe, 1 kOe and 2 kOe. The number of spins flipped and magnetization shooting up to the positive scale explicitly observed through the time stamps confirming their stability and shows the robust dependency of the Zeeman energy on the externally applied magnetic field. The path-independent nature of the spin flip transition has been observed through the cooling and heating under different magnetic fields, CHUF protocol as shown in the Fig. 6.6(c). The magnetization recorded under the FCC condition by applying a magnetic field of H_{DC} = 200 Oe. This reflects the absence of the spin-flip transition. At 3 K the magnetic field has been raised to 70 kOe, and the FCW curve has been recorded while warming. The magnetization curve during the warming cycle reflects the completely flipped spins containing the Γ_4' configuration.

6.3.4.2. Time dependent magnetization

The stability and consistency of the magnetization polarity and its' switching nature between positive and negative magnetizations were studied through the time stamp measurements of magnetization. In Fig. 6.7(a), under the applied magnetic field of H_{DC} = 100 Oe in FCC condition, the sample has been taken to 120 K below the T_{Comp} into the negative magnetization region. Magnetization has been recorded for 300 secs and the temperature is raised to 140 K just above the T_{Comp} and magnetization measured for 300 secs by holding the temperature constant. Again, the sample is cooled to 120 K and magnetization measured for 300 secs followed by measurements at 140 K. Across the T_{Comp}, the samples explicitly and consistently show the switching behaviour of the magnetization without any decay for 4000 secs during several repeated measurements. In Fig. 6.7(b), the field dependent magnetization switching measurements performed under FCC condition between the 100 Oe and 400 Oe at 120 K near T_{Comp}. The system is cooled to 120 K under FCC condition at 100 Oe external field. The temperature and magnetic field kept constant, and magnetization recorded for 300 secs. Followed by the external magnetic field raised to 400 Oe by keeping the temperature remain constant and magnetization recorded for 300 secs. Again, the magnetic field taken back to 100 Oe at the same temperature and magnetization recorded for 300 secs. This cycle is repeated for five times and magnetization recorded with the time stamps. The observed magnetization response signifies the reversible nature of the magnetic spins and their alignment sensitive to the external magnetic field. This switching across the negative and positive magnetization sought to be very consistent and stable with time and this reversible behaviour persists as the system doesn't enter the lower temperatures crossing the T_{SF} which is favourable for spin flipped configuration Γ_4'. The time dependent magnetization response suggests the reliability of the magnetization polarity switching at different temperatures and fields making the examined system applicable

for switching devices in large scale for its multiple switching character [223, 228].

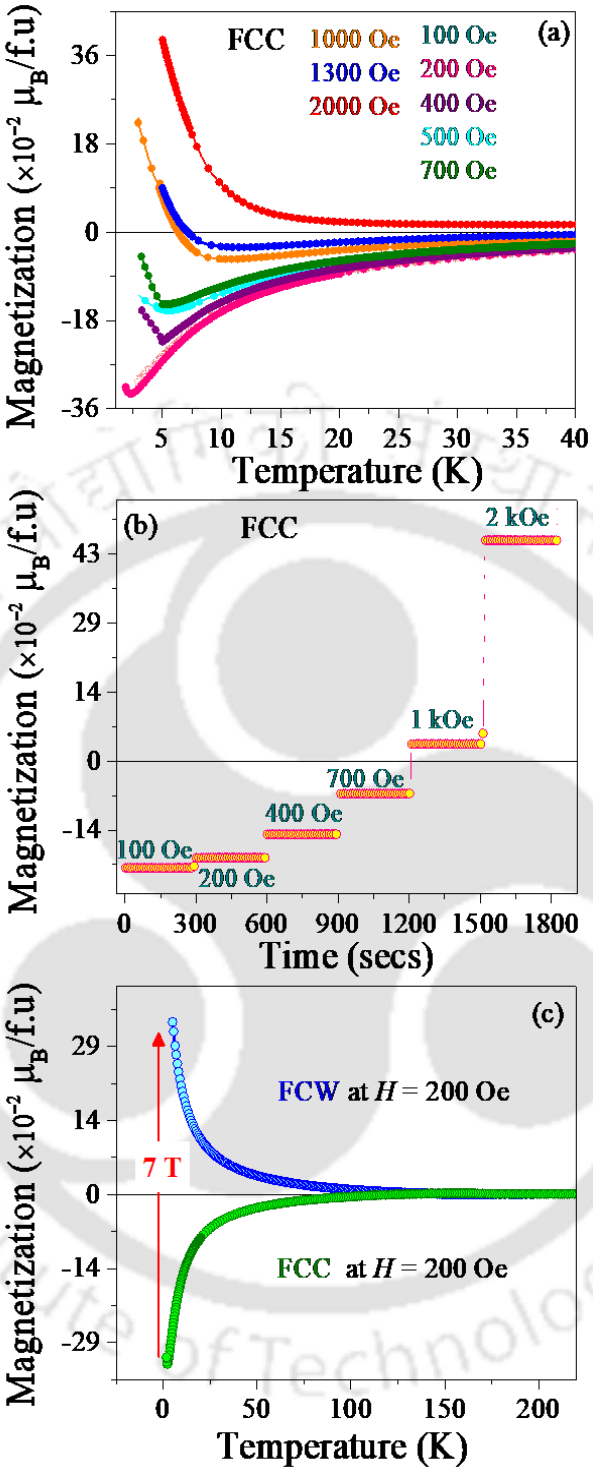

Fig. 6.6. (*a*) Temperature dependent magnetization of $Gd_{0.9}Ce_{0.1}CrO_3$ under FCC at different magnetic applied magnetic fields 100 Oe, 200 Oe, 400 Oe, 500 Oe, 700 Oe, 1 kOe, 1.3 kOe, 2 kOe. It displays the gradual activation of spin flip transitions induced by increasing the external field. (*b*) Magnetization versus time measurements at different magnetic fields represents the gradual increase in the no. of spins that flip *w.r.t.* applied field. (*c*) Temperature dependent magnetization under the FCC condition by applying external field of H = 200 Oe. Raise the magnetic field to 70 kOe at 5 K. Followed by decreasing the magnetic field again to 200 Oe and measurement was recorded under FCW condition.

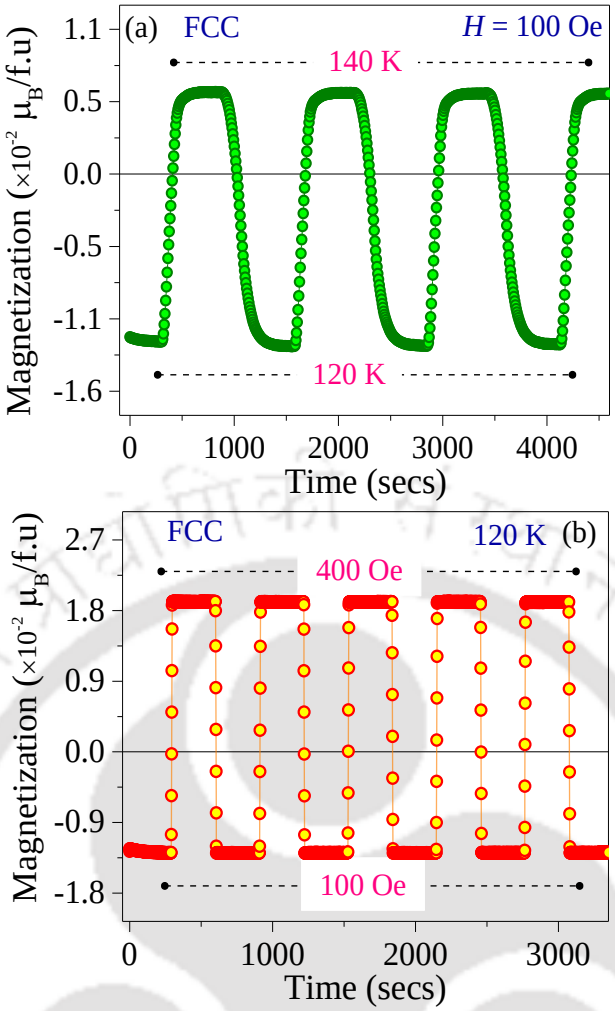

Fig. 6.7. Time stamp measurements of (*a*) temperature dependent magnetization switching of $Gd_{0.9}Ce_{0.1}CrO_3$ between 120 K and 140 K under FCC condition at applied field, *H* = 100 Oe, (*b*) field dependent magnetization switching between 400 Oe and 100 Oe under FCC condition at 120 K.

6.3.4.3. Field dependant magnetization

In order to investigate the influence of the A-site doping at on the magnetocaloric effect (MCE), I executed the first quadrant ZFCW isotherm hysteresis curves at different temperatures and within the field range from 0 Oe to +90 kOe. The experimental data is plotted in Fig. 6.8(a) for specific temperatures within 3 K to 20 K which includes the T_{SR} region. The MCE shows a direct proportional relation with the temperature derivative of magnetization ($\partial M/\partial T$) [33]:

$$\Delta S_M = \sum_i \frac{M_{i+1}(T_{i+1},H) - M_i(T_i,H)}{T_{i+1} - T_i} \Delta H \qquad 6.3$$

$$\Delta S_M = \int_0^H \left(\frac{\partial M(T,H)}{\partial T}\right) dH \qquad 6.4$$

with ΔS_M as the isothermal magnetic entropy change. From the above equation, it can be easily interpreted that higher the value of ($\partial M/\partial T$), larger the MCE value.

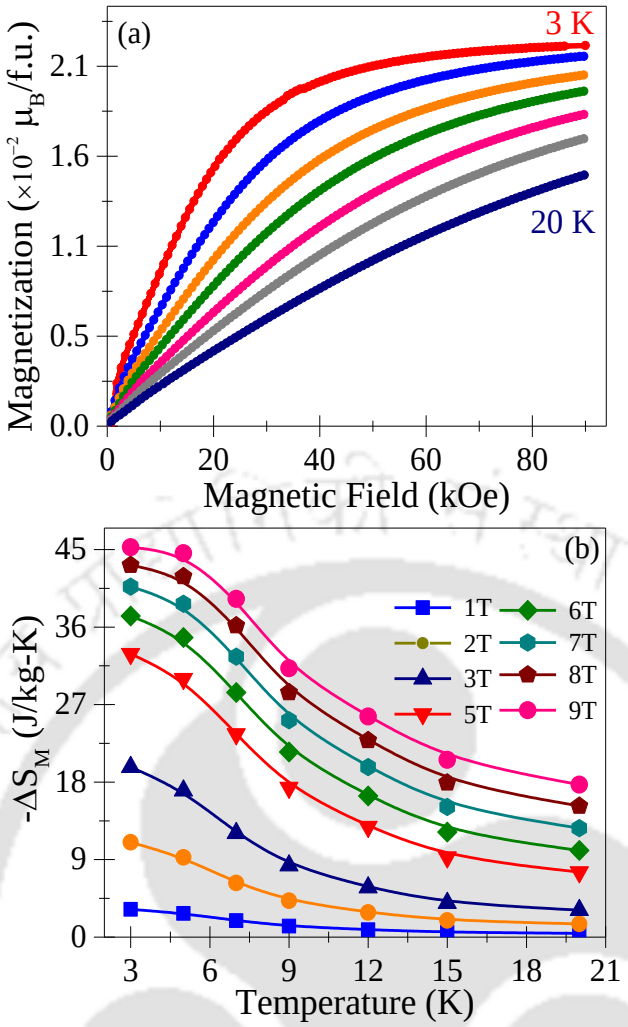

Fig. 6.8. (a) Magnetic field dependence of magnetization at different temperatures from 3 K to 20 K under ZFC. (b) Temperature dependence of isothermal entropy change, −ΔS.

On integrating the (∂M/∂T) with respect to chosen field values, the ΔS_M curves are plotted in Fig. 6.8(b). I observed the single polarity dominated curves with a hint of phase transition near the temperature 3 K starting at higher field value of 30 kOe which perfectly matches with the temperature dependent magnetization data. I can see the increment in ΔS_M value with the increase in magnetic field ΔH with the broadening of the peaks near the T_{SR} asymmetrically and shifts towards higher temperature with the increasing ΔH. I tabulated the comparative ΔS_M values with the similar systems previously reported in Table 6.2. Gd has already attained great attention for its higher MCE value as well as the potential candidate for the magnetocaloric refrigeration with the ΔS_M value of 10.2 J/kg-K [225]. The pristine $GdCrO_3$ polycrystalline material holds ΔS_M value as large as 31.6 J/kg-K under ΔH= 70 kOe at 5 K [226] and hence the highest till date among the Gd systems. In our sample I attained the value of 40.70 J/kg-K under ΔH = 70 kOe at 3 K and even higher (45.27 J/kg-K) at higher ΔH= 90 kOe which is the new maximum among the rare earth orthochromite and even among the Gd system in other crystal systems as well. Here, I can infer that numerous factors can control the MCE value for this A-site doped distorted system. One of these factors

Table 6.2. $-\Delta S_M$, RCP of various potential magnetic refrigerant materials having operating temperatures below 20 K along with $GdCrO_3$.

Material	μ_0H (T)	$-\Delta S_M$ (J/kg-K)	T (K)	RCP (J/kg)	δT_{FWHM} (T)	Reference
$Gd_{0.9}Ce_{0.1}CrO_3$	5	32.9	3			This work
$Gd_{0.9}Ce_{0.1}CrO_3$	6	37.3	3			This work
$Gd_{0.9}Ce_{0.1}CrO_3$	7	40.7	3			This work
$Gd_{0.9}Ce_{0.1}CrO_3$	9	45.3	3			This work
Gd	5	10.2	-	410		[225]
$La_{0.7}Ca_{0.3}MnO_3$	2	2.2		55		[229]
$La_{0.67}Sr_{0.1}Ca_{0.23}MnO_3$	5	6	-	278.55	46.65	[230]
$HoCrO_3$	7.2	7	20	408	-	[231]
$DyCrO_3$	4	8.4	15	217	-	[232]
$GdCrO_3$ (single crystal)	4	26.1	5	-	-	[233]
$GdCrO_3$ (polycrystalline)	7	36.9	5	542	-	[74]
$GdMnO_3$	8	31	19	-	-	[234]
$HoMnO_3$	7	12.5	10	312	-	[224]
$ErCrO_3$	7	10.7	15	416	-	[235]
$Er_{0.33}Gd_{0.67}CrO_3$	7	27.6	5	252	-	[235]
$TbCrO_3$	4.5	12.2	4.5	125	-	[216]
$DyCr_{0.7}Fe_{0.3}O_3$	7	13.1	5	500		[236]
$HoFeO_3$ (single crystal)	7	19.2	4.5	220		[237]
$HoCr_{0.7}Fe_{0.3}O_3$	7	6.8	20	387		[236]
$Ho_{0.67}Tm_{0.33}CrO_3$	7	6.7	17	-		[231]
$La_{0.6}Ca_{0.4}MnO_3$	5	8.3	61.2	508		[238]
$EuTi_{0.9}Cr_{0.1}O_3$	2	30	4.2	125	-	[239]
$La_{0.7}(Sr, Ba)_{0.3}MnO_3$	5	2.8	103.8	285.8	-	[240]
$La_{0.57}Nd_{0.1}Sr_{0.18}Ag_{0.15}MnO_3$	5	5.1		146.74	68.03	[241]

can be: this sample shows higher magnetization than the similar compounds with small coercive field leading to preserving more energy during the thermal process. Other than this, other elements possess higher magnetic moment (Dy ~ 10.63 μ_B) [214] but as the ΔS_M depends on the thermal derivative, the slope for this particular sample is higher resulting to enhancement in ΔS_M. The magnetic spin reorientation near T_{SR} (~ 3K) corresponds to the ordering of the Gd^{3+} spins due to the Gd^{3+}-Gd^{3+} interaction greatly influences the ΔS_M value.

6.4. Conclusion

In this chapter, I dealt with the structural and magnetization studies on a polycrystalline perovskite $Gd_{0.9}Ce_{0.1}CrO_3$ prepared from the standard solid-state reaction technique. PPMS based temperature and field (100 Oe $\leq H_{DC} \leq$ 1 kOe) dependent magnetization measurements under Field Cooled Cooling (FCC) protocol reveals the temperature and field-controlled spin-flip transition and negative magnetization phenomena which are the key features of the present investigated system. Under H_{DC}, the Cr^{3+} sublattice creates a local field to which the R^{3+} sublattice aligns anti-parallel and compensates the magnetization of the

Cr^{3+} sublattice which in turn gives to negative magnetization (M_N ~ -7.15 emu/g at T = 3 K). The overall magnetization M(T) undergoes a second transition at the low temperatures associated with spin-flip transition triggered by the critical field, H_C = 200 Oe at T_{SF} (10 K). Gradual increase in the overall magnetization and cross-over due to spin-flip transition can be understood by the Zeeman interaction term $E_{zeeman} = -\mu_0 M_{Net} H_{Ext} \text{Cos } \theta$. The preferred magnetic ordering is the Γ_4 structure which reconfigures into the Γ_4' which is due to the spins flip from $(00\bar{1})$ to (001) where, the *c*-axis is the easy axis. The system demonstrates an improved magneto-entropy value with $-\Delta S_M$ = 42 J/Kg-K, surpassing the previously documented values for $GdCrO_3$. The substitution of Ce^{3+} at the Gd^{3+} site leads to a decrease in the Cr-O-Cr bond angle, resulting in the enhancement of the magnetic entropy value. The reduction in the Cr-O-Cr bond angles through the substitution of Ce^{3+} at the Gd^{3+} site deduce such betterment in the magnetic entropy value. Such multiple thermo-magnetic switching of the investigated system plays a significant role in the development of the field of MRAM devices and as well as magnetic refrigeration.

Chapter 7
Conclusions and future work

This chapter discuss a brief summary of the key experimental findings on strongly correlated electron systems in the present study. It outlines the scope for future research on these complex oxides as well. The thesis work encompasses a systematic investigation of the effects of elastic strain on the magnetic and electronic structure experienced by the thin film heterostructures. And investigations on the magnetic, structural, and electronic properties of some grain-sized perovskite complex oxides. To facilitate understanding, I present a chapter-wise overview of the key findings from the previous chapters. Additionally, I conclude this section by discussing potential future research directions and the outlook for novel perovskite compounds, which may contribute to the development of this field and stand-in the progress of magneto-electronic technologies.

7.1. Conclusions

Our investigations in the **Chapter 3** demonstrates the main role of elastic-strain on the magnetic properties of $[Pr_{1-x}Ca_xMnO_3/SrTiO_3]_{15}$ superlattices. In this chapter, I focus on the fabrication of $[Pr_{0.7}Ca_{0.3}MnO_3/SrTiO_3]_{15}$ and $[Pr_{0.5}Ca_{0.5}MnO_3/SrTiO_3]_{15}$ superlattices on (001) oriented $LaAlO_3$ and $SrTiO_3$ single crystal substrates by PLD technique. Our findings and analysis offer compelling evidence supporting the significant influence of strain between the substrate and thin films on determining the overall magnetic ordering of the superlattices. The XRR and XRD investigations demonstrate the ratio of out-of-plane lattice to the in-plane lattice parameter, c/a is greater than 1 and less than 1 for the superlattices grown on $LaAlO_3$ and $SrTiO_3$. The occurrence of Kiessig fringe patterns confirms sharp interfaces between the manganite layer from $Pr_{1-x}Ca_xMnO_3$ and Titanite layer from $SrTiO_3$. Additionally, the RSM analysis demonstrate a weak tetragonal distortion in the grown superlattice structures. The *M-H* curves under isothermal condition exhibits an unconventional FM behaviour from the grown $[Pr_{0.7}Ca_{0.3}MnO_3/SrTiO_3]_{15}$ superlattice on $SrTiO_3$. The LAS analysis estimates the magneto-crystalline anisotropy constant, K_1 value to be 8×10^5 erg/cc with magneto-crystalline anisotropy field, H_K ~ 9 kOe which is two orders greater than the values of other superlattices. Superlattices on $LaAlO_3$ exhibit decrease in the T_C values less than 100 K but observed an enhancement in the saturation magnetization values. Our results demonstrate that the distortions in MnO_6 octahedra are brought by the elastic strain results in a possibility of non-orthogonal orbital overlapping. Substantial crystal field splitting observed at the e_g levels lead to the diminishing of FM double exchange interactions and the investigations as a whole assures the potentiality of the strain engineering in altering the magnetic structures from conventional to exotic which finds applications in the magneto-electronic industry.

In this **Chapter 4**, I conducted an extensive investigation into the structural, electronic, and magnetic properties of bulk polycrystalline $Y_{1-x}Ce_xCrO_3$ solid solutions. I found that the incorporation of Ce has a notable impact on the magnetic properties of the polycrystalline $YCrO_3$ system. Polycrystalline

$Y_{1-x}Ce_xCrO_3$ (x = 0, 0.05, 0.1, 0.2) synthesized using oxalate-based sol-gel technique. Substitution of the Ce^{3+} cation with radius, ($r_{Ce^{3+}}$) having larger radius than Y^{3+} cation ($r_{Y^{3+}}$) distorts the CrO_6 octahedra from 11.9 to 9.3, quantified by the octahedral distortion parameter (Δ). Magnetic properties reveal $YCrO_3$ exhibits Γ_4 (G_Z, F_y, A_x) phase consists of AFM and FM configurations within the magnetic spin structure. The magnetic Ce^{3+} incorporation ($x \geq 0.05$) at the non-magnetic Y^{3+}- sites enables the Γ_2 $(F_Z, G_y, C_x; F_z^R, C_x^R)$ at the low temperatures below the T_{SR} as a result of the rotation of spins in the *bc*-plane. A meticulous analysis of the differential M-H isotherms provides a definitive determination of the field-induced transitions at approximately 50 kOe (for x = 0.1 at 50 K). The asymmetric and symmetric exchange interaction constants quantified with the J_{AS} ~ 0.11 meV and J_S ~ 0.85 meV, respectively. Magnetic Ce^{3+} and Cr^{3+} contributes to the generation of anisotropy field constants of fourth order, H_{K_4} ~ 2.85 × 10^2 Oe and second order, H_{K_2} ~ 5.93 × 10^2 Oe. In contrast to the $YCrO_3$, the Ce^{3+} substituted $YCrO_3$ exhibits a substantial fourth-order magneto-crystalline anisotropy constant, K_4 ~ 1.35 × 10^5 erg/cc. One of the key findings from $Y_{0.9}Ce_{0.1}CrO_3$ is the significant exchange bias, H_{EB} ~ 2.5 kOe observed at the low temperature. The investigated system exhibits unique characteristic features, including a tuneable spin-flopped transition (~ 30 kOe), a large coercive field (H_C ~ 22 kOe), and a substantial negative magnetization (ΔM ~ 280 emu/mole). Overall, our results highlight the potentiality of the present investigated system in the field of thermo-magnetic sensors and switches and spintronic applications.

In **Chapter 5**, our focus shifts towards the study of irreversible metamagnetic transitions in distorted tetragonal $(Pr_{0.45-x}Yb_x)Sr_{0.55}MnO_3$. From the XPS investigations, the ratio of Mn^{3+} and Mn^{4+} that arise due to the divalent Sr cations is nearly 39 % : 61 %. The spin-orbit splitting, Δ_{S-O} value is measured to be 11.57 eV between the $2p_{\frac{3}{2}}$ and $2p_{\frac{1}{2}}$ orbitals. The distortions that occur in the MnO_6 octahedra due to the elongation of Mn-$O_{(2)}$ bond lengths in the *ab*-plane results in the multiple magnetic phases in the range of temperatures as low as 3 K to temperatures as high as 330 K. The substitution of Yb^{3+} (x = 0.05) bends the Mn-$O_{(2)}$-Mn bond angles to the highest value of ~ 123.7° which is far from its' x = 0.02 value of nearly ~ 158°. This distortion pursues high magnetic field and high temperature to enable and sustain the double exchange interaction bearing the T_C ~ 302 K which is the average *RT*. The metamagnetic transitions from AFM to FM are irreversible in nature *w.r.t.* the magnetic fields. These field-induced transitions prevail up to 220 K remarkably high compared to the pristine $Pr_{0.5}Sr_{0.5}MnO_3$. The FM to AFM orderings are sensitive to the external parameters such as temperature and magnetic field, where CHUF protocols reveals the magnetic glass signatures that enables FM islands in the AFM equilibrium phase. Overall, our results stand out in the race of potential candidates suitable for the applications of Mott insulators and magnetic memory storage devices.

In **Chapter 6**, I present compelling evidence for field-induced spin-flip transitions and large magneto-caloric value in $Gd_{0.9}Ce_{0.1}CrO_3$. Structural investigations and Rietveld refinement analysis reveal $Pbnm$ space group and No. 62 with orthorhombic crystal structure. The bond angles in the CrO_6 octahedra

i.e., Cr-$O_{(1)}$-Cr and Cr-$O_{(2)}$-Cr are found to be 155.3° and 145.5°, respectively. Magnetic properties suggest canted AFM with T_N ~ 173.4 K lead by the Cr^{3+}-anisotropy. Under H_{DC} = 100 Oe through different measurement protocols such as ZFCW, FCC and FCW, the system exhibits rich magnetic anomalies likely in the temperature range of 3 K to 300 K. Magnetization spin reversal of Gd^{3+} and Ce^{3+} w.r.t. the local field applied by the Cr^{3+} sublattice exhibits a negative magnetization under FCC and FCW which is further evident from the shifting of T_{Comp} with the external magnetic field by compensating the Cr^{3+} sublattice magnetic moments. Depending on the Zeeman energy, $(= -\mu_0 M_{Net} H_{Ext} \cos\theta)$ which can be tuned by the external magnetic field, the system goes into a transition from Γ_4 to Γ_4' as the spins-flip from $(00\bar{1})$ to (001). The critical field, H_{Cri} to induce such spin flip transition is ~ 200 Oe occurring at T_{SF} ~ 5 K and a gradual trend is observed *w.r.t.* H_{Ext} and a full-fledged irreversible transition taking the negative magnetization to positive magnetization value observed at 1 kOe. The investigated system demonstrates an improved magneto-entropy value of $-\Delta S_M$ = 45.3 J/Kg-K at 9 T, surpassing previously reported values for $GdCrO_3$. This enhancement in magnetic entropy can be attributed to the reduction in the Cr-O-Cr bond angles resulting from the substitution of Ce^{3+} at the Gd^{3+} site. Finally, I establish connections between all the magnetic properties, including the magnetic entropy change and thermo-magnetic switching, by highlighting the role of Ce substitution in $GdCrO_3$ which are making the present investigated system a suitable candidate for the magnetic storage and magnetic refrigeration applications.

7.2. Prospective for Future Work

This thesis presents a comprehensive investigation into the structural, electronic, magnetic, heat capacity, and phonon modes of various rare earth manganite and chromite systems, with a focus on their significant industrial applications. However, due to the extensive number of such materials and the current limitations of available state-of-the-art tools and techniques for exploring their fundamental physical properties, it was not possible to cover all the intriguing features associated with these promising materials. In this section, I provide a concise overview of the different experimental and theoretical explorations, serving as a valuable roadmap for future research. Our findings in this thesis serve as a foundational basis for further studies in this field.

1. In **Chapter 3**, I have synthesized and characterized the structural, electronic, and magnetic properties of $[Pr_{0.7}Ca_{0.3}MnO_3/SrTiO_3]_{15}$ and $[Pr_{0.5}Ca_{0.5}MnO_3/SrTiO_3]_{15}$ superlattices on (001) oriented $SrTiO_3$ and $LaAlO_3$ single crystal substrates. However, it would be very interesting to undergo the scanning SQUID microscopic studies of the superlattices $[Pr_{0.7}Ca_{0.3}MnO_3/SrTiO_3]_{15}$ for the confirmation and growth of FM islands in the Insulating and non-magnetic $SrTiO_3$ layer. Besides, exploration of ac-magnetic properties, resistivity, phonon modes with variable temperature, power and laser sources will provide a deeper understanding into these systems. It would be nice to extend the ab-initio calculations of these superlattices which will be helpful in making the structural and magnetic response of these superlattices more systematic.
2. In **Chapter 4**, I have analysed the magnetization reversal, exchange bias and field-induced transitions

in $Y_{1-x}Ce_xCrO_3$ polycrystalline solids. Expanding our analysis to investigate the ac-magnetic properties, resistivity, and phonon modes under varying temperature, would yield fascinating insights, developing our understanding of these systems. Additionally, extending the ab-initio calculations for these superlattices would contribute to a more systematic characterization of their structural and magnetic responses, further enhancing our knowledge in this area.

3. In **Chapter 5**, I have established an intimate connection between the structural, and magnetic characteristics for $(Pr_{0.45-x}Yb_x)Sr_{0.55}MnO_3$. Fabrication of heterostructures of $(Pr_{0.45-x}Yb_x)Sr_{0.55}MnO_3$ aiming to understand their charge-ordering (CO)/orbital-ordering (OO) characteristics for the room temperature metal-insulator transition applications would bring a better results and extend our understanding of this system for spintronic applications.
4. In **Chapter 6**, $Gd_{0.9}Ce_{0.1}CrO_3$ polycrystalline system reveals the remarkable demonstration of a giant magneto-caloric effect in $Gd_{1-x}Ce_xCrO_3$ stands out among all the rare-earth chromate perovskites. Further, specific heat measurements at different fields and ac-magnetic measurements reveal better understanding about the present system. Further advancements in this specific composition, whether through low-dimensional or large-scale studies, have the potential to make it suitable for magnetic refrigeration applications on a smaller industrial scale.

Bibliography

[1] Manchon *et al*., *Rev. Mod. Phys.* **91**, 035004 (2019).
[2] A. Ohtomo, and H. Y. Hwang, *Nature* **427**, 423 (2004).
[3] R. Ramesh, and D. G. Schlom, *Nat. Rev. Mater.* **4**, 257 (2019).
[4] Q. A. Akkerman, and L. Manna, *ACS Energy Lett.* **5**, 604 (2020).
[5] Q. A. Akkerman, G. Rainò, M. V. Kovalenko, and L. Manna, *Nat. Mater.* **17**, 394 (2018).
[6] K. Hirose *et al*., *Science* **358**, 734 (2017).
[7] R. H. Mitchell et al., *Mineral Mag.* **81**, 411 (2017).
[8] Y. Tokura, *Gordon and Breach Science*, New York, (2000).
[9] H. A. Jahn, and E. Teller, *Proc. R. Soc. Lond. A.* **161**, 220 (1937).
[10] H. Kawano *et al*., *Phys. Rev. Lett.* **78**, 4253 (1997).
[11] E. O. Wollan *et al*., *Phys. Rev.* **100**, 545 (1955).
[12] H. Fujishiro *et al*., *J. Phys. Soc. Jpn.* **67**, 2582 (1998).
[13] E. Pollert *et al*., *J. Phys. Chm. Solids*. **43**, 1137 (1982).
[14] C. N. R. Rao, *J. Phys. Chem. B.* **104**, 5877 (2000).
[15] J. P. Zhou *et al*., *Appl. Phys. Lett.* **75**, 1146 (1999).
[16] Y. Tomioka *et al*., *Phys. Rev. B* **53**, 1689 (1996).
[17] A. Urushibara *et al*., *Phys. Rev. B* **51**, 14103 (1995).
[18] J. S. Zhou *et al*., *Phys. Rev. B.* **81**, 214115 (2010).
[19] M. C. Weber *et al*., *Phys. Rev. B*. **85**, 054303 (2012).
[20] M. Taheri *et al*., *Phys. Rev. B.* **99**, 054411 (2019).
[21] K. Sardar *et al*., *Chem. Mater.* **23**, 48 (2011).
[22] N. Shamir, *Phys. Rev. B.* **24**, 6642 (1981).
[23] M. Taheri, *Phys. Rev. B.* **93**, 104414 (2016).
[24] H. Kronmueller, Crystallography and Chemistry of Perovskites *John Wiley & Sons Ltd* (2007).
[25] J. A. Brehm *et al*., *J. Chem. Phys.* **140**, 224703 (2014).
[26] O. Muller et al., *Science* **188**, 143 (1974).
[27] D. J. Boulay, *PhD thesis, The University of Western Australia*, (1996).
[28] S. Geller, *Kristallogr. Cryst. Mater.* **124**, 136 (1967).
[29] J. L. G. Munoz *et al., Phys. Rev. B.* **46**, 4414 (1992).
[30] J. E. Greedan, *J. Solid State Chem.* **116**, 118 (1995).
[31] V. M. Goldschmidt, *Die Naturwissenschaften*, **19**, 477 (1926).
[32] J. M. D. Coey, *Magnetism, and magnetic materials, Cambridge University Press*, (2010).
[33] H. Morrish, *The Physical Principles of Magnetism*, *IEEE Press* (2001).
[34] D. Zakharov, *Quantum Magnetism*, *Springer* 193 (2008).
[35] J. B. Goodenough *et al., Phys. Rev.* **98**, 391 (1955).
[36] J. B. Goodenough *et al., Phys. Rev.* **100**, 564 (1955).
[37] J. Kanamori, *J. Phys. Chem. Solids* **10**, 87 (1959).
[38] P.W. Anderson, *Phys. Rev.* **115**, 2 (1959).
[39] C. Zener, *Phys. Rev.* **81**, 440 (1951).
[40] P. W. Anderson and H. Hasegawa, *Phys. Rev.* **100**, 675 (1955).
[41] W.P. Meiklejohn, C.P. Bean, *Phys. Rev.* **102**, 1413 (1956).
[42] T. Moriya, *Phys. Rev.* **120**, 91 (1960).
[43] Y. S. Chen *et al., Appl. Phys. Lett.* **119**, 232401 (2021).
[44] J. Hejtmánek *et al., J. Appl. Phys.* **91**, 8275 (2002).
[45] A. N. Bogdanov *et al., Phys. Rev. B.* **75**, 094425 (2007).
[46] D. G. Oh *et al., Sci. Rep.* **13**, 3391 (2023).
[47] Y. Cao *et al., Appl. Phys. Lett.* **104**, 232405 (2014).
[48] R. L. Stamps, *J. Phys. A: Appl. Phys.* **33**, R247 (2000).
[49] H. Morita *et al., J. Phys. F: Met. Phys.* **16**, 507 (1986).
[50] E. V. Shipil *et al., IEEE Trans. Mag.* **30**, 797 (1994).
[51] G. L. Bona *et al., Appl. Phys. Lett.* **52**, 166 (1988).
[52] X. Lin *et al., J. Appl. Phys.* **76**, 6543 (1994).

[53] H. Danan, *Coll.* **32**, C1-131 (1971).
[54] J. Nogues, *Phys. Rev. B* (in press).
[55] R.D. Hempstead, *IEEE Trans. Magn.* **14**, 521 (1978).
[56] T. Lin *et al.*, *Appl. Phys. Lett.* **65**, 1183 (1994).
[57] S. M. Wu *et al.*, *Nat. Mater* **9**, 756–761 (2010).
[58] D. Deng. *et al.*, *Appl. Phys. Lett.* **107**, (2015).
[59] R. K. Dokala *et al.*, *J. Phys.: Condens. Matt.* **34**, (2022).
[60] W. Thomson, *Second edition, Richard Green, and Company: London*, 838 (1860).
[61] E. Warburg, *Ann. Phys. Chem.* **13**, 141 (1881).
[62] B. D. Cullity, and C. D. Graham, *Introduction to magnetic materials*, **7,** 197 (2009).
[63] A. Kumar, and S. M. Yusuf, *Phy. Rep.* **556**, 1 (2015).
[64] S. Biswas, and S. Pal, *Rev. Adv. Mater. Sci.* **53**, 206 (2018).
[65] S. Kasap and P. Capper, *Springer Handbook of Electronic and Photonic Materials*, 1023 (2006).
[66] G. A. Baraff *et al.*, *Phys. Rev. Lett.* **38**, 237 (1977).
[67] W. A. Harrison *et al.*, *Phys. Rev. B* **18**, 4402 (1978).
[68] H. Kroemer, *J. Cryst. Growth* **81**, 193 (1987).
[69] W. Prellier *et al.*, *Appl. Phys. Lett.* **77**, 1023 (2000).
[70] S. K. Singh *et al.*, *Appl. Phys. Lett.* **69**, 263 (1996).
[71] M. Ziese *et al.*, *Appl. Phys. Lett.* **98**, 132504 (2011).
[72] M. Ziese *et al.*, *J. Appl. Phys.* **113**, 063911 (2013).
[73] P. Chaddah *et al.*, *Phys. Rev. B* **77**, 100402(R) (2008).
[74] S. Mahana, *J. Phys. D: Appl. Phys.* **51**, 305002 (2018).
[75] H.M. Smith, and A.F. Turner, *Appl. Opt.* **4** 147 (1965).
[76] D. Dijkkamp *et al.*, *Appl. Phys. Lett.* **51** 619-621 (1987).
[77] S. Metev *et al.*, *John Wiley & Sons, Inc.*, 255-264 (1994).
[78] E. S. Toberer *et al.*, *Appl. Phys. Lett.* **93**, 062110 (2008).
[79] S. S. Mao *et al.*, *Appl. Phys. Lett.* **77**, 2464 (2000).
[80] Y. Du *et al.*, *J. Appl. Phys.* **108**, 093914 (2010).
[81] D. H. A. B. Guus Rijnders, *Pulsed Laser Deposition of Thin Films, John Wiley & Sons, Inc.*, 177 (2007).
[82] J. A. S. James, *Pulsed Laser Deposition of Thin Films, John Wiley & Sons, Inc.*, 229 (1994).
[83] K. Charles, *Introduction to Solid State Physics, John Wiley & Sons, Inc.*, 8th Edition (2005).
[84] D. Graef and M. E. McHenry, *Structure of Materials: An Introduction to Crystallography, Diffraction, and Symmetry, Cambridge University Press* (2007).
[85] G. Binnig *et al.*, *Phys. Rev. Lett.* **56**, 930 (1986).
[86] Y. Martin *et al.*, J. Appl. Phys. **61**, 4723–4729 (1987).
[87] D.A. Long, "Raman Spectroscopy", Michael Hollas, Modern Spectroscopy, Peter Bernath, Spectra of Atoms and Molecules.
[88] Schrieffer, *J. of Supercond.* (1983).
[89] L. P. Gorkov, *Sov. Phys.* 1364 (1959).
[90] K. Kopitzki, *Springer Berlin Heidelberg*, (2017).
[91] Clarke, *Wiley Online Library, The SQUID handbook*, **1** (2004).
[92] Johnson, *IEEE Spectrum* **51**, 40–61 (2014).
[93] Kraft, *Superconducting quantum interference device* (2017).
[94] R. von Helmolt *et al.*, *Phys. Rev. Lett.* **71**, 2331 (1993).
[95] S. Das *et al.*, *J. Appl. Phys.* **115**, 143902 (2014).
[96] A. Asamitsu *et al.*, *Nature* **388**, 50 (1997).
[97] A. Brinkman *et al.*, *Nat. Mater.* **6**, 493 (2007).
[98] H. Y. Hwang *et al.*, *Nat. Mater.* **11**, 103 (2012).
[99] J. Wu *et al.*, *Functional Metal Oxide Nanostructures, Springer Science & Business Media*, **149,** (2011).
[100] S. Thota *et al.*, *Appl. Phys. Lett.* **113**, 122405 (2018).
[101] P. Zubko *et al.*, *Annu. Rev. Condens. Matter Phys.* **2**, 141–165 (2011).
[102] D. Qu *et al.*, *Phys. Rev. Mater.* **2**, 102001 (2018).
[103] S. Das *et al.*, *APL Mater.* **6**, 100901 (2018).
[104] Y. Ijiri, *J. Condens. Mat. Phys.* **14**, R947 (2002).
[105] J. Ma *et al.*, *Phys. Rev. B* **79**, 174424 (2009).

[106] C. Kwon *et al*., *J. Appl. Phys.* **81**, 4950 (1997).
[107] X. Ke *et al*., *J. Appl. Phys.* **97**, 10K115 (2005).
[108] H. J. Molegraaf *et al*., *Adv. Mater.* **21**, 3470 (2009).
[109] Y. Konishi *et al*., *J. Phys. Soc. Jpn* **68**, 3790 (1999).
[110] Z. Fang *et al*., *Phys. Rev. Lett.* **84**, 3169 (2000).
[111] A. Millis *et al*., *J. Appl. Phys.* **83**, 1588 (1998).
[112] A. J. Millis *et al*., *Phys. Rev. Lett.* **74**, 5144 (1995).
[113] A. Antonakos *et al*., *J. Appl. Phys.* **104**, 063508 (2008).
[114] H. Yoshizawa *et al*., *Phys. Rev. B* **52**, R13145 (1995).
[115] S. Das *et al*., *Phys. Rev. B* **91**, 134405 (2015).
[116] C.-H. Chang *et al*., *Phys. Rev. B* **96**, 184408 (2017).
[117] S. Das *et al*., *Phys. Rev. B* **99**, 024416 (2019).
[118] S. Das *et al*., *J. Phys. D Appl. Phys.* **51**, 325001 (2018).
[119] V. Kiryukhin *et al*., *Nature* **386**, 813 (1997).
[120] Y. Tomioka *et al*., *Phys. Rev. B* **53**, R1689 (1996).
[121] W. Prellier *et al*., *J. Phys. Chem. Solids* **64**, 1665 (2003).
[122] G. Yang *et al*., *AIP Adv.* **6**, 055115 (2016).
[123] F. Chen *et al*., *Appl. Phys. Lett.* **80**, 2889 (2002).
[124] K. Baek *et al*., *Nanoscale* **9**, 582 (2017).
[125] S. L. Li *et al*., *J. Appl. Phys.* **105**, 033710 (2009).
[126] S. Asanuma *et al*., *Phys. Rev. B* **80**, 235113 (2009).
[127] Y. A. Freiman and H.-J. Jodl, *Phys. Rep.* **401**, 1 (2004).
[128] M. E. Fisher, *Philos. Mag.* **7**, 1731 (1962).
[129] M. Sahana *et al*., *J. Appl. Phys.* **89**, 6834 (2001).
[130] M. Ziese *et al*., *J. Appl. Phys.* **91**, 9930 (2002).
[131] S. Chakrabarty *et al*., *J. Alloys Compd.* **625**, 216 (2015).
[132] Y. Tomioka *et al*., *J. Phys. Soc. Jpn.* **64**, 3626 (1995).
[133] N. Jiang *et al*., *J. Alloys Compd.* **805**, 50 (2019).
[134] S. Komogortsev and R. Iskhakov, *J. Magn. Magn. Mater.* **440**, 213 (2017).
[135] X. Zhang and J.-P. Wang, *Appl. Phys. Lett.* **114**, 152401 (2019).
[136] E. C. Devi and I. Soibam, *J. Alloys Compd.* **772**, 920 (2019).
[137] N. M. Nemes *et al*., *IEEE Trans. Magn.* **44**, 2926 (2008).
[138] Y. Gao *et al*., *Prog. Nat. Sci.: Mater. Int.* **23**, 127 (2013).
[139] S. Ghosh *et al*., *Phys. Rev. B* **99**, 115135 (2019).
[140] M. Agarwal and E. Mishchenko, *Phys. Rev. B* **99**, 085439 (2019).
[141] S. Ghosh *et al*., *J. Magn. Magn. Mater.* **500**, 166261 (2019).
[142] X. Li *et al*., *Sci. Rep.* **7**, 40068 (2017).
[143] H. Meskine *et al*., *Phys. Rev. B* **64**, 094433 (2001).
[144] M. Schwickert *et al*., *Phys. Rev. B* **57**, 13681 (1998).
[145] M. Ahlberg *et al*., *Phys. Rev. B* **81**, 214429 (2010).
[146] C. R. Serrao *et al*., *Phys. Rev. B* **72** 220101 (2005).
[147] T. Ahmad T *et al*., *New J. Chem.* **40** 3216 (2016).
[148] A. K. Mall, and A. K. Pramanik *J. Phys.: Condens. Matter.* **33** 125803 (2021).
[149] J. Mao J *et al*., *Appl. Phys. Lett.* **98** 192510 (2011).
[150] J. Wang J *et al*., *Adv. Mater.* **31** 1904059 (2019).
[151] I. Ennen *et al*., *Sensors* **16** 904 (2016).
[152] T. Yamaguchi *et al., Phys. Rev. B* **8** 5187 (1973).
[153] T. Yamaguchi, *J. Phys. Chem. Solids* **35** 479 (1974).
[154] T. Morishita *et al., Phys. Rev. B* **24** 341 (1981).
[155] G. V. Subba Rao *et al., Solid State Commun.* **6** 177 (1968).
[156] J. R. Sahu *et al., J. Mater. Chem.* **17** 42 (2007).
[157] H. Thoma *et al., Phys. Rev. X* **11** 011060 (2021).
[158] I. A. Sergienko *et al., Phys. Rev. B* **73** 094434 (2006).
[159] D. Treves, *Phys. Rev.* **125** 1843 (1962).
[160] A. Durán *et al., Phys. Rev. Mater.* **2** 014409 (2018).

[161] S. W. Cheong *et al., Nat. Mater.* **6** 1476 (2007).
[162] I. S. Jacobs *et al., J. Appl. Phys.* **42** 1631 (1971).
[163] A. K. Mall *et al., J. Phys.: Condens. Matter.* **29** 495805 (2017).
[164] R. Goyal *et al., Solid State Communications* **226** 44 (2016).
[165] A. Makino *et al., Sci. rep.* **5** 16627 (2015).
[166] P. Dutta, *J. Phys.: Condens. Matter.* **20** 015218 (2007).
[167] G. Williamson and W. Hall, *Acta Metall.* **1**, 22 (1953).
[168] S. Farhadi *et al., J. Alloys Compd.* **471**, L5 (2009).
[169] J. Ding *et al., Mater. Sci. Eng. B* **171**, 31 (2010).
[170] A. M. Ektessabi, *Thin Solid Films* **377,** 621 (2000).
[171] E. E. Bragg, *Phys. Rev. B* **7** 4197 (1973).
[172] A. Durán *et al., J. Solid State Chem.* **183** 1863 (2010).
[173] K. Tsushima *et al., J. Appl. Phys.* **41** 1238 (1970).
[174] Y. Sharma *et al., J. Appl. Phys.* **115** 183907 (2014).
[175] W. N. Lawless, *Phys. Rev. B* **14** 134 (1976).
[176] W. N. Lawless, *Phys. Rev. B* **18** 2394 (1978).
[177] M. Tachibana *et al., Phys. Rev. B* **72** 064434 (2005).
[178] A. Durán A *et al., J. Phys.: Condens. Matter.* **20** 085219 (2008).
[179] A. Durán *et al., Mater. Chem. Phys.* **133** 1011 (2012).
[180] M. E. Wieser *et al., Pure Appl. Chem.* **78** 2051 (2006).
[181] A. McDannald *et al., Phys. Rev. B* **91** 224415 (2015).
[182] A. K. Mall, *Mater. Res. Express* **4** 076104 (2017).
[183] B. Tiwari *et al., J. Phys.: Condens. Matter*. **25** 216004 (2013).
[184] A. N. L. Jara *et al., Physica B* **546** 67 (2018).
[185] G. N. P. Oliveira *et al., J. Phys. Chem. Solids* **91** 182 (2016).
[186] G. Cinader, *Phys. Rev.* **155** 453 (1967).
[187] G. Vashisht *et al., J. Phys.: Condens. Matter.* **33** 335805 (2021).
[188] A. Elahi, *Polym. Sci. Ser. B* **57** 738 (2015).
[189] H. Zhang *et al., J. Appl. Phys.* **122** 204103 (2017).
[190] E. F. Bertaut *Acta Crystallogr. A* **24** 217 (1968).
[191] B. Tiwari *et al., Mater. Res. Express* **1** 036102 (2014).
[192] J. Mira *et al., Phys. Rev. B* **60** 2998 (1999).
[193] J. Y. Law *et al., Nat. Commun.* **9** 2680 (2018).
[194] A. Manchon *et al., Rev. Mod. Phys.* **91**, 035004 (2019).
[195] A. Urushibara *et al., Phys. Rev. B* **51**, 14103 (1995).
[196] A. Yakubovskii *et al., Phys. Rev. B.* **67**, 064414 (2003).
[197] T. Sarkar *et al., Phys. Rev. B.* **83**, 214428 (2011).
[198] M. Manekar *et al., J. Phys.: Condens. Matter*. **23**, 086001 (2011).
[199] P. Zhang *et al., J. Appl. Phys.* **113**, 17E144 (2013).
[200] Y. Tomioka *et al., Phys. Rev. Lett.* **74**, 5180 (1995).
[201] V. B. Naik *et al., Appl. Phys. Lett.* **98**, 112506 (2011).
[202] A. Ben J. Kharrata *et al., Solid State Sciences* **87**, 27 (2019).
[203] A. Mleiki *et al., J. Alloys. Compd.* **688**, 1214 (2016).
[204] M. Hervieu *et al., Chem. Mater.* **12**, 1456 (2000).
[205] J. Fontcuberta *et al., J. Appl. Phys.* **103**, 07B722 (2008).
[206] G. Qiang *et al., Appl. Phys. Lett.* **108**, 022906 (2016).
[207] F. Yen *et al., J. Mater. Res.* **22**, 2163 (2007).
[208] A. K. Pramanik and A. Banerjee, *Phys. Rev. B* **79**, 214426 (2009).
[209] R. Hornreich, *J. Mag. Mag. Mater.* **7**, 280 (1978).
[210] H. Rietveld, *J. App. Crystallo.* **2**, 65 (1969).
[211] A. M. A. López and M. A. A. Franco, *Inorg. Chem.* **48**, 11843 (2009).
[212] S. Wang *et al., Inorg. Chem.* **58**, 2315 (2019).
[213] J. A. Alonso *et al., Inorg. Chem.* **39**, 917 (2000).
[214] S. Das *et al., J. Phys.: Condens. Matter* **34**, 345803 (2022).
[215] T. M. Pan, and C. H. Lu, *Appl. Phys. Lett.* **99**, 113509 (2011).

[216] L. H. Yin, *J. Mater. Chem. C* **4**, 11198 (2016).
[217] S. Sasart, *Am. Mineral* **68**, 1189 (1983).
[218] H. Schuchert, *Physik* **222**, 105 (1969).
[219] M. Balkanski *et al.*, *Phys. Rev. B* **28**, 1928 (1983).
[220] A. M. Glazer, *Acta Cryst. B* **28**, 3384 (1972).
[221] L. H. Yin *et al.*, *Appl. Phys. Lett.* **104**, 032904 (2014).
[222] S. M. Yusuf *et al.*, *Appl. Phys. Lett.* **95**, 182506 (2009).
[223] A. Pal *et al.*, *Phys. Rev. Mat.* **4**, 044407 (2020).
[224] M. Shao *et al.*, *Appl. Phys. Lett.* **100**, 222404 (2012).
[225] M. H. Phan, and S.C. Yu, *J. Mag. Mag. Mater.* **308** 325 (2007).
[226] S. Yin, and M. Jain *J. Appl. Phys.* **120**, 043906 (2016).
[227] Taheri M *et al., Surface and Interface Analysis* **49**, 122 (2017).
[228] P. Mandal *et al., Phys. Rev. B.* **82**, 100416(R) (2010).
[229] M. Pękała *et al., Appl. Phys. A.* **90**, 237 (2008).
[230] Z. Mohamed *et al., J. Alloys. Comp.* **646**, 231 (2015).
[231] L. Meng *et al., RSC Adva.* **6**, 74765 (2016).
[232] A. McDannald *et al., J. Appl. Phys.* **114**, 113904 (2013).
[233] L. H. Yin *et al., J. Appl. Phys.* **117**, 133901 (2015).
[234] A. A. Wagh *et al., J. Phys. D: Appl. Phys.* **48**, 135001 (2015).
[235] J. Shi *et al., J. Appl. Phys.* **123**, 193901 (2018).
[236] G. Kotnana *et al., AIP Advan.* **8**, 056407 (2018).
[237] M. Shao *et al., Solid Stat. Comm.* **152**, 947 (2012).
[238] V. M. Andrade *et al., Acta Mater.* **102**, 49 (2016).
[239] Z. J. Mo *et al., J. Alloys Comp.* **649**, 674 (2015).
[240] R. Tlili *et al., Cer. Int.* **41**, 10654 (2015).
[241] S. Gharbi *et al., J. Mater. Sci.: Mater. Elec.* **31**, 11983 (2020).